

**Structural studies on novel antimicrobial peptides and target protection mechanisms in bacterial pathogens.**



**Timm Oliver Koller**

Hamburg, 2023

Dissertation zur Erlangung des Doktorgrades  
eingereicht an der Universität Hamburg  
Institut für Biochemie und Molekularbiologie  
Fachbereich Chemie



1. Gutachter: **Prof. Dr. Daniel N. Wilson**, Universität Hamburg, Hamburg, Deutschland, Institut für Biochemie und Molekularbiologie, Fachbereich Chemie

2. Gutachter: **Prof. Dr. Yury Polikanov**, University of Illinois, Chicago, USA, Biological Sciences

3. Gutachter: **Prof. Dr. Axel Innis**, University of Bordeaux, Bordeaux, France, European Institute of Chemistry and Biology

Prüfungskommission:

**Prof. Dr. Daniel N. Wilson**, Universität Hamburg, Hamburg, Deutschland, Institut für Biochemie und Molekularbiologie, Fachbereich Chemie

**Prof. Dr. Tobias Beck**, Universität Hamburg, Hamburg, Deutschland, Institut für Physikalische Chemie, Fachbereich Chemie

**Prof. Dr. Zoya Ignatova**, Universität Hamburg, Hamburg, Deutschland, Institut für Biochemie und Molekularbiologie, Fachbereich Chemie

Disputation: 10.03.2023

Druckfreigabe: 13.03.2023

Die für die Dissertation notwendigen Arbeiten wurden zwischen Juli 2018 und August 2022 an der Universität Hamburg im Institut für Biochemie und Molekularbiologie am Fachbereich Chemie in der Arbeitsgruppe von Prof. Dr. Daniel N. Wilson durchgeführt.

## 1. List of publications

**Structural basis for HflXr-mediated antibiotic resistance in *Listeria monocytogenes*.** Timm O. Koller†, Kathryn J. Turnbull†, Karolis Vaitkevicius, Caillan Crowe-McAuliffe, Mohammad Roghanian, Ondrej Bulvas, Jose A. Nakamoto, Tatsuaki Kurata, Christina Julius, Gemma C. Atkinson, Jörgen Johansson, Vasili Hauryliuk and Daniel N. Wilson. *Nucleic Acids Research*, 2022, <https://doi.org/10.1093/nar/gkac934> - **Published**

**The Myxobacterial Antibiotic Myxovalargin: Biosynthesis, Structural Revision, Total Synthesis and Molecular Characterization of Ribosomal Inhibition.** Timm O. Koller†, Ullrich Scheid†, Teresa Kösel†, Jennifer Herrmann, Daniel Krug, Helena I. Boshoff, Bertrand Beckert, Joanna C. Evans, Jan Schlemmer, Becky Sloan, Danielle M. Weiner, Laura E. Via, Atica Moosa, Thomas R. Ioerger, Michael Graf, Boris Zinshteyn, Maha Abdelshahid, Fabian Nguyen, Stefan Arenz, Franziska Gille, Maik Siebke, Tim Seedorf, Oliver Plettenburg, Rachel Green, Anna-Luisa Warnke, Joachim Ullrich, Ralf Warrass, Clifton E. Barry 3rd, Digby F. Warner, Valerie Mizrahi, Andreas Kirschning, Daniel N. Wilson and Rolf Müller, *Journal of the American Chemical Society*, 2023, 145, (2), 851-863. <https://doi.org/10.1021/jacs.2c08816> - **Published**

**Structural basis for translation inhibition by the glycosylated antimicrobial peptide Drosocin from *Drosophila melanogaster*.** Timm O. Koller†, Martino Morici†, Max Bergert†, Haaris A. Safdari, Deepti S. Lele, Bertrand Beckert, Kanwal J. Kaur, Daniel N. Wilson. <https://doi.org/10.1038/s41589-023-01293-7> - **accepted** at *Nature Chemical Biology* as of March 2023.

**Context-specific action of macrolide antibiotics on the eukaryotic ribosome.** Maxim S. Svetlov, Timm O. Koller, Sezen Meydan, Vaishnavi Shankar, Dorota Klepacki, Norbert Polacek, Nicholas R. Guydosh, Nora Vázquez-Laslop, Daniel N. Wilson, Alexander S. Mankin. *Nat Commun*, **12**, 2803, (2021). <https://doi.org/10.1038/s41467-021-23068-1> - **Published**

**Total Synthesis and Biological Evaluation of Paenilamicins from the Honey Bee Pathogen *Paenibacillus larvae*.**

Timur Bulatov, Sebastian Gensel, Andi Mainz, Tam Dang, Timm O. Koller, Kerstin Voigt, Julia Ebeling, Daniel N. Wilson, Elke Genersch, Roderich D. Süssmuth. Journal of the American Chemical Society, 2022, 144, (1), 288-296. <https://doi.org/10.1021/jacs.1c09616> - **Published**

**The cyclic octapeptide antibiotic argyrin B inhibits translation by trapping EF-G on the ribosome during translocation.** Maximiliane Wielandt†, Mikael Holm†, Emily J. Rundlet†, Martino Morici, Timm O. Koller, Tinashe P. Maviza, Domen Pogorevc, Ilya A. Osterman, Rolf Müller, Scott C. Blanchard, Daniel N. Wilson. PNAS, 2022, 119, (19), 1-9. <https://doi.org/10.1073/pnas.2114214119> - **Published**

## 2. Table of Contents

<b>1. List of publications .....</b>	<b>4</b>
<b>3. Acknowledgements.....</b>	<b>10</b>
<b>4. Abbreviations .....</b>	<b>12</b>
<b>5. Zusammenfassung.....</b>	<b>16</b>
<b>6. Summary.....</b>	<b>18</b>
<b>7. Introduction .....</b>	<b>20</b>
<b>7.1. The bacterial ribosome and its composition.....</b>	<b>20</b>
<b>7.2. Translation.....</b>	<b>22</b>
7.2.1. Initiation.....	23
7.2.2. Elongation .....	26
7.2.3. Termination .....	31
7.2.4. Ribosome recycling.....	32
<b>7.3. Antibiotics and antimicrobial peptides targeting the ribosome .....</b>	<b>33</b>
7.3.1. Antimicrobial peptide myxovalargin .....	36
7.3.2. Proline-rich antimicrobial peptide drosocin .....	38
7.3.3. Context-specific action of macrolide antibiotics on the eukaryotic ribosome .....	40
<b>7.4. Target protection.....</b>	<b>42</b>
7.4.1. HflX and HflXr .....	43
<b>8. Methods.....</b>	<b>46</b>
<b>8.1. Polymerase chain reaction.....</b>	<b>46</b>
<b>8.2. In vitro transcription .....</b>	<b>47</b>
<b>8.3. Purification of mutant ribosomes .....</b>	<b>48</b>
<b>8.4. Firefly luciferase in vitro translation assay with mutant ribosomes.....</b>	<b>48</b>
<b>8.5. Complex preparation for Cryo-EM.....</b>	<b>49</b>
8.5.1. Myxovalargin.....	49
8.5.2. E. coli 70S-Dro1-complex .....	51
8.5.3. G2400A mutant S. cerevisiae 80S-Tel-complex.....	51
8.5.4. L. monocytogenes complexes .....	51
<b>8.6. Cryo-electron microscopy data collection .....</b>	<b>52</b>

<b>8.7. Single-particle reconstruction of cryo-EM datasets and molecular modelling</b>	<b>53</b>
8.7.1. Single-particle reconstruction of cryo-EM datasets.....	53
8.7.2. Local resolution and local filtering calculations .....	54
8.7.3. Molecular modelling .....	54
8.7.4. Single particle analysis of myxovalargin complexes .....	55
8.7.5. Single particle analysis of <i>Escherichia coli</i> -70S-Dro1 complex .....	61
8.7.6. Single particle analysis of <i>S. cerevisiae</i> 80S-Tel-complex.....	65
8.7.7. Single particle analysis of <i>L. monocytogenes</i> complexes.....	68
<b>8.8. Figure making.....</b>	<b>75</b>
<b>9. Aim of this thesis .....</b>	<b>76</b>
<b>10. Results.....</b>	<b>78</b>
<b>10.1. Myxovalargins .....</b>	<b>78</b>
10.1.1. Myxovalargin A – high resolution structure reveals binding mode and molecular interactions.....	78
10.1.2. Myxovalargin B – mechanism of action to inhibit translation .....	81
<b>10.2. Cryo-EM structures of the O-glycosylated proline-rich antimicrobial peptide drosocin</b>	<b>84</b>
10.2.1. Drosocin inhibits <i>in vitro</i> translation during termination by trapping ribosomes at stop codons	84
10.2.2. Cryo-EM structure of O-glycosylated Dro1 on the ribosome .....	86
10.2.3. Cryo-EM structure of the elongating 70S ribosome in complex with drosocin.....	88
10.2.4. Interactions of drosocin within the NPET of the terminating 70S-Dro1-complex .....	90
10.2.5. Interactions of the Dro1 glycosylation with the ribosome.....	94
<b>10.3. Cryo-EM structure of telithromycin bound to the G2400A mutant 80S <i>S. cerevisiae</i> ribosome .....</b>	<b>96</b>
<b>10.4. <i>L. monocytogenes</i> structures .....</b>	<b>99</b>
10.4.1. Cryo-EM structure of Lincomycin on the <i>L. monocytogenes</i> 50S subunit .....	101
10.4.2. Cryo-EM structure and modelling of the GTPase HflXr in complex with <i>L. monocytogenes</i> 50S subunit.....	103
10.4.3. Conformational changes in the PTC induced by HflXr is incompatible with drug binding	106
<b>11. Discussion.....</b>	<b>110</b>
<b>11.1. Mechanism of action of the antimicrobial peptide MyxA and MyxB .....</b>	<b>110</b>



11.2.	Proline-rich antimicrobial peptide drosocin and importance of O-glycosylation for translation inhibition.....	115
11.3.	Context-specificity of macrolide antibiotics on eukaryotic translation....	119
11.4.	Target protection by GTPase HflXr .....	122
<b>12.</b>	<b>References .....</b>	<b>126</b>
<b>13.</b>	<b>Supplementary Information.....</b>	<b>160</b>
13.1.	Myxovalargin .....	160
13.2.	Drosocin.....	164
13.3.	Telithromycin 80S .....	168
13.4.	<i>Listeria monocytogenes</i> complexes .....	171
<b>14.</b>	<b>Auflistung der Gefahrstoffe nach GHS.....</b>	<b>178</b>
<b>15.</b>	<b>Eidesstattliche Erklärung.....</b>	<b>180</b>



### 3. Acknowledgements

I would like to thank Prof. Dr. Daniel N. Wilson for accepting me as a graduate student and providing a very supportive atmosphere, not only in a work perspective but also making the group feel like a small family. I really enjoyed the four years of my PhD. The constant feedback helped me to improve my own work to an extent I couldn't imagine before I started. Especially in the two years of Corona, when we were not able to talk in person, Daniel was always available to videocall and never hesitated to look out for our well-being. Also, allowing me to come to the lab and have a structured day helped me to keep my sanity and productivity throughout this time period.

A very special thank you goes to Dr. Helge Paternoga, who not only proved to be one of the best post-docs that I have met so far, but without whom I would not have managed some of the scientific, modelling and processing struggles that the PhD brought along. Also, he is one of the nicest people you can meet and discuss with. The same goes for Dr. Michael Graf, Dr. Caillan Crowe-McAuliffe and Dr. Bertrand Beckert, who guided me when I arrived in the group, shared an office for a long time, and who suffered through way too many questions that I asked in the years.

The warmest of thank you goes to Daniela Hess-Otto. Without her administrative advice and support, me and the group would have not worked as efficient and countless of my projects would have been delayed. We also had the nicest and longest conversations about anything one can imagine.

A huge thank you to Martino Morici and Max Berger, who have not only been friends, and lab mates but with who I was able to share a first author publication. And of course Martino has been an outstanding office roommate for the last year, a time that I will never forget.

A big thank you also to all members of the group that have supported me, namely: Karoline Raulf, Lucy (Dr. Lyudmila Dimitrova-Paternoga), Witek (Dr. Witold Szaflarski), Katrin Möller, Andrea Dallapè, Dr. Maximiliane Wieland, Dr. Claudia Müller, Dr. Maha Abdelshahid, Haaris Ahsan Safdari, Dr. Patrick Ziegel Müller, Tatjana Claussen and Elena Wasiljew. And not to be forgotten, all students that were supervised directly or indirectly by me and that helped me to prepare samples for some of the work presented in this thesis.

The work presented in this thesis has been prepared involving many collaborators who I would like to thank and without whom these publications would have not been possible.

A huge thank you to Prof. Vasili Haurlyiuk and his lab members for data and sample preparation, as well as Dr. Gemma Atkinson for phylogenetic analysis for the HflXr paper.

Thank you to Prof. Dr. Rolf Müller for organizing the Myxovalargin project and all labs that were involved to finalize this paper.

A special thank you also to Prof. Alexander S. Mankin, Dr. Nora Vázquez-Laslop, and Dr. Maxim Svetlov for giving me the opportunity to work on context-specificity in eukaryotes and supporting us with strains for a variety of projects.

I would also like to thank Dr. Jiří Nováček (Central European Institute of Technology (CEITEC)), Dr. Michael Hall (Umeå Centre for Electron Microscopy) and Bertrand (Dubochet Center for Imaging) and their respective facilities for cryo-EM data collection.

As the most important people in my life, not only during the Doctor but also in every situation of my life, I want to thank my parents Andreas and Martina for the endless support and unconditional love they show me every single day. I am more than grateful that you supported me emotionally, even when this meant enduring hours of complaining. I was always able to come with whatever problem life threw at me and get advice from both of you. I still can't think of anything that makes me feel better and more protected than having lunch together, cooking together or simply drinking a coffee at your home.

A huge thank you also goes to my grandparents, my aunts, uncles, and cousins, both in Hamburg and in Switzerland, to support me in the last four years, even more than they did before. We enjoyed countless family meetings and holidays together and I can't be more thankful to everyone listening to me talking about experiments not working.

I also want to thank all my friends for support, advice and most importantly spending free time outside of work. A special thank you goes to Dominique Kehlenbeck for providing feedback to this work.

Finally, I would like to thank the Deutsche Forschungsgemeinschaft (DFG) for financially supporting my PhD.

## 4. Abbreviations

Å	Ångstrom
A-site	Amino acyl-site
aa	amino acyl
ABC	ATP-binding cassette
ABCF	ATP-binding cassette F family
AG	Agmatine
AMP	Antimicrobial peptide
ASD	anti-Shine-Dalgarno
ASL	anticodon stem loop
ATP	Adenosine triphosphate
Azy	Azithromycin
C-terminus	Carboxyl terminus
Cam	Chloramphenicol
Cln	Clindamycin
cryo-EM	Cryogenic electron microscopy
CTD	C-terminal domain
CTF	Contrast transfer function
Dal	Dalfopristin
DC	Decoding center
ddH <sub>2</sub> O	nuclease-free deionized water
DDM	Dodecyl-β-D-maltoside
DMS	Dimethyl sulfate
DNA	Deoxyribonucleic acid
Dro	Drosocin
E-site	Exit-site
Ec (Eco)	<i>Escherichia coli</i>
ED	effective dose
EF	Elongation factor
eIF5A	Eukaryotic initiation factor 5A

Ery	Erythromycin
Fig	Figure
Fluc	Firefly luciferase
fMet	N-formylmethionine
FSC	Fourier shell correlation
FWD	forward
GDP	Guanosine diphosphate
GDPNP	Phosphoaminophosphonic acid-guanylate ester
GGQ (-motif)	Glycine-Glycine-Glutamine (-motif)
GTD	GTPase domain
GTP	Guanosine triphosphate
h/H	helix
IB	Isobutric acid
IBX	Iboxamycin
IC	Initiation complex
IC	Inhibitory concentration
IF	Initiation factor
Klb	Klebsazolicin
LD	lethal dose
Lmo	<i>Listeria monocytogenes</i>
Lnc	Lincomycin
Lnz	Linezolid
LSU	large subunit
MBA	3-methylbutanoic acid
MIC	minimal inhibitory concentration
mRNA	messenger RNA
Mtu	<i>Mycobacterium tuberculosis</i>
MyxA/B	Myxovalargin A/B
N-terminus	Amino terminus
NC	nascent chain
NPET	nascent peptide exit tunnel

NTD	N-terminal domain
Ocu	<i>Oryctolagus cuniculus</i>
OD	optical density
P-site	peptidyl-site
PCR	Polymerase chain reaction
PDB	Protein data bank
Pha	Phasolizin
P <sub>i</sub>	inorganic phosphate
PIC	Preinitiation complex
PrAMPs	Proline-rich antimicrobial peptides
PTC	Peptidyl transferase center
px	pixel
Qin	Quinupristin
REV	reverse
RF	Release factor
RNA	Ribonucleic acid
RRF	Ribosome recycling factor
rRNA	ribosomal RNA
RRP	Ribosome protection protein
Sau	<i>Staphylococcus aureus</i>
Sc	<i>Saccharomyces cerevisiae</i>
SD	Shine-Dalgarno
SQ	Squires
SRL	Sarcin ricin loop
SSU	small subunit
Sup.Fig.	supplementary figure
TC	Ternary complex
TcmX	Tetracenomycin X
Tel	Telithromycin
Tia	Tiamulin
tRNA	transfer RNA

UTR	untranslated region
Vg	Virginiamycin
W	Water
wt	wildtype

For amino acids the standardized and commonly accepted single- and triple-letter and for nucleotides the single-letter nomenclature is used. For bacteria the genus is used abbreviated after the first entry.



## 5. Zusammenfassung

Die steigende Zahl multi-resistenter pathogener Bakterien macht verfügbare Antibiotika auf lange Zeit gesehen wirkungslos und erfordert eine umgehende Erforschung neuer antimikrobieller Substanzen. Eine Vielzahl der aktuell klinisch verwendeten Antibiotika hat das Ribosom als Ziel, spezifisch die Translation. In allen lebenden Zellen synthetisiert das Ribosom während der Translation die Proteine basierend auf einer mRNA-Vorlage. Jede Stufe der Translation wird von mindestens einer Antibiotika-Klasse als Ziel genutzt und basierend auf einer großen Vielfalt chemischer Verbindungen und Wirkmechanismen bietet sich ein großes Potential für zukünftiges strukturbasiertes Wirkstoffdesign. Eine der Methoden der Wahl für das strukturbasierte Wirkstoffdesign von antimikrobiellen Verbindungen, die das Ribosom als Ziel haben, ist die Kryo-Elektronenmikroskopie. Die großen Ribosomen-Komplexe können im schockgefrorenen Zustand, durch Vitrifizierung in einer amorphen Eisschicht eingehüllt, in einem nahezu physiologischen Zustand analysiert und durch „Single Particle Analysis“ in fast atomarer Auflösung 3-dimensional rekonstruiert werden. In dieser Arbeit wurden zwei natürlich vorkommende antimikrobielle Peptide im Komplex mit den *Escherichia coli* 70S Ribosomen aufgeklärt, genauer die Myxovalargin-Derivate MyxA/B aus *Myxococcus fulvus* und die Prolin-reichen und O-glykosylierten Drosocin-Derivate aus *Drosophila melanogaster*. Während beide Peptide im ribosomalen Tunnel binden, verwenden sie sehr unterschiedliche Mechanismen, die verschiedene Stufen der Translation behindern. MyxA/B füllen den Tunnel in einer sehr kompakten Konformation aus und werden dabei durch direkte und Wasser-vermittelte Interaktionen mit 23S ribosomalen RNA-Nukleotiden stabilisiert. In Anwesenheit von MyxA/B kann die Initiator fMet-tRNA<sup>fMet</sup> in der P-Stelle des Ribosoms binden, wird jedoch durch die C-terminalen hydrophoben Reste von MyxA/B an der korrekten Akkommodation des CCA-Endes gehindert. Aminoacyl-tRNAs, die in der A-Stelle des Ribosoms binden, würden nahe dem Peptidyltransferase-Zentrum sterisch mit MyxA/B überlappen. Dies führt zur Inhibierung der letzten Stufe der Initiation. Während Drosocine ebenfalls im Tunnel binden und direkte sowie Wasser-vermittelte Interaktionen bilden, weisen diese natürliche O-Glykosylierungen an ihrem Thr11 auf, welche das A752-U2609 Basenpaar der 23S rRNA-Nukleotide spalten und hierdurch die Bindung im Tunnel

weiter verstärken. Drosocine verhindern die Dissoziation der „Release“ Faktoren von den Ribosomen in einem Post-Hydrolyse Status und inhibieren die Terminierung und das anschließende Recycling des Ribosoms.

Neben Antibiotika, die das Ribosom als Ziel haben, um mittels bakterizider Effekte die Bakterien zu töten oder mittels bakteriostatischen das Wachstum zu stören, ist auch die Untersuchung der Antibiotika, die zur Krebsbekämpfung auf die Translation von spezifischen Proteinen in eukaryotischen Zellen abzielen. In der eukaryotischen Translation ist Kontextspezifität von Antibiotika essenziell, um die Behinderung von genereller Proteinsynthese zu vermeiden. In dieser Arbeit wurde das für seine kontextspezifische Inhibierung der Peptidbildungs-Bildung in Bakterien bekannte Makrolid-Antibiotikum Telithromycin, an mutierten *Saccharomyces cerevisiae* Ribosomen getestet. Eine identische Bindungsstelle für das Antibiotikum in den eukaryotischen Ribosomen wurde identifiziert. Forschungspartner bestätigten eine kontextspezifische Inhibierung der eukaryotischen Translation, welches eine neue Basis für diese Klasse von Antibiotika in Eukaryoten schafft.

Für die Zukunft der Antibiotika-Landschaft ist neben dem strukturbasiertem Wirkstoffdesign von Verbindungen, die sowohl bakterielle als auch eukaryotische Translation als Ziel haben, die Aufklärung der Mechanismen wichtig, die Antibiotikaresistenz in Bakterien verursachen. In dieser Arbeit wurde die Struktur eines neuartigen Resistenz-Homologes des „Housekeeping Splitting“ Faktors GTPase HflX aus *Listeria monocytogenes*, HflX<sub>r</sub>, aufgeklärt. Diese zeigt, dass das Arg149 aus der „loop“-Region der N-terminalen Domäne II von HflX<sub>r</sub> deutlich tiefer in das Peptidyltransferase-Zentrum eindringt, als nicht Resistenz-bringendes HflX, dessen „loop“ zwei Aminosäuren kürzer ist. Der HflX<sub>r</sub> „loop“ induziert Konformationsänderungen in den 23S rRNA-Nukleotiden, welche die Bindung von Antibiotika nahe dem Peptidyltransferase-Zentrum unmöglich machen, wodurch im geringem Maße Resistenz gegen diese Antibiotika erzeugt wird.

Die hier beschriebenen Arbeiten zur strukturellen Aufklärung verschiedener antimikrobieller Verbindungen, sowie biochemischer und molekularbiologischer Methoden an Ribosomen-spezifischen Antibiotika, vermitteln ein tieferes Verständnis in Mechanismen der Antibiotikaresistenz und bekräftigen die Wichtigkeit von strukturellem Wirkstoffdesign im Kampf gegen multiresistente Pathogene und Krankheiten.

## 6. Summary

The rise in multidrug resistance in bacterial human pathogens may soon render our current repertoire of antibiotics obsolete and it requires immediate action to research new antimicrobial substances. Most clinically used antibiotics target the ribosome and more specifically interfere with translation. In all living cells, during translation the ribosome synthesizes proteins based on a mRNA template. Each step of this process is targeted by at least one class of known antibiotics and provides a huge variety of chemical scaffolds and mechanisms of action that have potential for future structure-based drug design. One of the methods of choice for structure-based drug design of antimicrobials targeting the ribosome is cryo-electron microscopy. Ribosomal complexes can be analyzed in a flash-frozen, near-physiological state through vitrification in a layer of amorphous ice and single particle analysis achieves near atomic resolution of 3D reconstructions. In this study two naturally occurring antimicrobial peptides were structurally investigated in complex with the *Escherichia coli* 70S ribosome, namely the myxovalarginins MyxA/B from *Myxococcus fulvus* and the proline-rich and O-glycosylated drosocins from *Drosophila melanogaster*. While both peptides bind within the nascent peptide exit tunnel of the ribosome, they have very different mechanisms of inhibition and interfere with different stages of translation. MyxA/B occludes the tunnel in a very compacted conformation and is stabilized by both direct and water-mediated interactions with the 23S ribosomal RNA nucleotides of the tunnel. In the presence of MyxA/B, the binding of an initiator fMet-tRNA<sup>fMet</sup> in the P-site of the ribosome is possible but the C-terminal hydrophobic moieties of MyxA/B interfere with proper accommodation of the CCA-end. Incoming amino acyl-tRNAs in the A-site would sterically clash close to the peptidyl transferase centers with MyxA/B and as a result translation is inhibited at a late stage of initiation. While drosocins also bind in the nascent peptide exit tunnel and form both direct and water-mediated interactions with the ribosome, they are naturally O-glycosylated on Thr11 which splits the base-pair of A752-U2609 of the 23S rRNA stabilizing their binding in the tunnel. They lock the release factors on the ribosome in a post-hydrolysis state and interfere with translation termination and subsequent recycling.

While antibiotics targeting bacterial translation are meant to kill the bacteria with a bactericidal effect or stop their growth with a bacteriostatic effect, the use of

antibiotics targeting the synthesis of specific proteins in eukaryotic cells to fight cancer are similarly important. In eukaryotic translation the context-specificity of antibiotics is essential to avoid interfering with general protein synthesis. In this study a macrolide antibiotic, telithromycin, which is known to cause context-specific inhibition of peptide bond formation in bacteria, was tested on mutant *Saccharomyces cerevisiae* ribosomes, which revealed an identical binding site for the drug in the eukaryotic ribosome. Additionally, collaborators confirmed context-specificity in eukaryotic translation, opening a new scaffold for this class of antibiotics on eukaryotes.

While structure-based drug design of compounds targeting both bacterial and eukaryotic translation is essential for the future of the antibiotic landscape, the mechanisms conferring resistance in bacteria similarly deserve attention. In this study a structure of a novel resistance homolog of the housekeeping splitting factor GTPase HflX in *Listeria monocytogenes*, HflX<sub>r</sub>, is presented. The structure revealed that Arg149 of the loop region of the N-terminal domain II of HflX<sub>r</sub> penetrates deeper into the peptidyl transferase center than the non-resistance providing homolog HflX, which has a loop that is two amino acids shorter. The loop of HflX<sub>r</sub> induces a conformational change in the 23S rRNA nucleotides of the PTC which is incompatible with antibiotic binding near the PTC, thereby providing a low level of resistance to these antibiotics.

The structural investigation of different antimicrobial compounds presented in this study, combined with other biochemical and molecular biology approaches, on antibiotics targeting bacteria and eukaryotes, as well as a deeper understanding of resistance mechanisms, could provide insight into the importance of structure-based drug design efforts in the fight against multi-drug resistant pathogens and human diseases.

## 7. Introduction

### 7.1. The bacterial ribosome and its composition

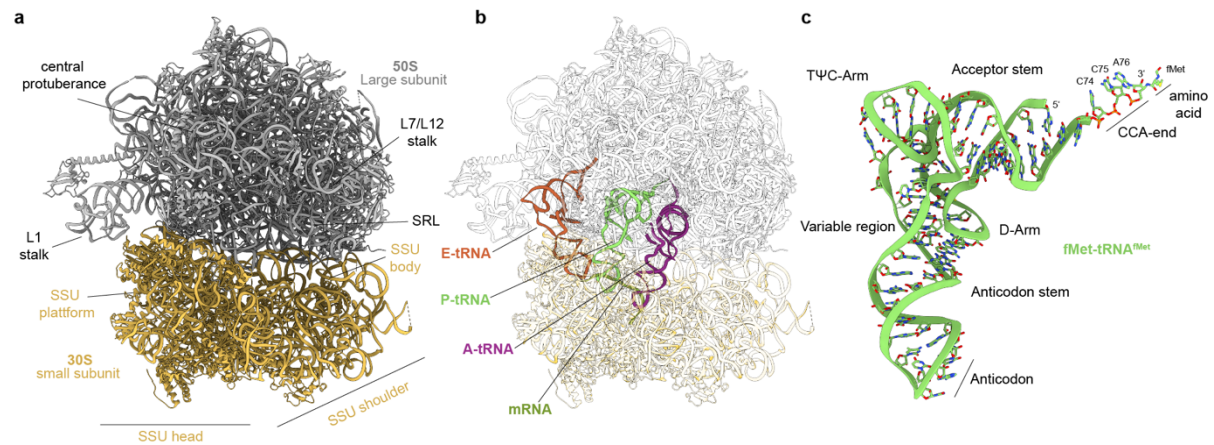


**Figure 1: An overview of the bacterial ribosome.** **a**, The 70S *Thermus thermophilus* ribosome with the large 50S subunit (grey) and the small 30S subunit (yellow) (PDB ID 1VY4) (Polikanov et al., 2014a). Structural features were highlighted. **b**, Binding sites of the mRNA (dark green) on the 30S subunit and the amino acyl-tRNA (A-tRNA, purple) in the A-site, the peptidyl-tRNA (P-tRNA, light green) in the P-site and exit-site tRNA (E-tRNA, red) in the E-site (PDB ID 1VY4) (Polikanov et al., 2014a). **c**, Peptidyl-tRNA (fMet-tRNA<sup>fMet</sup>, light green) with highlighted structural features (PDB ID 1VY4) (Polikanov et al., 2014a).

The Central Dogma of molecular biology is describing the transfer of information in living organisms in a directional way, which includes the three main steps of DNA replication, RNA transcription and protein synthesis (translation) (Crick, 1970). The ribosome is a large ribonucleotide complex composed of ribosomal RNA (rRNA) and ribosomal proteins and can be found in the cytoplasm of every living organism through all kingdoms of life and is essential to facilitate the protein synthesis (McQuillen et al., 1959; Palade, 1955). High-resolution crystal structures of bacterial ribosomes have been available for nearly two decades (Agrawal et al., 2000; Clemons et al., 1999; Nissen et al., 2000; Schluenzen et al., 2000). Recent improvements in the cryo-EM technology allowed reaching near atomic resolution, like the recently published cryo-EM structure of an *E. coli* ribosome at 2 Å and with structures of 1.55 Å resolution on the horizon, the gap to crystal structure resolutions closes further (Fromm et al., 2022; Watson et al., 2020). The 70S bacterial ribosome consists of two subunits, the large 50S subunit (LSU) and the small 30S subunit (SSU) (**Fig. 1a**). The LSU consists of a 23S rRNA and a 5S rRNA and around 30 proteins and can be divided into domains I-

VI, while the SSU consists of a 16S rRNA and around 20 proteins, dependent on the organism and can be divided in domains I-IV. The SSU domains are more flexible to each other and labeled as: 3' major domain (head), 3' minor domain (h44-45), the central domain (platform) and the 5' domain (body) (**Fig. 1a**) (Ban et al., 2000; Nierhaus, 1991). The rRNA builds the catalytic core of the ribosome with the peptidyl transferase center (PTC) on the LSU being highly conserved through different species. The nascent peptide exit tunnel (NPET) stretches through the LSU from the PTC to the top with ribosomal proteins L4 and L22 forming the vicinity of the tunnel (Ban et al., 2000; Cech, 2000; Hansen et al., 2002; Harms et al., 2001; Nissen et al., 2000; Noller, 2012; Schluenzen et al., 2000). The SSU harbors the decoding center (DC) that is decoding messenger RNA and recruiting transfer RNAs (tRNAs) through different factors (Loveland et al., 2017; Loveland et al., 2020). The ribosome has three designated binding sites for tRNAs, the amino acyl-site (A-site), the peptidyl-site (P-site) and the exit-site (E-site) (**Fig. 1b**) (Rheinberger et al., 1981). The amino acids are delivered by amino acylated-tRNAs that are charged on their CCA-end by aminoacyl-tRNA synthetases (Arnez and Moras, 1997). tRNAs have a cloverleaf like secondary structure, which is composed of an acceptor stem that is at 3'-position of the CCA-end amino acylated, a variable loop region, a T- and a D-arm, as well as an anticodon stem loop that is essential for the specificity of the tRNA (**Fig. 1c**) (Holley et al., 1965; Kim et al., 1974). The next chapters will introduce the processes of translation mediated through the ribosome. Numbering of nucleotides and ribosomal proteins in this study will be based on *E. coli* numbering if not otherwise specified.

## 7.2. Translation

Translation is the highly controlled synthesis of a peptide chain through the ribosome. This involves four major phases: Initiation, Elongation, Termination and Recycling. The mRNA is translated sequentially and unidirectional in 5' to 3' direction from codons of three nucleotides out of the pool of adenosine, guanosine, cytidine and uridine into one of the 20 proteinogenic natural amino acids (Crick et al., 1961). Amino acids are connected by a peptide bond, mediated through the ribosome during peptide bond formation, from amino (N)- to carboxy (C)-terminus (Bishop et al., 1960; Dintzis, 1961). Most steps of prokaryotic translation are facilitated by GTPases (Leipe et al., 2002). An overview of the individual steps of translation is shown in **Fig. 2**.

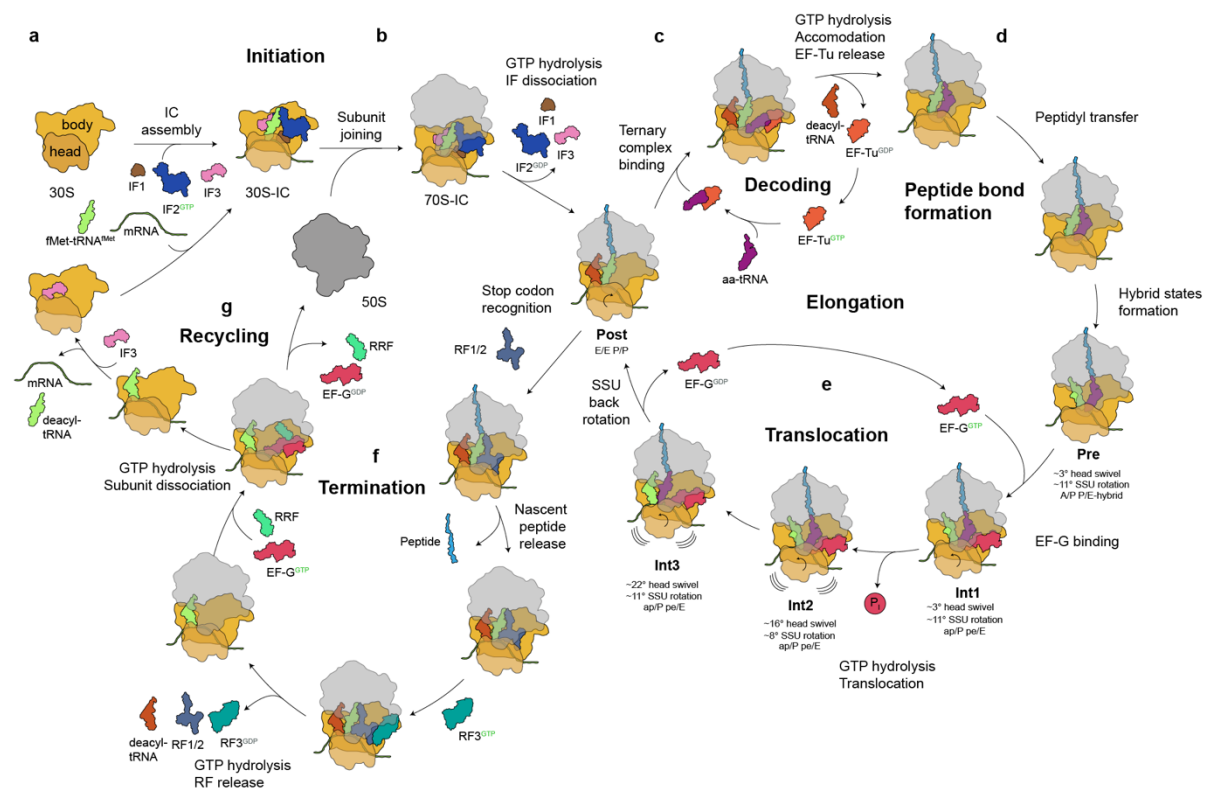


**Figure 2: Schematic overview of bacterial translation cycle.** a-g, Simplified overview of the different steps of the bacterial translation cycle with 50S subunit (grey), 30S subunit (yellow), P-site tRNA (light green), A-site tRNA (purple), E-site tRNA (red) nascent chain (light blue) and mRNA (green). **a, Initiation** – assembly of the 30S-IC with initiation factors 1 (IF1, brown), IF2 (blue) and IF3 (pink). **b, Subunit joining.** **c, Decoding** - Ternary complex formed by EF-Tu (orange), amino acyl-tRNA (purple) and GTP is delivering aa-tRNA. **d, Peptide bond formation.** **e, Translocation** - EF-G translocates the peptidyl-tRNA in a ratchet-like motion from A- to P-site in a multi-step process, involving GTP hydrolysis and increasing amount of swivel of the SSU head. **f, Termination** – Upon recognition of a stop codon, release factor 1/2 (RF1/2, dark blue) binding in the A-site, catalyzing the hydrolysis of

nascent chain (NC) followed by NC release. RF1/2 is recycled by RF3 (turquoise) and both RF1/2 and E-tRNA dissociated. **g, Recycling** - Ribosome recycling factor (RRF, green) and EF-G (red) split the subunits. IF3 binds and ejects both mRNA and deacylated-tRNA. Adapted and modified from (Korostelev, 2022; Nishima et al., 2022; Schmeing and Ramakrishnan, 2009).

## 7.2.1. Initiation

### 7.2.1.1. 30S-preinitiation and 30S initiation complex

The initial step of initiation is the formation of an early intermediate 30S preinitiation complex (30S-PIC) consisting of the small ribosomal subunit (SSU), the initiation factors 1-3 (IF), messenger RNA (mRNA) and the initiator fMet-tRNA<sup>fMet</sup> (**Fig. 2a**) (Antoun et al., 2006; Milon et al., 2012). Initiation fidelity is only achieved with all three initiation factors combined (Julian et al., 2011; Milon et al., 2008). The order in which the complex assembles is not restricted but has a kinetically favored sequence. Initially an unstable complex of 30S, IF3 and IF2 forms, which is joined by IF1 locking the factors on the SSU and as a result stabilizing the complex (Milon et al., 2012; Simonetti et al., 2008). IF1 binds the 30S A-site and by providing anchoring points, enhances activity of IF2 and IF3, amplifying both stabilizing and destabilizing effects of the complex, respectively (Antoun et al., 2006; Hussain et al., 2016; Wintermeyer and Gualerzi, 1983). The GTPase IF2 recognizes the N-formylmethionine moiety (fMet) on the CCA-end of the initiator tRNA and promotes the recruitment of the fMet-tRNA<sup>fMet</sup> to the 30S-PIC, protecting it from premature deacylation (Guenneugues et al., 2000; Wu and RajBhandary, 1997). IF2 has a higher affinity for the initiator tRNA than for other formylated tRNAs and by discriminating elongator tRNAs reducing the risk for frameshifting (Antoun et al., 2006; Wu and RajBhandary, 1997). Additionally, IF3 can distinguish the anticodon stem loop (ASL) of the initiator tRNA and prevents elongator tRNA binding by destabilizing the tRNA in non-cognate initiation complexes or leaderless mRNA (Hartz et al., 1990; O'Donnell and Janssen, 2002; Petrelli et al., 2001). IF3 protects the start codon in absence of the fMet-tRNA<sup>fMet</sup> while IF1 blocks the A-site (Hussain et al., 2016). The N- and C-terminal IF3 domains are connected by a highly flexible linker necessary for its conformational changes (Elvekrog and Gonzalez, 2013; Petrelli et al., 2001). IF3 prevents premature subunit joining by destabilizing the tRNA binding sites in E- and P-site by positioning of N- and C-terminal



regions of IF3 along the mRNA (Grigoriadou et al., 2007b; Grunberg-Manago et al., 1975; Hussain et al., 2016). In absence of a canonical codon-anticodon interaction IF1 can alter h44 of the SSU into a unfavorable position for subunit joining, which can be restored by placement of initiator tRNA in the P-site (Qin et al., 2012). Binding of the mRNA to the 30S-PIC can occur at any time and is promoted by conformational changes of the mRNA entry tunnel in presence of IF1 and IF2 (Hussain et al., 2016; Milon et al., 2012). However, the stability and secondary structures formed by the mRNA in the ribosome-binding site, the cellular concentration and how abundant the expressed gene is in the cell influences the rate in which the mRNA binds the 30S-PIC (Milon et al., 2012; Studer and Joseph, 2006). Binding of the mRNA and start codon recognition by codon-anticodon interactions of mRNA and fMet-tRNA<sup>fMet</sup> leads to transition from 30S-PIC to the stable 30S-IC undergoing a series of conformational changes with a distinct rotational SSU head movement (Lopez-Alonso et al., 2017; Milon et al., 2012). Additionally, in response to codon recognition IF3 undergoes conformational changes stabilizing the 30S-IC (Elvekrog and Gonzalez, 2013; Hussain et al., 2016).

#### **7.2.1.2. 70S initiation complex**

Following the formation of the stable 30S-IC the large 50S ribosomal subunit (LSU) joins to form the 70S initiation complex (70S-IC) (**Fig. 2b**) (Milon et al., 2008). The SSU head moves into a closed state closer to the body, stabilizing the tRNA and triggering dissociation of IF3 C-terminal domain from the start codon and IF1 (Hussain et al., 2016). The docking of subunits initially leads to the formation of an unstable intermediate 70S-IC. Interactions of the H69 of the 50S subunit with IF3 and the initiator tRNA lead to the rapid dissociation of IF3 and transition the 70S-IC into a more stable complex by forming intersubunit bridges (Liu and Fredrick, 2015). IF3 dissociating while subunit joining is highly influenced by the start codon and mRNA secondary structures (Milon et al., 2008). Subunit joining in presence of IF3 becomes reversible for a very short period by altering the stabilization of the SSU through conformational changes (MacDougall and Gonzalez, 2015). IF2 is necessary to coordinate the assembly of the 70S-IC. Positioning of IF2s GTP-binding domain in close proximity to the 50S GTPase-activated center (Sarcin-ricin loop) allows rapid

GTP hydrolysis triggered by the subunit joining and leads to accommodation of the Initiator tRNA in the P-site with the fMet moiety in the PTC (Grigoriadou et al., 2007a; Simonetti et al., 2008; Tomsic et al., 2000). GTP hydrolysis by IF2 is essential for the transition of the 70S-IC to an elongation-competent conformation (Marshall et al., 2009). This is accomplished by a 10 Å tilt of the SSU head and 25 Å movement of the CCA-end of the Initiator tRNA towards the body of the SSU allowing the interaction of IF2 and tRNA. The head of the SSU has to swivel and rotate by about 4° while the subunits join. The nonrotated 70S is adopted by the dissociation of IF2 and opening of the L1 stalk (Kaledhonkar et al., 2019; Ling and Ermolenko, 2015). Dissociation of IF2 from the initiator tRNA by GTP-hydrolysis is independent of the other IFs and promotes the dissociation of IF1 and IF2 from the complex (Goyal et al., 2015; Myasnikov et al., 2005).

### **7.2.1.3. Start codon selection**

As mentioned before the start codon selection and correct placement of the mRNA is essential for initiation fidelity and correct translation of an open reading frame. mRNA secondary structures upstream of the initiation site, Shine-Dalgarno (SD) sequence, interaction of start codon and ASL with the initiation factors are important checkpoints to control stability of the 30S-IC (**Fig. 2a**) and therefore, efficient initiation (Milon et al., 2008). This involves discrimination of cognate AUG and near-cognate GUG, CUG and UUG start codons, achieved through a wobble-base pair in the first position (O'Connor et al., 2001). The anticodon stem of the initiator tRNA contains three G-C base pairs which are important for most efficient translation initiation by constraining the mRNA position on cognate start codons (Roy et al., 2018). Shine-Dalgarno sequences are conserved purine-rich sequences in the 5' untranslated region in the ribosome binding site of prokaryotic mRNAs that support placing of the AUG start codon in the P-site of the ribosome. This sequence on the mRNA base pairs with the anti-Shine-Dalgarno (ASD) sequence in the 3' end of the 16S rRNA and forms a helix docking into the vicinity between head and platform of the SSU (Kaminishi et al., 2007; Korostelev et al., 2007; Shine and Dalgarno, 1974; Steitz and Jakes, 1975). However, the SD sequence is not essential for initiation as structured mRNA sequences can be unfolded by the highly mobile ribosomal S1 protein, which is located upstream of the E-site,

which helps positioning the mRNA correctly. mRNAs lacking a 5' untranslated region (5' UTR), so called leaderless mRNAs can also be sufficiently translated (Byrgazov et al., 2015; Duval et al., 2013; Nakagawa et al., 2010; Ringquist et al., 1995). The expression levels of genes are predicted to be higher in presence of a SD sequence in a context of a cognate AUG start codon (Ma et al., 2002). mRNA sequences without a SD-anti-SD interaction are more susceptible to destabilization induced by IF3 (O'Connor et al., 2001).

## 7.2.2. Elongation

Elongation is the iterative process of decoding the mRNA, accommodating the correct tRNA in the A-site, following peptide bond formation and translocation of the peptidyl-tRNA from the A-site to the P-site and exit of the E-site tRNA. The individual steps are explained in the following sections (**Fig. 2c-e**).

### 7.2.2.1. Decoding

After transition from initiation the 70S-elongation complex has an empty A-site that allows delivery of an aminoacyl tRNA (aa-tRNA) delivered by the GTPase elongation factor Tu (EF-Tu) (**Fig. 2c**). The ternary complex (TC) of EF-Tu, GTP and amino acyl-tRNA is recruited initially independent of the mRNA sequence and is supported by interactions with ribosomal proteins L7 and L12 (Diaconu et al., 2005; Nissen et al., 1995; Rodnina et al., 1996). The delivered amino acyl-tRNAs ASL is, by conformational changes in EF-Tu, placed in the decoding center of the SSU (Schmeing et al., 2009). The cognate tRNA will be selected by the decoding center of the ribosome based on the codon on the mRNA with up to 20 amino acids per second and discriminates against non-cognate tRNAs (Liang et al., 2000). The ternary complex initially binds the SSU without base pairing of the ASL of the tRNA with the codon nor the direct contact of EF-Tu with the SRL on the LSU in a pre-hydrolysis state. The tRNA stays in a relaxed T-tRNA position with the ASL 15 Å distant to the codon (Loveland et al., 2017). The decoding center in the SSU is formed by the universally conserved 16S ribosomal RNA nucleotides A1492 and A1493 in h44 and G530. In response to binding of a cognate tRNA and proper codon-anticodon

recognition conformational changes of the SSU are induced. A1492 and A1493 flip out and interact with the minor groove of the first two positions of the codon, forming an A-minor motif and sensing the correct Watson-Crick base pairing geometry. G530 switches into an anti-conformation and interacts with all three positions (Ogle et al., 2001). The third position of the codon can accommodate a wobble base pair (Crick, 1966a; Ogle et al., 2001). During this process EF-Tu stays distant from the SRL of the LSU and the SSU remains in an open conformation while the tRNA kinks downwards to reach the codon in a state known as A\*/T-tRNA (Loveland et al., 2017). If cognate codon-anticodon interactions are achieved, G530 functions as a latch and stabilizes the codon-anticodon helix in the decoding center which induces SSU domain closure by a 4 Å movement of the SSU shoulder closer to the body and the LSU. If a near-cognate tRNA is sensed, G530 disengages from the codon-anticodon helix and favors a domain-open SSU, therefore suppressing GTP hydrolysis (Fislagé et al., 2018; Loveland et al., 2017). In the cognate state the tRNA adopts the A/T-state and becomes distorted allowing simultaneous contact of the ASL with the codon and the GTPase-domain of EF-Tu shifted towards the SRL in the LSU (Loveland et al., 2017; Schmeing et al., 2009; Stark et al., 1997; Valle et al., 2003). The distortion of native tRNAs and adaption of unique conformations is essential for accurate decoding (Schmeing et al., 2011). The SRL functions as an activator upon positioning of EF-Tu GTPase domain. Asp21 in the P-loop stabilizes GTP and the universally conserved His84 in the switch II region of EF-Tu interacts with A2662 of the SRL which positions a catalytically important water in position for a nucleophilic attack on the  $\gamma$ -phosphate of GTP (Maracci et al., 2014; Voorhees et al., 2010; Wool et al., 1992). The hydrolysis of GTP is irreversible and upon release of an inorganic phosphate ( $P_i$ ) EF-Tu\*GDP undergoes conformational changes extending the switch II domain away from its switch I domain and disengaging the SRL. The tRNA remains stabilized by the switch II domain with the ASL in the decoding center. The SSU changes between open and closed conformations and continuously samples as an additional step of EF-Tu dependent proofreading potentially allowing dissociation of EF-Tu\*GDP\*tRNA. Finally, EF-Tu releases from the ribosome, allowing the CCA-end of the tRNA to accommodate in the A-site of the LSU by an 80 Å movement from its EF-Tu bound state and a 2.5° rotation of the SSU (Loveland et al., 2020).

### 7.2.2.2. Peptide bond formation

Following tRNA accommodation the ribosome provides the essential catalytic steps for peptide bond formation of the incoming aa-tRNA in the A-site and the peptidyl-tRNA in the P-site (**Fig. 2d**). The peptide bond formation occurs in the peptidyl transferase center (PTC) which is formed by 23S ribosomal RNA in domain V in the LSU surrounding the CCA-ends of the P- and A-tRNA at the P- and A-loop, respectively (Ban et al., 2000; Moazed and Noller, 1989; Nissen et al., 2000; Polikanov et al., 2014a). The catalytic environment is provided by the rRNA making the ribosome itself a ribozyme with the catalysis being mostly entropic by positioning reactive groups closely together while facilitating a hydrogen bond network and thereby accelerating the reactions  $10^7$ -fold as compared to the same reaction in solution (Bieling et al., 2006; Nissen et al., 2000; Sievers et al., 2004; Zaher et al., 2011). Accommodation of the aa-tRNA in the A-site induces reorientation of G2583 and U2584 through hydrogen bond interaction of U2585 with the tRNA's A76. Additionally, A2602 is essential for stabilizing the tRNAs in the active site (Kuhlenkoetter et al., 2011; Schmeing et al., 2005).

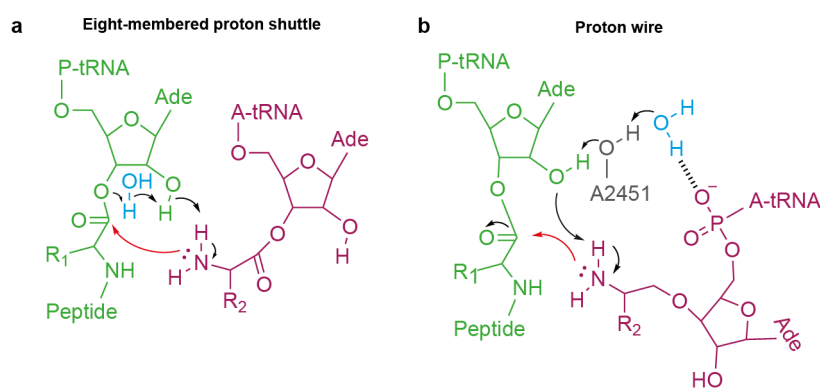


**Figure 3: Schemes for peptide bond formation. a-b**, P-tRNA shown in green, A-tRNA shown in purple, water in blue and A2451 nucleotide in grey. Nucleophilic attack indicated by red arrows and proton transfer by black arrows. **a**, Eight-membered proton shuttle (Kuhlenkoetter et al., 2011; Wallin and Aqvist, 2010). **b**, Proton wire (Polikanov et al., 2014a). Adapted and modified from (Rodnina, 2018).

A nucleophilic attack on the carbonyl carbon of the ester bond of the P-tRNA by the amino-group of the A-tRNA enables peptide bond formation. The rate limiting step of the peptide bond formation is the movement of three protons (Kuhlenkoetter et al.,

2011). Two potential models of proton transfer are currently proposed (**Fig. 3a,b**) (Erlacher et al., 2006; Polikanov et al., 2014a; Wallin and Aqvist, 2010; Zaher et al., 2011). The “proton shuttle”-model (**Fig. 3a**) describes the movement of the protons through an eight-membered transition state after the initial nucleophilic attack of the amino group on the ester carbonyl center (Kuhlenkoetter et al., 2011; Wallin and Aqvist, 2010). A proton from the attacking amino group is received by the 2'O of A76 ribose of the P-tRNA which itself donates a proton to the carbonyl oxygen through an adjacent water molecule bridging 2'O and 3'O. Independent of the rate limiting step the protonation of the 3' OH occurs at rapid speed (Kuhlenkoetter et al., 2011; Wallin and Aqvist, 2010). The more recent “proton wire”-model (**Fig. 3b**), involves the ribosomal protein bL27 and the 2'OH of 23S rRNA nucleotide A2451 (Polikanov et al., 2014a). A water molecule bridges the attacking amine with the negatively charged 5'-phosphate oxygen of the A76 of the A-tRNA, the 2'OH of A2451 and the 2'OH of the A76 of the P-tRNA providing a proton wire for proton transfer. The water is further stabilized by Ala2 of bL27 and N6 of A2602 and forming an ideal tetrahedral intermediate for the proton transfer. An additional water molecule in the reaction pocket allows delocalization of positive and negative charges. Reversal of the proton-transfer leads to the breakdown of the tetrahedral intermediate and resulting in the peptide on the A-tRNA with a deacylated tRNA in the P-site (Polikanov et al., 2014a). However, deletion of bL27 does not affect the peptide bond formation giving a reasonable doubt for the proton wire model, suggesting the proton shuttle model to be more precise (Maracci et al., 2015).

### 7.2.2.3. Translocation

Upon successful peptide bond formation, the peptidyl-tRNA has to move into the P-site while the deacylated-tRNA needs to shift into the E-site to accept the next tRNA in the A-site (**Fig. 2e**). This movement has to keep base pairing of the mRNA and ASL of the tRNA to keep the open reading frame while moving it in the 5'-direction, as frameshifting in either direction would lead to non-functional or defective proteins (Choi et al., 2020b; Gamper et al., 2021). Translocation of the tRNAs in prokaryotic ribosomes is facilitated by the GTPase elongation factor G (EF-G) in a ratchet-like fashion (Conway and Lipmann, 1964; Frank and Agrawal, 2000). Rotation of the SSU

by 10-11° occurs independently of EF-G while the tRNAs sample from the classic P/P- and A/A-state (PRE-C) to the hybrid P/E- and A/P-states (PRE-H state) (Blanchard et al., 2004; Carbone et al., 2021; Moazed and Noller, 1989; Rundlet et al., 2021). EF-G\*GTP binds the ribosome with rotated SSU with the elbow of the peptidyl-tRNA shifted by about 25 Å in an A/P\*-state. The tip of the translocase domain IV (loop I) is positioned near the tRNA and next to G530 in the DC. By shifting loop I towards A1493 the codon-anticodon-helix is disengaged from G530, and the DC is unlocked. A 5°-rotation of the SSU shifts the domain 4 placed in the A-site deeper and moves the peptidyl-tRNA about 20 Å into the P-site and the deacylated-tRNA into the E-site of the SSU leading to the chimeric (intra-subunit hybrid) states ap/P and pe/E (INT1) (Carbone et al., 2021; Ramrath et al., 2013; Ratje et al., 2010; Rundlet et al., 2021). Different from EF-Tu the GTPase domain I of EF-G is positioned near the SRL of the LSU as soon as the factor arrives, adopting an elongated confirmation. However, Pi release is not observed in the INT1 state probably resulting from the catalytic switch I and II domains staying well-ordered, encapsulating the GTP primed for hydrolysis. Non-hydrolysable GTP showed reduced INT1 transition which leads to the assumption that GDP is more likely to be present than GTP with the Pi stabilized by hydrogen bonds with surrounding switch I and switch II sidechains (Maracci et al., 2014; Rundlet et al., 2021), which was supported by time-resolved cryo-EM structures (Carbone et al., 2021). Rotation of the SSU head by 16° in the direction of the tRNA translocation shifts loops I and II of EF-G closer to mRNA and peptidyl-tRNA (INT2). In the final state the SSU head is in a hyper swiveled position of 22° while the body stays at a nearly nonrotated state (INT3). The tRNAs are translocated by additional 4 Å to the ap\*/P for the peptidyl-tRNA (Carbone et al., 2021; Nishima et al., 2022). After complete translocation, Pi release allows EF-G to detach from the LSU while the translocase domain stays in the SSU A-site. EF-G dissociation is concurrent with back swivel of the SSU head preparing the ribosome for the next round of elongation decoding with an empty A-site with the deacyl-tRNA likely dissociating from the E-site (POST-state) (Carbone et al., 2021; Nishima et al., 2022; Rundlet et al., 2021). The findings in the single molecule-FRET (Rundlet et al., 2021) and time-resolved cryo-EM (Carbone et al., 2021) studies argue against EF-G generating force from GTP hydrolysis by large scale conformational changes (Petrychenko et al., 2021), and rather propose the

translocation mainly driven by conformational changes and movements of the SSU head and body with EF-G functioning as a mostly rigid steric barrier.

### 7.2.3. Termination

Translation elongation cycles continue until a stop codon (UAA, UAG, UGA) (Crick, 1966b) is recognized in the A-site (**Fig. 2f**). In prokaryotic termination the stop codon UAG and UAA are recognized by class-1 release factor 1 (RF1) and UGA and UAA by RF2. Upon stop codon recognition the RF bind in their open conformation at the A-site of the ribosome with a recognition motif in domain IV at the DC. In both RFs the uracil in the first position of the stop codons is recognized by two conserved glycines in helix  $\alpha 5$  in domain II (Korostelev et al., 2008; Korostelev et al., 2010; Weixlbaumer et al., 2008). The recognition motif in RF1 consists of Pro-Val-Thr and the threonine contacts the first and second position of the stop codon in the DC by forming hydrogen bonds. The third base stacks onto G530 of the 23S rRNA DC and interacts with a neighboring isoleucine and glutamine (Korostelev et al., 2010; Rawat et al., 2006). The recognition motif in RF2 consists of Ser-Pro-Phe, of which only the serine directly interacts with the second base of the UAA or UGA stop codon. Discrimination of A at the third position is achieved through a stacking interaction with G530 of the DC and hydrophobic interactions with a surrounding valine of RF2 (Korostelev et al., 2008; Rawat et al., 2003; Weixlbaumer et al., 2008). Both RFs have a conserved threonine which interacts with the third position of the stop codon and helps recognizing adenosine (Korostelev et al., 2008; Korostelev et al., 2010). Recognition of the stop codon leads to stabilization of RFs switch loop placing the conserved GGQ motif of domain III in the PTC essential for catalysis of the hydrolysis at the CCA-end of the peptidyl-tRNA. Binding of the GGQ motif in the PTC induces conformational changes to U2506 and U2585 in order to avoid steric clashing. U2585 protects the peptidyl-tRNA in the uninduced state and allows a nucleophilic attack by water when opening in the induced state which gets coordinated by the glutamines side chain of the RFs GGQ motif, by the 2'OH of A76 and N3 of A2451. A tetrahedral transition-state intermediate formed during hydrolysis gets stabilized by the backbone amide of the glutamine and upon release of the peptide stabilizes the deacylated tRNA (Jin et al., 2010; Korostelev et al., 2008; Santos et al., 2013; Trobro and Aqvist, 2009;



Weixlbaumer et al., 2008). Additionally, the efficiency of termination, especially for RF2, is greatly enhanced by a methylation of the glutamine of the GGQ motif, improving the RFs binding affinity and optimal geometry for ester hydrolysis (Dincbas-Renqvist et al., 2000; Mora et al., 2007; Trobro and Aqvist, 2009). The efficiency of the termination is not only dependent on the RFs but also depends significantly on the fourth nucleotide following the stop codon, with UAAU being the most and UGAC the least strong stop codon (Poole et al., 1995). After peptide chain release the dissociation of the RFs is promoted by the class-II GTPase release factor 3 (RF3) (Zavialov et al., 2001; Zavialov et al., 2002). RF3\*GTP is supposed to bind the ribosome and induce SSU rotation and head swivel while the P-site tRNA partially rotates in the direction of the E-site and destabilizes the binding of RF1. The subunit rotation also positions the GTPase domain of RF3 close to the SRL on the LSU and facilitates the dissociation of RF3\*GDP and RF1 (Graf et al., 2018; Jin et al., 2011; Koutmou et al., 2014; Pallesen et al., 2013; Shi and Joseph, 2016).

#### **7.2.4. Ribosome recycling**

Following dissociation of RF1 and RF3, the ribosome needs to be recycled to reinitiate translation (**Fig. 2g**). This process is called ribosome recycling which facilitates disassembly of the 70S-termination complex and releases mRNA, tRNA and separates the subunits. In eubacteria this process is catalyzed by the ribosome recycling factor (RRF), EF-G and IF3. RRF binds after RF1 and RF3 dissociation from the rotated ribosome in the A-site and stabilizes it with the deacylated-tRNA in the P-site in a hybrid P/E-state (Dunkle et al., 2011; Gao et al., 2005; Prabhakar et al., 2017). EF-G\*GTP has to bind the ribosome after RRF to allow efficient subunit splitting, as EF-G was found to inhibit binding of RRF if arriving prior to the ribosome and leading to GTP hydrolysis without ribosome splitting (Borg et al., 2016). RRF domain II moves, supported by EF-G and subsequent GTP hydrolysis and slightly delayed  $P_i$  release, towards the inter-subunit bridge B2a of H69 on the LSU and h44 on the SSU, splitting the 70S ribosome. EF-G\*GDP and RRF dissociate rapidly from the split subunits (Fu et al., 2016; Prabhakar et al., 2017; Savelsbergh et al., 2009). IF3 promotes tRNA dissociation from the SSU as soon as the subunits are split and subsequent mRNA leaves the SSU (Fu et al., 2016). However, mRNA sequences that have no SD

sequence can leave the SSU prior to subunit splitting, resulting of tRNA dissociation from the 70S ribosome without IF3 before subunit splitting is promoted by RRF and EF-G (Chen et al., 2017).

### 7.3. Antibiotics and antimicrobial peptides targeting the ribosome

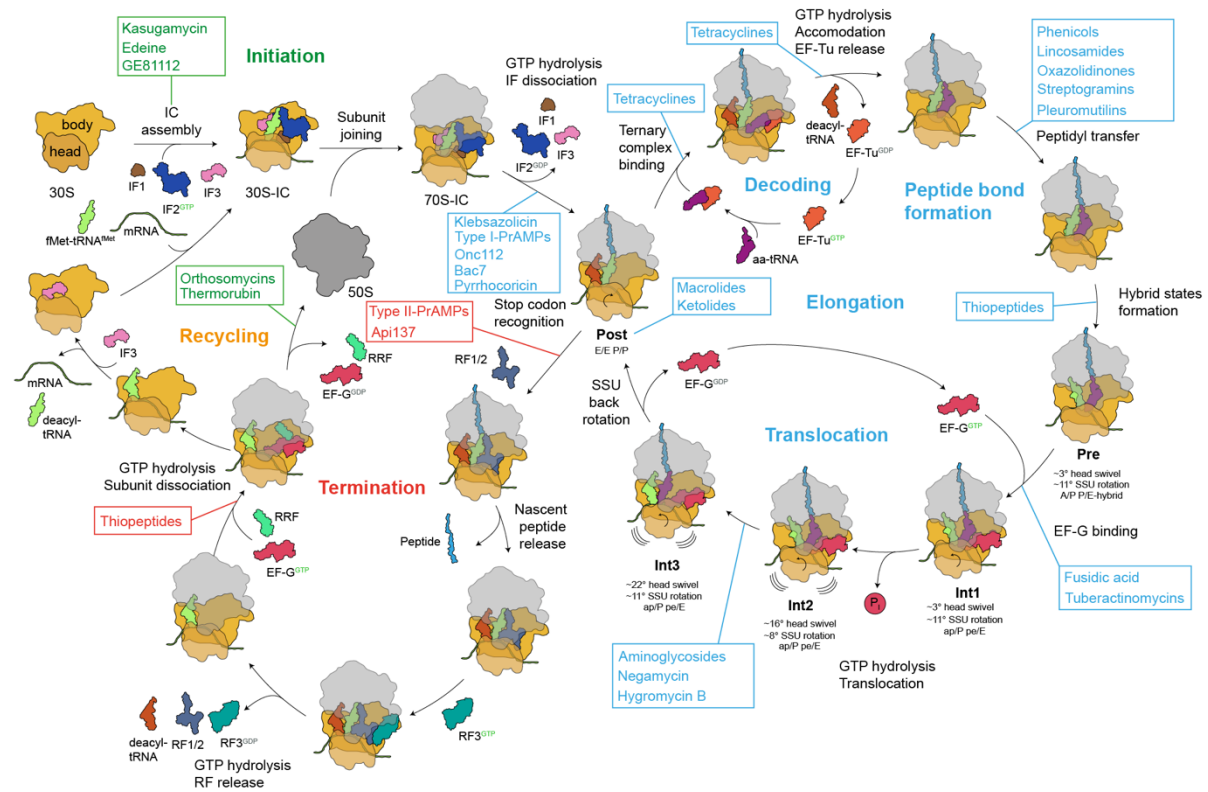


**Figure 4: Overview of ribosome-targeting antibiotics.** Steps of the translation cycle are color-coded with antibiotics targeting the step highlighted in the same color: Initiation (green), Elongation (blue), Termination (red) and Recycling (orange). Adapted and modified from (Arenz and Wilson, 2016a; Schmeing and Ramakrishnan, 2009; Sohmen et al., 2009; Wilson, 2009)

A rising threat to humankind is multi-drug resistance of bacterial pathogens and renders our current arsenal of available antimicrobials obsolete. The majority of clinically used antibiotics target the ribosome and inhibit either translation by stalling the ribosome in conformations incapable of peptide synthesis or targeting individual proteins necessary for translation (Wilson, 2009, 2014). Antimicrobial resistance highlights the need for investigation of new antibiotics utilizing unique chemical scaffolds and novel modes of actions to interact and specifically inhibit bacterial ribosomes (Arenz and Wilson, 2016b). Ribosome-targeting antibiotics either target the

LSU, SSU or individual factors during the translation cycle and for most of them structures have been readily available to provide insight into their mechanism of action (extensively reviewed in (Arenz and Wilson, 2016a; Lin et al., 2018; Wilson, 2009)). Additionally to antibiotics targeting the ribosome, there are a wide variety of ribosome-targeting peptide antibiotics with different mechanisms of action and interfering with distinct stages of translation (as reviewed in (Polikanov et al., 2018)). The following provides a brief overview of relevant antibiotic classes and antimicrobial peptides targeting the ribosome. Most of the antibiotics targeting the SSU are binding either to the decoding center or the tRNA binding sites. Aminoglycosides, like kanamycin and gentamycin, bind close to h44 and interfere with decoding and induce miscoding by stabilizing A1492 and A1493 in their flipped-out conformation (Carter et al., 2000). Other aminoglycosides like neomycin and hygromycin B increase the binding affinity of A-tRNA and block translocation (Borovinskaya et al., 2008; Polikanov et al., 2014b). Kasugamycin, while also being an aminoglycoside, binds close to P- and E-site and overlaps with mRNA and fMet-tRNA<sup>fMet</sup>, preventing formation of the 30S-IC (Schluenzen et al., 2006; Schuwirth et al., 2006). Kasugamycin was found to exhibit context-specificity based on the nature of the mRNA, especially with guanine preceding the start codon (Zhang et al., 2022). Tetracyclines, including tigecycline and eravacycline, interfere with translation by blocking accommodation of tRNAs in the A-site (Jenner et al., 2013). Thermorubin is structurally related to tetracyclines but binds at the intersubunit bridge B2a between h44 of the SSU and H69 of the LSU and interferes with elongation and termination (Bulkley et al., 2012; Paranjpe et al., 2022). In a recently published preprint, it has been suggested that thermorubin binding flips-out C1914 of the 23S rRNA, which reduces A-tRNA binding affinity. This slows down and destabilizes the accommodation of the A-tRNA, interfering both with decoding and translocation. Additionally, thermorubin is suggested to interfere with RF accommodation at the DC (Paranjpe et al., 2022). Tuberactinomycins, like viomycin and capreomycin 1A, are circular peptide antibiotics that stabilize conformations of the SSU head and body and interfere with dynamical changes necessary for translocation (Brilot et al., 2013; Stanley et al., 2010). Edeine, a cationic peptide, prevents binding of the fMet-tRNA<sup>fMet</sup> to the P-site of the SSU and thereby blocks initiation (Pioletti et al., 2001). GE81112, a tetrapeptide antibiotic, also interferes with initiation by binding to the P-site but instead of preventing the binding of the initiator tRNA, it stabilizes the

ASL in a distorted conformation blocking decoding (Fabbretti et al., 2016). While many antibiotic classes target the SSU, a similarly large number of antibiotics and antimicrobial peptides target the LSU. Chloramphenicol, a member of the phenicols, binds the A-site crevice at the PTC and prevents peptide bond formation in a context-specific manner with Ala, Ser or Thr as penultimate amino acids of the nascent chain, and based on the nature of the amino acid residue of the incoming A-tRNA (Marks et al., 2016). Chloramphenicol was shown to inhibit peptide bond formation through specific interactions of the PTC and incoming tRNA stabilizing the drug and showed inability of inhibition in presence of glycine in the A-site (Choi et al., 2020a; Syroegin et al., 2022a; Syroegin et al., 2022b). Oxazolidinones, like linezolid, bind in a similar fashion as the phenicols and also prevent peptide bond formation through A-site tRNA accommodation in a context-specific manner, with an Ala-residue in the penultimate position of the nascent chain stabilizing the drug within its binding site (Bozdogan and Appelbaum, 2004; Eyal et al., 2015; Tsai et al., 2022; Wilson et al., 2008). Lincosamides, like lincomycin and the semi-synthetically optimized clindamycin and especially the recently described fully synthetic oxepanoprolinamide iboxamycin (IBX), are highly potent against various Gram-positive and Gram-negative bacterial infections and are either in clinical use or preclinical trial. They bind the A-site crevice of the LSU and sterically clash with incoming A-tRNAs and, in case of IBX, prove the concept of structure-based drug design against Erm-, Cfr- and ABCF-mediated antibiotic resistance in bacteria (Dunkle et al., 2010; Mitcheltree et al., 2021; Tu et al., 2005). Pleuromutilins, like tiamulin and lefamulin, bind at the PTC and disturb the coordination of incoming A-tRNAs through steric hinderance and proper P-tRNA positioning (Eyal et al., 2016). Orthosomycins, like evernimicin and avilamycin, are large oligosaccharide antibiotics that bind the aa-tRNA accommodation corridor on the LSU and sterically hinder the correct placement of the A-tRNA (Adrian et al., 2000; Arenz et al., 2016b; Belova et al., 2001; Krupkin et al., 2016). Recently the orthosomycins have been reported to exhibit a context-specificity based on the nature of the incoming aa-tRNA and the C-terminal residues of the nascent chain (Mangano et al., 2022). While these antibiotics bind mostly close to the PTC or interfere with tRNA accommodation, many antibiotics bind within the NPET and occlude the path of a growing nascent chain, inhibiting elongation or termination. Structurally similar to the aforementioned tetracyclines, tetracenomycin X (TcmX) binds the NPET instead of

the SSU, occluding the tunnel and interfering context-specific with peptide bond formation of an incoming aa-tRNA and a C-terminal Gln-Lys-motif, by sequestering the 3'-end of the peptidyl-tRNA (Leroy et al., 2022; Osterman et al., 2020). Macrolide antibiotics are macrocyclic lactone ring systems, with erythromycin (Ery) being the prototype for the class, occlude the NPET partially and inhibit elongation in a context-specific manner described in detail later (Davis et al., 2014; Kannan et al., 2014; Kannan et al., 2012). Some antibiotics function in a synergistic way, only partially inhibiting translation alone, but fully disable the ribosome from protein synthesis when combined. Streptogramin A (like virginiamycin M1 or dalfopristin), a class of 23-membered unsaturated ring antibiotics with lactone and peptide bonds binds close to the PTC spanning the P- and A-site blocking either proper CCA-end positioning or interfering with tRNA accommodation and therefore blocking peptide bond formation. Streptogramin B (like virginiamycin S1 or quinupristin) are depsipeptide antibiotics that bind within the NPET similar to a macrolide antibiotic and occlude the tunnel (Chinali et al., 1984; Hansen et al., 2002; Noeske et al., 2014; Osterman et al., 2017; Vannuffel and Cocito, 1996). Dalfopristin and quinupristin are used clinically against MRSA in a 70/30 mixture (Manzella, 2001). Klebsazolicin, a ribosomally-synthesized and post translationally modified peptide, binds through stacking interactions with rRNA bases to the NPET and blocks translation by occluding the tunnel (Metevlev et al., 2017). Thiopeptides, like thiostrepton, different from other described antibiotic classes target the GTPase functionality of essential factors during translation by binding close to the GTPase-associated center of loop H43 and H44 and blocking  $P_i$  and factor release (Harms et al., 2008). EF-G is also a target for fusidic acid or Argyrin B. These compounds trap the factor on the ribosome and block translocation (Gao et al., 2009; Wieland et al., 2022; Zhou et al., 2013).

### **7.3.1. Antimicrobial peptide myxovalargin**

Microorganisms, like the soil-dwelling predatory myxobacteria, are a major source for research of novel antibiotics but are severely understudied, even though they have proven to be a good source of compounds with antimicrobial activity (Baumann et al., 2014; Herrmann et al., 2017). In 1983 members of the linear antimicrobial peptides myxovalargins (Myx) from *Myxococcus fulvus* strain Mx f65 were isolated from soil of

the Kaiserstuhl mountains (Germany). Four different myxovalgins MyxA-D were originally identified. Additionally, myxovalgins were isolated from *Myxococcus xanthus* strains (Mx x4 and Mx 48) as well as from an *Archangium* strain (Ar D8) (Irschik et al., 1983).

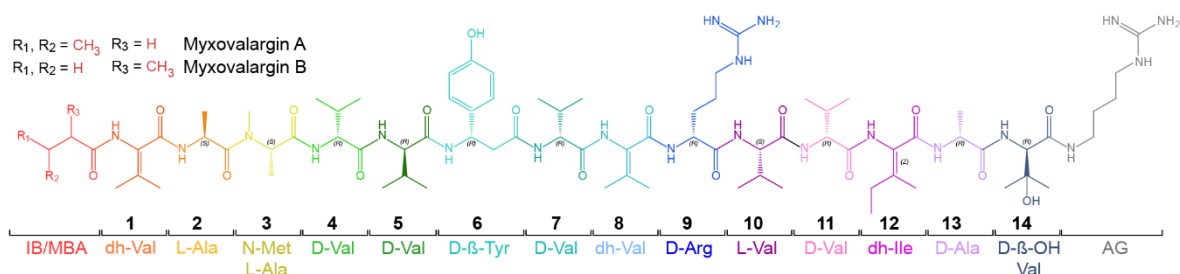


**Figure 5: Chemical structure of myxovalargin A/B colored by residues** (Steinmetz et al., 1987).

MyxA and MyxB are chemically similar, revealed by acid hydrolysis experiments, and are composed of 14 amino acids with a C-terminal agmatine residue and a N-terminal 3-methylbutanoic acid (MBA) or isobutric acid (IB), respectively (**Fig. 5**) (Steinmetz et al., 1987). Myxovalgins contain, in addition to the canonical amino acids L-valine and L-alanine, eight D-amino acids (D-alanine, D-arginine and D-β-tyrosine, D-β-hydroxyvaline and three D-valines) and four highly modified amino acids, specifically one N-methyl-alanine, one α,β-dehydroisoleucine and two α,β-dehydrovalines. The presence of D-amino acids in myxovalgins suggests their production to be achieved by a non-ribosomal peptide synthetase cluster (Hoffmann et al., 2018). MyxA was described to display excellent activity against a broad panel of bacteria, including *Staphylococcus aureus* and *Mycobacterium tuberculosis*, with minimum inhibitory concentrations (MICs) between 0.3 to 5 µg/ml against Gram-positive and 6 to 100 µg/ml against Gram-negative bacteria (Irschik et al., 1983). Additionally, an unspecific membrane effect was observed above 18 µg/ml causing damage to cells including human erythrocytes (Irschik and Reichenbach, 1985). Mice infected with *Escherichia coli*, *Staphylococcus aureus* and *Streptococcus pyogenes* in mouse models shown the efficacy at median effective doses (ED<sub>50</sub>) of 2.3, 2 x 0.4 and 2 x 10 mg/kg subcutaneously (s.c.). A median lethal dose (LD<sub>50</sub>) in mice was determined to be 10 mg/kg s.c.. MyxA was shown to target protein synthesis by metabolic labeling experiments in *S. aureus*, which was further confirmed using *E. coli in vitro* translation

assays monitoring poly(U)-dependent poly(Phe) synthesis. Myxovalgins were shown to be poor inhibitors of eukaryotic *in vitro* translation systems, such as wheat germ and rabbit reticulocyte lysate. Partial translation assays indicated that myxovalgins do not affect binding of the initiator fMet-tRNA to the P-site, but rather exert an inhibitory effect on binding of amino acyl-tRNAs to the A-site of the ribosome (Irschik and Reichenbach, 1985). However, the binding site of myxovalgins on the ribosome and the exact mechanism of action remain to be elucidated.

### **7.3.2. Proline-rich antimicrobial peptide drosocin**

Proline-rich antimicrobial peptides (PrAMPs), different from the previously discussed AMPs, kill bacteria by passing through the membrane and targeting intracellular processes like protein synthesis (Castle et al., 1999; Graf et al., 2017; Graf and Wilson, 2019; Krizsan et al., 2014; Mardirossian et al., 2014; Scocchi et al., 2011). There are two types of identified PrAMPs differing in their mechanism of action to inhibit protein synthesis. PrAMPs blocking the accommodation of the aminoacyl-tRNA in the A-site of the ribosome directly following translation initiation are type I and PrAMPs blocking the dissociation of release factors RF1 and RF2 during translation termination and not acting on initiation or elongation are type II (Graf and Wilson, 2019). Structural analysis of various type I PrAMPs originating from insects (metanikowin I, oncocin and pyrrococin) or mammals (Bac7 and Tur1A) revealed binding sites overlapping with their N-terminus at the A-site of the PTC and spanning through the NPET (Gagnon et al., 2016; Mardirossian et al., 2018b; Mardirossian et al., 2020; Roy et al., 2015; Seefeldt et al., 2016; Seefeldt et al., 2015). Translational arrest through type I PrAMPs is proposed to arise from the steric clashing with an incoming aminoacyl-tRNAs CCA-end in the A-site of the LSU (Gagnon et al., 2016; Graf et al., 2017; Graf and Wilson, 2019; Roy et al., 2015; Seefeldt et al., 2016; Seefeldt et al., 2015). Structural analysis of the type II PrAMP Api137, a synthetic derivative of apidaecin, a PrAMP naturally originating from honeybees, showed a similar binding site spanning through the NPET overlapping with the binding site of the type I PrAMPs. Different from the type II PrAMPs Api137 is oriented with the C-terminus at the PTC and not encroaching on the A-site. Api137 is known for stabilizing RF1 and trapping it right after peptidyl-tRNA hydrolysis and peptide release (Chan et al., 2020; Florin et al., 2017; Graf et al., 2018).

*Drosophila melanogaster* produces cecropins, defensins and dipterocins, which are classical membrane-targeting AMPs, but also produces the PrAMP drosocin. Drosocin is composed of 19 amino acids and rich in prolines and arginine residues, similar to other PrAMPs and shows good activity against Gram-negative bacteria like *E. coli* (Bikker et al., 2006; Bulet et al., 1993; Bulet et al., 1999).

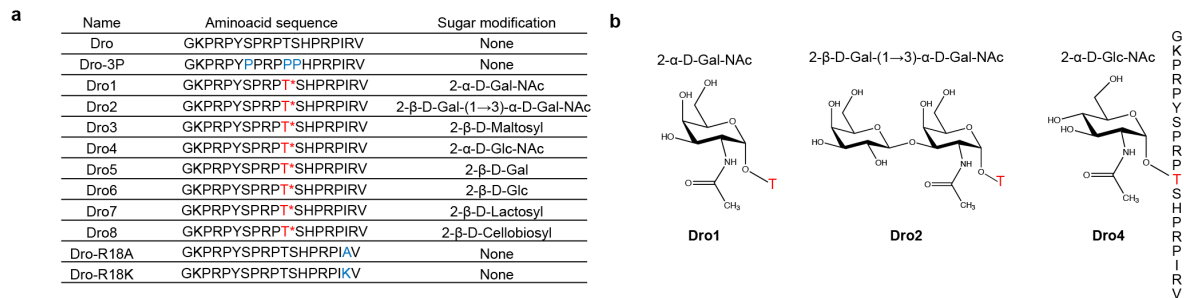


**Figure 6: O-glycosylation of drosocin peptide on Thr11.** **a**, Drosocin peptide sequences with varying O-glycosylation highlighted by a T\* and mutations shown in blue. **b**, Chemical structures of modifications on the Thr11 of Dro1, Dro2 and Dro4.

Unlike most other PrAMPs, drosocin is O-glycosylated with either the N-acetylgalactosamine ( $\alpha$ -D-GalNac) monosaccharide or N-acetylgalactosamine linked to a galactose ( $\beta$ -Gal(1 $\rightarrow$ 3)- $\alpha$ -D-GalNac) disaccharide on the Thr11 residue (**Fig. 6a-b**) (Bulet et al., 1993; Uttenweiler-Joseph et al., 1998). Drosocin bearing two individual monosaccharide modifications on residues Ser7 and Thr11 has been reported (Rabel et al., 2004). Infected *Drosophila* hemolymph showed formation of both mono- and disaccharide forms of drosocin with increasing concentrations of up to 40  $\mu$ M for up to 24 hours. The monosaccharide was present for up to three weeks while the disaccharide persisted for two weeks (Uttenweiler-Joseph et al., 1998). Decreased activity of the synthetic unmodified drosocin lacking the O-glycosylation compared to the naturally modified drosocin suggests the necessity of the post-translational modification for full activity (Bulet et al., 1993; Bulet et al., 1999; Bulet et al., 1996; Gobbo et al., 2002; Hoffmann et al., 1999). The unmodified form of drosocin showed a generally reduced activity compared to modified ones with varying sugar modifications in many studies (Ahn et al., 2011a; Ahn et al., 2011b; Gobbo et al., 2002; Lele et al., 2015a; Marcaurelle et al., 1998; Otvos et al., 2000; Rodriguez et al., 1997; Talat et al., 2011). While both forms, either modified or unmodified, adopt an extended conformation in solution, the glycosylation was proposed to help establish a stable



extended conformation when binding intracellular targets of drosocin. The exact role of the modification for drosocin's activity remains unclear, but improves solubility, serum stability and increases biological activity (Bulet et al., 1999; Bulet et al., 1996; Gobbo et al., 2002; Lele et al., 2015b; McManus et al., 1999; Talat et al., 2011). Inhibition of protein synthesis both *in vivo* and *in vitro* were shown but the exact mechanism of action of drosocin currently remains unclear (Lele et al., 2015b; Ludwig et al., 2022). Pyrrhocoricin, a type I PrAMP, is known to be O-glycosylated at Thr11 with a N-acetylgalactosamine at the same position as drosocin and a less abundant disaccharide modified form has been detected as well (Cociancich et al., 1994). Based on the sequence similarities, drosocin was proposed to have a similar mechanism of action analogously to pyrrhocoricin or metalnikowins (type I PrAMPs) and different from abaecins or apidaecins (type II PrAMPs) (Bulet et al., 1999). However, unmodified pyrrhocoricin showed better activity than unmodified drosocin suggesting that drosocin might be more similar to apidaecin (Hoffmann et al., 1999). Ribosome-binding antibiotic competition assays of drosocin showed similarities to apidaecin-like PrAMPs by competing better with type II PrAMP Api137 and less with type I PrAMP Onc-112, an oncocin derivative produced by the milkweed bug (Krizsan et al., 2015). Additionally, the removal of drosocin's C-terminal Arg18 and Val19 residues reduced the antimicrobial activity drastically (Hoffmann et al., 1999), in a similar fashion as for Api137 (Berthold and Hoffmann, 2014), and different from type I PrAMPs like Bac7 of which truncations of N-terminal residues inactivated the antimicrobial activity (Benincasa et al., 2004; Seefeldt et al., 2016).

### **7.3.3. Context-specific action of macrolide antibiotics on the eukaryotic ribosome**

The expression of defective and unwanted proteins is the cause of many human diseases (Archacki and Wang, 2004; Goedert, 2015; Maxwell et al., 2005). Therapies against these diseases usually block the functions of the proteins and thereby reducing their harmful activities, but in many cases don't actively remove them from the system. A more suitable strategy to combat these diseases would be ribosome-targeting compounds inhibiting the production of the malicious proteins. However, ribosome-targeting compounds need to be very specialized not to inhibit the translation

machinery of all proteins but discriminate healthy from unwanted proteins. PF846 is a compound that was recently discovered, which is able to bind eukaryotic ribosomes in the NPET and inhibit translation on a very specific set of nascent chains that accommodate in a peculiar conformation in the NPET (Li et al., 2020b; Li et al., 2019). The mechanism of action of PF846 still needs to be elucidated as the prediction of targeted nascent chains is currently very difficult. Based on the selective inhibition of PF846 the concept of small compounds targeting the eukaryotic ribosome similar to the bacterial ribosome pushed it more into the focus of researchers. Bacteria are known to have inducible resistance mechanisms against macrolide antibiotics by very specific programmed translational arrest that targets only ribosomes translating specific mRNA codons and does not interfere with translation of other sequences (Horinouchi and Weisblum, 1980; Shivakumar et al., 1980). Most of the known antibiotics, with macrolides being the best understood, act on bacterial ribosomes in a context-specific manner, which includes specific nascent chain sequences, nature of the tRNA and mRNA sequences or structures that are beneficial for antibiotic activity (Vazquez-Laslop and Mankin, 2018a, b). Macrolides are macrocyclic lactone ring systems, that like their most known member erythromycin (Ery) and later developed ketolides telithromycin (Tel) and solithromycin bind the NPET of the bacterial ribosome in close proximity to the PTC (Bulkley et al., 2010; Dunkle et al., 2010; Schlunzen et al., 2001; Tu et al., 2005). All three of the aforementioned macrolides contain a C5-desosamine sugar, however, the improved ketolides have no cladinose sugar like Ery but contain a keto group in the C3 position and are modified on the C12 with an alkyl-aryl group (Svetlov et al., 2021a). All macrolides form interactions with 23S rRNA residues, most importantly with the N6 of A2058, which coordinates a water molecule that forms hydrogen bonds with the dimethylamino group of the desosamine sugar. This water was shown to be essential for the binding of macrolides and is displaced in resistant Erm-dimethylated 70S ribosomes (Svetlov et al., 2021b). While the A2058 is conserved in bacteria, the equivalent adenosine is replaced by a guanine in eukaryotic ribosomes (G2400 in *Saccharomyces cerevisiae* 25S rRNA) and is supposed to be an important difference for bacterial selectivity of macrolide antibiotics (Tu et al., 2005). Additionally, the ketolides C12 alkyl-aryl sidechain stacks onto A752 and U2609 in bacteria improving the stability in the NPET which are conserved in eukaryotes and bacteria (Dunkle et al., 2010). Macrolides were thought to occlude the NPET and block

it for most amino acid sequences over a certain length by their bulky shape (Mankin, 2008; Tenson et al., 2003). However, subsequent studies of macrolides bound to the ribosome revealed nascent chains in the macrolide occluded NPET are selectively blocking specific amino acid sequences being translated by ribosomes while others bypass the antibiotic instead. Besides the translated amino acid sequence, also the chemical and structural features of the antibiotic in the NPET are important for the context specificity. (Almutairi et al., 2017; Davis et al., 2014; Kannan et al., 2014; Kannan et al., 2012; Vazquez-Laslop et al., 2011; Vazquez-Laslop and Mankin, 2018a). The context-specificity of macrolides arises not from the ability to bypass the antibiotic but from the inability to execute peptide bond formation on specific amino acid sequences being translated (Arenz et al., 2016a; Arenz et al., 2014a; Ramu et al., 2011; Sothiselvam et al., 2014; Sothiselvam et al., 2016). The context-specific properties of macrolides make them a promising target for selective eukaryotic translation inhibitors. Currently, the set of available macrolides and context-specificity could not be extrapolated for use in eukaryotic translation due to substantial differences in structural and functional properties of the NPET in eukaryotic ribosomes (Ben-Shem et al., 2011; Dao Duc et al., 2019; Ito and Chiba, 2013; Metelev et al., 2017; Vazquez-Laslop and Mankin, 2011). And lastly the mutation of G2400 (EcoA2058) to an adenosine did not yield the eukaryotic ribosome susceptible to Ery (Bommakanti et al., 2008).

#### **7.4. Target protection**

Similarly interesting as antibiotics and antimicrobial peptides targeting the ribosome are antibiotic resistance mechanisms. Target protection is one of the mechanisms allowing antibiotic resistance by physical interactions of a resistance protein with an antibiotic target and thereby rescuing it from antibiotic-induced inhibition (Antimicrobial Resistance, 2022; Wilson et al., 2020). Ribosome protection proteins (RRPs) are the best characterized target protection mechanisms against ribosome-targeting antibiotics. TetO and TetM are representatives of type I RRP, which bind the target and overlap with the antibiotic, in this case tetracyclines binding site and thereby inducing its dissociation of the antibiotic (Arenz et al., 2015; Dönhöfer et al., 2012; Li et al., 2013; Wilson et al., 2020). Type II RRP induce allosteric changes within a

drug's binding site by binding to a distinct site of the target and confer resistance by promoting drug dissociation. Representatives of type II RRPS are adenosine triphosphate (ATP) binding cassette type F (ABCs) proteins which are members of the large family of antibiotic resistance proteins (ARE) that are conferring resistance to various antibiotics binding near the PTC of the LSU (Crowe-McAuliffe et al., 2022; Crowe-McAuliffe et al., 2021; Ero et al., 2019; Mohamad et al., 2022; Murina et al., 2018; Sharkey and O'Neill, 2018; Wilson et al., 2020). Lastly, type III RRP restore the activity of the target by conformational changes without actively displacing the bound antibiotic, which fusidic acid resistance proteins FusB and FusC are examples of (Cox et al., 2012; Tomlinson et al., 2016; Wilson et al., 2020).

#### **7.4.1. HflX and HflXr**

The resistance protein HflX<sub>r</sub> (*encoded by the gene Imo0762*) has recently been identified in *Listeria monocytogenes* and has been shown to confer resistance to lincosamides, such as clindamycin or lincomycin, and macrolides, such as azithromycin or erythromycin, but did not confer resistance to chloramphenicol or retapamulin. However, only in absence of the ARE-ABC VgaL (encoded by gene *Imo0919*) in *L. monocytogenes* the effect of the loss of HflX<sub>r</sub> on the antibiotic susceptibility was observable, suggesting a certain redundancy between these two proteins that show a partially overlapping spectrum of antibiotics (Duval et al., 2018). The more abundant GTPase HflX (encoded by the gene *Imo1296* in *L. monocytogenes*) is a homolog of HflX<sub>r</sub>, which is widely distributed in bacteria, and shares a sequence identity of 37%, however, does not confer resistance to antibiotics (Duval et al., 2018). HflX is proposed to recycle 70S ribosomes by splitting them into the individual subunits that have been stalled in stress conditions. Additionally, it was shown to disassemble 100S hibernating ribosomes in *S. aureus* (Basu and Yap, 2017; Coatham et al., 2016; Dey et al., 2018; Srinivasan et al., 2019; Zhang et al., 2015b). Accumulation of 70S ribosomes was observed upon deletion of the gene encoding HflX<sub>r</sub>, suggesting the mechanism of action of HflX<sub>r</sub> conferring resistance might be splitting and recycling the antibiotic-stalled ribosomes (Duval et al., 2018). Structures of HflX from *E. coli* on the LSU and more recently the human mitochondrial HflX homolog GTPBP6 bound to the LSU biogenesis intermediate are available, however,

the direct interaction of HflXr with either LSU or 70S ribosomes has not been demonstrated (Dey et al., 2018; Hillen et al., 2021; Zhang et al., 2015b). Similar to *E. coli* HflX, the HflX homolog in *L. monocytogenes* does not show antibiotic resistance functionality, which raises the question whether recycling of ribosomes by splitting the subunits of antibiotic-stalled ribosomes is sufficient to confer resistance, or whether HflXr uses a different mechanism of action for its target protection role with the LSU as a target for drug release (Duval et al., 2018). The cryo-EM structure of *E. coli* HflX bound to the ribosome in complex with GDPNP revealed the loop connecting two helices of subdomain II of the N-terminal HflX domain is in close proximity to the lincomycin binding site near the PTC. The *L. monocytogenes* HflXr was found to have a two-residue longer loop than the *E. coli* HflX which offers, based on differences in their sequence, a possibility to reach deeper into the PTC by adopting a distinct conformation and thereby overlapping with the antibiotic binding sites. Based on these observations, the HflX and HflXr proteins that have longer loops could confer antibiotic resistance similar to type I or type II target protection mechanisms (Wilson et al., 2020; Zhang et al., 2015b).



## 8. Methods

### 8.1. Polymerase chain reaction

The polymerase chain reaction was used to amplify linear DNA from a pIVEX-2.3MCS plasmid containing the firefly luciferase gene. A Phusion high fidelity (HF) polymerase (New England Biolabs) was used, and the reaction mix and cycle based on a NEB protocol (M0530, [dx.doi.org/10.17504/protocols.io.cdjs4m](https://doi.org/10.17504/protocols.io.cdjs4m)). The composition of the reaction mix is listed in table 1 and the PCR cycle is listed in table 2. The PCR was performed in a thermocycler (peqStar, VWR peqlab).

**Table 1: PCR reaction mix.**

Components	Volume ( $\mu\text{L}$ )
5x Phusion HF buffer	10
dNTP mix (10 mM)	1
T7 FWD primer (10 mM)	2.5
T7 REV primer (10 mM)	2.5
Fluc pIVEX-2.3MCS plasmid	X (<250 ng)
Phusion HF polymerase	0.5 (1.0 units)
Water (ddH <sub>2</sub> O, nuclease free)	X to 50 $\mu\text{L}$

**Table 2: PCR cycle.**

Step	Temperature	Time (sec)
Initial denaturation	98°C	30
32 x cycles	98°C	5
	56°C	15
	72°C	90
Extension	72°C	300
Hold	4°C	$\infty$

## 8.2. *In vitro* transcription

Linear Fluc-DNA was *in vitro* transcribed using T7 polymerase and was upscaled and optimized from a ThermoScientific user guide (EP0112, MAN0016017) as described in (Krieg and Melton, 1984). In table 3 the components of the reaction mix are listed. The 5x transcription buffer (200 mM Tris-HCl (pH 7.9 at 25°C), 30 mM MgCl<sub>2</sub>, 50 mM DTT, 50 mM NaCl and 10 mM spermidine), T7 polymerase, NTP mix (25 mM each, freshly prepared from NTP set) and RNase inhibitor were used from ThermoScientific.

**Table 3: Reaction mix for *in vitro* transcription using T7 polymerase.**

Component	Volume (μL)
5x transcription buffer.	100
NTP mix (25 mM each)	40
T7 polymerase	15
RNase inhibitor	5
Linear Fluc-DNA	X (~10 μg)
Water (ddH <sub>2</sub> O, nuclease free)	X to 500 μL

The reaction mix was incubated at 30°C for 16 hours. The mRNA was purified by LiCl precipitation as described in (Barlow et al., 1963; Cathala et al., 1983). 500 μL LiCl (7.5 mM + 1 mM EDTA, ThermoScientific) was added to the reaction mix and stored for 30 min at -20°C. The frozen reaction mix was centrifuged for 10 min at 18,000 x g at 4°C in a tabletop centrifuge (Eppendorf 5425R). The supernatant was discarded, the resulting pellet was washed with 500 μL of 75% Ethanol chilled at -20°C and again centrifuged for 2 min at 18,000 x g at 4°C. The supernatant was discarded and the pellet air dried for 45 min. The pellet was resuspended in 50 μL ddH<sub>2</sub>O and the concentration determined at optical density at 260 nm and the quality checked on an agarose bleach gel (1% agarose with 0.5% NaOCl) as described in (Aranda et al., 2012). The mRNA was stored at -20°C.



### 8.3. Purification of mutant ribosomes

*Escherichia coli* Squires strains (Quan et al., 2015) SQ171 $\Delta$ tolC bearing only one rRNA operon from a plasmid pAM552 with either no, or a single A2503G or U2609C mutation in the 23S rRNA were provided by Prof. Alexander S. Mankin from University of Illinois (Chicago, Illinois, USA). Wildtype and mutant strains were grown in 2xYPTG (16 g/L peptone, 10 g/L yeast extract, 5 g/L NaCl, 3 g/L NaH<sub>2</sub>PO<sub>4</sub>, 7.1 g/L Na<sub>2</sub>HPO<sub>4</sub>, 19.8 g/L glucose) until reaching an optical density (OD) 600 nm at 0.6 as described for S12 extracts in (Kim et al., 2006). Cells were harvested at 8,000 x g in a JLA-8.1000 fixed-angle rotor (Beckman Coulter) for 20 min at 4°C, supernatant removed and cells resuspended in Hico buffer (50 mM HEPES-KOH (pH 7.2 at 4°C), 500 mM KOAc, 10 mM Mg(OAc)<sub>2</sub>, 0.1% DDM), and spun down again at 3,000 x g for 10 min at 4°C. The cells were resuspended again in Hico buffer with protease inhibitor cComplete (Roche) and RNase inhibitor (New England Biolabs) and lysed by three iterative passes through a microfluidizer LM10 (Microfluidics) at 15,000 psi. The lysates were cleared by centrifugation at 12,000 x g for 20 min at 4°C using a JA 25.50 fixed angle rotor (Beckman Coulter). The cleared lysate was layered onto a sucrose cushion (Hico buffer, 25% sucrose) and centrifuged for 16 hours at 100 000 x g at 4°C in a Ti45 fixed angle rotor (Beckman Coulter), the supernatant removed, the pellet resuspended in Hico buffer and layered again onto a sucrose cushion (Hico buffer, 25% sucrose) and centrifuged for 3 hours at 70 000 x g at 4°C in a TLA110 fixed angle rotor (Beckman Coulter). The pellet was resuspended in Hico buffer (50 mM HEPES-KOH (pH 7.2 at 4°C), 100 mM KOAc, 10 mM Mg(OAc)<sub>2</sub>, 2 mM DTT) and adjusted to an OD<sub>260</sub>/ ml of 800-100.

### 8.4. Firefly luciferase *in vitro* translation assay with mutant ribosomes

The translation efficiency was monitored using a firefly luciferase (Fluc) template (Mardirossian et al., 2018b; Seefeldt et al., 2015), which was *in vitro* transcribed as described in methods section 8.2. The assays were performed in an *E. coli* PURExpress® system  $\Delta$ ribosome kit (NEB E3313) and ribosomes were substituted by the purified wildtype, A2503G and U2609 mutant ribosomes (methods section 8.3)

at the same concentration as the ribosomes provided by the kit. The assay was performed in absence and presence of increasing concentrations of MyxB. 4.75  $\mu\text{L}$  of PURExpress® system  $\Delta$ ribosome mix were mixed with 1  $\mu\text{L}$  antibiotic solution, 10 ng/ $\mu\text{L}$  mRNA and 0.25  $\mu\text{L}$  RNase inhibitor (New England Biolabs) and incubated at 32°C for 30 min while shaking (600 rpm). The reaction was stopped by adding 5  $\mu\text{L}$  kanamycin (50 mg/ml) and transferred into a 96-well microtiter plate (Greiner Lumitrac, non-binding, white, chimney). Luminescence was measured using a plate reader (Tecan Infinite®200 Pro) after addition of 40  $\mu\text{L}$  luciferase substrate solution (Promega E1501). The absolute luminescence was normalized against a reaction in absence of antibiotic and in presence of nuclease-free water. To validate the function of the assay both telithromycin and chloramphenicol were tested at increasing concentrations (data not shown).

## **8.5. Complex preparation for Cryo-EM**

The preparation procedure of the complexes for the individual projects are listed below. Grids were prepared using a Vitrobot Mark IV (FEI) at 4°C and 100% chamber humidity. 3.5  $\mu\text{L}$  ribosome complexes at 5-8 OD<sub>260</sub>/ml were applied to cryo-grids and blotted for 5 s and vitrified immediately by plunge-freezing them in liquid ethane-propane and stored under liquid N<sub>2</sub> conditions. Cryo-grids were used from Quantifoil with different specifications (R2/2 or R3/3) made from copper with holey or continuous carbon of 2-3 nm thickness. Cryo-grids were glow-discharged before preparation.

### **8.5.1. Myxovalargin**

#### **8.5.1.1. MyxA-70S-complex**

For the MyxA-70S-complex reassociated *Escherichia coli* Keio wildtype (strain K-12 BW2511370S) ribosomes were used. These were prepared as previously described in (Blaha et al., 2000) by Dr. Bertrand Beckert (Koller et al., 2022a). 8 OD<sub>260</sub>/ml of ribosomes were mixed with 200  $\mu\text{M}$  MyxA and incubated at 30°C for 15 min at 600 rpm and applied to cryo-grids (Quantifoil R3/3 Cu300 3 nm holey carbon) at 8 OD<sub>260</sub>/ml.

### 8.5.1.2. MyxB-70S-complex

The MyxB-70S-complex was prepared by Maha Abdelshahid from our group as shown in **Fig. 7** and as described in (Koller et al., 2022a). Briefly, the complex was prepared using a disome approach (Arenz et al., 2016a; Arenz et al., 2015; Arenz et al., 2014b), by translating a *2XermCL* dicistronic mRNA in presence of 100  $\mu$ M MyxB in the Rapid Translation System RTS 100 *E. coli* HY kit.

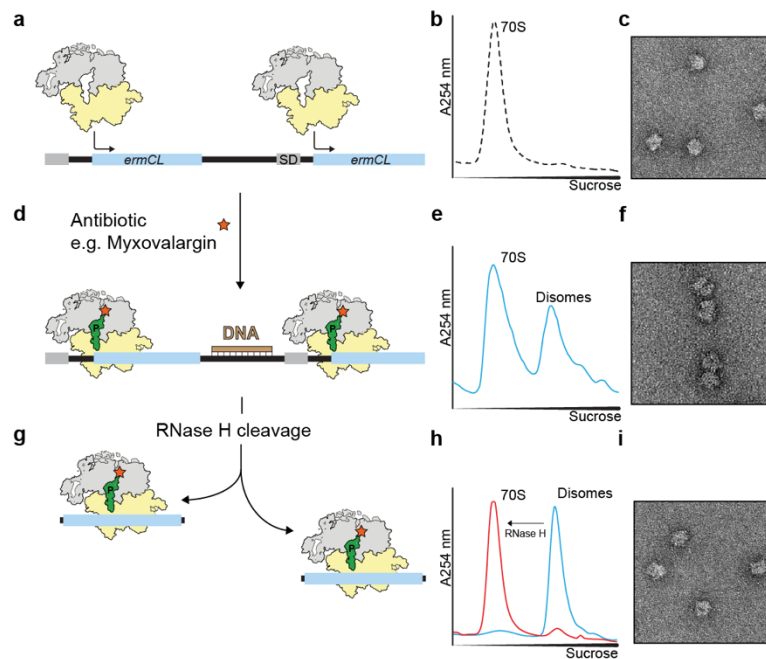


**Figure 7: Preparation of the MyxB-70S-complex.** **a-c**, Schematic depiction of the translation of the dicistronic *ermCL* mRNA construct in absence of MyxB, leads to single 70S peaks on a sucrose gradient (**b**) and results in individual 70S ribosomes observed in negative stain electron microscopy (**c**). **d-f**, Schematic depiction of the translation of the dicistronic *ermCL* mRNA construct in presence of MyxB, leads to both 70S peaks and disome peaks on a sucrose gradient (**e**) and results in disomes being observed in negative stain electron microscopy (**f**). **g-i**, Annealing a DNA oligonucleotide to the *ermCL* construct and cleavage by RNase H allows splitting of the disomes to monosomes, supported by a shift of the disome peak (blue) to a monosome peak (red) on a sucrose gradient (**h**) and individual 70S ribosomes observed by negative stain electron microscopy (**i**). Modified from (Koller et al., 2022a).

The complex was purified by sucrose density gradient (10-55% sucrose) centrifugation and analyzed by negative stain microscopy (80 kV). The complex was applied to cryo-grids (Quantifoil R2/2 Cu300 3 nm holey carbon) at 5 OD<sub>260</sub>/ml.

### **8.5.2. *E. coli* 70S-Dro1-complex**

The *Escherichia coli* 70S-Dro1-complex was prepared by *in vitro* transcription-translation reaction on a linear DNA template with the sequence AUG-MLIF-UAA in the PURExpress® system  $\Delta$ RF123 (New England Biolabs, E6850S) with 10x release factor 1 (RF1) and 1x RF3 added in presence of 30  $\mu$ M Dro1. The reaction was incubated for 15 min at 37°C and isolated by layering on a sucrose cushion (40% sucrose, Hico buffer (50 mM HEPES-KOH (pH 7.4 at 4°C), 100 mM KOAc, 25 mM Mg(OAc)<sub>2</sub>, 0.01% DDM) supplemented with 10x RF1, 1x RF3 and 30  $\mu$ M Dro1) and centrifuged for 3 hours at 80,000 x g in an Optima™ Max-XP tabletop ultracentrifuge in a TLA 120.2 fixed angle rotor. The ribosome pellet was resuspended in Hico buffer (50 mM HEPES-KOH (pH 7.4 at 4°C), 100 mM KOAc, 25 mM Mg(OAc)<sub>2</sub>, 0.01% DDM) supplemented with 10x RF1, 1x RF3 and 30  $\mu$ M Dro1) and applied to cryo-grids (Quantifoil R3/3 Cu300 3 nm holey carbon) at 8 OD<sub>260</sub>/ml.

### **8.5.3. G2400A mutant *S. cerevisiae* 80S-Tel-complex**

The G2400A mutant *S. cerevisiae* 80S ribosomes were purified by Dr. Maxim Svetlov as described in (Svetlov et al., 2021a) and incubated with 50  $\mu$ M Tel for 15 min at 4°C in Hico buffer (10 mM HEPES-KOH (pH 7.5 at 4°C), 50 mM KOAc, 10 mM NH<sub>4</sub>OAc, 5 mM Mg(OAc)<sub>2</sub>, 2 mM DTT). The complex was applied to cryo-grids (Quantifoil R3/3 Cu300 3 nm holey carbon) at 5 OD<sub>260</sub>/ml.

### **8.5.4. *L. monocytogenes* complexes**

*L. monocytogenes* complexes were purified by Dr. Kathryn Turnbull and Prof. Vasili Hauryliuk as described in (Koller et al., 2022b). Briefly, 70S ribosomes were purified from *L. monocytogenes* EGDe strain through sucrose gradient centrifugation and incubated with 100  $\mu$ M lincomycin for 15 min at 4°C for the Lmo-70S-lincomycin complex and applied to cryo-grids (Quantifoil R2/2 Cu300 with 2 nm continuous carbon) at 5 OD<sub>260</sub>/ml. For both the HflXr-50S-GDPNP-complex and HflX-50S-GDPNP-complex the *L. monocytogenes* EGDe strain  $\Delta$ *hflXr* were used and the factors were over expressed from a pIMK3:*hflXr* or pIMK3:*hflX* plasmid, induced by 0.5 mM

IPTG, harvested, lysed and cell debris removed. The complexes were purified by FLAG-M2 affinity purification in the presence of 0.5 mM GDPNP and the complex eluted in presence of 0.2 mg/ml FLAG peptide in polymix buffer (20 mM HEPES-KOH (pH 7.5 at 4°C), 5 mM Mg(OAc)<sub>2</sub>, 95 mM KCl, 15 mM NH<sub>4</sub>Cl, 0.5 mM CaCl<sub>2</sub>, 8 mM putrescine, 1 mM spermidine, 0.5 mM EDTA, 0.05% Nikkol) and applied to cryo-grids (Quantifoil R2/2 Cu300 with 2 nm continuous carbon) at 5 OD<sub>260</sub>/ml.

## 8.6. Cryo-electron microscopy data collection

All grids were screened using a 200 kV Talos Arctica (FEI) with a field emission gun (X-FEG) and a Falcon 3EC direct detector at the Centre for Structural Systems Biology (CSSB, Hamburg, Germany). Data collection was performed at four different facilities with different setups of Titan Krios 300kV microscopes and exact specifications are listed in table 4.

**Table 4: Cryo-electron microscopy data collections.**

Dataset	Facility	Detector	Pixel size (Å/px)	Movies collected
MyxA-70S	CEITEC	Gatan K2 summit	0.828	8,208
Dro-70S	DCI	FEI Falcon 4	0.8	8,861
MyxB-70S	Gene Center LMU	FEI Falcon 2	0.1053	5,132
Tel-80S	Gene Center LMU	Gatan K2 summit	0.822	4,371
HfIXr-50S	UCEM	Gatan K2 summit	0.82	4,255
HfIX-50S	UCEM	Gatan K2 summit	0.82	4,480
Lnc-70S	UCEM	Gatan K2 summit	0.7725	14,982

## 8.7. Single-particle reconstruction of cryo-EM datasets and molecular modelling

### 8.7.1. Single-particle reconstruction of cryo-EM datasets

Processing was performed both in RELION 3.1 and RELION 4.0 (Zivanov et al., 2018) on Linux-based GPU workstations. Motion correction of the collected multi-frame movies was performed with RELION's implementation of MotionCor2 with 5x5 patches in unbinned pixel size (Zheng et al., 2017). CTF values were estimated with CTFFIND 4.1.14 using power spectra within RELION (Min. res. 30 Å, Max. res 2 Å, Min. defocus 2500 Å, Max. defocus 50,000 Å, defocus step size 500 Å) (Rohou and Grigorieff, 2015). Particles were picked from the motion corrected micrographs using crYOLO with a general model through the command line (`cryolo_predict.py -c config.json -w gmodel.h5 -i *.mrc -o picked_particles -t 0.2 -pbs 3 -gpu_fraction 1.0 -nc -1 -mw 100 -sr 1.4`) (Wagner et al., 2019) and were manually inspected on a random set of 10-30 micrographs using `relion_display` (`relion_display --i micrograph.mrc --pick --angpix --lowpass 20 --scale 0.2`). Particles were imported to RELION and extracted at 5x reduced pixel size, based on an appropriate box size for the pixel size used during data collection. 2D classification was performed using RELION's EM algorithm with 50 classes for 100 iterations. Ribosome-like particles were selected manually in RELION's subset selection. Particles were re-extracted at 3x reduced pixel size and initially 3D refined. A cryo-EM map from the same organism was used as reference adjusted to correct pixel size (`relion_image_handler --i reference.mrc --o reference_pix_box.mrc --angpix --rescale_angpix --new_box`). 3D classification, and subsequent focus sorting, was performed until stable classes were observed. Particles were selected and re-extracted at undecimated pixel size and subjected to 3D refinement, followed by subsequent CTF refinement (4<sup>th</sup> order aberrations, beam-tilt, anisotropic magnification, and per-particle defocus value estimation). For Bayesian polishing a training was performed on a subset of 10,000 particles and optimized parameters used for the final polishing (Zivanov et al., 2019). 3D refinements after each step were performed to improve the overall resolution of the complexes. The resulting maps after each 3D refinement were post-processed with a mask created at appropriate threshold (extended by 6 px, with 6 px soft-edge) or from a molmap at 4 Å (created in ChimeraX (Goddard et al., 2018; Pettersen et al., 2021)), and automatically

estimated B-factor applied. During 3D refinement steps the modulation transfer function (MTF) of the detector was applied. The final resolution of the final masked reconstructions was estimated at  $FSC_{0.143}$  (gold-standard) (Zivanov et al., 2018; Zivanov et al., 2019). Some of the resulting maps were lowpass filtered for molecular modelling skipping the FSC weighting step in RELION post processing and applying an ad hoc filter.

### **8.7.2. Local resolution and local filtering calculations**

Bsoft was used for local resolution calculations and local filtering (Heymann, 2018). The half-maps were normalized (`bimg -data float -rescale 0,1 half.mrc half_norm.mrc`) and a mask was created in ChimeraX 1.4 (`volume onesmask`) (Goddard et al., 2018; Pettersen et al., 2021). Blocres was run with both normalized half-maps, mask and max. resolution from the FSC curve created by RELION (Zivanov et al., 2018) (`blocres -maxres -box -sampling -cutoff 0.143 -verbose 1 -fill -origin 0,0,0 -Mask half1_norm.mrc half2_norm`). Maps were locally filtered with the calculated local resolution (`blocfilt -box -sampling -verbose -origin 0,0,0 -Resolution localres.mrc -Mask`). Coloring according to local resolution was performed in ChimeraX 1.4 (Goddard et al., 2018; Pettersen et al., 2021) (`color sample map offset 0.1 update true palette range X, Y`) on the 3D refined and/or post-processed maps.

### **8.7.3. Molecular modelling**

Modelling was performed in Coot (Emsley et al., 2010) from the CCP4 software suite (Winn et al., 2011). Initial models were taken from the PDB database (Berman et al., 2000; Burley et al., 2021) and are cited in the methods section and rigid body fitted in ChimeraX (Goddard et al., 2018; Pettersen et al., 2021). Molecular restrains were created using aceDRG within the CCP4 software suit (Long et al., 2017). Initial refinements were performed in Phenix 1.19.2-4158 and 1.20.1-4487 (Liebschner et al., 2019; Moriarty et al., 2009), and final refinements were performed with Refmac5 within Servalcat (Yamashita et al., 2021). Servalcat was also used to prepare difference maps to place waters in Coot. The final model was validated in Phenix comprehensive Cryo-EM validation (Chen et al., 2010; Liebschner et al., 2019)

## 8.7.4. Single particle analysis of myxovalargin complexes

### 8.7.4.1. MyxA-70S-complex

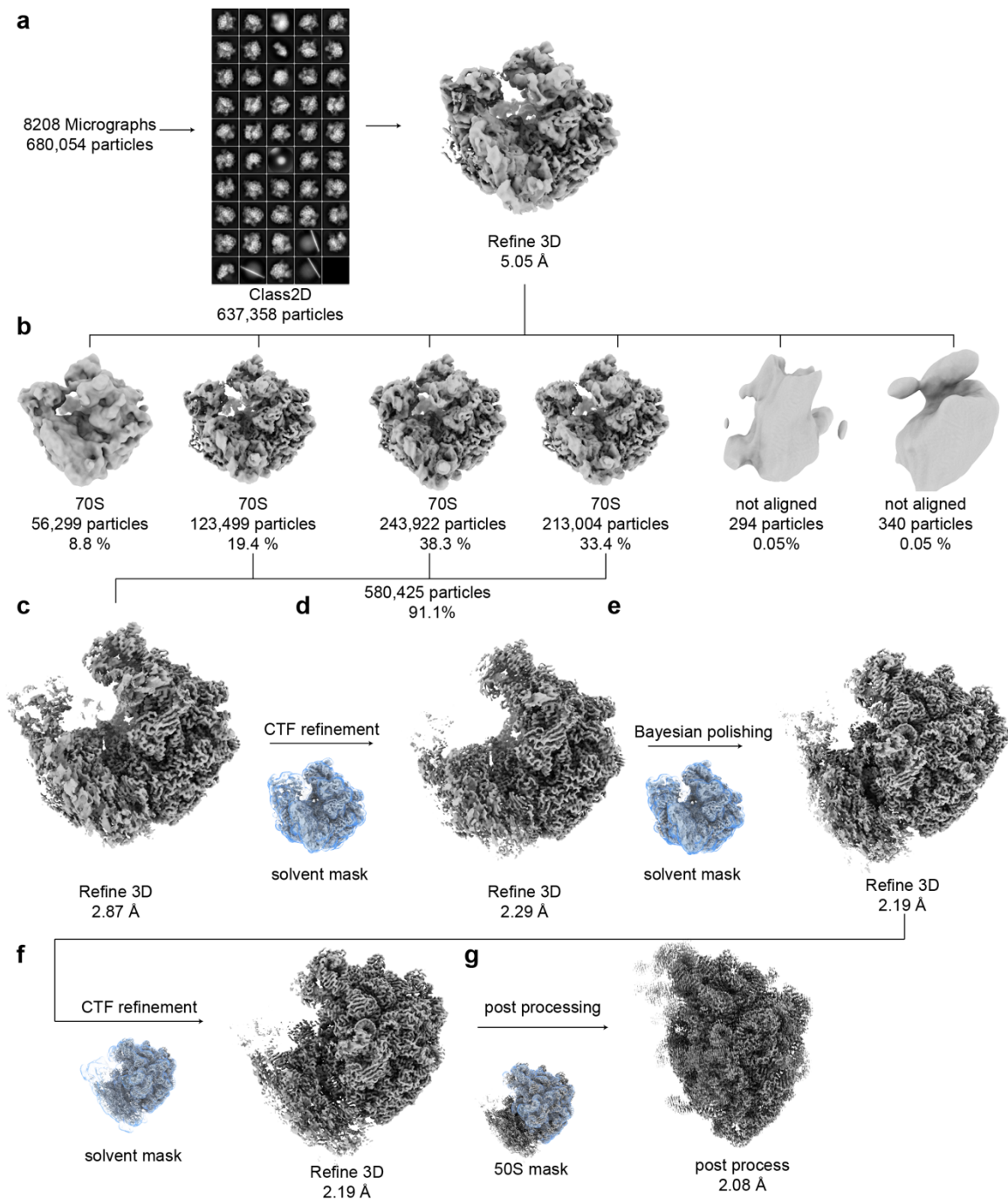


**Figure 8: *In silico* sorting for the MyxA-50S-complex.** **a**, From 8,208 micrographs a total of 680,054 particles were picked and subjected to 2D classification, resulting in 637,358 ribosome-like particles which were extracted in three times decimated pixelsize (2.46 Å/px) and initially 3D refined. **b**, Particles subjected to 100 iterations of 3D classification yielded four classes of 70S ribosomes with a density in the NPET. **c-e**, Combined particles (580,425 particles) of well-resolved 70S ribosomes (despite the rotation of the 30S subunit) were 3D refined (**c**), CTF refined (**d**, 4<sup>th</sup> order aberration, beamtilt, anisotropic magnification and per-particle defocus value estimation) and Bayesian



polished (e). **f-g**, the final reconstruction of the MyxA-50S-complex reached a final average masked resolution of 2.08 Å using a 50S solvent mask.

The *E. coli*-70S-MyxA dataset was processed at a pixel size of 0.828 Å/px. A total of 8,208 movies were collected with a total dose of 44 e<sup>-</sup>/Å<sup>2</sup>, 40 frames and a defocus range of -1.0 to -3.0 μm. A box size of 360 px<sup>3</sup> was used for the undecimated 3D refinement. Motion correction, defocus value estimation and particle picking were performed as described in method section 8.7.1. A total of 680,054 particles were picked and extracted at 6x decimated pixel size (60 px<sup>3</sup>, 4.968 Å/px) and subjected to 2D classification, resulting in 637,358 ribosome-like particles (Fig. 8a). Ribosome-like particles were extracted at 3x decimated pixel size (120 px<sup>3</sup>, 2.484 Å/px) and an initial 3D refinement was performed with the map of an *E. coli*-70S-ErmBL-complex (EMD-8175 (Arenz et al., 2016a)) as reference, resulting in a 70S ribosome with P- and E-site tRNAs (Fig. 8a). Non-aligning 3D classification was performed for 100 iterations (Fig. 8b). Three classes containing high resolution 70S ribosomes (91.1%, 580,425 particles) with additional density in the NPET were combined, despite their 30S subunit rotation (Fig. 8c). The particles were brought to high resolution, as described in methods section 8.7.1 and FSC curve are shown in Fig. 9a.

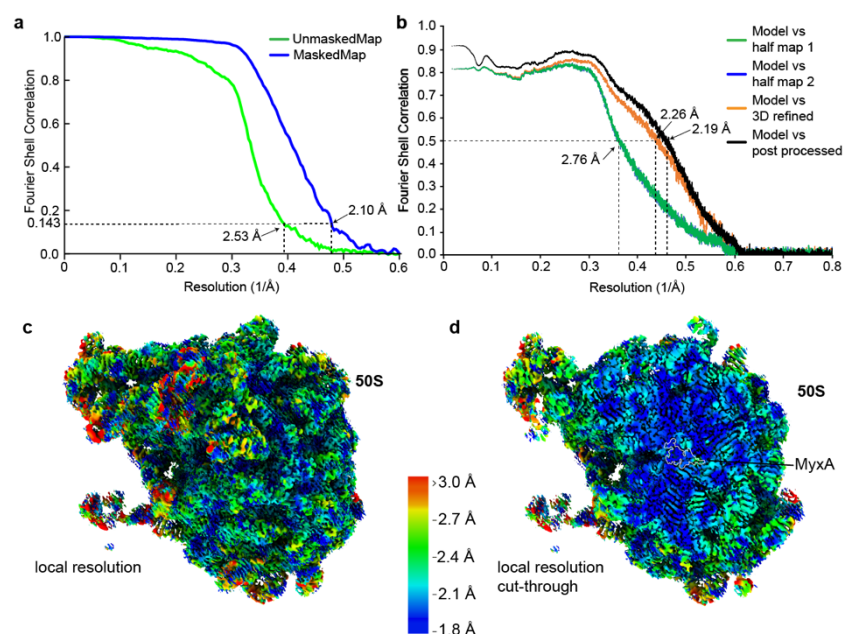


**Figure 9: FSC curves and local resolution of the MyxA-50S-complex.** a, Fourier shell correlation (FSC) curves of unmasked (green) and masked (blue) reconstruction of the MyxA-50S-complex with indicated average resolutions of 2.53 Å and 2.1 Å (at FSC<sub>0.143</sub>), respectively. b, Map-vs-model cross correlation curves for the cryo-

EM half-maps 1 (green) and 2 (blue) and for the unmasked 3D refined (orange) and post processed (black) with resolution indicated at  $FSC_{0.5}$ . **c-d**, Cryo-EM map of the masked post-processed volume (**c**) and transverse section (**d**) colored according to local resolution with binding site of MyxA indicated.

A final average resolution of 2.53 Å for the unmasked and 2.1 Å for the masked (50S mask) reconstruction was reached. The local resolution was calculated as described in methods section 8.7.2 and is shown in **Fig. 9c-d** with density in the NPET at a local resolution of 1.8 - 2.1 Å. Molecular modelling of MyxA was performed *de novo* with the chemical structure prepared in Chemdraw (PerkinElmer Informatics) and molecular restraints for modified residues and ligands were created using aceDRG within the CCP4 software suit (Long et al., 2017). A high-resolution *E. coli* 50S subunit (PDB ID 7K00 (Watson et al., 2020)) was rigid body fitted and modelled and refined as described in methods section 8.7.3 and final statistics are listed in table 5. The overall quality of the cryo-EM density was very good (**Fig. 10**) and allowed placement of putative magnesium ions and water molecules (**Fig. 10b-c,e**) and also revealed known modifications of nucleotides, like the methylation of m<sup>2</sup>A2503 (**Fig. 10d**) (Watson et al., 2020).

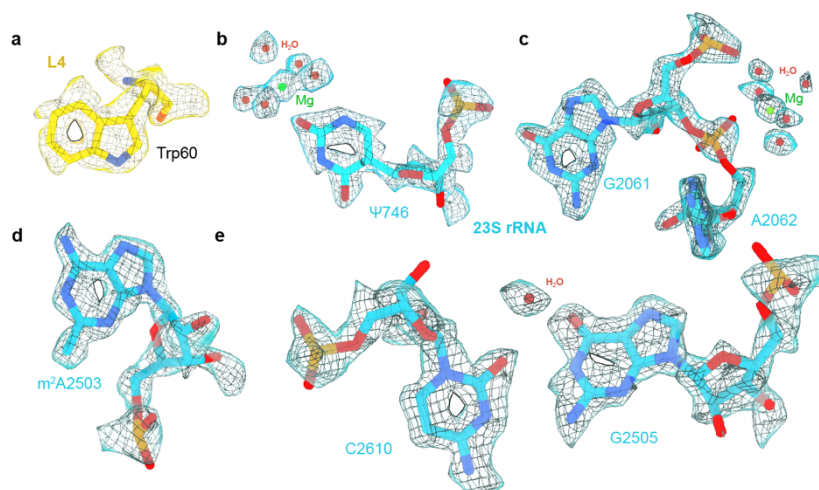


**Figure 10: Quality of the cryo-EM map of the MyxA-50S complex.** **a-e**, Isolated density of the cryo-EM map of MyxA-50S-complex with molecular models of **(a)** Trp60 of ribosomal protein L4, **(b)** Ψ746 of the 23S rRNA (blue) with coordinated magnesium (Mg, green) and surrounding waters (red), **(c)** G2061 and A2062 with coordinated magnesium (Mg, green), **(d)** methylation on A2503 (m<sup>2</sup>A2503) and **(e)** C2610 and G2505 with coordinated water molecule (red).

### 8.7.4.2. MyxB-70S-complex

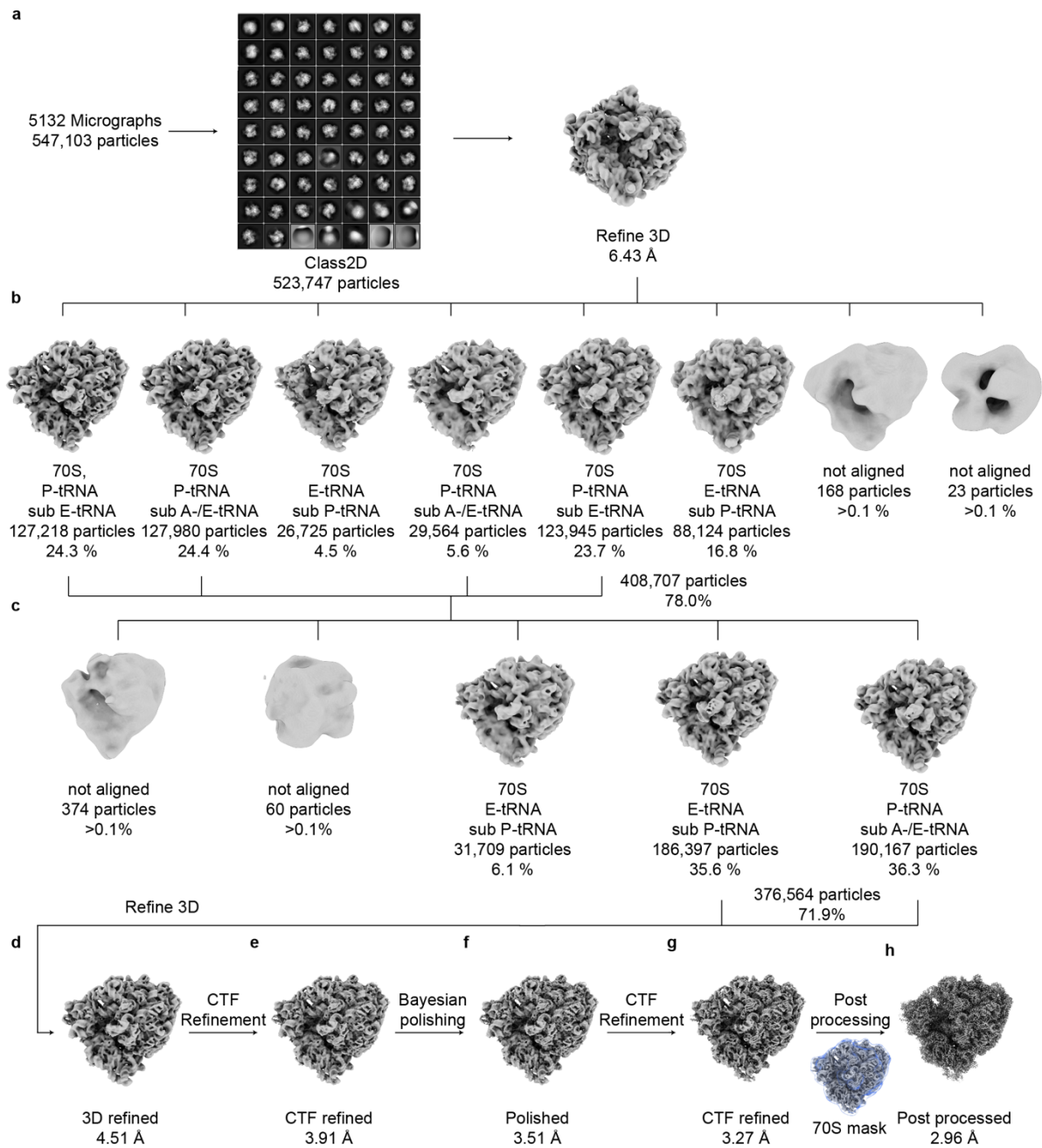


**Figure 11: *In silico* sorting of the MyxB-70S-complex.** **a**, From 5132 micrographs a total of 547,103 particles were picked and subjected to 2D classification yielding 523,747 ribosome-like particles that subsequently were 3D refined at three times decimated pixel size (3.159 Å/px). **b-c**, 100 iterations of 3D classification yielded 6 classes of 70S ribosomes with different tRNAs and high resolution particles of similar classes were combined (408,707 particles) and further subsorted for another 100 iterations (**c**). **d-h**, Combined particles of 70S ribosome with density in the NPET and P- and E-tRNA (376,564 particles) were 3D refined, CTF refined (**e**, 4<sup>th</sup> order aberration, beamtilt, anisotropic magnification and per-particle defocus value estimation), Bayesian polished (**f**) and again CTF refined (**g**), resulting in a reconstruction with a final average masked resolution of 2.96 Å (at FSC<sub>0.143</sub>).

The *E. coli*-70S-MyxB dataset was processed at a corrected pixel size of 1.053 Å/px as the detector pixel size of 1.067 Å was found to be incorrect. A total of 5,132 movies were collected with 2.54 e<sup>-</sup>/Å<sup>2</sup> per frame, a defocus range of -0.7 to -1.2 μm. A box size of 360 px<sup>3</sup> was used for the undecimated 3D refinement. Motion correction, defocus value estimation and particle picking were performed as described in method section 8.7.1. A total of 547,103 particles were picked and extracted at 6x decimated pixel size (60 px<sup>3</sup>, 6.318 Å/px) and subjected to 2D classification, resulting in 523,747 ribosome-like particles (Fig. 11a). These ribosome-like particles were extracted at 3x decimated pixel size (120 px<sup>3</sup>, 3.159 Å/px) and an initial 3D refinement was performed with the map of an *E. coli*-70S-ErmBL-complex (EMD-8175 (Arenz et al., 2016a)) as reference, resulting in a 70S ribosome with sub-stoichiometric A-, P-, and E-tRNAs (Fig. 11a). Non-aligning 3D classification was performed for 100 iterations (Fig. 11c). Four classes with high-resolution 70S particles (Fig. 11b, 78.0%, 408,707 particles) were combined and further sub-sorted (Fig. 11c). Two classes containing 70S ribosomes with P- and E-tRNA were combined (Fig. 11c, 71.9%, 376,564 particles) and re-extracted at undecimated pixel size and brought to high resolution as described in methods section 8.7.1. The final reconstruction contains density for a tRNA in the P-site and additional density assigned to MyxB in the NPET, similar to the aforementioned MyxA-70S-complex.

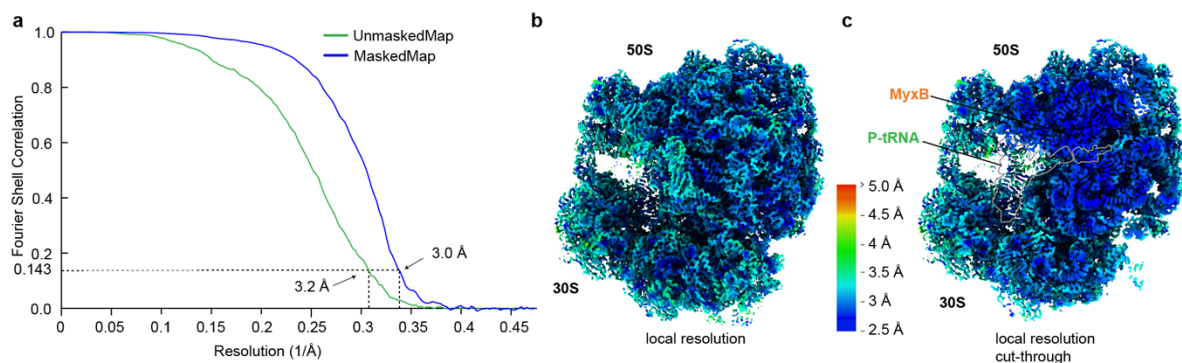


**Figure 12: FSC curves and local resolution of the MyxB-70S-complex.** a, Fourier shell correlation (FSC) curves of unmasked (green) and masked (blue) reconstruction of the MyxB-70S-complex with indicated average resolutions of 3.2 Å and 2.0 Å (at FSC<sub>0.143</sub>), respectively. b-c, Cryo-EM map of the masked post-processed volume (b) and transverse section (c) colored according to local resolution with binding site of MyxB and the P-tRNA indicated.

A final average resolution for the unmasked reconstruction of 3.2 Å and the masked reconstruction of 3.0 Å was reached (**Fig. 12a**) with local resolution (**Fig. 12b-c**) going as low as 2.7 Å in the core of the ribosome. Molecular modelling of MyxB was performed *de novo* with the chemical structure prepared in Chemdraw (PerkinElmer Informatics) and molecular restraints for modified residues and ligands were created using aceDRG within the CCP4 software suit (Long et al., 2017). The high-resolution *E. coli* 70S ribosome (PDB ID 7K00 (Watson et al., 2020)) and P-tRNA, taken from the pre-attack state (PDB ID 1VY4, (Polikanov et al., 2014a)), were rigid body fitted, modelled and refined as described in methods section **8.7.3** and final statistics are listed in table **5**. The sequence for the P-tRNA was adjusted in Coot (Emsley et al., 2010).

## 8.7.5. Single particle analysis of *Escherichia coli*-70S-Dro1 complex

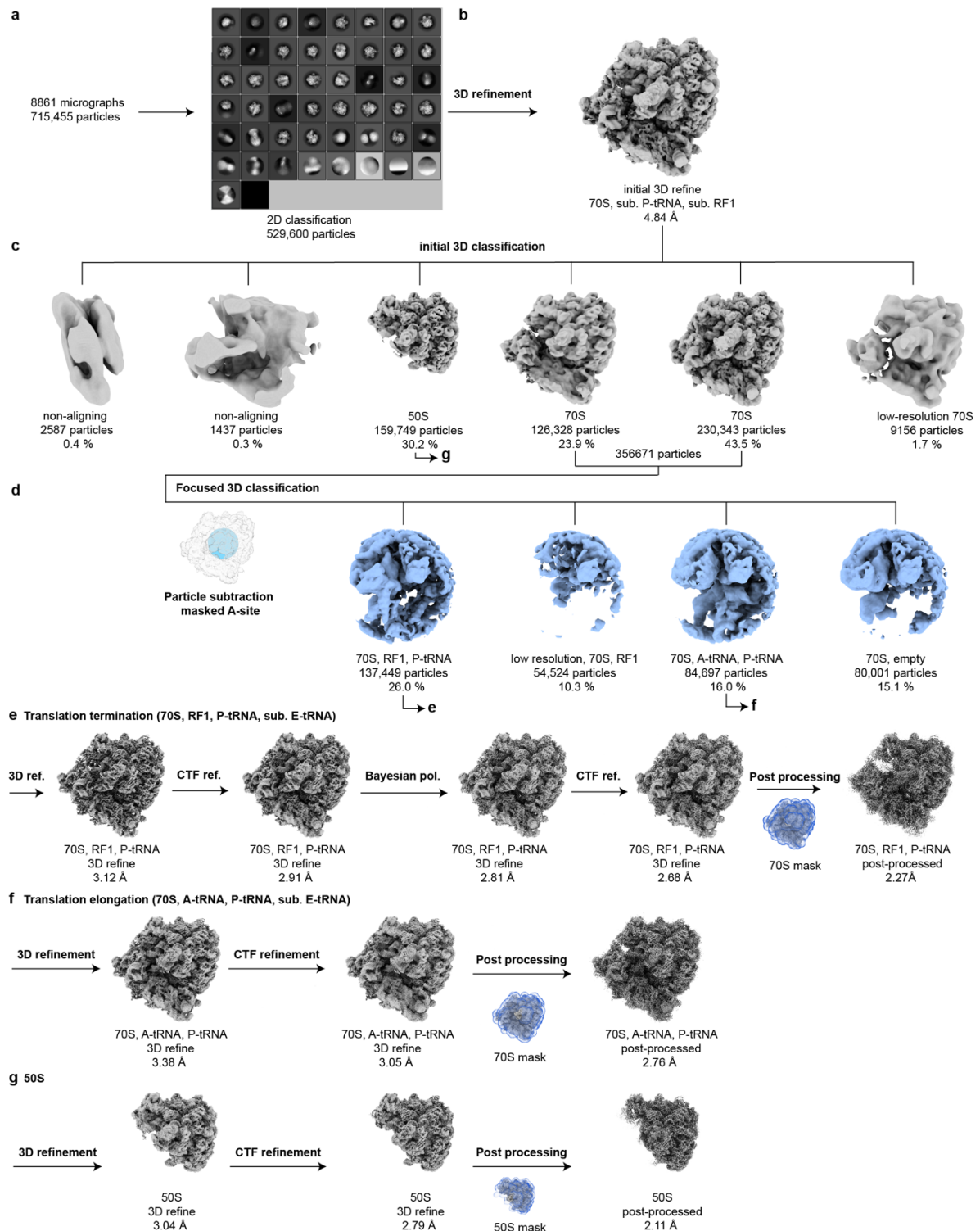


**Figure 13: *In silico* processing of the drosocin dataset.** 715,455 particles were picked from 8,861 micrographs and subjected to 2D classification resulting in 529,600 ribosome-like particles. **b**, Particles were extracted at three times decimated pixel size (2.4 Å/px) and 3D refined. **c**, 70 iterations of initial 3D classification resulted in six classes of which classes containing 70S were combined and sub-sorted (356,671 particles). A class containing

large 50S subunit (159,749 particles) was further processed. **d**, Partial particle subtraction of 70S ribosomes with a mask around the A-site was performed and sub-sorted for 150 iterations. **e**, 3D refinement of the termination complex containing RF1, P-tRNA and sub. E-tRNA density at undecimated pixel size, CTF refinement (4<sup>th</sup> order aberrations, beam-tilt, anisotropic magnification and per-particle defocus value estimation), Bayesian polishing and another round of CTF refinement resulting in a final average resolution for the masked reconstruction of 2.3 Å (at FSC<sub>0.143</sub>). **f**, 3D refinement of the elongation complex containing A-tRNA and P-tRNA density at undecimated pixel size and subsequent CTF refinement (4<sup>th</sup> order aberrations, beam-tilt, anisotropic magnification and per-particle defocus value estimation), resulting in a final average resolution for the masked reconstruction of 2.8 Å (at FSC<sub>0.143</sub>). **g**, 3D refinement of the 50S complex at undecimated pixel size and subjected to CTF refinement (4<sup>th</sup> order aberrations, beam-tilt, anisotropic magnification and per-particle defocus value estimation), resulting in a final average resolution for the masked reconstruction of 2.1 Å (at FSC<sub>0.143</sub>).

The *E. coli*-70S-Dro1 dataset was processed at a corrected pixel size of 0.8 Å/px as the detector pixel size of 0.83 Å was found to be incorrect. A total of 8,861 movies were collected with a total dose of 40 e<sup>-</sup>/Å<sup>2</sup> and with 40 frames, a magnification of 96,000x and a defocus range of -0.4 to -0.9 μm. A box size of 600 px<sup>3</sup> was used for the undecimated 3D refinement. Motion correction, defocus value estimation and particle picking were performed as described in method section 8.7.1. A total of 715,455 particles were picked and extracted at 5x decimated pixel size (120 px<sup>3</sup>, 4 Å/px) and subjected to 2D classification, resulting in 529,600 ribosome-like particles (**Fig. 13a**). These ribosome-like particles were extracted at 3x decimated pixel size (200 px<sup>3</sup>, 2.4 Å/px) and an initial 3D refinement was performed with the map of an *E. coli*-70S-ErmBL-complex (EMD-8175 (Arenz et al., 2016a)) as reference, resulting in a 70S ribosome with sub-stoichiometric P-tRNA and sub-stoichiometric release factor 1 (RF1) (**Fig. 13b**). Non-aligning 3D classification was performed for 100 iterations (**Fig. 13c**). A class containing exclusively large 50S subunits (30.2%, 159,749 particles), with additional density in the NPET were further processed (**Fig. 13g**), while two classes containing high resolution 70S ribosomes (67.4%, 356,671 particles) with additional density in the NPET were combined and subjected to focus classification (**Fig. 13d**). A circular mask was created around the binding position of the release factor 1 in the A-site, observed in the initial refinement, and used for partial particle subtraction. As reference a reconstruction from RELION was used for the sub-sorting (`relion_reconstruct --i particles_subtracted.star --o reconstruction.mrc --ctf`). Two classes were selected, namely a 70S with RF1 and P-tRNA (26.0%, 137,449 particles, termination complex) and a 70S with A- and P-tRNA (16.0%, 84,697 particles, elongation complex). The termination complex (2.3 Å, **Fig.**

13e), elongation complex (2.8 Å, **Fig. 13f**) and 50S (2.1 Å, **Fig. 13g**) were brought to high resolution, as described in methods section 8.7.1 and FSC curves are shown in **Fig. 14a-c**, respectively.

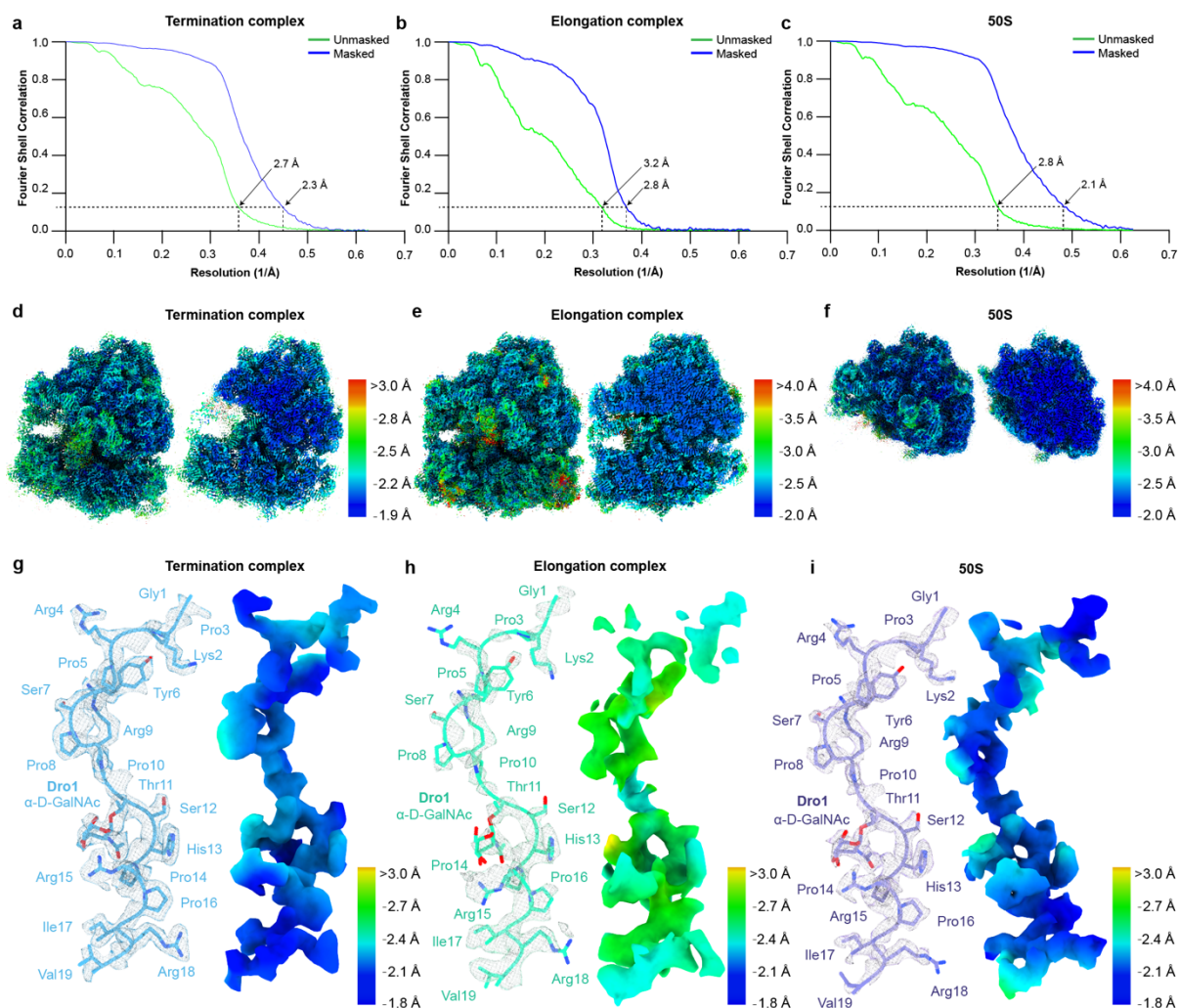


**Figure 14: FSC curves and local resolution for the drosocin data collection.** **a-c**, Fourier shell correlation curves for the termination complex (**a**), elongation complex (**b**) and the 50S complex (**c**) with unmasked (green) and masked (blue) FSC curves with resolution indicated at  $FSC_{0.143}$ . **d-f**, Cryo-EM density of the termination complex (**d**), elongation complex (**e**) and the 50S complex (**f**) colored according to resolution for the full ribosome and transverse section. **g-i**, Molecular model of Dro1 in isolated density and colored according to local resolution of the termination complex (**g**), elongation complex (**h**) and the 50S complex (**i**).

Local resolution was calculated as described in methods section 8.7.2 and is shown in **Fig. 14d-f**. Density assigned to Dro1 was observed in all three models (**Fig. 14g-i**), with the elongation complex having the lowest local resolution (**Fig. 14h**) and the termination complex showing the highest (**Fig. 14g**). The molecular model of Dro1 was



created *de novo* and the  $\alpha$ -D-GalNAc (2-acetamido-2-deoxy-alpha-D-galactopyranose) modification on Thr11 was taken from the ligand database (Ligand A2G, PDB ID 1D0H,(Emsley et al., 2000)) and linked through Refmac 5 (Vagin et al., 2004). For all three complexes a high-resolution *E. coli* 70S (PDB ID 7K00, (Watson et al., 2020) was used as starting model. For the termination complex, the release factor 1 was assembled from an AlphaFold model (AF-P0A7I0-F1) (Jumper et al., 2021; Varadi et al., 2022) and the deacylated Phe-tRNA from a crystal structure (PDB ID 6Y3G (Bourgeois et al., 2020)) with the sequence adjusted. For the elongation complex the fMet-tRNA was taken from the pre-attack state (PDB ID 1VY4, (Polikanov et al., 2014a) and the Leu-tRNA from ErmDL-70S-complex (PDB ID 7NSQ, (Beckert et al., 2021), both adjusted to their correct sequence. Starting models were rigid body fitted into the individual cryo-EM maps, modelled, and refined as described in methods section **8.7.3** and final statistics are listed in table **6**.

## 8.7.6. Single particle analysis of *S. cerevisiae* 80S-Tel-complex

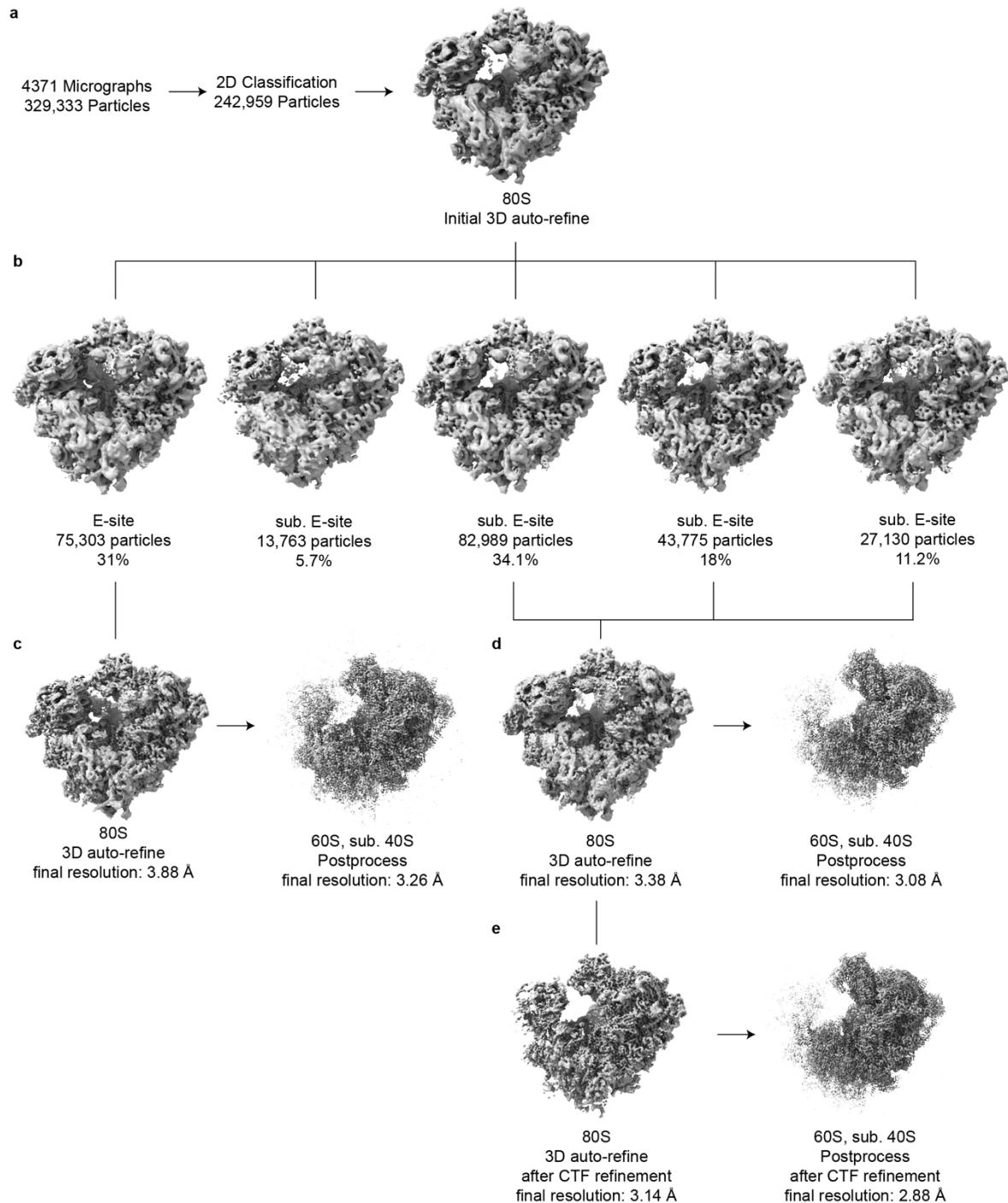


**Figure 15: *In silico* processing of the G2400A mutant Tel-80S-complex.** **a**, From 4,371 micrographs a total of 329,333 particles were picked and subjected to 2D classification, resulting in 242,959 ribosome-like particles, which were initially 3D refined at three times decimated pixel size (2.466 Å/px). **b**, 200 iterations of 3D classification yielded six classes of 80S ribosomes with either E-tRNA (**c**, 75,303 particles) or sub-stoichiometric E-tRNA (**d**, 153,893 particles) which were 3D refined. **e**, The final reconstruction resulted from CTF refinement (4<sup>th</sup> order aberrations, beam-tilt, anisotropic magnification and per-particle defocus value estimation) with an average masked resolution of 2.88 Å (at FSC<sub>0.143</sub>). Modified from (Svetlov et al., 2021a).

The G2400A mutant *S. cerevisiae*-80S-Tel dataset was processed at a pixel size of 0.822 Å/px. A total of 4,371 movies were collected with a total dose of 40 e<sup>-</sup>/Å<sup>2</sup>, 40 frames, and a defocus range of -1 to -3 μm. A box size of 420 px<sup>3</sup> was used for the undecimated 3D refinement. Motion correction, defocus value estimation and particle picking were performed as described in method section **8.7.1**. A total of 329,333 particles were picked and extracted at 5x decimated pixel size (70 px<sup>3</sup>, 4.932 Å/px) and subjected to 2D classification, resulting in 242,959 ribosome-like particles (**Fig. 15a**). These ribosome-like particles were extracted at 3x decimated pixel size (140 px<sup>3</sup>, 2.466 Å/px) and an initial 3D refinement was performed with the map of an *S. cerevisiae*-80S-Xrn1-complex (EMD-4474 (Tesina et al., 2019)) as reference, resulting in a 80S ribosome (**Fig. 15a**). Non-aligning 3D classification was performed for 200 iterations (**Fig. 15b**). Classification resulted in one class containing 80S ribosome with E-site tRNA (31.0%, 75,303 particles) and three classes containing 80S ribosomes with sub-stoichiometric E-site tRNA (63.3%, 153,894 particles) all with additional density in the NPET. Both sets of particles were brought to high resolution (**Fig. 15c-d**), however, only the class with sub-stoichiometric E-site tRNA was CTF refined (**Fig. 15e**). The FSC curve is shown in **Fig. 16a**.

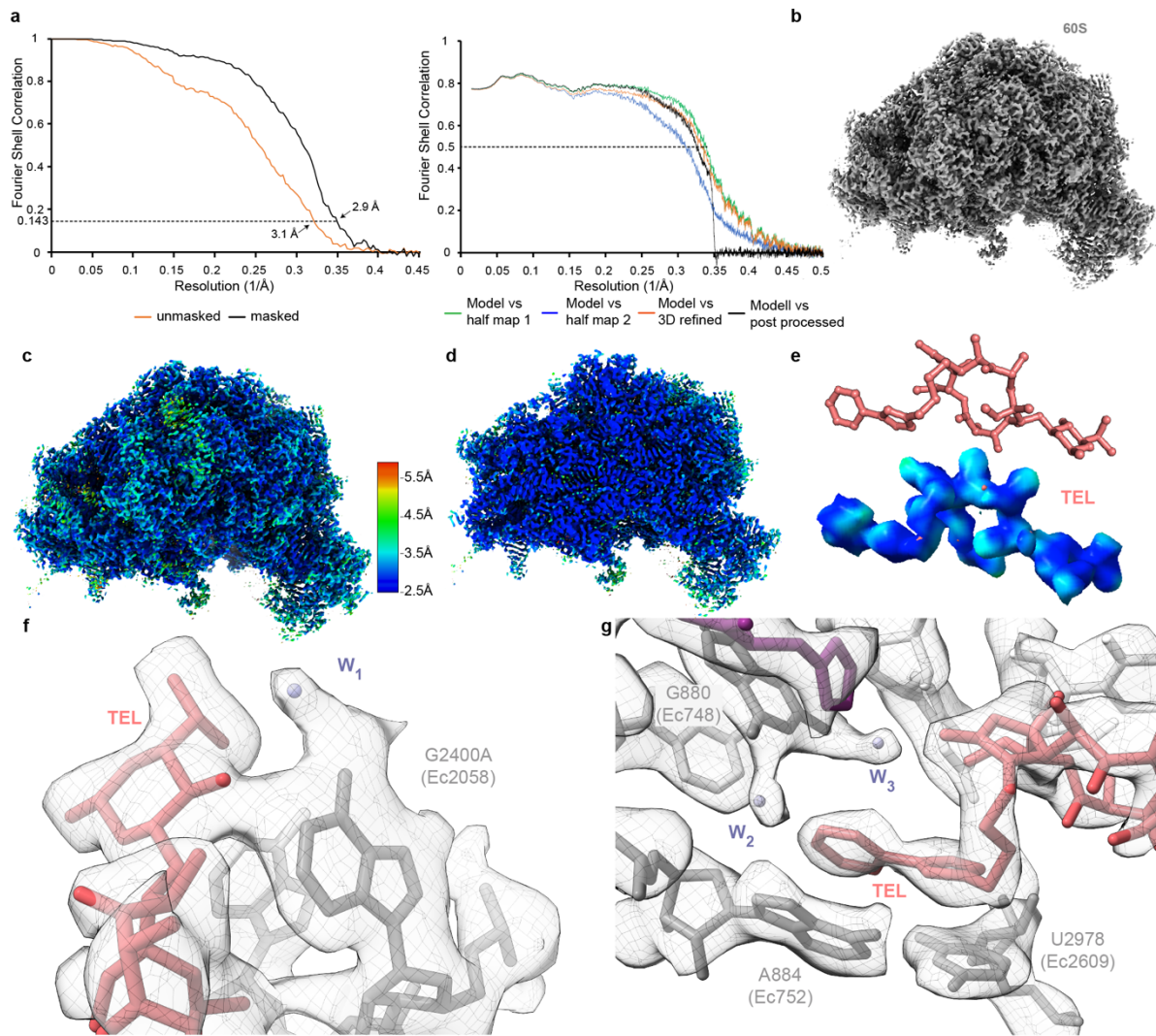


**Figure 16: Quality of the G2400A mutant Tel-60S-complex cryo-EM map.** **a**, Fourier shell correlation (FSC, left) of the unmasked (orange) and masked (black) final reconstruction with resolution indicated at  $FSC_{0.143}$  and map-vs-model cross correlation (right) of the half-map1 (green), half-map 2 (blue), 3D refined map (orange) and post-processed map (black) with resolution indicated at  $FSC_{0.5}$ . **b-d**, Cryo-EM map of the masked 60S-Tel-complex (**b**, grey), colored according to local resolution (**c**) and as transverse section (**d**). **e**, molecular model of Tel (salmon) and isolated density colored according to local resolution with scale from (**c**). **f-g**, Tel (salmon) with surrounding 23S rRNA nucleotides (grey), ribosomal protein uL4 (purple) and putative water molecules (light blue) in isolated density (mesh). Modified from (Svetlov et al., 2021a).

A final average resolution of the unmasked 80S of 3.1 Å and the masked 60S subunit of 2.9 Å was reached (**Fig. 16a-b**) with local resolution going as low as 2.5-2.7 Å in the core of the large subunit and for Tel in the NPET (**Fig. 16c-e**). The molecular model of the 60S subunit was taken from the 80S-Xrn1-complex (PDB ID 6Q8Y) (Tesina et al., 2019) and Tel was taken from the *E. coli* Tel-70S-complex (PDB ID 4V7S) (Dunkle et al., 2010). Starting models were rigid body fitted into the cryo-EM map, modelled,

and refined as described in methods section 8.7.3 and for Tel shown in Fig. 16e-g, with additional putative waters  $W_1$ - $W_3$  modelled and final statistics are listed in table 7.

## 8.7.7. Single particle analysis of *L. monocytogenes* complexes

### 8.7.7.1. Lmo-70S-lincomycin-complex

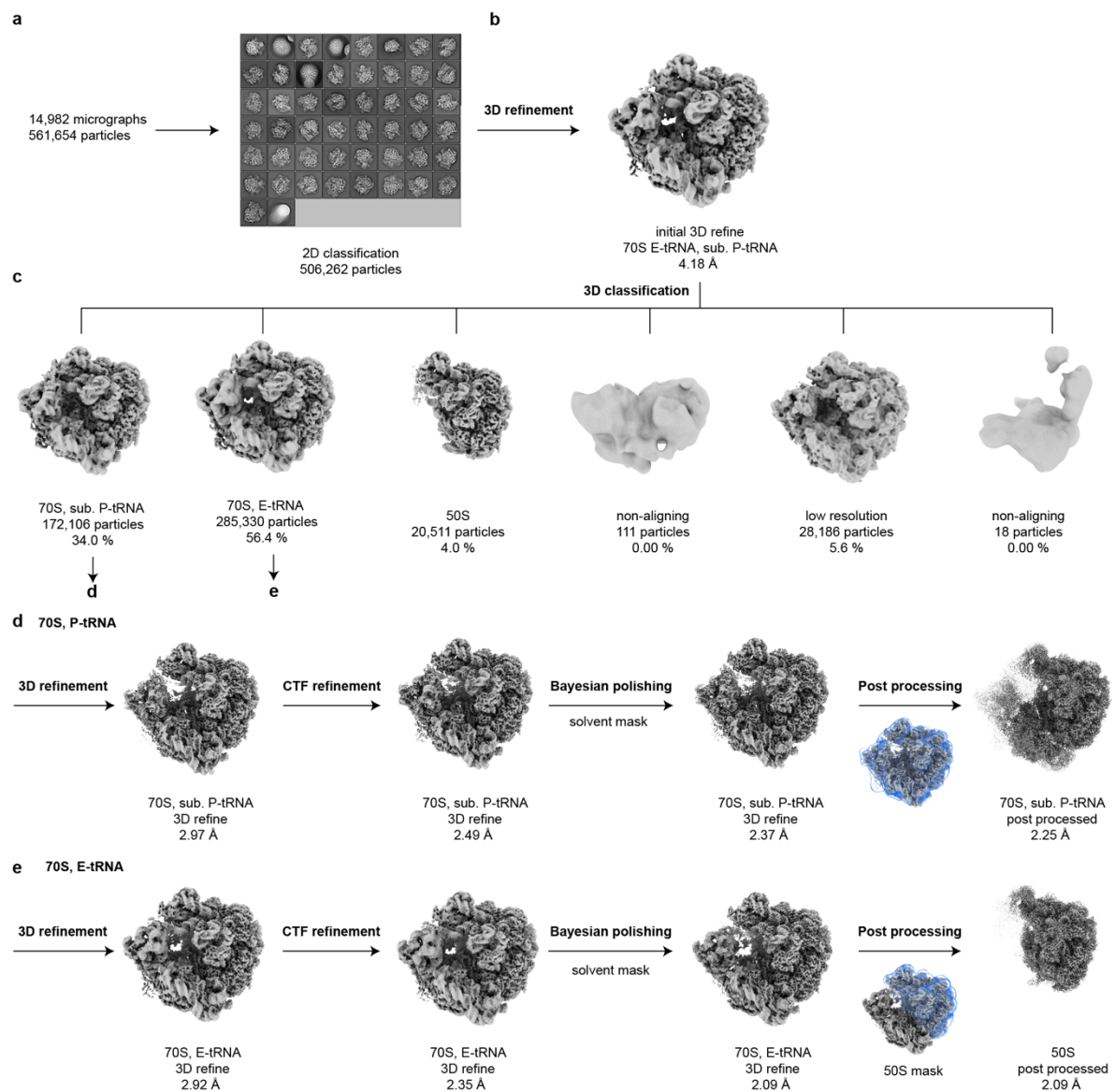


**Figure 17: In silico processing of the *L. monocytogenes* lincomycin dataset.** **a**, From 14,982 micrographs a total of 561,654 particles were picked and subjected to 2D classification yielding 506,262 ribosome-like particles. **b**, Initial 3D refinement with particles extracted at decimated pixel size. **c**, 3D classification (200 iterations) yielded four high resolution classes of which two populations with P-tRNA (**d**, 172,106 particles) or E-tRNA (**e**, 285,330 particles) were further processed. **d-e**, The 70S with P-tRNA (**d**) and with E-tRNA (**e**) were 3D refined, CTF refined (4<sup>th</sup> order aberrations, beam-tilt, anisotropic magnification and per-particle defocus value estimation), Bayesian

polished and yielding final masked reconstructions at 2.25 Å for the Lnc-70S-complex (d) and 2.09 Å for the Lnc-50S-complex (e) (at FSC<sub>0.143</sub>). Modified from (Koller et al., 2022b).

The *L. monocytogenes*-70S-Lnc dataset was processed at a 1.5x binned pixel size of 0.7725 Å/px as the data was collected in super-resolution mode with a pixel size of 0.515 Å/px. A total of 14,982 movies were collected with a total dose of 40.3 e-/Å<sup>2</sup> and with 40 frames, a magnification of 270,000x and a defocus range of -0.4 to -1.4 μm. A box size of 600 px<sup>3</sup> was used with 400 px<sup>3</sup> used for the 1.5x decimated final 3D refinement. Motion correction, defocus value estimation and particle picking were performed as described in method section 8.7.1. A total of 561,654 particles were picked and extracted at 6x decimated pixel size (100 px<sup>3</sup>, 3.09 Å/px) and subjected to 2D classification, resulting in 506,262 ribosome-like particles (Fig. 17a). These ribosome-like particles were extracted at 4x decimated pixel size (150 px<sup>3</sup>, 2.06 Å/px) and an initial 3D refinement was performed with the map of an *L. monocytogenes*-70S-VgaL-complex (EMD-12334 (Crowe-McAuliffe et al., 2021)) as reference, resulting in a 70S ribosome with E-site tRNA and sub-stoichiometric P-tRNA (Fig. 17b). Non-aligning 3D classification was performed for 200 iterations (Fig. 17c). Two class, one with 70S and sub-stoichiometric P-site tRNA (34.0%, 172,106 particles, Fig. 17d), and one with 70S and E-site tRNA (56.4%, 285,330 particles, Fig. 17e). Both classes were brought to high-resolution as described in methods section 8.7.1, resulting in 2.3 Å and 2.1 Å for the Lmo-70S-Lnc-complex (Fig. 18a) and Lmo-50S-Lnc-complex (Fig. 18b), respectively. For both complexes the local resolution in the core of the 50S subunit is as low as 1.8 Å (Fig. 18c-h) and density near the PTC, assigned to lincomycin, was observed (Fig. 18i-k). Molecular modelling of lincomycin was performed *de novo* with the chemical structure prepared in Chemdraw (PerkinElmer Informatics) and molecular restrains for the ligand was created using aceDRG within the CCP4 software suit (Long et al., 2017). The ligand and the 50S subunit taken from the *L. monocytogenes*-70S-VgaL-complex were rigid body fitted, modelled, and refined as described in method section 8.7.3 and final statistics are listed in table 8.

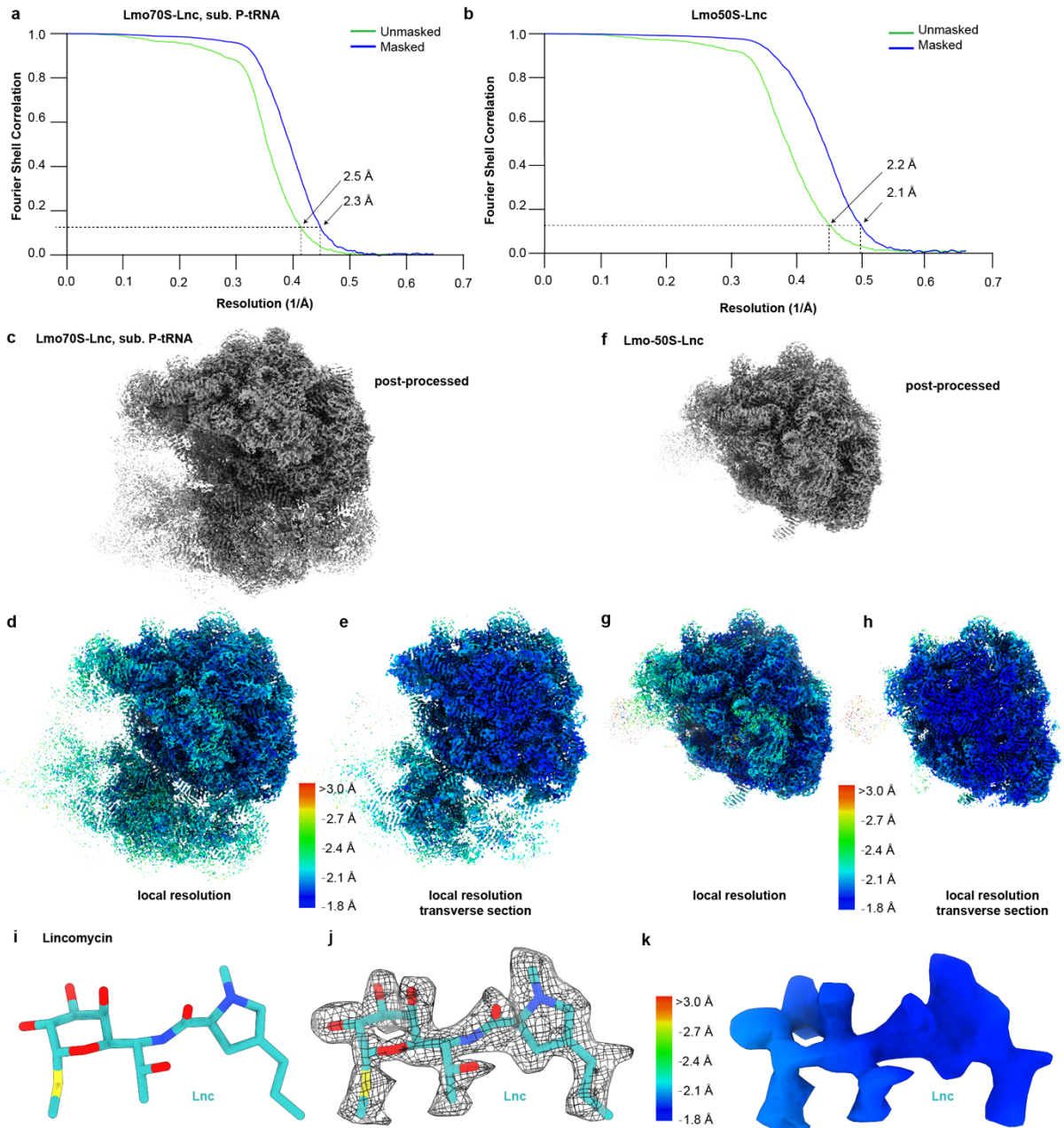


**Figure 18: FSC curves and local resolution of the *L. monocytogenes* lincomycin dataset.** a-b, Fourier shell correlation (FSC) curves of the Lnc-70S-complex (a) and the Lnc-50S-complex (b) with unmasked (green) and masked (blue) with resolution indicated at  $FSC_{0.143}$ . c-f, Cryo-EM map of the Lnc-70S-complex (c, grey) and Lnc-50S-complex (f, grey), colored according to local resolution of the Lnc-70S-complex (d) and Lnc-50S-complex (g) and transverse section of the Lnc-70S-complex (e) and Lnc-50S-complex (h) colored according to local resolution. i-k, Molecular model of lincomycin (i, turquoise), in isolated density (j, mesh) from the Lnc-70S-complex and colored according to local resolution (k). Modified from (Koller et al., 2022b).

### 8.7.7.2. Lmo-50S-HflXr-GDPNP-complex

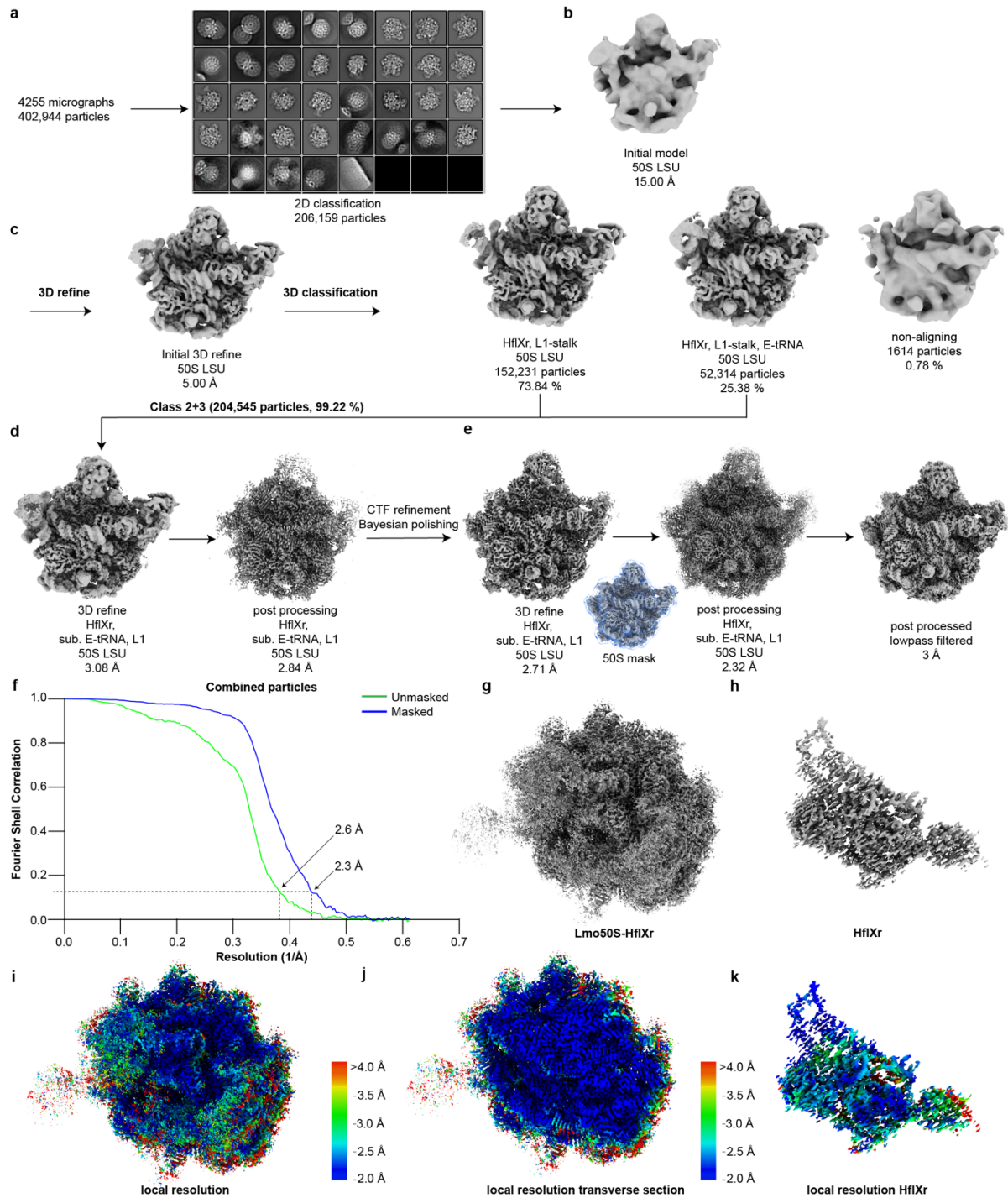


**Figure 19: *In silico* processing of the HflXr-50S-GDPNP-complex, FSC curve and local resolution. a**, From 4,255 micrographs a total of 402,944 particles were picked and subjected to 2D classification resulting in 206,159 ribosome-like particles. **b**, An initial model was calculated at 15 Å and used as reference for initial 3D refinement (**c**) and subjected to 200 iterations of 3D classification. **d**, Two classes of high resolution 50S with additional density in the A-site were combined (204,545 particles) and 3D refined. **e**, CTF refinement (4<sup>th</sup> order aberrations, beam-tilt, anisotropic magnification, and per-particle defocus value estimation) and Bayesian polishing yielded a final masked reconstruction with an average resolution of 2.32 Å (at FSC<sub>0.143</sub>). For modelling the map was low pass



filtered at 3 Å. **f**, Fourier shell correlation curves of the unmasked (green) and masked (blue) reconstruction with resolution indicated at  $FSC_{0.143}$ . **g-k**, Cryo-EM map (g, grey) and isolated density for HflXr (**h**, grey) of the HflXr-50S-GDPNP-complex and colored according to local resolution for the full map (**i**), transverse section and isolated density of HflXr (**k**). Modified from (Koller et al., 2022b).

The *L. monocytogenes*-50S-HflXr-GDPNP dataset was processed at 0.82 Å/px. A total of 4,255 movies were collected with a total dose of 35.022 e<sup>-</sup>/Å<sup>2</sup> and with 30 frames, a magnification of 165,000x and a defocus range of -0.8 to -2.0 μm. A box size of 360 px<sup>3</sup> was used for the final 3D refinement. Motion correction, defocus value estimation and particle picking were performed as described in method section 8.7.1. A total of 402,944 particles were picked and extracted at 5x decimated pixel size (72 px<sup>3</sup>, 4.1 Å/px) and subjected to 2D classification, resulting in 206,159 ribosome-like particles (**Fig. 19a**). These ribosome-like particles were extracted at 3x decimated pixel size (120 px<sup>3</sup>, 2.46 Å/px) and an *ab initio* model generated in RELION (Scheres, 2012) at 15 Å and used as reference for 3D refinement. 3D refinement resulted in a 50S subunit with E-site tRNA and extra density in the A-site assigned to HflXr (**Fig. 19c**) which was subjected to non-aligning 3D classification for 200 iterations (**Fig. 19c**). Two classes, one with and one without E-site tRNA, were combined (99.22%, 204,545 particles) and brought to high-resolution as described in methods section 8.7.1. The complex reached a final average resolution of 2.6 Å for the unmasked and 2.3 Å for the masked cryo-EM map (**Fig. 19f**) with local resolution of the ribosomal core going as low as 2.0 Å (**Fig. 19i-j**). The density assigned to HflXr is overall well resolved, however, the loop region close to the PTC is poorly ordered and for modelling had to be low pass filtered to 3 Å (**Fig. 19h, k**). The molecular model of HflXr was calculated with AlphaFold (Jumper et al., 2021; Varadi et al., 2022), GDPNP was taken from the ligand database (ligand GNP, PDB ID 1CTQ, (Scheidig et al., 1999) and the 50S subunit from the *L. monocytogenes*-70S-VgaL-complex (PDB ID 7NHN (Crowe-McAuliffe et al., 2021)). All starting models were rigid body fitted, modelled, and refined as described in methods section 8.7.3 and final statistics are listed in table 8.

### 8.7.7.3. Lmo-50S-HflX-GDPNP-complex

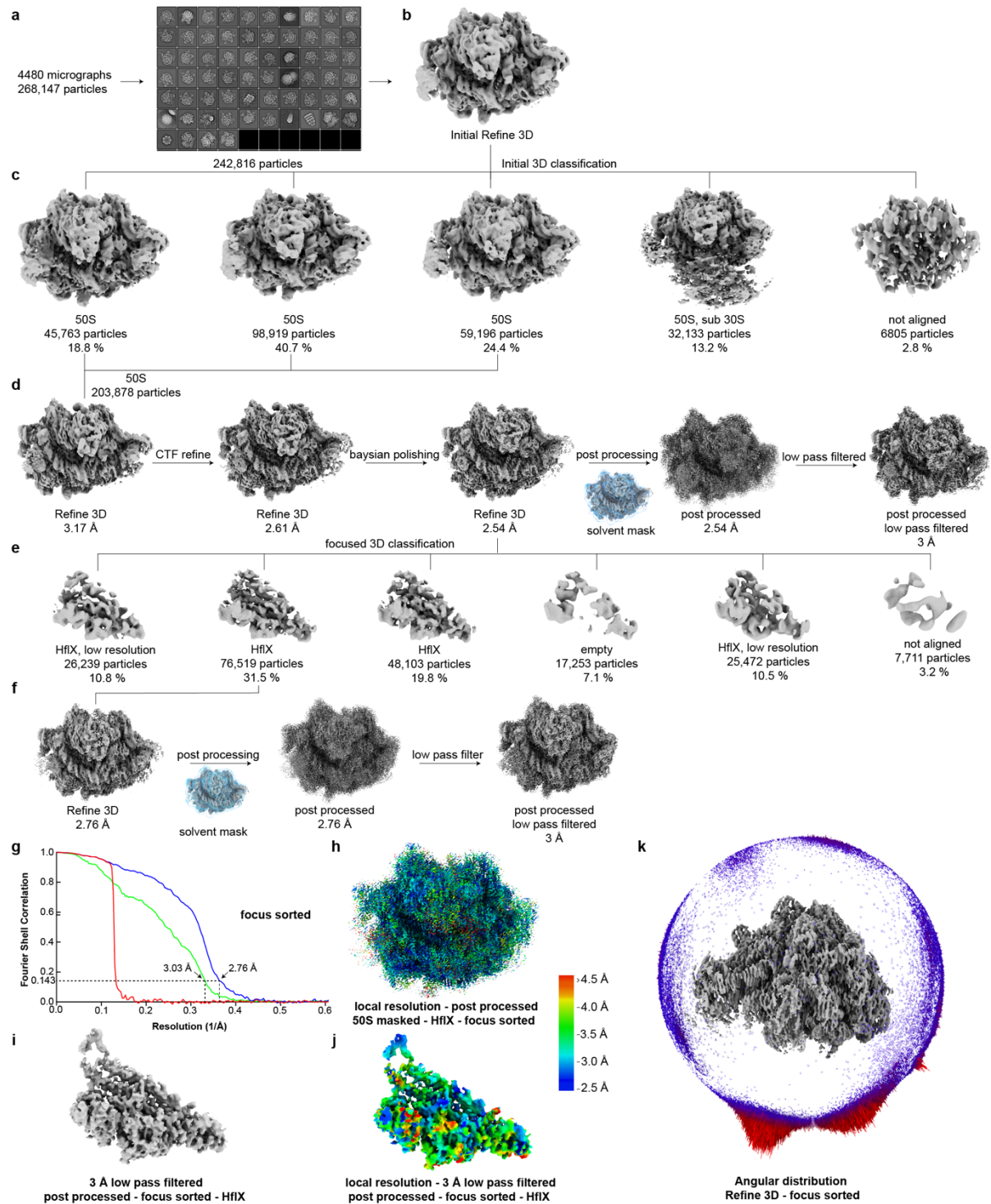


**Figure 20: *In silico* processing of the HflX-50S-GDPNP-complex.** **a**, From 4,480 micrographs a total of 268,147 particles were picked and subjected to 2D classification, resulting in 242,816 particles. **b**, With the Lmo50S-Lnc volume as reference an initial 3D refinement was performed. **c**, 3D classification for 100 iterations resulted in six classes, of which three subpopulations with density for HflX in the A-site were combined. **d**, 3D refinement, CTF refinement (4<sup>th</sup> order aberrations, beam-tilt, anisotropic magnification, and per-particle defocus value estimation)

and Bayesian polishing yielded a post processed masked 50S volume with a final average resolution of 2.54 Å (at FSC<sub>0.143</sub>). **e**, The refined volume was sub sorted with partial particle subtraction with a mask around the factor resulting in six classes. **f**, High resolution HflX (31.5% of the particles) was 3D refined and post processed resulting in a final average masked reconstruction of 2.76 Å (at FSC<sub>0.143</sub>). **g**, Fourier shell correlation (FSC) for the masked (blue) and unmasked (green) reconstruction of the focus sorted HflX-50S-GDPNP-complex. **h**, Cryo-EM map of the post processed HflX-50S-GDPNP-complex coloured by local resolution. **i**, Isolated density (grey mesh) of HflX low pass filtered at 3 Å. **j**, as (i) but coloured according to local resolution. **k**, Angular distribution of the focused sorted cryo-EM map of the HflX-50S-GDPNP-complex. Modified from (Koller et al., 2022b).

The *L. monocytogenes*-50S-HflX-GDPNP dataset was processed at 0.82 Å/px. A total of 4,480 movies were collected with a total dose of 30 e<sup>-</sup>/Å<sup>2</sup> and with 20 frames, a magnification of 165,000x and a defocus range of -0.6 to -1.6 μm. A box size of 360 px<sup>3</sup> was used for the final 3D refinement. Motion correction, defocus value estimation and particle picking were performed as described in method section 8.7.1. A total of 268,147 particles were picked and extracted at 5x decimated pixel size (72 px<sup>3</sup>, 4.1 Å/px) and subjected to 2D classification, resulting in 242,816 ribosome-like particles (**Fig. 20a**). These ribosome-like particles were extracted at 3x decimated pixel size (120 px<sup>3</sup>, 2.46 Å/px) and an initial 3D refinement was performed with the map of an *L. monocytogenes*-70S-VgaL-complex (EMD-12334 (Crowe-McAuliffe et al., 2021)) as reference, resulting in a 50S ribosome with extra density in the A-site assigned to HflX (**Fig. 20b**) which was subjected to non-aligning 3D classification for 100 iterations (**Fig. 20c**). Three classes with 50S subunit and density in the A-site were combined (83.9%, 203,878 particles) and brought to high-resolution as described in methods section 8.7.1. The complex reached a final average resolution of 2.54 Å for the masked cryo-EM map (**Fig. 20d**). However, the cryo-EM density for the factor was poorly resolved, and did not improve by low-pass filtering at 3 Å. Partial particle subtraction with a mask around HflX density, created from a molmap of an AlphaFold model (Jumper et al., 2021; Varadi et al., 2022), was used for focus sorting (**Fig. 20e**). A class containing well-resolved density of the factor was brought to high-resolution as described in methods section 8.7.1 and resulted in 3.03 Å for the unmasked and 2.76 Å for the masked reconstruction (**Fig. 20f**) and local resolution for both ribosome and factor in a similar range (**Fig. 20h**). Different from the Lmo-50S-HflXr-complex, the Lmo-50S-HflX-complex suffered from severe orientation bias (**Fig. 20k**), not allowing the refinement of a proper molecular model. A rigid body fit and

small adjustments of a vacant *L. monocytogenes* 50S subunit (PDB ID 8A63 (Koller et al., 2022b)) was used to compare the conformations of PTC nucleotides.

## **8.8. Figure making**

Figures were prepared using Adobe Illustrator. ChimeraX was used to assemble molecular models (Goddard et al., 2018; Pettersen et al., 2021). PyMol v2.5 was used to align molecular models (Ribosomes based on their 23S/25S/28S rRNA) and split PDB files (Schrödinger inc). Local resolution was calculated using Bsoft (Heymann, 2018) or ResMap (Kucukelbir et al., 2014) and visualized with ChimeraX.

## 9. Aim of this thesis

The aim of this study can be separated into four individual projects. These projects have the general target to investigate the mechanisms of actions and binding sites of ribosome-targeting antimicrobial peptides, proving context-specificity for an antibiotic binding a eukaryotic ribosome and a resistance mechanism that interferes with antimicrobial activity. The method of choice for all projects is cryo-EM which provides a detailed look at interactions at near atomic resolution and will be the core of the work.

AMP myxoalargin A and B – Cryo-EM structures of MyxA on the vacant and MyxB on the translating ribosome should give an insight into the binding mode and mechanism of action of members of the antimicrobial peptide class of myxoalargins. Of particular interest is the interaction of the mostly hydrophobic modified and D-amino acids and if water-mediated interactions support the binding position on the ribosome.

PrAMP drosocin – Cryo-EM should be used to shed a light on the binding mechanism of drosocin and how the inhibition of translation is facilitated, and which factors are involved. The O-glycosylation on Thr11 is of particular interest as it seems to have a direct impact on the activity of drosocin and other peptides in previous studies.

Context-specificity of macrolide antibiotics – The eukaryotic *S. cerevisiae* 80S A2400G (Eco2058) mutant ribosome in complex with the macrolide antibiotic telithromycin should be analyzed by Cryo-EM to give a deeper insight into the binding mode of macrolide antibiotics in eukaryotic ribosome and provide a basis for structural based drug design of selective inhibitors for eukaryotic translation of defective or unwanted proteins.

GTPase HflXr – Target protection as an antibiotic resistance mechanism increases the defense mechanisms that bacterial pathogens can use against antibiotics. For structure-based drug design it is essential to understand the resistance mechanisms facilitated by bacteria to directly prone compounds against these mechanisms. A complex of HflXr, a homolog of ribosome-splitting factor HflX found in various bacteria, on the ribosome should provide a structural basis for the mechanism of action of target protection in *L. monocytogenes*.



## 10. Results

### 10.1. Myxovalargins

#### 10.1.1. Myxovalargin A – high resolution structure reveals binding mode and molecular interactions

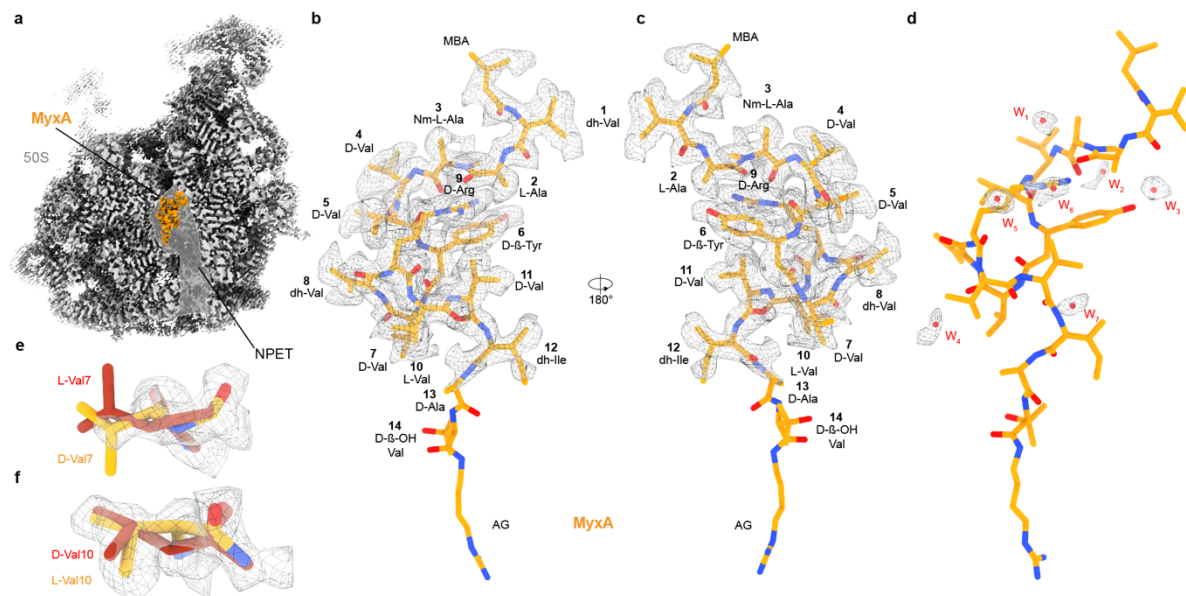


**Figure 21: MyxA bound to the large 50S subunit of the *E. coli* ribosome.** **a**, Transverse section of the cryo-EM map of the MyxA-50S-complex with MyxA (orange) bound within the NPET of the large 50S subunit (grey). **b-c**, Two views of the molecular model of MyxA within isolated cryo-EM density shown as mesh. **d**, Isolated cryo-EM density of seven putative water molecules W<sub>1</sub>-W<sub>7</sub> (red) around the molecular model of MyxA (orange). **e-f**, Structural investigation of D-Val7 and L-Val10 (orange) in isolated density shown as mesh to the previously annotated stereocenter nomenclature of L-Val7 and D-Val10 (red) (Steinmetz et al., 1987).

To investigate the interactions of the myxovalargins with the ribosomes, a cryo-EM structure of MyxA in complex with the vacant *E. coli* ribosome was determined at 2.1 Å for the masked 50S subunit (**Fig. 21a** and **Fig. 8**). An additional density was observed in the NPET that was unambiguously assigned to MyxA (**Fig. 21a-c**). The map reveals high-resolution information for the MBA moiety up to the dh-Ile12 and allowed for the majority to be modelled, however, D-Ala13 up to the terminal AG moiety are only visible at lower map thresholds and are less well-resolved (**Sup.Fig. 1**). Additional density was observed that was attributed to seven putative water molecules W<sub>1</sub>-W<sub>7</sub> (**Fig. 21d**). Two of these waters are present in wildtype *E. coli* ribosomes (Watson et al., 2020) in the absence of MyxA, whereas the others seem to be stabilized by MyxA

binding (**Sup.Fig. 2**). The high-resolution map also revealed a structural revision of the chemical structure of previous studies, with Val7 and Val10 having D- and L-configurations as shown in **Fig. 21e-f**, rather than L- and D-configurations, respectively (Gille and Kirschning, 2016; Irschik et al., 1983; Irschik and Reichenbach, 1985; Steinmetz et al., 1987).

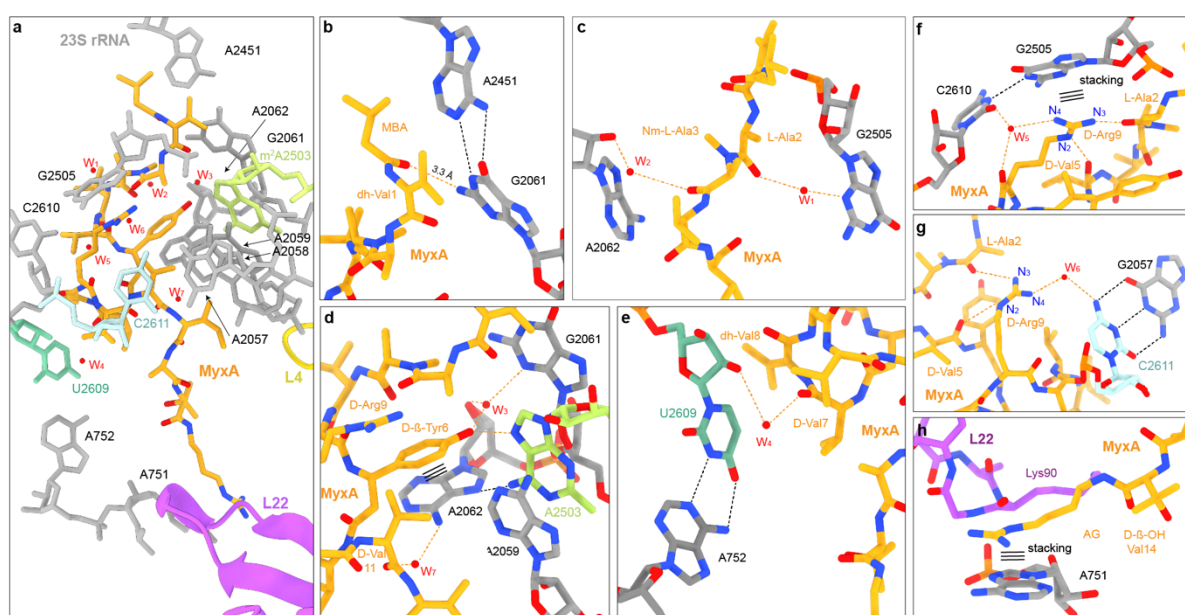


**Figure 22: Interactions of MyxA with elements of the NPET on the *E. coli* ribosome.** a-h, MyxA (orange) with surrounding 23S rRNA nucleotides (grey), with highlighted possible resistance mutations identified in *M. tuberculosis* mapped onto *E. coli* (A2503 (lime), U2609 (turquoise), C2611 (light blue)), putative waters  $W_1$ - $W_7$  (red) and ribosomal proteins L4 (yellow) and L22 (purple). b-h, Potential hydrogen bond and water mediated interactions of MyxA with the ribosome are indicated by orange dotted lines, while intramolecular interactions of ribosomal nucleotides are indicated by black dotted lines and stacking interactions by three lines. b, O1 of MBA moiety of MyxA forms a potential hydrogen bond with N2 of G2061. c, the backbone of L-Ala2 and Nm-L-Ala3 forms water-mediated ( $W_1$  and  $W_2$ ) interactions with N3 of G2505 and 2'OH of the ribose of A2062, respectively. d, D- $\beta$ -Tyr6 of MyxA is stabilized by stacking on A2062 which forms a water-mediated ( $W_7$ ) interaction with O1 of D-Val11. The hydroxy group of D- $\beta$ -Tyr6 of MyxA forms potential hydrogen bond interaction with N6 of  $m^2$ A2503 and water-mediated ( $W_3$ ) interactions with N3 of G2061 and 2'OH of A2062. e, O1 of D-Val7 forms a potential water-mediated ( $W_4$ ) interaction with 2'OH of U2609. f-g, D-Arg9 is stabilized by stacking onto G2505 and N4 forms potential water-mediated ( $W_5$  and  $W_6$ ) interactions with C2610 (f) and C2611 (g) and forms intramolecular interactions of N3 and N2 with O1 of L-Ala2 and O1 of D-Val5, respectively. h, the AG moiety forms a stacking interaction with A751.

Myxovalgins bound within the NPET are overall oriented with their hydrophobic N-terminus positioned at the PTC and the C-terminal AG moiety down the NPET close to the constriction of ribosomal proteins L4 and L22 (**Fig. 22a**). MyxA adopts a highly



compacted conformation, likely stabilized by stacking interactions of D- $\beta$ -Tyr6 and D-Arg9 with 23S rRNA nucleotides A2062 and G2505, respectively (**Fig. 22d,f**). Intramolecular interactions within MyxA of D-Arg9 with the backbone carbonyls of L-Ala2 and D-Val5 are further stabilizing this compacted conformation (**Fig. 22f,g**). Additionally, two potential direct hydrogen bond interactions of MyxA with 23S rRNA were observed, namely the OH group of D- $\beta$ -Tyr6 with N7 of m<sup>2</sup>A2503 and the backbone carboxyl of dh-Val 1 to N2 of G2061 (**Fig. 22b,d**). Both mentioned interactions are the only observed direct hydrogen bond interactions, while nine additional hydrogen bonds are predicted to be mediated by the seven putative water molecules W<sub>1</sub>-W<sub>7</sub> (**Fig. 22c-g**). As expected from the highly hydrophobic nature of the myxovalargin sidechains (Ala, Val and Ile) the majority of interactions of MyxA mediated by waters involves the backbone carbonyls. Exceptions to this are the polar sidechains of the OH group of D- $\beta$ -Tyr6 (with W<sub>3</sub>, **Fig. 22d**) and nitrogen of D-Arg9 (with W<sub>5</sub> and W<sub>6</sub>, **Fig. 22f-g**). Some of the observed water mediated interactions are abolished by potential resistance mutations in the 23S rRNA nucleotides of the *Mycobacterium tuberculosis* ribosome provided by our collaborators from University of Cape Town, South Africa (Valerie Mizrahi). The high structural conservation of the PTC and NPET of the *M. tuberculosis* and *E. coli* ribosomes (**Sup.Fig. 2c**) (Cui et al., 2022) suggest a similar binding mode of MyxA to both ribosomes, and allow a mapping of these resistance mutations onto our structure. Mutations at position A2503G (MtuA2741G, lime), U2609C (MtuU2847C, turquoise) and C2611G (MtuU2849G, light blue) were highlighted in **Fig. 22a,d-e,g** and **Sup.Fig. 3a** and are predicted to induce conformational changes and break potential water-mediated hydrogen bonds of 23S rRNA and MyxA (**Fig. 22d-e,g** and **Sup.Fig. 3b-d**). While findings in prokaryotes seem to explain the interactions and roles of rRNA mutation based-resistance nicely, myxovalarginins are reported to have a poor activity on eukaryotic ribosomes which could result from conformational differences in rRNA and ribosomal protein composition (**Sup.Fig. 2d**) (Chandrasekaran et al., 2019; Irschik and Reichenbach, 1985).

## 10.1.2. Myxovalargin B – mechanism of action to inhibit translation

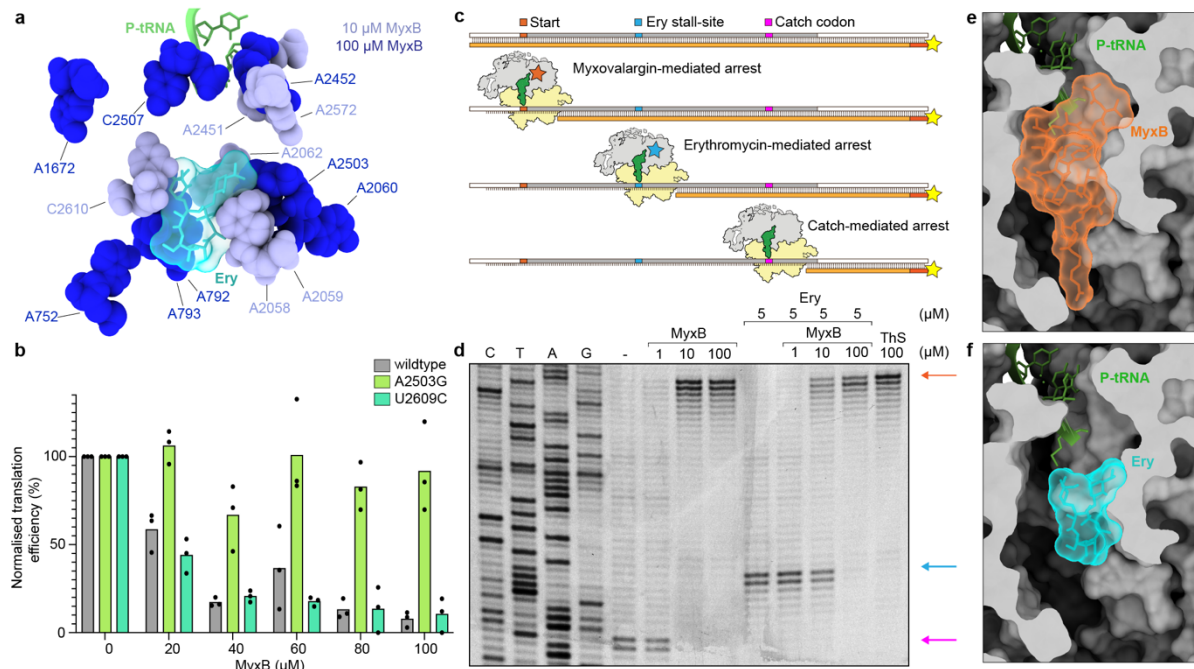


**Figure 23: Mechanistic studies of translation inhibition of MyxB on the ribosome.** **a**, Nucleotides protected by 10  $\mu\text{M}$  MyxB (light blue) and 100  $\mu\text{M}$  (dark blue) from DMS modification in relative position to the P-tRNA (light green) and erythromycin (Ery, cyan) (PDB ID 4V7U) (Dunkle et al., 2010). **b**, *In vitro* firefly luciferase translation assay of wildtype (grey), A2503G mutant (lime) or U2609C mutant (turquoise) with increasing concentrations of MyxB (0-100  $\mu\text{M}$ ). Translation efficiency was normalized to 100% luminescence in absence of drug. **c**, Scheme of a toeprinting assay. Reverse transcription product (yellow) in presence of MyxB-mediated (orange), Ery-mediated (cyan) and Ile-catch-codon mediated (pink) translational arrest. **d**, Toeprinting assay on a ErmBI leader peptide encoding mRNA transcript, in presence of increasing concentrations of MyxB (1-100  $\mu\text{M}$ ) and with pre-incubation of 5  $\mu\text{M}$  Ery, and thiosprepton (ThS) as positive control and in absence (-) of drug. Sequencing lanes are labeled C, T, A, G and colored arrows indicate translational arrest for MyxB (orange), Ery (cyan) and Ile-catch-codon (pink). **e-f**, NPET (grey) depicted as surface with P-tRNA (light green) and molecular model with surface representations of MyxB (**e**, orange) and erythromycin (**f**, Ery, cyan) (PDB ID 4V7U) (Dunkle et al., 2010).

DMS-MaPseq (kindly provided by Boris Zinshteyn and Rachel Green, Johns Hopkins University, United States) confirmed our findings of myxovalargin binding within the NPET of *E. coli* ribosomes. In the DMS-MaPseq assay (Limbrick et al., 2020; Zubradt et al., 2017) MyxB bound to the NPET of the *E. coli* ribosome protects different 23S rRNA nucleotides in close proximity to the binding site of the AMP from chemical modification, namely methylation, by dimethyl sulfate (DMS) at 10  $\mu\text{M}$  (Fig. 23a, light blue) or 100  $\mu\text{M}$  (Fig. 23a, blue). Resistance mutations (Sup.Fig. 3a-d), DMS-MaPseq

(**Fig. 23a**) and high resolution MyxA structure (**Fig. 22a**) included A2503 as important interaction partner. To demonstrate the resistance mutation A2503G (*M. tuberculosis* A2741G) and U2609C (*M. tuberculosis* U2847) a firefly luciferase *in vitro* translation assay was performed as described in methods section 8.4. Ribosomes had to be purified from a Squires-strains bearing a single rRNA operon with a single mutation of A2503G or U2609C (methods section 8.3), as *E. coli*, and other Gram-negative bacteria are naturally resistant to myxovalargins (Quan et al., 2015; Vazquez-Laslop et al., 2010). Purified mutant and wildtype ribosomes were tested for their translation activity in absence and presence of increasing doses of MyxB and revealed a dose-dependent inhibition of wildtype and U2609C mutant ribosomes. On the opposite, the *E. coli* ribosomes bearing the A2503G mutation showed a resistance against MyxB even at concentrations of 100  $\mu$ M. To investigate the mechanism of action a toeprinting assay (**Fig. 23c,d**) was performed by a member of our group (Dr. Michael Graf) which uses reverse transcription to monitor the position of stalled ribosomes on a mRNA (Hartz et al., 1988). Using the Isoleucine (Ile)-tRNA synthetase inhibitor mupirocin in the reaction mix allowed the assays to be performed in the absence of Ile (Hughes and Mellows, 1978). The absence of Ile was used as positive control. In the absence of antibiotics, ribosomes can initiate translation at the AUG start codon, and translate 15 amino acids until encountering the Ile “catch-codon” in the A-site which accommodates a deacylated-tRNA and therefore pauses translation (**Fig. 23c-d**). In a dose-dependent manner MyxB reduces the amount of ribosomes reaching the Ile catch-codon and at 100  $\mu$ M resulting in a loss of the band, while a new band can be observed at the AUG start codon in the P-site, as seen for the antibiotic positive control thiostrepton (**Fig. 23d**) (Harms et al., 2008). Additionally, the toeprinting reaction was performed in the presence of 5  $\mu$ M Ery, which leads to a stalling on the ErmBL mRNA used in a context-specific manner (**Fig. 23c-d**) (Arenz et al., 2016a; Arenz et al., 2014b). The translation mix was preincubated with 5  $\mu$ M Ery and titrated with increasing concentrations of MyxB (10-100  $\mu$ M) resulting in a loss of the Ery-dependent stalling band, with the appearance of the same initiation stalling band as observed with MyxB alone (**Fig. 23c-d**). This can be explained with the overlapping binding sites of MyxB and Ery in the NPET as shown in (**Fig. 23e-f**). Together with previous studies on myxovalargins we suggest that myxovalargins do not prevent the

fMet-tRNA from binding, but rather interferes with aa-tRNA accommodation to the A-site (Irschik and Reichenbach, 1985).

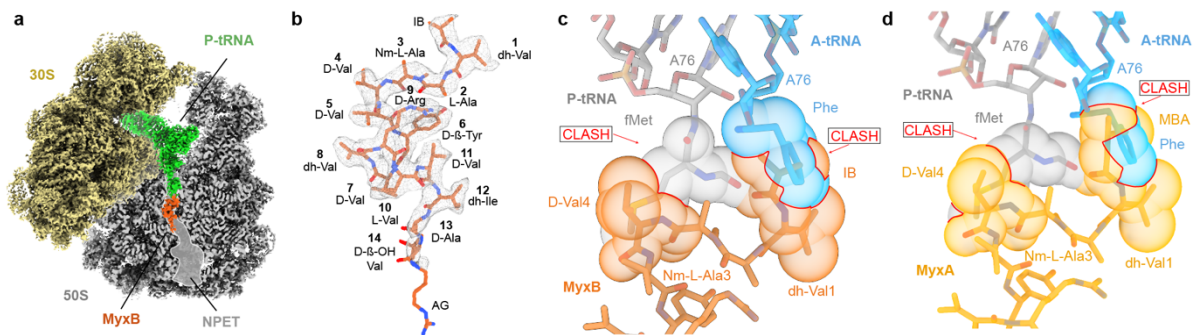


**Figure 24: MyxB bound to the 70S *E. coli* ribosome.** **a**, Cryo-EM map of the 70S-MyxB-complex with the large 50S subunit shown as transverse section with MyxB (orange) bound to the NPET, the P-tRNA (light green) and the small 30S subunit (yellow). **b**, Molecular model of MyxB (orange) in isolated cryo-EM density shown as mesh. **c-d**, Superimposition of the fMet-tRNA<sup>fMet</sup> (grey) in the P-site and Phe-tRNA<sup>Phe</sup> (blue) in the A-site of the pre-attack state (PDB ID 1VY4) with MyxB (**c**, orange) or MyxA (**d**, yellow), with steric clashes indicated by red lines and spherical representation of the involved atoms.

To further investigate the mechanism of action, a second cryo-EM structure was produced with an active translating ribosome stalled by MyxB. For this a disome approach was established (**Fig. 7**) by a previous member of the group, as shown in (Arenz et al., 2016a; Arenz et al., 2015; Arenz et al., 2014b) and yielded a MyxB-stalled ribosome complex (70S-MyxB-complex) at a final masked resolution of 2.96 Å (**Fig. 24a** and **Fig.11-12**). Besides the difference in the N-terminal hydrophobic region of MyxB bearing an IB-moiety instead of an MBA, the additional density in the NPET has striking similarity to MyxA in the high-resolution structure on the vacant *E. coli* ribosome consistent with their highly conserved chemical structure (**Fig. 24b**). Similarly, to MyxA, the AG was poorly resolved and even in lower resolution some of the putative waters were visible supporting the findings in the MyxA structure. The 70S-MyxB-complex also revealed an accommodated tRNA in the P-site that was identified as an fMet-tRNA<sup>fMet</sup> representing an initiation complex, but no additional presence of A-tRNA density (**Fig. 24a** and **Sup.Fig. 4a-c**). In comparison to a fully accommodated pre-attack state P-site tRNA, the P-tRNA in the 70S-MyxB-complex has not fully accommodated and the acceptor arm has shifted by 1.5 Å to prevent steric clashing of the fMet moiety with the D-Val4 of MyxB (**Sup.Fig. 4d-f**) (Polikanov et al., 2014a). The flexibility of the CCA-end allowing to avoid sterically clashing also

results in poor density for the fMet moiety in the 70S-MyxB-complex (**Sup.Fig. 4d-e**). Both MyxA and MyxB are suggested to clash with both the P-tRNA in the fully accommodated state, but also with their hydrophobic IB (MyxB) and MBA (MyxA) moieties with the incoming amino acid of the fully accommodated A-site tRNA as shown in (**Fig. 24c-d**).

## 10.2. Cryo-EM structures of the O-glycosylated proline-rich antimicrobial peptide drosocin

### 10.2.1. Drosocin inhibits *in vitro* translation during termination by trapping ribosomes at stop codons

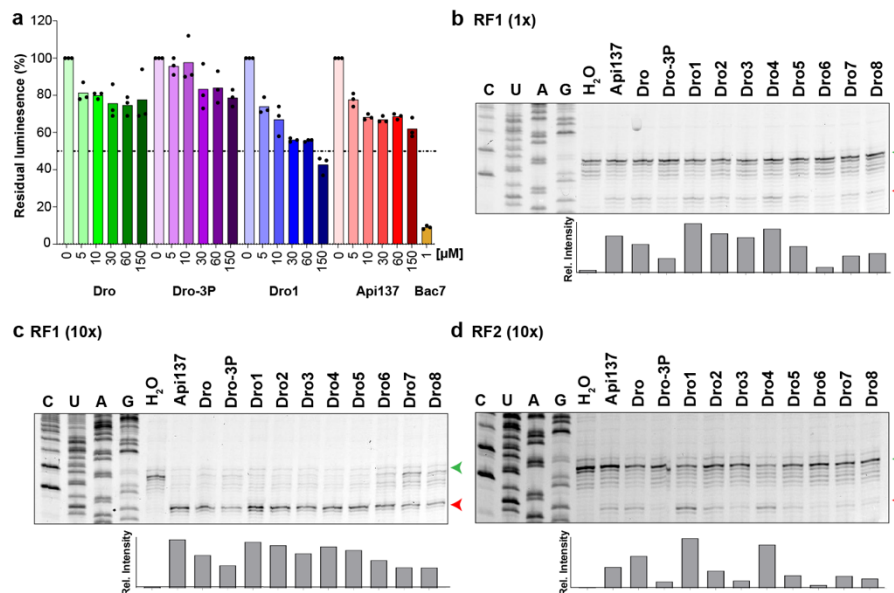


**Figure 25: Translation inhibition by drosocin derivatives.** **a**, *In vitro* firefly luciferase translation assay with increasing concentrations of Dro (green), Dro-3P (purple), Dro1 (blue), Api137 (red) and 1 μM Bac7 (gold). The residual luminescence was normalized to 100% in absence of each compound in triplicates. **b-d**, Toeprinting assay of ribosomes translating a MLIF\*-mRNA in presence of 30 μM of different drosocin derivatives, 30 μM Api137 and either 1x release factor 1 (**b**), 10 x release factor 1 (**c**) or 10x release factor 2 (**d**). Start codon (green) and stop codon (red) position are indicated by arrows. Histograms represent relative band intensity corresponding to the stop codon.

Wildtype drosocin without the sugar modification and the mutated Dro-3P have been shown to inhibit *in vitro* translation reactions, while the naturally produced O-glycosylated drosocin has not been tested (Lele et al., 2015b; Ludwig et al., 2022). In

preparation for the structural elucidation of drosocin on the ribosome, our group performed experiments to understand the conditions necessary for proper complex formation. Increasing concentrations (0-150  $\mu\text{M}$ ) of  $\alpha$ -D-GalNAc-modified Dro1 were compared to unmodified Dro, the mutant Dro-3P and the synthetic Api137 in a cell-free *in vitro* translation system (**Fig. 25a**). Firefly luciferase (Fluc) mRNA was used as template to demonstrate translation activity as shown in previous publications (Mardirossian et al., 2018a; Mardirossian et al., 2018b; Mardirossian et al., 2019; Mardirossian et al., 2020; Seefeldt et al., 2016; Seefeldt et al., 2015; Sola et al., 2020). These assays were prepared by Martino Morici from our group. Dose-dependent inhibition was observed for Dro1, with a maximum of 60% at the highest tested concentration of 150  $\mu\text{M}$  and with an  $\text{IC}_{50}$  of 78  $\mu\text{M}$  (**Fig. 25a**). Dro and Dro-3P were shown to be poor inhibitors, exhibiting a maximum of 20% inhibition at 150  $\mu\text{M}$ , while Api137 was more effective with 40% inhibition at 150  $\mu\text{M}$  (**Fig. 25a**). In comparison to these results, the type-I PrAMP Bac7 and the reported inhibition of Onc112 in the same system displaying  $\text{IC}_{50}$  values of  $<1$   $\mu\text{M}$  suggest drosocin to be a similar inhibitor to Api137, rather than oncocin, as suggested in previous studies (Krizsan et al., 2015). To investigate which step during translation is affected by drosocin, toeprinting assays were performed by Max Berger, that use reverse transcription to monitor the stalling of ribosomes on a defined mRNA template (**Fig. 25b**) (Hartz et al., 1988). In the presence of RF1, the translation reaction without drosocin shows no band corresponding to the UAA stop codon, while the addition of 25  $\mu\text{M}$  Api137 shows a significant stalling of ribosomes on the stop codon (**Fig. 25b**), as shown in previous studies (Florin et al., 2017). A stop codon band of differing intensities was also observed for all drosocin derivatives at 30  $\mu\text{M}$ , which intensified with 10-fold increased RF1 concentrations, which is consistent with drosocin acting on translation termination in a similar fashion as Api137 (**Fig. 25c**) (Florin et al., 2017; Graf et al., 2018). The reaction was repeated with 10-fold RF2, and lead to a similar stalling band, but with much lower efficiency (**Fig. 25d**). Dro1 showed the strongest stalling efficiency in all toeprints, followed by Dro4, a trend which was most evident in presence of aforementioned 10-fold RF2 (**Fig. 25b-d**). Very weak stalling was observed for Dro-3P mutant (**Fig. 25b-d**), also seen in the *in vitro* translation assay. Contrary to expected behavior, the unmodified Dro still showed good stalling activity in the toeprints (**Fig. 25b-d**), suggesting the O-glycosylation to be important for cellular

uptake. Both assays provide a base for the cryo-EM structures, revealing drosocin trapping ribosomes during translation termination involving RFs, a mechanism observed in type II PrAMP apidaecin, and different from type I PrAMPs, like Bac7 and Onc112.

### 10.2.2. Cryo-EM structure of O-glycosylated Dro1 on the ribosome

The structural elucidation of drosocin on the ribosome was prepared as described in Methods section 8.5.2 using the same mRNA template used in the toeprint assay in presence of a 10-fold excess of RF1 and 30  $\mu$ M Dro1 (**Fig. 25c**). *In silico* processing and extensive sorting of the data set lead to three high resolution sub-populations, namely, a 70S terminating ribosome with RF1 and P-site tRNA (26.0%), a 70S elongating ribosome with A- and P-site tRNAs (16%), as well as a vacant 50S ribosomal subunit (30.2%), which yielded a masked final average resolution of 2.3 Å, 2.8 Å and 2.1 Å, respectively (**Fig. 26a-c** and **Fig. 13-14**). For all three classes an additional density was observed in the NPET that was unambiguously assigned to drosocin peptide (**Fig. 26a-f**). This drosocin density was particularly well-resolved in the terminating 70S ribosome containing RF1 and allowed the modelling of all 19 amino acid sidechains of drosocin, including the observed  $\alpha$ -D-GalNAc modification linked to Thr11 (**Fig. 26a,d,f**). The ribosomal subunit was very well resolved in the 50S cryo-EM map, with the drosocin density being slightly less resolved on the N- and C-terminal regions compared to the terminating ribosome (**Fig. 26c,f,i**). In contrast to these two, the elongating 70S cryo-EM was generally less well resolved and especially the  $\alpha$ -D-GalNAc modification was poorly resolved, suggesting the drosocin peptide to be less stably bound as in the other states (**Fig. 26b,e,h** and **Fig. 14g-i**). The overall orientation of drosocin in the NPET is remarkably similar to the type II PrAMP Api137, with the C-terminus located at the PTC and the N-terminus extending deeper into the tunnel, similar to an elongating nascent polypeptide chain (**Sup.Fig. 5a-b**) (Chan et al., 2020; Florin et al., 2017; Graf et al., 2018). This is opposite to the type I PrAMPs Bac7 and pyrrococoricin (**Sup.Fig. 5c-d**) (Gagnon et al., 2016; Mardirossian et al., 2018b; Mardirossian et al., 2020; Roy et al., 2015; Seefeldt et al., 2016; Seefeldt et al., 2015).





### 10.2.3. Cryo-EM structure of the elongating 70S ribosome in complex with drosocin

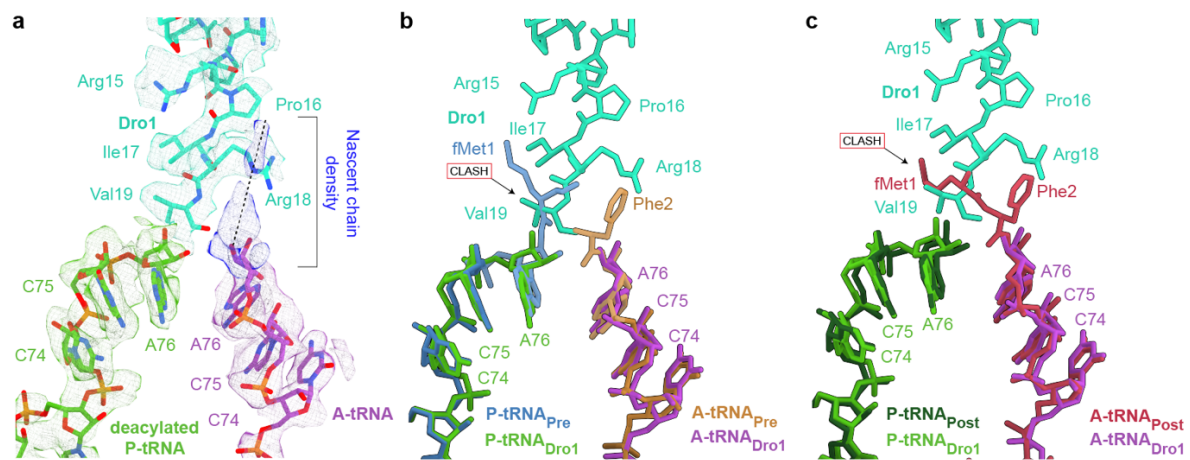


**Figure 27: Cryo-EM structure of the elongating ribosome with drosocin bound in the NPET.** **a**, Molecular models for P-tRNA (light green), A-tRNA (purple) and Dro1 (teal) in isolated cryo-EM densities of the elongating 70S Dro1-complex. Density connected to the A-site tRNA is highlighted but was not modelled due to poorly ordered and less-well resolved density. **b**, Superimposition of the pre-attack state (P-tRNA<sub>Pre</sub> (blue) and A-tRNA<sub>Pre</sub> (dark purple) (PDB ID 1VY4) (Polikanov et al., 2014a) with P-tRNA<sub>Dro1</sub> (light green), A-tRNA<sub>Dro1</sub> (purple) and Dro1 (teal) from (a). C-terminus of Dro1 is predicted to clash with the fMet of the pre-attack peptidyl-tRNA in the P-site. **c**, Superimposition of the post-attack state (P-tRNA<sub>Post</sub> (dark green) and A-tRNA<sub>Post</sub> (red)) (PDB ID 1VY5) (Polikanov et al., 2014a) with P-tRNA<sub>Dro1</sub> (light green), A-tRNA<sub>Dro1</sub> (purple) and Dro1 (teal) from (a). The C-terminus of Dro1 is predicted to clash with fMet-Phe of the post-attack peptidyl-tRNA in the A-site.

The observed density in the elongating 70S-Dro1-complex (**Fig. 27a**) for the P-site in comparison with the pre- and post-attack state tRNAs (**Fig. 27b,c**) reveals a deacylated CCA-end, while the A-site tRNA seems to carry the nascent chain, suggesting the ribosome being in post-peptide bond formation state, but prior to translocation (Polikanov et al., 2014a). The anticodon-interactions, revealed by well resolved cryo-EM density, suggest an initiator tRNA<sup>fMet</sup> in the P-site decoding an AUG codon, while a tRNA<sup>Leu</sup> is in the A-site decoding a UUC codon on the mRNA (**Sup.Fig. 6a-b**), suggesting that the density on the CCA-end of the A-tRNA was for the dipeptide fMet-Leu, which is consistent with the reduced space available with drosocin bound in the NPET and occluding most of the space of the tunnel and PTC.

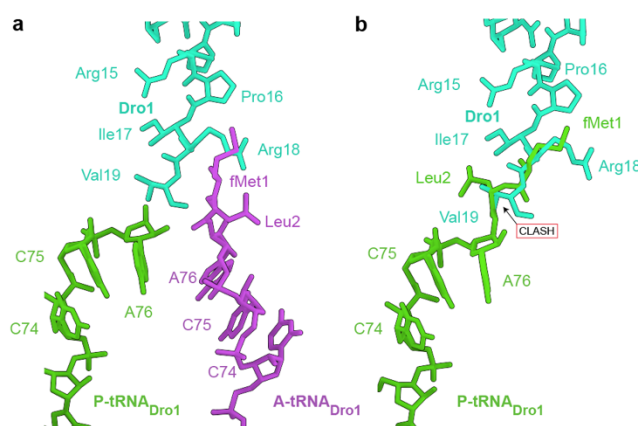


**Figure 28: Potential steric clash of the fMet-Leu nascent chain with Dro1.** **a,b**, Hypothetical molecular model of fMet-Leu nascent chain on the A-site tRNA<sub>Dro1</sub> (purple) based on the post-attack state (**a**) (PDB ID 1VY5) (Polikanov et al., 2014a), and on the P-tRNA<sub>Dro1</sub> (light green) based on a canonical peptidyl-tRNA (**b**) (PDB ID 7RQE) (Syroegin et al., 2022b) predicted to sterically clash with the C-terminus of Dro1.

A tentative model was generated for the dipeptide fMet-Leu nascent chain based on the post-peptide bond formation structure of fMet-Phe reported previously (**Fig. 27c**) (Polikanov et al., 2014a) but was not properly modelled *de novo* due to the poorly resolved density near the CCA-end of the A-tRNA (**Fig. 27a**) but allowed to observe a different positioning of the sidechains compared to the post-state that would clash with the fMet moiety and the Val19 of drosocin (**Fig. 28a**). The apparent shift of the fMet in our model towards the Arg18 would provide an explanation as to why both the Arg18 as well as the dipeptide nascent chain were poorly ordered (**Fig. 27a**). Based on the insights from the elongating complex, it can be suggested that drosocin allows translation initiation, despite the predicted steric overlap of fMet with Val19 of drosocin, and subsequent accommodation of an amino acylated-tRNA in the A-site and proper peptide bond formation, but severely interferes with translocation. To highlight the steric clash and translocation inhibition of a dipeptide on the P-tRNA with drosocin in our structure, a fMet-Leu nascent chain was modelled based on available P-site peptidyl-tRNAs (Syroegin et al., 2022a), supporting our predictions (**Fig. 28b**). In previous studies on apidaecin, similar to our findings on drosocin, a strong termination inhibition but also a moderate effect on initiation has been reported and given the similar binding position of the C-terminus of Api137 an interference with the first step of translocation similar to drosocin may be predicted (**Sup.Fig. 5b**) (Mangano et al., 2020).

## 10.2.4. Interactions of drosocin within the NPET of the terminating 70S-Dro1-complex

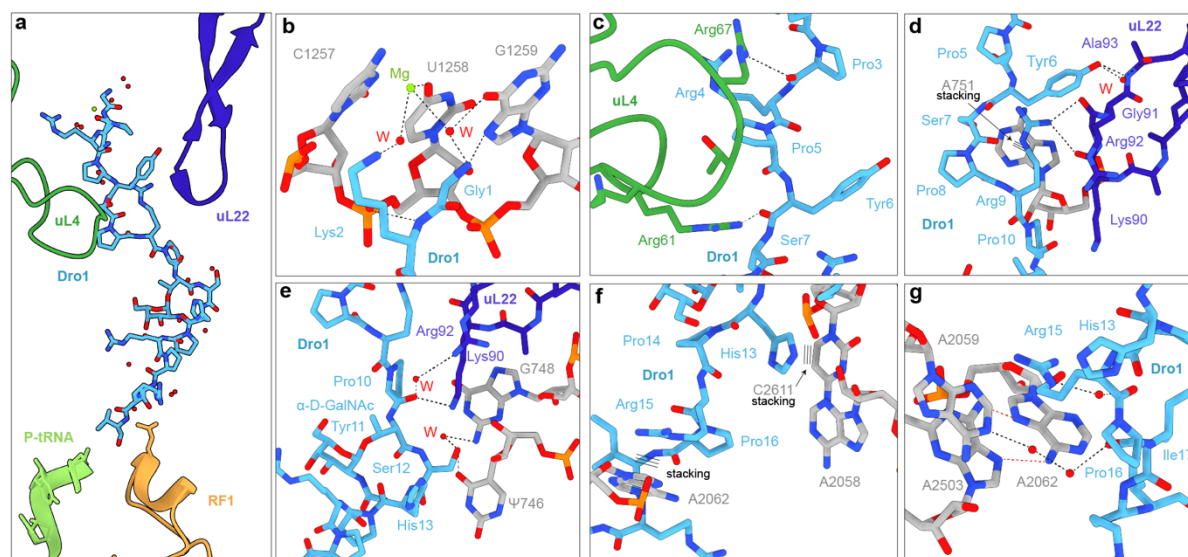


**Figure 29: Interactions of Dro1 with the terminating 70S ribosome.** **a-g**, Overview of Dro1 (blue) in the NPET surrounded by ribosomal proteins uL4 (green) and uL22 (dark blue) and P-tRNA<sub>Dro1</sub> (light green), release factor 1 (orange), waters (red) and 23S rRNA nucleotides (grey). Stacking interactions are indicated by three lines, hydrogen bond interactions by black dotted lines. **b**, Hydrogen bond interactions mediated by water of Gly1 and Lys2 of Dro1 with U1258 and G1259. **c**, Hydrogen bond interactions of the backbone of Pro3 and Tyr6 of Dro1 with Arg61 and Arg67 of uL4. **d**, Stacking interaction of Arg9 with A751 and direct and water-mediated interactions of Tyr6 and Arg9 of Dro1 with uL22 side chains Lys90, Gly91, Arg92 and Arg93. **e**, Direct and water-mediated interactions of the backbone of Pro10 and hydroxy-group of Ser12 of Dro1 with uL22 side chains Lys90 and Arg92, as well as 23S rRNA nucleotides Ψ746 and G748. **f**, Stacking interactions of His13 and Arg15 of Dro1 with C2611 and A2062, respectively. **g**, Direct and water-mediated interactions of Arg15 and Pro16 of Dro1 with backbone of A2059, A2062 and A2503.

The high resolution of the terminating 70S-Dro1-complex and the well resolved Dro1 in the NPET allowed molecular descriptions of interactions of the drosocin peptide with the 23S rRNA nucleotides and ribosomal proteins (**Fig. 29**). The N-terminus of drosocin extends deep into the NPET near the constriction of uL4 and uL22 (**Fig. 29a**). N7 of 23S rRNA nucleotide G1259 is forming potential hydrogen bond interactions with the N-terminal amino group of drosocin (**Fig. 29b**). Lys2 forms interactions from the backbone amine to the phosphate-oxygen of U1258 and another water mediated contact between O4 of U1258 and the ε-amino group of Lys2 (**Fig. 29b**). Dro1 establishes multiple interactions with the ribosomal proteins uL4 and uL22 with the residues Pro3 to Pro10 located closely (**Fig. 29c-e**). uL4 sidechains Arg61 and Arg67

are within hydrogen bond distance of the backbone carboxyl of Tyr6 and Pro 3 of Dro1, respectively (**Fig. 29c**). Dro1 sidechains Tyr6 and Arg9 interact through potential hydrogen bonds with the backbone of uL22 sidechains Ala3, Lys90 and Gly91, respectively (**Fig. 29d**). While removal of the first five N-terminal residues (GKPRP) abolishes Dro1 activity completely, the Tyr6 interaction appears not to be critical since replacing it with a Phe that lacks the hydroxy group essential for the hydrogen bond interaction does not lead to loss of antimicrobial activity (Bulet et al., 1996; de Visser et al., 2005). Lys90 of uL22 forms an additional hydrogen bond interaction and an indirect water mediated interaction from Arg92 with the backbone carboxyl of Pro10 of Dro1 (**Fig. 29e**). Potential altering of the drosocin peptide conformation by mutation of Pro10 to Ala does also abolish antimicrobial activity (Ahn et al., 2011b). U746 forms a direct and G748 a water-mediated hydrogen bond interaction with Ser12 of Dro1 (**Fig. 29e**). The Thr11 modification establishes multiple hydrogen bond interactions with U2609 which will be discussed later in this study. Dro1 residues Arg9, His13 and Arg15 stack onto 23S rRNA nucleotides A751 (**Fig. 29e**), C2611 and A2062 (**Fig. 29f-g**), respectively, and mutation of both stacking Arg9 and Arg15 to Lys reduces the antimicrobial activity significantly by 4- and 8-fold (Lele et al., 2013).

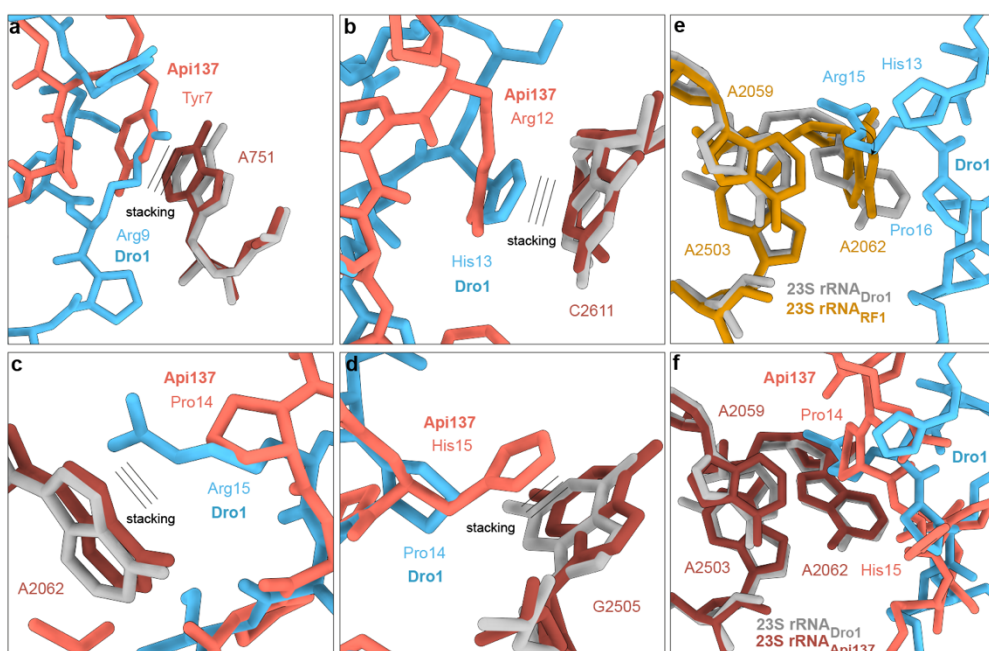


**Figure 30: Interactions of Api137 within the NPET compared to Dro1.** a-d, Stacking interactions of Api137 (salmon) indicated by three lines with 23S rRNA nucleotides (dark red) (PDB ID 5O2R) (Florin et al., 2017) superimposed with Dro1 (blue) and 23S rRNA nucleotides (grey). e-f, Comparison of Dro1 (blue) with 23S rRNA nucleotides (grey) with (e) 23S rRNA nucleotides (yellow) of the canonical termination complex (PDB ID 4V63)

(Laurberg et al., 2008) and (f) Api137 (salmon) with 23S rRNA nucleotides (dark red) (PDB ID 5O2R) (Florin et al., 2017).

In comparison, Api137 forms similar stacking interactions with A751 and C2611 but show distinct differences in sidechains and mode of interaction (**Fig. 30a-d**) (Chan et al., 2020; Florin et al., 2017; Graf et al., 2018). Both our structure and the Api137 structure show a rotated conformation for A2062 in comparison to a canonical RF1-bound terminating ribosome (**Fig. 29g** and **Fig. 30e-f**) (Chan et al., 2020; Florin et al., 2017; Fu et al., 2019; Graf et al., 2018; Laurberg et al., 2008; Pierson et al., 2016; Zhou et al., 2012). A2059 and A2503 are known to confer resistance to Api137 when mutated and are both interacting with A2062 (**Fig. 30g**), suggesting a similar behavior for Dro1 which needs to be further investigated (Florin et al., 2017).

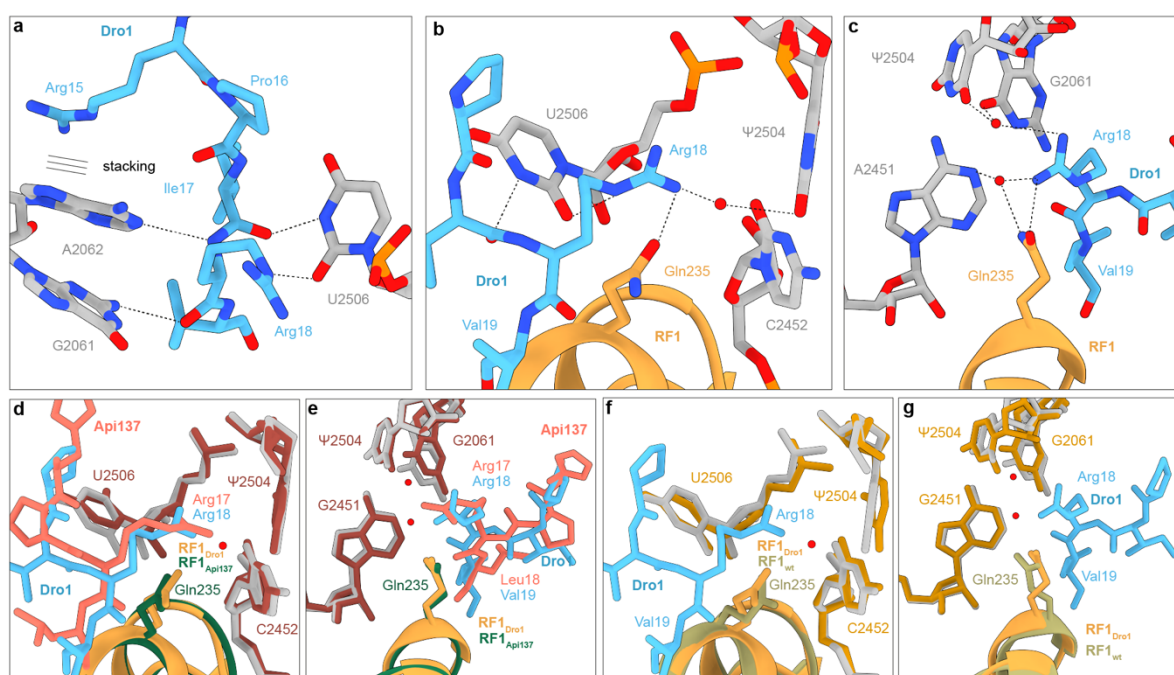


**Figure 31: Interactions of Dro1 and Api137 with release factor1.** a-c, Dro1 (blue) interacting with 23S rRNA nucleotides (grey), release factor 1 (orange) and water (red) indicated by dotted lines, while stacking interaction is indicated by three lines. a, Stacking interaction of Arg15 of Dro1 with A2062 and hydrogen bond interactions of Ile17 and Arg18 of Dro1 with G2061, A2062 and U2506. b-c, Direct and water-mediated interactions of Arg18 of Dro1 with Gln235 of release factor1 viewed from two sides with surrounding 23S rRNA nucleotides (b)  $\Psi$ 2504, U2506 and C2452 and (c) G2061, A2451 and  $\Psi$ 2504. d-e, Superimposition of (b-c) with Api137 (salmon) and Gln235 of RF1<sub>Api137</sub> (dark green) and surrounding 23S rRNA (dark red) (PDB ID 5O2R) (Florin et al., 2017). f-g, Superimposition of (b-c) with canonical termination complex Gln235 of RF1<sub>wt</sub> (olive) and surrounding 23S rRNA nucleotides (yellow) (PDB ID 4V63) (Laurberg et al., 2008).

Three backbone interactions of residues Ile17 and Arg18 of Dro1 with 23S rRNA nucleotides U2506, G2061 and A2062 stabilize the C-terminus of Dro1 (**Fig. 31a**). The nucleotides U2506 and C2452 form additional direct hydrogen bond interactions with Arg18, which inserts into this pocket (**Fig. 31b**), and forms water-mediated interactions with U2504, G2061 and A2451 (**Fig. 31b-c**). In this pocket Arg18 of Dro1 comes in hydrogen bond distance of 2.9 Å with the conserved GGQ motif of RF1, more specifically the Gln235, which also forms another water-mediated interaction stabilizing RF1 on the ribosome (**Fig. 31b-c**). This interaction is very similar to the Arg17 of Api137 with the same Gln235 of RF1 in previous studies (**Fig. 31d-e**), supported by the decrease of ribosome affinity and antimicrobial activity in mutational studies of Arg to an Ala, highlighting the importance of Arg in this position to stabilize the RFs (Chan et al., 2020; Florin et al., 2017; Graf et al., 2018; Krizsan et al., 2014). This is also supported by deletions in Dro1 of Arg18 and Val19 which showed a complete loss of in vitro biological activity (Hoffmann et al., 1999). Additionally, the nucleotide positioning is identical in the canonical termination state (**Fig. 31f-g**) (Fu et al., 2019; Laurberg et al., 2008; Pierson et al., 2016; Zhou et al., 2012).

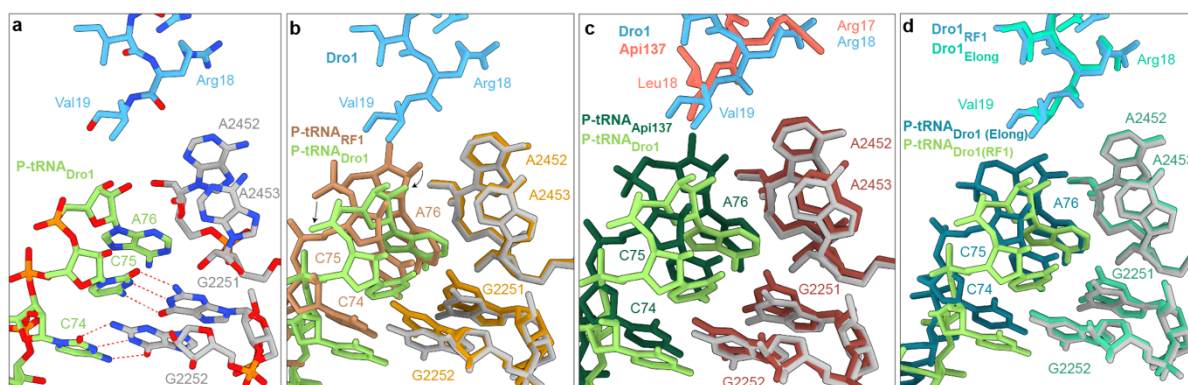


**Figure 32: P-tRNA in the termination complex with Dro1 bound in the NPET.** **a-d**, CCA-end of the deacylated P-tRNA<sub>Dro1(RF1)</sub> (light green), Dro1 (light blue) and 23S rRNA nucleotides (grey). **b**, Superimposition of the canonical termination state P-tRNA<sub>RF1</sub> (brown) and 23S rRNA nucleotides (yellow) (PDB ID 4V63) (Laurberg et al., 2008) with (**a**). The C-terminus of Dro1 displaces the CCA-end of the deacylated P-tRNA<sub>Dro1(RF1)</sub>, keeping the canonical base-pairing interactions of G2252 and G2251 with C74 and C75, respectively, compared to the canonical state. **c**, Superimposition of the P-tRNA<sub>Api137</sub> (dark green) and 23S rRNA nucleotides (dark red) in presence of Api137 (PDB ID 5O2R) (Florin et al., 2017) with (**a**). **d**, Superimposition of the P-tRNA<sub>Dro1(Elong)</sub> (dark teal) and 23S rRNA nucleotides (cyan) in presence of Dro1<sub>Elong</sub> (teal) in the elongation complex. The CCA-end of the deacylated P-tRNA<sub>Dro1(Elong)</sub> is not displaced, as Val19 of Dro1<sub>Elong</sub> is poorly ordered.

The C-terminus of Dro1 with the Val19 is poorly ordered in the cryo-EM map but at lower thresholds shows a position at the PTC overlapping with the CCA-end of a canonical P-site tRNA (**Fig. 32a**). The CCA-end of the bound P-site tRNA in this complex is as a consequence also poorly ordered, but shows a 2-3 Å shifted deacylated CCA-end compared to a canonical P-site tRNA in a terminating ribosome (**Fig. 32b**) (Fu et al., 2019; Laurberg et al., 2008; Pierson et al., 2016; Zhou et al., 2012). Despite the shift of the CCA-end the nucleobases of C74 and C75 maintain their canonical Watson-Crick base-pairs with nucleotides G2252 and G2251 of the P-loop, respectively (**Fig. 32a**). Api137 on the other hand is known to interact directly with A76 of the P-site tRNA stabilizing it in the canonical position, which is similar to the position observed in the elongating 70S-Dro1-complex, but as observed in the terminating 70S-Dro1-complex does not interact directly with the tRNA (**Fig. 32d**). The binding position and other interactions of RF1 in the terminating 70S-Dro1-complex are identical those observed in canonical termination complexes, including the decoding of the stop codon (**Sup.Fig. 6c-e**). The high resolution of our structure allowed us to observe additional water-mediated interactions of RF1 and the UAA stop codon (**Sup.Fig. 6f-i**), which have not been reported in the lower resolved structures from previous studies (Fu et al., 2019; Laurberg et al., 2008; Pierson et al., 2016; Zhou et al., 2012).

### 10.2.5. Interactions of the Dro1 glycosylation with the ribosome

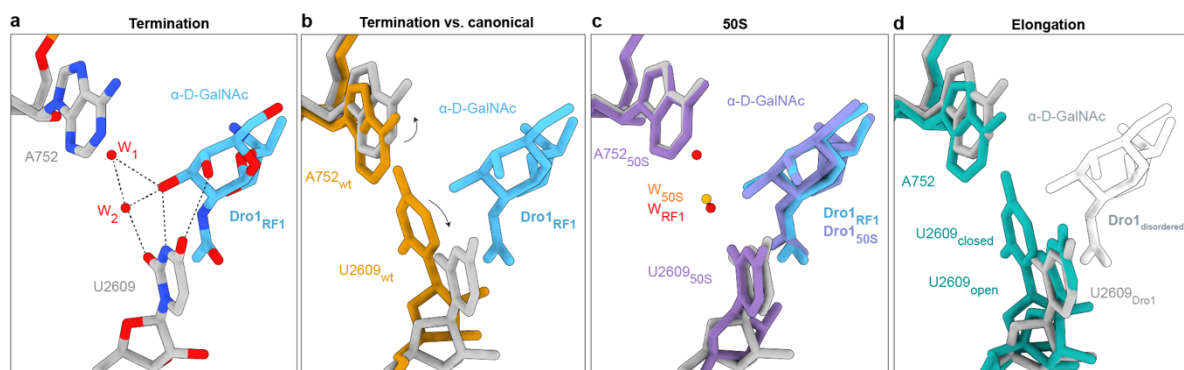


**Figure 33: Interaction of U2609 of the 23S rRNA with the O-glycosylation of Dro1.** **a**, Direct interactions and water mediated interactions of the  $\alpha$ -D-GalNAc modification of Thr11 of Dro1<sub>RF1</sub> (blue) with 23S rRNA nucleotide U2609 (grey) of the terminating 70S Dro1-complex. The two putative water molecules W<sub>1</sub> and W<sub>2</sub> (red) form potential hydrogen bond interactions with both the  $\alpha$ -D-GalNAc modification of Dro1 and U2609. **b-d**, Superimposition of (**a**) with (**b**) the Watson-Crick-base-pair of A752<sub>wt</sub> with U2609<sub>wt</sub> (yellow) from the canonical RF1-

bound termination complex (PDB ID 4V63) (Laurberg et al., 2008), with (c) Dro1<sub>50S</sub> (dark blue) bound to the large 50S subunit with 23S rRNA nucleotides (purple), and with (d) Dro1 (white outline) from the elongating 70S Dro1-complex with A752 and U2609 in both opened and closed state (dark teal). Dro1 was poorly ordered in the elongating 70S Dro1-complex and depicts Dro1<sub>RF1</sub> as reference, which is incompatible with U2609 in the closed state.

Multiple interactions of the  $\alpha$ -D-GalNAc modification linked to Thr11 of Dro1 with U2609 of the 23S rRNA in both the terminating 70S drosocin-complex and the 50S drosocin-complex were observed (**Fig. 33a**). The C3 hydroxyl of the  $\alpha$ -D-GalNAc comes in 2.6 Å distance with N3 and 2.7 Å with O2 of the base of U2609 (**Fig. 33a**). The C4 hydroxyl potentially forms a weak hydrogen bond with the 3.5 Å distant O4 of U2609 (**Fig. 33a**). The  $\alpha$ -D-GlcNAc modification of Dro4 would maintain the interactions with O2 and N3 but lose the weaker O4 interaction with U2609, which is consistent with activity of Dro4 in the toeprinting assays (**Fig. 25b-d** and **Sup.Fig. 7d-e**). We propose based on the structure and the toeprinting results that the  $\beta$ -D-linked drosocin variants Dro3 and Dro5-8 are incompatible to form the aforementioned interactions leading to their reduced translation inhibition activity. In canonical *E. coli* termination complexes (Fu et al., 2019; Laurberg et al., 2008; Pierson et al., 2016; Zhou et al., 2012) and vacant 70S ribosomes (Watson et al., 2020) the U2609 appears base-paired with A752 (**Fig. 33b**). In the terminating and 50S-Dro1-complexes the  $\alpha$ -D-GalNAc modification overlaps with the base-paired position of these nucleotides and forces U2609 to shift away from A752 stabilizing two water molecules that form indirect hydrogen bond interactions between the sugar and U2609 (**Fig. 33a-c** and **Sup.Fig. 7a-b**). Surprisingly, in the elongating 70S drosocin-complex we observed a very poorly resolved  $\alpha$ -D-GalNAc modification that allowed both the closed base-paired and a shifted conformation of U2609 which presumably is the reason why Dro1 cannot fully accommodate within the NPET due to higher flexibility (**Fig. 33d** and **Sup.Fig. 7c**).



### 10.3. Cryo-EM structure of telithromycin bound to the G2400A mutant 80S *S. cerevisiae* ribosome

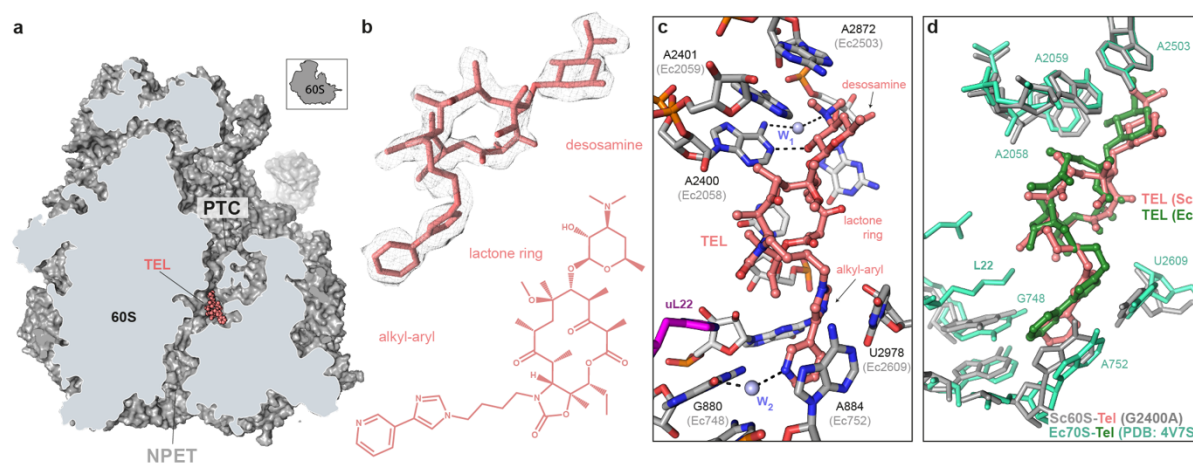


**Figure 34: Cryo-EM structure of TEL bound to the G2400A mutant *S. cerevisiae* ribosome.** **a**, Transverse section of the cryo-EM density (grey) of the TEL-60S-complex with TEL (salmon) bound in the NPET. **b**, Molecular model of TEL (salmon) in isolated cryo-EM density (mesh) with the chemical structure in the same orientation. **c**, TEL bound in the NPET with surrounding 25S rRNA nucleotides (grey), ribosomal protein uL22 (purple) and two putative water molecules  $W_1$  and  $W_2$  (light blue). Water-mediated and direct interactions are indicated by dotted lines.  $W_1$  bridges an interaction of N6 of A2400 (EcA2058) with the dimethylamine of the desosamine of TEL, while N1 of A2400 (EcA2058) forms a direct interaction with the Hydroxy group. The alkyl-aryl side-chain of TEL stacks onto the base-pair of A884 (EcA752)- U2978 (EcU2609) and forms a water-mediated interaction with G880 (EcG748). **d**, TEL bound to G2400A mutant *S. cerevisiae* 60S with 25S rRNA nucleotides (grey) superimposed with TEL (salmon) bound to *E. coli* 70S ribosome (green) with surrounding 23S rRNA nucleotides (teal) (PDB ID 4V7S) (Dunkle et al., 2010). Modified from (Svetlov et al., 2021a).

The *S. cerevisiae* G2400A (EcA2058) mutant 80S ribosome was engineered and purified by Maxim Svetlov from Mankin lab at University of Illinois at Chicago, IL, USA as described in methods section 8.5.3 (Svetlov et al., 2021a). *In silico* processing (methods section 8.7.6) resulted in a final reconstruction with an average resolution of the masked of 2.9 Å extending to 2.5 Å in the core (**Fig. 15-16a-d**). In the NPET a density was located that was assigned to Tel (**Fig. 16e-g**) based on superimposition of an *E. coli* Tel complex (Dunkle et al., 2010). The positions of the 14-membered macrolactone ring, the C5-desosamine sugar and the arm-like C10-C11 alkyl-aryl side chain were placed unambiguously in the well-resolved density (**Fig. 34b** and **Fig. 16e-f**). Within the mutant G2400A yeast ribosome, Tel binds in the NPET adjacent to 25S rRNA nucleotides A2400 (EcA2058) and A2401 (EcA2059) with the desosamine

sugar, present in all macrolides, extending towards the PTC (**Fig. 34a,c**). A potential hydrogen bond interaction of the desosamine sugar's hydroxyl group with N1 of A2400 (EcA2058). A putative water molecule ( $W_1$ ) observed in our structure mediates the hydrogen bond interactions of N6 amino group of A2400 with the dimethylamino group of Tel (**Fig. 34c** and **Fig. 16f**), which has been shown to be essential for macrolide binding (Svetlov et al., 2021b). A stacking interaction of the alkyl-aryl side chain's aromatic moieties of Tel, which is stretched in the opposite direction, with the Watson-Crick base-pair of U2978 (EcU2609) and A884 (EcA752) can be observed, as seen in *E. coli* (**Fig. 34d**) (Dunkle et al., 2010), *B. subtilis* (Schlunzen et al., 2003), and *T. thermophilus* (Bulkley et al., 2010) Tel complexes (**Sup.Fig. 9c-d, e-f**), and distinct from TEL bound to the bacterium *Deinococcus radiodurans* (Berisio et al., 2003) or archaeon *Haloarcula marismotui* (**Sup.Fig. 8a-b**) (Tu et al., 2005). An additional density for a putative water ( $W_2$ ) has been observed that mediates a potential hydrogen bond interaction of O6 of 25S rRNA nucleotide G880 (EcG748) and the alkyl-aryl side chain of Tel stabilizing the stacking interaction of Tel with U2978 (EcU2609) and A884 (EcA752) (**Fig. 16g**). Interestingly, the observed density for the aromatic rings of the alkyl-aryl side chain suggests a non-planar and slightly rotated orientation with respect to each other, which supports the optimal stacking on the slightly angled position of the nucleobases of U2978 (EcU2609) and A884 (EcA752) (**Fig. 34c**). Previously reported structures of Tel bound to bacterial or archaeal ribosomes showed a planar conformation of the alkyl-aryl side chain, regardless of planarity of the base-pair (**Sup.Fig. 9**). However, limited resolutions while modelling or species-specific differences in previous structures cannot be ruled out (Berisio et al., 2003; Bulkley et al., 2010; Crowe-McAuliffe et al., 2018; Dunkle et al., 2010; Schlunzen et al., 2003; Tu et al., 2005). Superimposition of our structure with a vacant *S. cerevisiae* ribosome revealed no significant conformational changes of 25S rRNA nucleotides around the Tel binding site, rather Tel adjusting to the ribosomal binding pocket in the NPET (**Sup.Fig. 8c**) (Tesina et al., 2019).

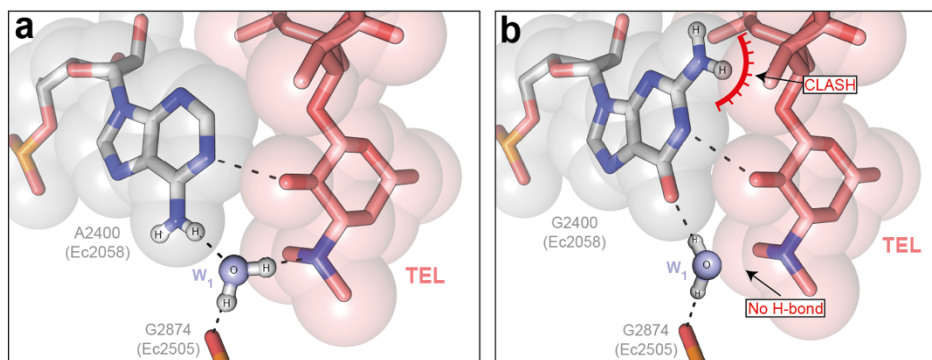


**Figure 35: Impact of G2400A mutation on the coordination of a water molecule.** **a**, G2400A (EcA2058) mutation coordinates Water  $W_1$  which can form a potential hydrogen bond interaction with dimethylamine group of the desosamine sugar of Tel (salmon) shown in sphere representation. **b**, The O6 of the canonical G2400 (EcA2058) forms a water-mediated interaction with G2874 (EcG2505). This does not allow a water-mediated interaction with the dimethylamino group of the desosamine of Tel (salmon). Additionally, the N2 amino group clashes into Tel (indicated by a red line). Modified from (Svetlov et al., 2021a).

An *in silico* mutation of A2400G (EcA2058) (**Fig. 35a**) back to G2400 (EcA2058) interfered with the putatively placed water ( $W_1$ ) and perturbs the water-mediated interaction between the 25S rRNA nucleotide and the dimethylamino group of Tel (**Fig. 35b**), as seen for Ery bound to bacterial ribosomes and Erm-mediated macrolide resistance (Svetlov et al., 2021b). Additionally, a steric clash of the N2 of the unmutated G2400 (EcA2058) with the desosamine sugar of Tel is predicted.

#### 10.4. *L. monocytogenes* structures

Collaborators of our group from Gemma Atkinsons lab from Lund University in Sweden did phylogenetic analysis, and Vasili Hauryliuk's labs *in vivo* assays on HflXr with different antibiotics that supported the work of this thesis and purified all *L. monocytogenes* complexes with data collection performed at UMCE. The resistance homolog of *E. coli* and *L. monocytogenes* HflX, HflXr, has a loop region in the N-terminal domain 2 that is extended by two additional amino acids. Bacteria containing two HflX homologs were found to have one homolog from the paraphyletic HflX group with a shorter loop and one homolog that shows an extended loop from HflXr group as shown in (Fig. 36). It should be noted that there are distinct exceptions to this, with bacteria having no HflXr homolog, like *Mycobacterium* species, and others having an extended loop in HflX homologs that have a resistance phenotype, like *S. fradiae* HflX (Karray et al., 2007). Phyla found to have long loop homologues, both HflX and HflXr, tend to be the ones carrying additional ARE versions of ABCFs (Koller et al., 2022b).

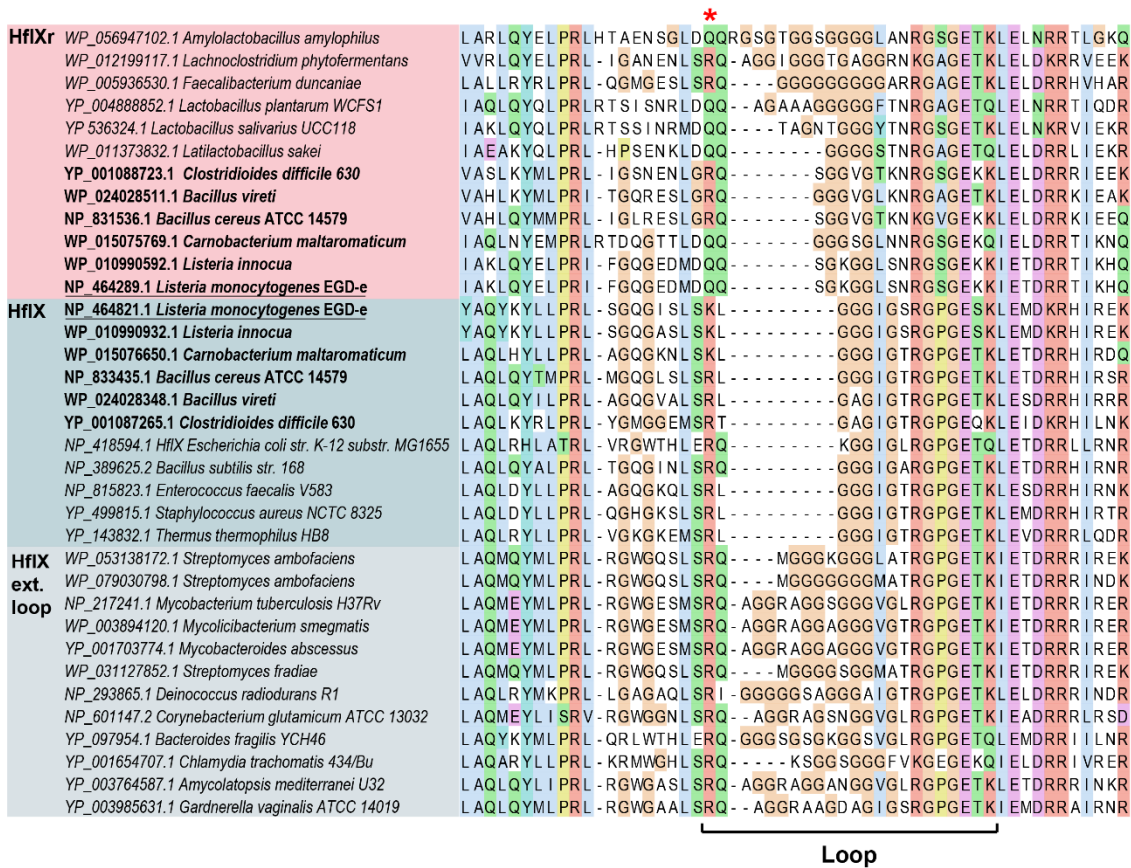


**Figure 36: Analysis of aligned sequences of HflX and HflXr proteins.** Alignment of the loop region of the N-terminal subdomain II of selected HflXr (red), HflX (blue) and extended loop HflX (grey) proteins. Bold organisms have both HflX and HflXr homologs. The red asterisk highlights the conserved R/Q residues, corresponding to Arg149 in *L. monocytogenes* HflXr. Modified from (Koller et al., 2022b).

In *L. monocytogenes* where the ARE-ABCF protein VgaL confers resistance to a variety of antibiotics, namely lincosamides, pleuromutilins and streptogramin As, the HflXr mediated resistance is masked (Brodiazhenko et al., 2022; Chesneau et al., 2005; Crowe-McAuliffe et al., 2021; Dar et al., 2016; Duval et al., 2018). The array of *in vivo* assays is shown in **Fig. 37**. The assays performed in  $\Delta vgaL \Delta hflXr$  strains with HflXr being overexpressed from a plasmid revealed an increase of resistance for macrolides, pleuromutilins and streptogramin Bs, but did not affect phenicols, lincosamides, oxazolidinones or tetracyclines (Koller et al., 2022b).

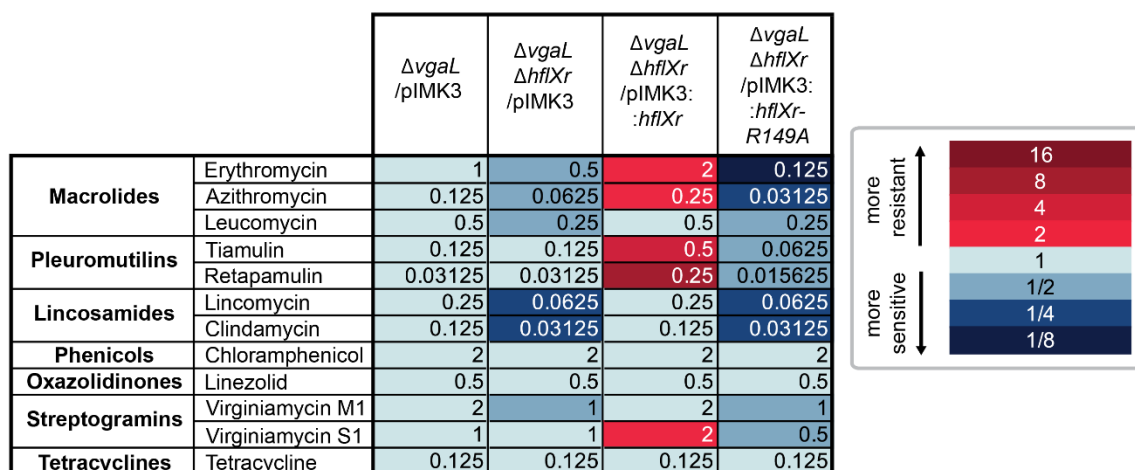


**Figure 37: Minimum inhibitory concentration data from in vivo assays.** Minimum inhibitory concentration (MICs) of antibiotics targeting the ribosome by class *against* *L. monocytogenes* EGDe strains  $\Delta vgaL$  in absence ( $\Delta hflXr$ ) or overexpression of HflXr from a plasmid (pIMK3::*hflXr*), and with a HflXr R149A mutant (pIMK3::*hflXr*-R149A). Modified from (Koller et al., 2022b).

### 10.4.1. Cryo-EM structure of Lincomycin on the *L. monocytogenes* 50S subunit

In order to compare antibiotic binding sites with the target protection capabilities of GTPase HflXr it was necessary to prepare an antibiotic bound ribosome of the same species. Purified *L. monocytogenes* ribosomes were incubated with 100  $\mu$ M lincomycin (Lnc) and applied to cryo-EM grids (methods section 8.5.4). The data collection and *in silico* processing (methods section 8.7.7.1) yielded two major classes with 56.4% of particles with E-site tRNA and 34% of particles with P-tRNA with a final average resolution of the masked reconstruction of 2.1 Å and 2.3 Å, respectively (**Fig. 38d** and **Fig. 17-18**).

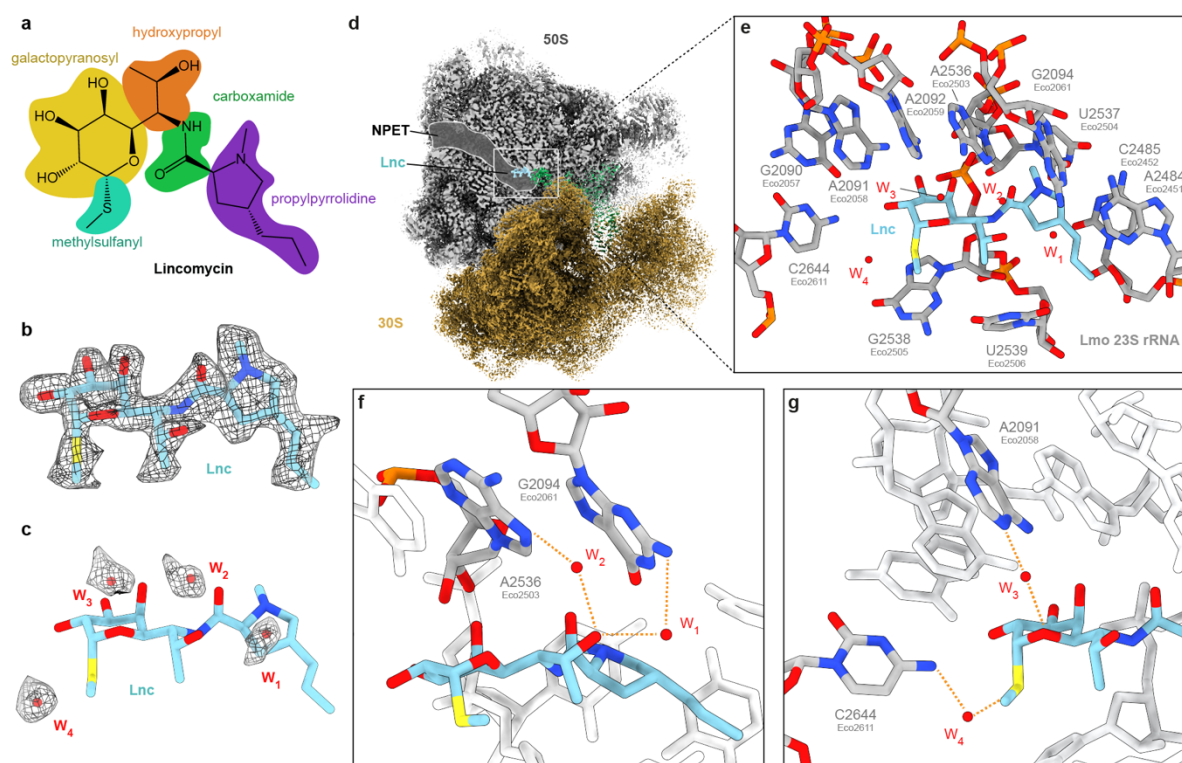


**Figure 38: Cryo-EM structure of lincomycin bound within the NPET of the *L. monocytogenes* ribosome. a,** Chemical structure of lincomycin (Lnc), with galactopyranosyl (yellow), methylsulfanyl (turquoise), hydroxypropyl (orange), carboxamide (green) and propylpyrrolidine (purple) moieties highlighted. **b,** Molecular model Lnc (light blue) in isolated cryo-EM density (mesh). **c,** Putative water molecules  $W_1$ - $W_4$  (red) around Lnc (light blue) in isolated cryo-EM density (mesh). **d,** Cryo-EM map of *L. monocytogenes* 70S-Lnc-complex with the large 50S subunit shown as transverse section (grey) with Lnc (light blue) bound at PTC near the NPET. **e,** 23S rRNA nucleotides (grey) surrounding the Lnc (light blue) binding site with putative water molecules  $W_1$ - $W_4$  (red). **f-g,** Water-mediated interactions of lincomycin (light blue) with 23S rRNA nucleotides (grey) indicated by orange dotted lines. **f,** The hydroxypropyl-group of Lnc interacts through  $W_1$  with N2 of G2094 (EcG2061) and through  $W_2$  with N7 of A2536 (EcA2503). **g,** The galactopyranosyl moiety forms a water-mediated ( $W_3$ ) interaction with A2091 (EcA2058) and the sulphur atom another with  $W_4$  and C2644 (EcC2611). Modified from (Koller et al., 2022b).

Lnc was assigned unambiguously in both cryo-EM maps to a density within the A-site crevice of the PTC (**Fig. 38b,d**) as seen in previous studies for both Lnc and the semi-synthetic derivative clindamycin (Cln) that differs only by a C7 steroinverted desoxychlorination of the amino sugar residue (Dunkle et al., 2010; Matzov et al., 2017; Tu et al., 2005). The observed orientations of the 23S rRNA nucleotides in the PTC around the Lnc binding site were identical to the ones observed in *S. aureus* 50S Lnc complex at 3.66 Å (Matzov et al., 2017). However, a slight rotation in the methylsulfanyl group of the galactopyranosyl ring as well as a different orientation of the pyrrolidinyl ring of Lnc were observed (**Sup.Fig. 10a-b**). Available structures of Cln

bound to the *E. coli* 70S (**Sup.Fig. 10e-f**) (Dunkle et al., 2010) and *H. marismortui* 50S (**Sup.Fig. 10c-d**) (Tu et al., 2005) ribosome at 3.3 and 3.0 Å, respectively, revealed a strong resemblance to the observed structure of Lnc bound to *L. monocytogenes* 70S in our structure and also differed from the *S. Aureus* complex, which may arise from limited resolution. Additionally, the structure of Cln bound to the 50S ribosomal subunit of *Deinococcus radiodurans* (**Sup.Fig. 10g-h**) (Schlunzen et al., 2001) at a resolution of 3.1 Å was reported to have a 180° degrees rotated propyl pyrrolidinyl tail compared to other Cln or the here reported Lnc structure. The high resolution of both our structures allowed the modelling of four putative water molecules ( $W_1$ - $W_4$ ) that seem to stabilize Lnc in the binding pocket by additional hydrogen bond interactions with 23S rRNA nucleotides (**Fig. 38e**). Waters  $W_1$  and  $W_2$  mediate two interactions with the C7-hydroxyl of Lnc with the N7 of A2536 (EcA2503) and N2 of G2094 (G2061) (**Fig. 38f**). Waters  $W_3$  and  $W_4$  mediate two additional possible interactions with the sulphur atom of the galactopyranosyl moiety with the N4 of C2644 (Ec2611) and the non-bridging oxygen with N1 of A2091 (EcA2058) (**Fig. 38g**). The importance of the water-mediated interactions are not known yet but it should be noted that the dimethylation of A2058 of the 23S rRNA nucleotide by Erm-methyltransferase displaces a water molecule essential for macrolide binding and confers resistance to that antibiotic class (Svetlov et al., 2021b).

#### **10.4.2. Cryo-EM structure and modelling of the GTPase HflXr in complex with *L. monocytogenes* 50S subunit**

The *L. monocytogenes* HflXr-50S complex for structural analysis was generated using an in vivo pulldown-approach within the aforementioned  $\Delta hflXr$  strains with a plasmid overexpressing a C-terminally FLAG<sub>3</sub>-tagged HflXr protein (method section **8.5.4**), as described for ARE-ABCF-ribosome complexes (Crowe-McAuliffe et al., 2022; Crowe-McAuliffe et al., 2021). *In silico* processing yielded a final reconstruction of Lmo-50S-HflXr-GDPNP with an average resolution of the masked reconstruction of 2.3 Å (**Fig. 19f, i-j**).



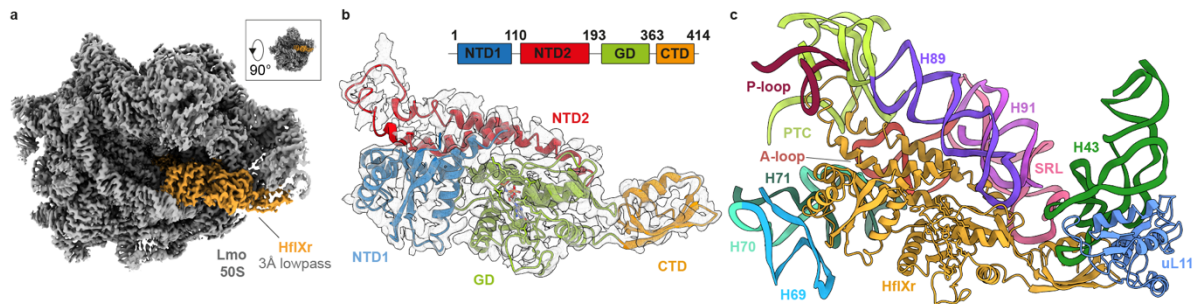


**Figure 39: Cryo-EM structure of HflXr bound to the *L. monocytogenes* large 50S subunit.** **a**, Cryo-EM density (lowpass filtered at 3 Å) of the 50S-HflXr-GDPNP complex with HflXr (orange) bound to the 50S subunit (grey). Inset shows relative orientation of **(a)** to the crown view. **b**, HflXr in isolated density (lowpass filtered at 3 Å, mesh) colored according to N-terminal subdomain I (NTD1, blue), N-terminal subdomain II (NTD2, red), G-domain (GD, green) and C-terminal domain (CTD, orange). **c**, Interactions of HflXr (orange) NTD1 with H69 (light blue), H70 (cyan), H71 (dark green), the  $\alpha$ -helices of NTD2 with H89 (dark purple) and H91 (light purple), NTD2-loop with the PTC (lime) and the CTD with uL11 (blue). Modified from (Koller et al., 2022b).

The core of the 50S subunit was well-resolved and well reflected by the estimated resolution, however, the HflXr density was less well-resolved and was low pass filtered at 3 Å for modelling (**Fig. 39a**). The overall density of the factor was good enough for a generous model based on the AlphaFold generated model for the two NTD subdomains, the central GTPase domain (GD) and the C-terminal domain (CTD), in contrast to this the loop of the N-terminal subdomain II formed by two  $\alpha$ -helices seemed to be flexible and was poorly ordered (**Fig. 39b**). As expected by the phylogenetic analysis and the high sequence conservation, the structure and overall conformation of the HflXr is very similar to the previously reported *E. coli* 50S-HflX-GDPNP complex (Zhang et al., 2015b) and the more recently reported structures of homologs of HflX, GTPBP6 bound to the large subunit biogenesis intermediate of human mitochondria (**Sup.Fig. 11**) (Hillen et al., 2021). As shown in **Fig. 39c**, the NTD subdomain I is in interaction distance with H69-H71, while the two  $\alpha$ -helices of NTD subdomain II run parallel to H89 and H91 with the loop region extending into the PTC, and the CTD close to the stalk base interacting with uL11.

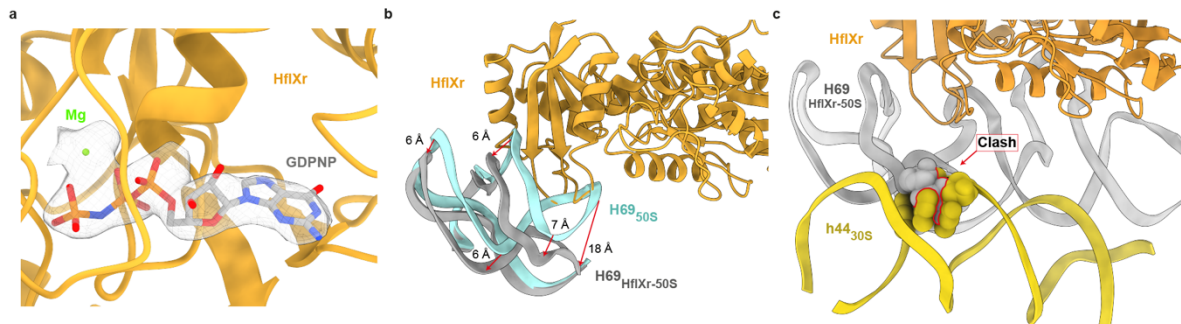


**Figure 40: Cryo-EM structure of HflXr bound to the *L. monocytogenes* large 50S subunit.** **a**, GDPNP (grey) in isolated density (mesh) with a putative magnesium-ion (green) coordinated in the GD binding pocket of HflXr (orange). **b**, HflXr (orange) binding to the ribosome induces a shift of H69 (grey) in comparison to the wildtype *L. monocytogenes* ribosome (cyan) by 6-7 Å. **c**, Shift of H69 (grey) induced by HflXr (orange) would sterically clash with h44 of the *L. monocytogenes* 30S subunit (yellow) (PDB ID 7NHN) (Crowe-McAuliffe et al., 2021). Modified from (Koller et al., 2022b).

Similar to HflX and different from translational GTPases, the nucleotide-binding pocket of the GTPase domain of HflXr is oriented away from the SRL (**Fig. 39c**). As expected, a density for a nucleotide triphosphate within the GTPase domain was observed and based on the preparation of the complex assigned to GDPNP in complex with a coordinated putative magnesium ion (**Fig. 40a**). Similar to the mode of action of HflX splitting the ribosome, we propose HflXr being able to induce a similar effect by causing a shift of H69 (**Fig. 40b**) that would be incompatible with a binding 30S to form a 70S ribosome by a steric clash with h44 of the SSU and inducing subunit splitting (**Fig. 40c**) (Zhang et al., 2015b).

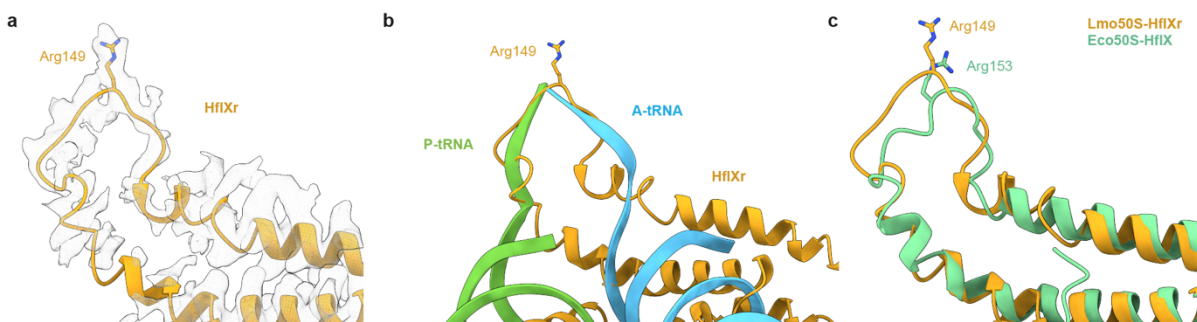


**Figure 41: Binding position of the HflXr NTD2 at the PTC overlaps with tRNAs.** **a**, Molecular model of Arg149 of the NTD2-loop of HflXr (orange) in isolated cryo-EM density (mesh). **b**, Superimposition of P-site and A-site tRNA (PDB ID 1VY4) of the pre-attack state with NTD2-loop of HflXr (Polikanov et al., 2014a). **c**, Superimposition of *E. coli* HflX (PDB ID 5ADY) with NTD2-loop of HflXr (Zhang et al., 2015b). Arg149 of HflXr reaches deeper into the PTC than Arg153 of HflX. Modified from (Koller et al., 2022b).

The poorly resolved loop region at the tip of the two  $\alpha$ -helices of the NTD subdomain II only allowed tracking of the backbone in this region (**Fig. 41a**). However, the position of both A- and P-site tRNAs CCA-end overlap significantly with the NTD2-loop at the PTC (**Fig. 41b**), which shows the incompatibility of HflXr binding to actively translating ribosomes, like observed for HflX (**Fig. 41c**) (Zhang et al., 2015b). Superimposition with HflX revealed that the HflXr NTD2-loop reaches deeper into the PTC, likely resulting from the longer loop with its additional two amino acids in *L. monocytogenes* HflXr compared to *E. coli* and *L. monocytogenes* HflX (Wilson et al., 2020). Due to the poorly ordered NTD2-loop finding the register of the amino acids sequence was challenging but a strong density was located at the tip of the NTD2-loop region which was assigned to the Arg149 that is equivalent to *E. coli* HflX Arg153 found in a similar location in the HflX-50S-GDPNP structure (Zhang et al., 2015b), however, lacking the two additional residues preceding the Arg less deep in the PTC (**Fig. 41c**).

### 10.4.3. Conformational changes in the PTC induced by HflXr is incompatible with drug binding

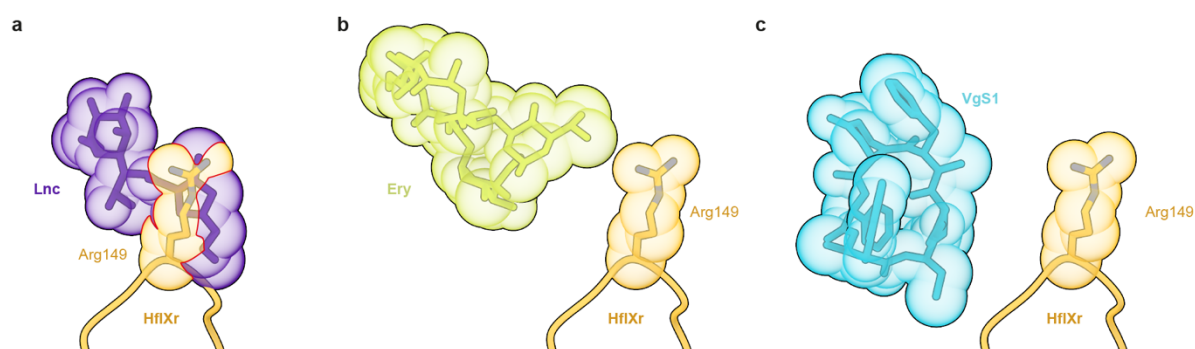


**Figure 42: Position of Arg149 of the NTD2-domain of HflXr at the PTC.** a-c, Arg149 of the NTD2-loop of HflXr (orange) in sphere representation superimposed with (a) lincomycin (Lnc, purple) bound to the *Staphylococcus aureus* ribosome (PDB ID 5HKV)(Matzov et al., 2017), with (b) erythromycin (Ery, yellow) bound to the *E. coli* ribosome (PDB ID 4V7U) (Dunkle et al., 2010) and with (c) virginiamycin S1 (VgS1, blue) on the *E. coli* ribosome (PDB ID 1YIT) (Tu et al., 2005). Steric clashing is indicated by red lines. Modified from (Koller et al., 2022b).

The HflXr-50S-GDPNP structure was aligned with the *S. aureus* Lnc structure to access the spatial relationship of PTC binding antibiotics and the NTD2-loop of HflXr, which revealed a significant overlap of the supposed position of the loops Arg149 and

the binding position of Lnc (**Fig. 42a**) (Matzov et al., 2017). As shown in our publication, the mutation of Arg149 to an Ala residue plays a critical role in conferring antibiotic resistance (Koller et al., 2022b). However, the Arg149 by itself is not able to confer resistance to macrolides, like Ery (**Fig. 42b**), nor streptogramin Bs, like virginiamycin S1 (**Fig. 42c**) as it does not overlap with these.

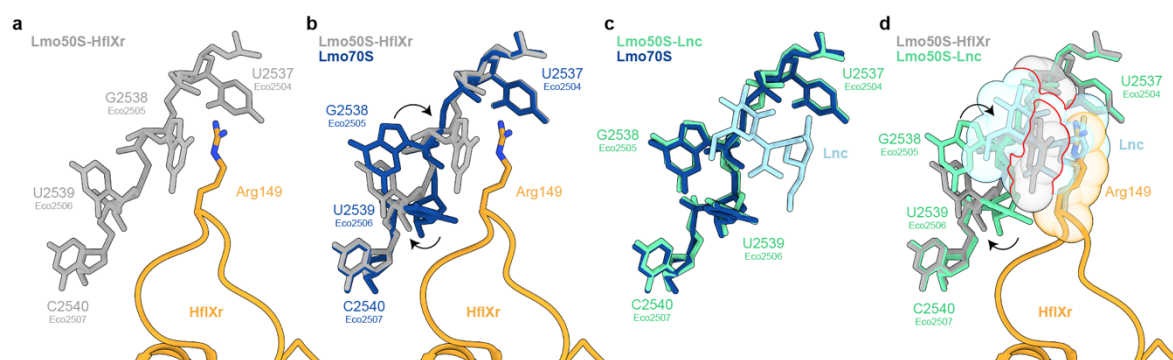


**Figure 43: Conformational changes induced by HflXr at the PTC are incompatible with lincomycin binding.** **a**, Arg149 of NTD2-loop of HflXr (orange) with surrounding *L. monocytogenes* 23S rRNA nucleotides (grey). **b**, Superimposition of (a) with 23S rRNA nucleotides (dark blue) of the vacant *L. monocytogenes* ribosome. Conformational changes induced by HflXr are indicated by black arrows. **c**, Superimposition of the 23S rRNA nucleotides (dark blue) of the vacant *L. monocytogenes* ribosome with lincomycin (Lnc, light blue) bound to the *L. monocytogenes* ribosome with 23S rRNA nucleotides (teal). **d**, Superimposition of Lnc (light blue) bound to the *L. monocytogenes* ribosome with 23S rRNA nucleotides (teal) with (a) Arg149 of NTD2-loop of HflXr and G2538 (EcG2505) represented as spheres and steric clashes indicated by red lines and conformational changes by black arrows. Modified from (Koller et al., 2022b).

The superimposition of the HflXr-50S-GDPNP complex (**Fig. 43a** and **Sup.Fig. 13a-b**) with a vacant *L. monocytogenes* 70S ribosome (**Fig. 43b** and **Sup.Fig. 13c-d**) revealed conformational changes of individual nucleotides within the PTC following HflXr binding (Koller et al., 2022b). 23S rRNA nucleotides U2539 (EcU2506) seemed to have shifted away from the NTD2-loop of HflXr to avoid clashing while rotating (**Fig. 43a-b** and **Sup.Fig. 13c-d**). Undergoing a dramatic shift of up to 10 Å, G2538 (EcG2505) has to avoid clashing by the shifted U2539 (EcU2506) (**Fig. 43a-b** and **Sup.Fig. 13c-d**). A shift that might not directly correlate with HflXr binding but was observed, is a change in position of A2095 (EcA2062), which was previously reported in structures bearing peptidyl-tRNA mimics within the PTC (**Sup.Fig. 14e-f**) (Syroegin et al., 2022b). Due to the poorly ordered loop region, and therefore resulting less well-resolved density a molecular description of the direct interactions of the loop with the

rotated A2095 (EcA2062) is not possible, but it is suggested to stabilize the loop. Directly comparing the vacant *L. monocytogenes* 70S ribosomes PTC with the Lnc-bound structure discussed in a previous chapter, it was observed that binding of Lnc did not induce conformational changes to the rRNA nucleotides (**Fig. 43c** and **Sup.Fig. 13e-f**) (Koller et al., 2022b). Superimposition of the HflXr-50S-GDPNP with antibiotic bound ribosome structures strongly suggests the steric overlap of the shifted G2538 (EcG2505) with the macrolide antibiotics Ery and azithromycin (Azy), the pleuromutilins tiamulin (Tia) and retapamulin (Ret), as well as the streptogramin A virginiamycin M1 (VgM) (**Sup.Fig. 14a-d, f-h**) consistent with our reported MICs (Koller et al., 2022b). However, the steric overlap of the shifted G2538 (EcG2505) would not directly occur with streptogramin B antibiotics, like virginiamycin S1 (VgS), but the A2095 (EcA2062) which usually forms stacking interactions with the aromatic C18 moiety is stabilized in the rotated conformation by HflXr disturbing this interaction (**Sup.Fig. 12i** and **Sup.Fig. 14g-h**) (Li et al., 2020a; Tu et al., 2005). The binding sites of oxazolidinone antibiotic linezolid and phenicol antibiotic chloramphenicol are strongly overlapping with the shifted position of G2538 (EcG2505) (**Sup.Fig. 12e,i**), however, the *in vivo* assays from our publication suggest HflXr to not confer resistance to these antibiotic classes (Koller et al., 2022b). Superimposition of the HflXr structure with the *L. monocytogenes* 70S-Lnc complex shows an incompatibility of Lnc binding to the ribosome upon HflXr binding with G2538 (EcG2505) in its shifted conformation suggesting HflXr to confer resistance to Lnc by perturbing the drug binding site by altering the PTC conformations (**Fig. 43d** and **Sup.Fig. 13g-h**).

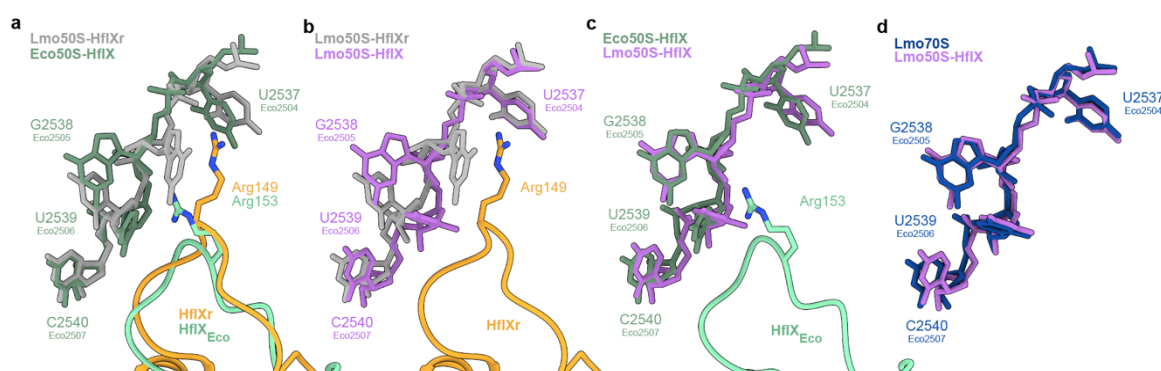


**Figure 44: Conformational changes induced by HflXr at the PTC compared to HflX.** a-b, Superimposition of Arg149 of NTD2-loop of HflXr (orange) bound to the *L. monocytogenes* ribosome with 23S rRNA nucleotides (grey) with (a) Arg153 of NTD2-loop of HflX (teal) bound to the *E. coli* ribosome with 23S rRNA nucleotides (dark teal) (PDB ID 5ADY) (Zhang et al., 2015b) or with (b) 23S rRNA nucleotides (purple) from the vacant *L. monocytogenes*

70S refined into the HflX-50S-GDPNP complex. **c**, Arg153 of NTD2-loop of HflX (teal) bound to the *E. coli* ribosome with 23S rRNA nucleotides (dark teal) (PDB ID 5ADY) superimposed with 23S rRNA nucleotides (purple) from the vacant *L. monocytogenes* 70S refined into the *L. monocytogenes* HflX-50S-GDPNP complex (Zhang et al., 2015b). **d**, Superimposition of 23S rRNA nucleotides from the vacant *L. monocytogenes* ribosome (dark blue) with 23S rRNA nucleotides (purple) from the vacant *L. monocytogenes* 70S refined into the HflX-50S-GDPNP complex. Modified from (Koller et al., 2022b).

These conformational changes are not observed in *E. coli* HflX structure (Zhang et al., 2015b) and support the idea of a specific mode for antibiotic-resistance protein HflXr in difference to the non-resistance HflX protein (**Fig. 44a** and **Sup.Fig. 14a-b**). An additional cryo-EM data collection was prepared on a *L. monocytogenes* HflX-50S-GDPNP complex, that was prepared similarly to the HflXr-50S-GDPNP complex, in order to rule out species specific differences that may arise from the *E. coli* HflX structure. Similar to the HflXr data processing, the majority of particles picked from the 4,480 micrographs contained density for HflX in the A and P-site of the 50S subunit (**Fig. 20**). *In silico* processing yielded a final reconstruction with an average resolution of the masked reconstruction of 2.6 Å (**Fig. 20d**). However, the density for the factor was very poorly resolved and a subsorting approach with partial signal subtraction was used (**Fig. 20e**) to bring a class with high resolution HflX density and with 31.5% of particles (76,519 particles) to a final average resolution of 2.8 Å (**Fig. 20f-h**). The map exhibited strong orientation bias, presumably originating from preferred orientation of the 50S particles on the cryo-grids, that did not allow proper refinement of a molecular model (**Fig. 20k**). A rigid body fit of the molecular model of the vacant *L. monocytogenes* 70S ribosome and small structural adjustments allowed to access the conformational state of the PTC nucleotides in the HflX-50S-GDPNP complex (**Sup.Fig. 14c-d**) (Koller et al., 2022b). As expected, no conformational changes were observed upon binding of HflX to the ribosome (**Fig. 44b** and **Sup.Fig. 14c-d**), identical to what was observed in the *E. coli* HflX complex (**Fig. 44c**) and in the vacant *L. monocytogenes* 70S structure (**Fig. 44d**).

## 11. Discussion

### 11.1. Mechanism of action of the antimicrobial peptide MyxA and MyxB.

The combination of cryo-EM structures of both MyxA on the vacant *E. coli* 50S subunit (**Fig. 21a**) and MyxB on the translating *E. coli* 70S ribosome (**Fig. 23a**) with DMS protection assays (**Fig. 22a**), *in vitro* translation inhibition assays (**Fig. 22b**), and resistance mutations in *Mycobacterium tuberculosis* (**Sup.Fig. 3**) by our collaborators lead us to determine the ribosome as molecular target of the antimicrobial class of the myxovalgins. Despite the myxovalgins showing a very similar binding site in the ribosomal NPET (**Fig. 21a** and **Fig. 22a-g**) to other antimicrobial peptides, like Api137 (**Fig. 45a**) (Florin et al., 2017), Bac7 (**Fig. 45b**) (Gagnon et al., 2016; Seefeldt et al., 2016), klebsazolicin (Klb, **Fig. 45c**) (Metevlev et al., 2017) and phazolicin (Pha, **Fig. 45d**) (Travin et al., 2019), the binding mode, conformation and interactions with the tunnel are significantly different.

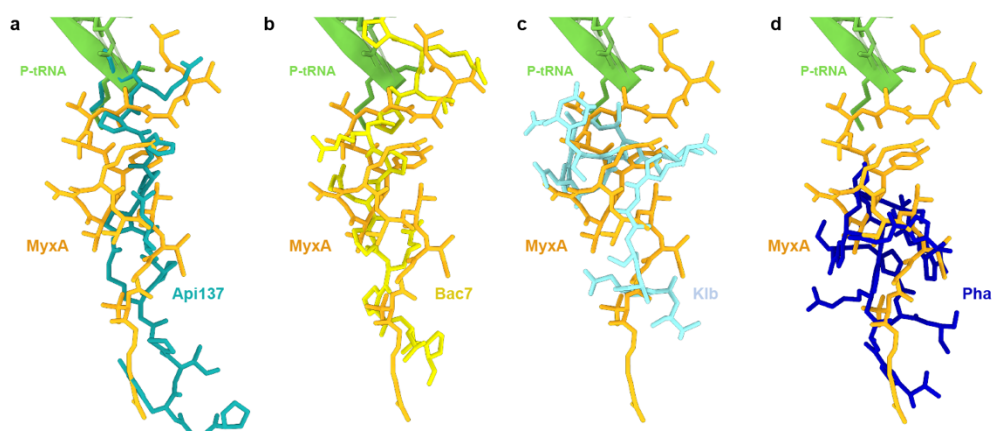


**Figure 45: Antimicrobial peptides binding to the NPET.** a-d, MyxA (orange) bound to the vacant *E. coli* 50S subunit with P-tRNA (light green, PDB ID 1VY4) (Polikanov et al., 2014a) superimposed with PrAMPs (a) Api137 (dark teal, PDB ID 5O2R) (Florin et al., 2017) and (b) Bac7 (yellow, PDB ID 5HAU) (Gagnon et al., 2016) and with post-translationally modified antimicrobial peptides (c) klebsazolicin (Klb, light blue, PDB ID 5W4K) (Metevlev et al., 2017) and (d) phazolicin (Pha, dark blue, PDB ID 6U48) (Travin et al., 2019). Alignments are based on the 23S rRNA.

Unlike from Drosocin, which has been discussed in detail in results section **10.2** and Api137, neither MyxA nor MyxB require an additional factor, such as a release factor

to inhibit translation (Florin et al., 2017; Graf et al., 2018). In contrast to both Klb and Pha which are ribosome-synthesized post-translationally modified peptides (Metelev et al., 2017; Travin et al., 2019), myxovalgins cannot be produced by the ribosome due to the presence of D- and modified-amino acids that originate from an extensive biosynthetic cluster that has been investigated by our collaborators (Koller et al., 2022a). Studying this biosynthetic cluster together with our structural analysis of the high resolution vacant MyxA-50S-complex (**Fig. 21a-c**) also revealed the wrong annotation of two stereocenters in MyxA/B, namely D-Val7 (**Fig. 21e**) and L-Val10 (**Fig. 21f**) (Steinmetz et al., 1987).

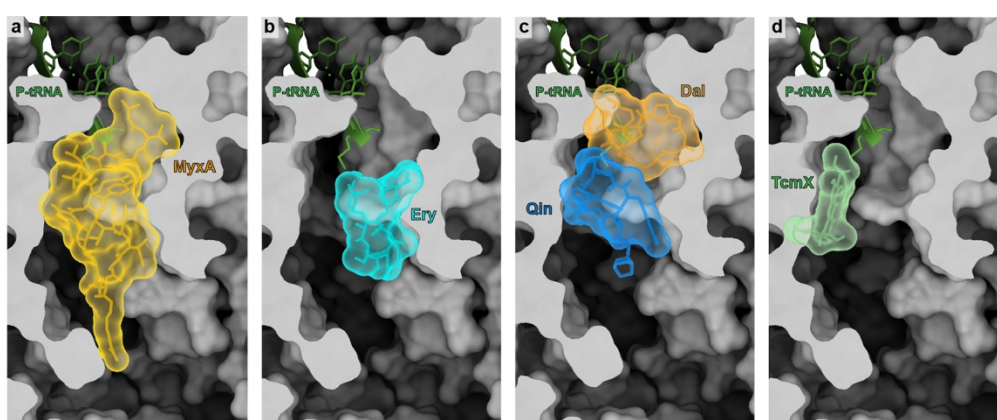


**Figure 46: Tunnel binding antibiotics occluding the NPET.** a-d, NPET shown as surface (grey) with P-tRNA (light green, PDB ID 1VY4) (Polikanov et al., 2014a) and (a) MyxA (orange, surface), (b) erythromycin (Ery, cyan, PDB ID 4V7U) (Dunkle et al., 2010), (c) dalfopristin (Dal, orange) and quinupristin (Qin, blue, PDB ID 4U26) (Noeske et al., 2014) and (d) tetracenomycin X (TcmX, green, PDB ID 6Y69) (Osterman et al., 2020). Alignments are based on the 23S rRNA.

The myxovalgins bind the NPET in a very compacted conformation (**Fig. 46a**) that completely occludes the tunnel, unlike Ery or tetracenomycin X (**Fig. 46b,d**) (Dunkle et al., 2010; Leroy et al., 2022; Osterman et al., 2020). The blockage of the tunnel by MyxA is very similar to the one by the synergistic streptogramin antibiotics dalfopristin and quinupristin (**Fig. 46c**) (Noeske et al., 2014).



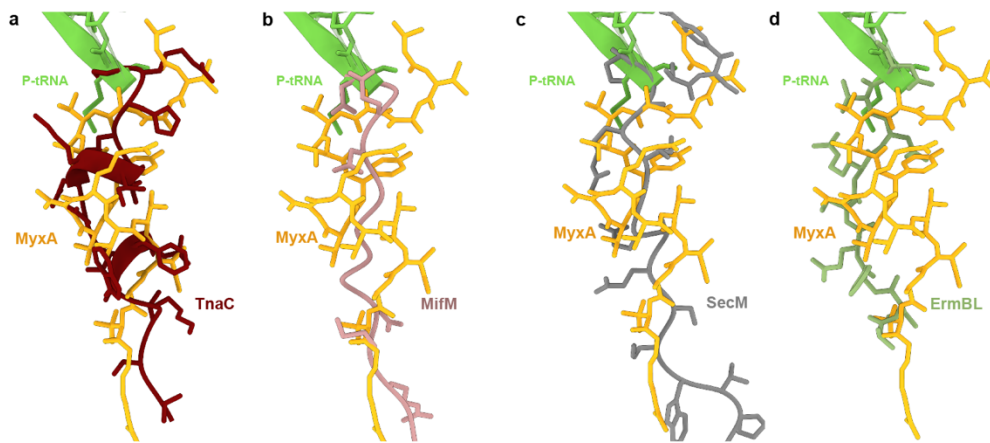


**Figure 47:** a-d, MyxA (orange) bound to the vacant *E. coli* 50S subunit with P-tRNA (light green, PDB ID 1VY4) (Polikanov et al., 2014a) superimposed with nascent polypeptide chain stallers (a) TnaC (dark red, PDB ID7O19) (van der Stel et al., 2021), (b) MifM (pink, PDB ID 3J9W) (Sohmen et al., 2015), (c) SecM (grey, PDB ID 3JBV)(Zhang et al., 2015a) and (d) ErmBL (green, PDB ID 5JU8) (Arenz et al., 2016a). Alignments are based on the 23S rRNA.

MyxA stretches similarly deep into the tunnel as the nascent chain stallers TnaC, MifM, SecM and ErmBL. The toeprinting assay (**Fig. 47c-d**) revealed that MyxB stalls ribosomes during translation initiation and together with the cryo-EM structure of the MyxB-70S-complex of a translating ribosome confirmed the presence of an accommodated initiator fMet-tRNA<sup>fMet</sup> in the P-site of the ribosome (**Fig. 47a** and **Sup.Fig. 4**). However, the CCA-end was displaced by the N-terminal hydrophobic IB moiety of MyxB and shifted by 1.5 Å compared to a canonical initiator tRNA. Both myxovalgins tested in our cryo-EM studies showed significant overlap with pre-attack state P-site and A-site tRNAs (**Fig. 24c-d**). This supports the previous findings of myxovalgins being able to partially allow tRNA binding in the P-site but not accommodating tRNAs in the A-site (Irschik and Reichenbach, 1985). Based on our findings and results presented in this thesis, we propose a mechanism of action for the myxovalgins shown in **Fig. 48**.

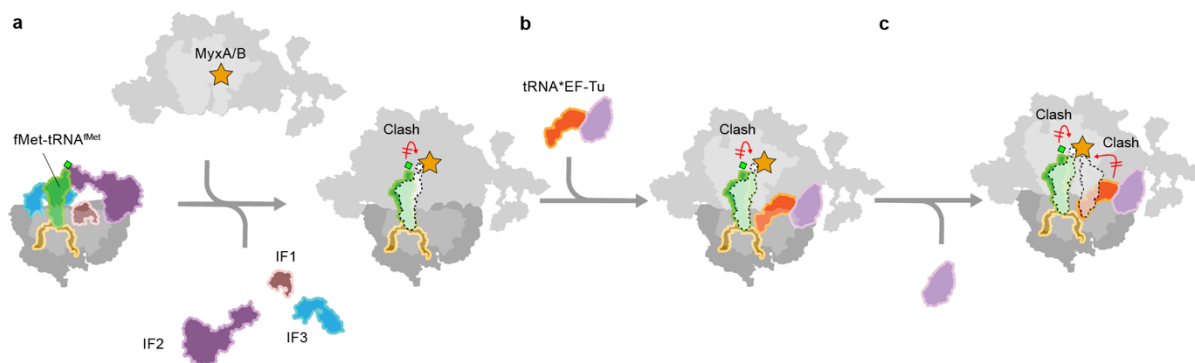


**Figure 48: Mechanism of action of myxovalargin to inhibit translation initiation.** Scheme to illustrate the proposed mechanism of myxovalargin inhibiting translation initiation by binding to the ribosomal NPET. **a**, Subunit joining of the 30S initiation complex, with fMet-tRNA<sup>fMet</sup> (light green), initiation factors 1 (IF1, brown), IF2 (purple), IF3 (blue) and mRNA (yellow) with the large 50S subunit (grey) with MyxA/B (orange) in the NPET, upon release of the IFs. The hydrophobic N-terminal moieties of MyxA/B interfere with the proper placement of the CCA-end of the initiator tRNA. **b**, Ternary complex (EF-Tu, purple) delivers an amino acyl-tRNA (orange) to the A-site. **c**, Accommodation of the delivered amino acyl-tRNA in the PTC is sterically hindered by MyxA/B, arresting translation after initiation.

Prior to formation of the 70S-initiation complex (70S-IC), MyxA/B can prime the 50S subunit by binding in the NPET (**Fig. 48a**). Upon formation of the 70S-IC the fMet-tRNA<sup>fMet</sup> would sterically clash with MyxA/B leading to the shift of both the CCA-end and the fMet-moiety preventing full accommodation. The ternary EF-Tu\*aa-tRNA\*GTP complex can deliver an amino acyl-tRNA to the A-site. However, the accommodation of the acceptor-arm of the A-tRNA at the PTC is not possible and ultimately traps the ribosome during the late steps of translation initiation (**Fig. 48b-c**). Besides the potential of myxovalargins to inhibit translation initiation, the unspecific membrane effect and resulting toxicity against eukaryotic cells has to be addressed (Irschik and Reichenbach, 1985). From the chemical structure the length and large number of hydrophobic sidechains could explain why myxovalargins supposedly intercalate into membranes. Removing D-Ala13, D-β-OH-Val14 and the AG moiety on the C-terminus of MyxA would hypothetically not interfere with the binding mode of the myxovalargins but could reduce the length of the molecule as most of the interactions are facilitated around the D-β-Tyr6 (**Fig. 22d**) and D-Arg9 (**Fig. 22f-g**), with the activity coming mostly from the N-terminus sterically clashing with both canonical P- and A-site tRNAs (**Fig. 24c-d**). Altering the hydrophobic chemical nature of myxovalargins is more challenging than simply removing hydrophobic sidechains and needs both extensive chemical synthesis and structural analysis followed by an array of additional *in vivo*

and *in vitro* assays. Introduction of hydrophilic sidechains would potentially reduce specificity in the NPET and open a variety of other binding sites. A much more promising direction would be a fully synthetic route as previously shown for iboxamycin (Mitcheltree et al., 2021), by using the structure-guided insights provided by our cryo-EM maps to extensively redesign the chemical structure of myxovalargins but keeping their binding mode and therefore overcoming the unspecific membrane-effect and keeping the antimicrobial activity.

## 11.2. Proline-rich antimicrobial peptide drosocin and importance of O-glycosylation for translation inhibition.

Based on the structural elucidation of Dro1 on the ribosome and supported by *in vitro* translation and toeprinting assays from our group we propose a mechanism of action of drosocin, highlighting the importance of the O-glycosylation on the Thr11 residue (Fig. 49).

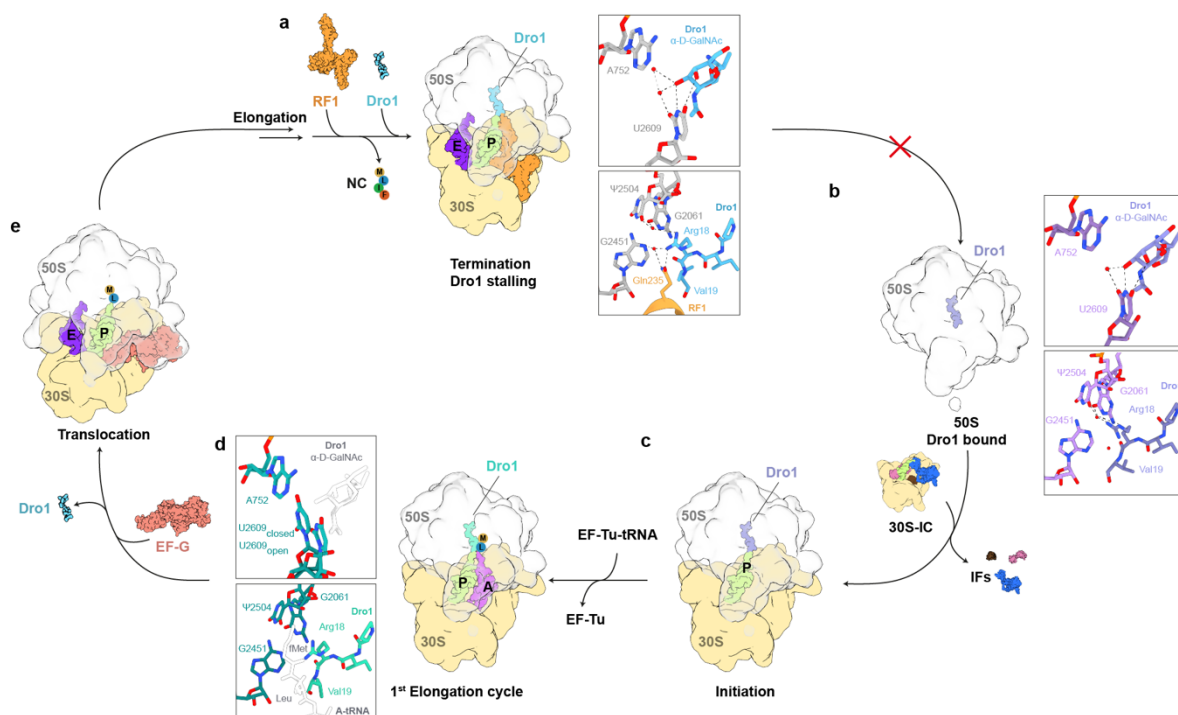


**Figure 49: Scheme of the mechanism of action of O-glycosylated Dro1 inhibition during translation. a,** Stop codon recognition by release factor RF1/2 (orange) which catalyzes the hydrolysis and subsequent release of the nascent chain (NC) from the peptidyl-tRNA (lime). Dro1 (light blue) binds within the NPET, inducing the open conformation of U2609 (grey) by stabilizing water-mediated and direct interactions with the  $\alpha$ -D-GalNAc on Thr11 of Dro1. Arg18 of Dro1 forms interactions with Gln235 of the conserved GGQ motif of RF1/2 (orange) and surrounding 23S rRNA (grey), stabilizing the RF1/2 on the ribosome and preventing subsequent ribosome recycling and re-initiation. **b,** Dro1 (purple) binds the free 50S subunit (grey) inducing the open conformation of U2609 (grey) by stabilizing water-mediated and direct interactions with the  $\alpha$ -D-GalNAc on Thr11 of Dro1, however, Arg18 is not fully stabilized in absence of Gln235 of RF1/2 but forms both direct and water-mediated interactions with 23S rRNA nucleotides (grey). **c,** Dro1 does not interfere with formation of translation initiation complexes, despite the overlap of the C-terminus of Dro1 (purple) with the fMet moiety of the P-site tRNA. **d,** Peptide bond formation is not interfered with by Dro1 presence but translocation of the dipeptidyl-tRNA from the A-site (purple) into the P-site (lime) is blocked. Both conformations of U2609 have been observed (dark teal) suggesting the dipeptidyl moiety (white) on the A-site destabilizing the C-terminus of Dro1 in the PTC. **e,** For subsequent translocation and elongation cycles the Dro1 (light blue) has to dissociate from the NPET of the ribosome until a stop codon is recognized in the A-site.

Drosocin inhibits translation termination in similar fashion as Api137, by trapping RFs on the ribosome following nascent polypeptide chain release and stabilizing the Gln235 of the conserved GGQ motif of the RF1 with direct and water-mediated interactions with Arg18 of the C-terminus of Dro1 (**Fig. 31a-c**) (Chan et al., 2020; Florin et al., 2017; Graf et al., 2018). A very important difference between Api137 and Dro1 is the O-glycosylation of Thr11 that from structural elucidation establishes a network of direct and water-mediated hydrogen bond interactions with U2609 of the 23S rRNA (**Fig. 49a**). These interactions support the previous findings that native modified drosocin has generally higher antimicrobial activity compared to unmodified or mutated variants (Ahn et al., 2011a; Ahn et al., 2011b; Gobbo et al., 2002; Lele et al., 2015b; Marcaurelle et al., 1998; Otvos et al., 2000; Rodriguez et al., 1997; Talat et al., 2011). Additionally, the shift of U2609 induced by the sugar modification breaking the canonical U2609-A752 base-pair underlines the importance of the sugar.

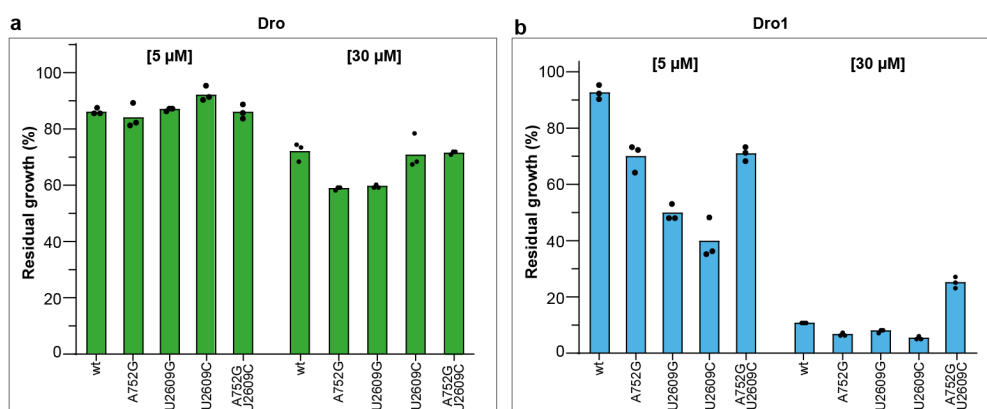


**Figure 50: Nature of the A752-U2609 base-pair impacts binding ability of the O-glycosylated Dro1.** a-b, *In vivo* assays of Squires strains SQ171 wildtype and mutants A752G, U2609G, U2609C and the double mutant A752G and U2609C in presence of 5 μM or 30 μM of Dro (a, green) without the Thr11 O-glycosylation and Dro1 (b, blue) with α-D-GalNAc modification on Thr11. Assays were performed in three biological replicates indicated as dots.

Additional *in vivo* assays on single and double mutants of U2609 and A752 were performed by Martino Morici of our group that should help understanding the role of the sugar modification. Mutant ribosomes carrying A752G, U2609G, U2609C or a double mutation U2609C-A752G mutations were tested in presence of 5 μM or 30 μM modified Dro1 and unmodified Dro (**Fig. 50**). Collectively these results showed that strains bearing a single mutation are more susceptible to Dro1 but not to Dro at 5 μM

with lower effects on higher concentrations of the peptides. The double mutation was more tolerant to higher doses of Dro1 underlining the breaking of the U2609-A752 base-pair as a key feature of O-glycosylated Dro1 mode of action. The same base-pair has been shown to be important in the binding activity of the ketolide Tel (Dunkle et al., 2010; Svetlov et al., 2020) and especially for its bactericidal activity. It is not known to be broken in *E. coli* but has been observed in an unpaired state in other bacterial ribosomes, like *Mycobacterium tuberculosis* (Yang et al., 2017), suggesting these ribosomes to be more susceptible to the O-glycosylated Dro1. Two more drosocin bound ribosome states, the vacant 50S and an elongating ribosome with A- and P-site tRNAs, were observed in the data collection. Given that the drosocin interactions formed in the NPET of both the vacant 50S and the terminating complex are identical, it implies that drosocin can potentially interact with the recycled 50S subunit following subunit splitting after recycling. As expected from the terminating complex the  $\alpha$ -D-GalNAc modification on Thr11 of Dro1 inserted in between the base-pair of U2609 and A752, inducing the shift of U2609 and stabilizing a potential water-mediated hydrogen bond interaction (**Fig. 49b**). In the absence of the Gln235 of RF1 the C-terminus of the drosocin on the vacant 50S is less well-resolved due to flexibility. A similar pattern was observed for Api137 being stabilized by RF1 on 70S ribosomes when compared to vacant ribosomes (Florin et al., 2017). The lack of initiation complexes within our data collection suggests that the initiator fMet-tRNA can actively compete with the C-terminus of drosocin and adopt unimpeded its canonical position in the P-site of the PTC (**Fig. 49c**). The presence of the major population of elongating post-peptide bond formation pre-translocation ribosomes, containing deacylated P-site tRNA<sup>fMet</sup> and a dipeptide fMet-Leu-tRNA<sup>Leu</sup> in the A-site, suggest that drosocin inhibits the first translocation step and blocks the movement of the peptidyl-tRNA from the A-site to the P-site of the PTC (**Fig. 49d**). The toeprinting assays support the hypothesis that this state is likely temporary as ribosomes are observed to translate the entire ORF and finally become trapped on the stop codon during termination (**Fig. 25b-d**). Drosocin is unstably bound in the elongating step and poorly resolved leading to the presence of both the closed (base-paired) and open (unpaired) conformations of the U2609-A752 base-pair and a poor density of the  $\alpha$ -D-GalNAc modification of Dro1 (**Fig. 49d** and **Sup.Fig. 7c**). In our proposed model the translocation event is triggered by the steric interference of the dipeptide fMet-Leu-tRNA<sup>Leu</sup> and the drosocin

Arg18 and Val19 at the P-site of the PTC, forcing a drosocin dissociation and subsequent elongation steps to occur (**Fig. 49e**). The extending nascent polypeptide chain interferes with a rebinding of drosocin to the NPET and only rebinds following the recognition of the stop codon and RF induced hydrolysis and dissociation of the nascent chain (**Fig. 49a**). While drosocin and apidaecin show a strong similarity in their mechanism of action to inhibit translation by trapping the RFs on the ribosome, the interactions of both peptides and binding mode within the NPET of the ribosome are completely distinct. Especially the O-glycosylation of the Thr11 plays a critical role for drosocin to exhibit its antimicrobial potential but is completely absent in apidaecin. As described earlier, other AMPs are glycosylated in a similar fashion, namely dipterocin, formaecins, lebocin and pyrrococin, with the latter being the most similar bearing the identical  $\alpha$ -D-GalNAc modification on Thr11 and was also found to have minor forms with naturally occurring disaccharide modifications (Bulet et al., 1999; Cociancich et al., 1994). Structures of the unmodified pyrrococin revealed an inverted orientation in the NPET compared to drosocin in our structure, however, the superimposition highlights the close proximity of both modified Thr11 (Gagnon et al., 2016; Seefeldt et al., 2016), allowing the assumption that glycosylated pyrrococin could establish analogous interactions as observed in our structures. This shines a light on how eukaryotic and prokaryotic organisms through convergent evolution can develop very similar techniques to target bacterial infections by inhibiting translation efficiently that are facilitated by unique scaffolds of antimicrobial (and proline rich) peptides that ultimately lead to the same result.

### 11.3. Context-specificity of macrolide antibiotics on eukaryotic translation

The cryo-EM structure of Tel on the G2400A (EcA2058) mutant *S. cerevisiae* ribosome reveals an identical binding mode of macrolides, more specific ketolides on eukaryotic ribosomes (**Fig. 34a-d** and **Sup.Fig. 9**) and provides an insight in the conservation of the ribosomal core, mainly the PTC and NPET between prokaryotes and eukaryotes in the context of macrolide binding. Macrolides have been shown to induce stalling in bacteria in a context-specific manner previously (Almutairi et al., 2017; Davis et al., 2014; Kannan et al., 2014; Sothiselvam et al., 2016). This functionality is utilized by Erm-resistance mechanisms to induce methylation of 23S rRNA nucleotide A2058 in response to macrolide binding (Arenz et al., 2016a; Arenz et al., 2014b; Beckert et al., 2021) and has been shown to interfere with coordination of a water molecule that was found to be essential for macrolide binding (Svetlov et al., 2021b). The same water-mediated binding-mode was found in the G2400A (EcA2058) mutant (**Fig. 35a**) and revealed the base of the species-specificity as the G2400 (EcA2058) in wildtype *S. cerevisiae* 25S rRNA coordinates the water in a different orientation and perturbs the interaction with the macrolide (**Fig. 35b**). Additionally, the N2 of G2400 (EcA2058) potentially clashes with the bound macrolide (**Fig. 35b**). In other eukaryotic ribosomes, like the 80S ribosome of *Oryctolagus cuniculus* (**Sup.Fig. 2d**) (Chandrasekaran et al., 2019), the 28S rRNA harbors G3904 (EcA2058) in the same position as the wildtype *S. cerevisiae* and based on our structural findings a reasoning behind certain antibiotics not being able to bind properly in the NPET can therefore be extended to other eukaryotic ribosomes. To support the structural findings and test context-specificity for macrolides on translation inhibition in eukaryotes our collaborators did Ribo-seq (Ingolia et al., 2009) to find specific motifs that stalling preferentially occurred on (Svetlov et al., 2021a). This revealed the classic +X+ motif to interfere with translation (Almutairi et al., 2017; Davis et al., 2014; Kannan et al., 2014; Sothiselvam et al., 2016), but additionally revealed PDX motif that also seemed to be problematic in yeast with Tel (Svetlov et al., 2021a). The findings support that eukaryotic translation gets interrupted during peptide bond formation between the specific donor and acceptor substrates and not by discrimination of the identity of the nascent polypeptide. *In vitro* assays performed on these arrest motifs with a variety of



macrolides found a strong impact on the chemical structure of the used macrolide, especially in ketolides on the efficiency of the inhibition (Svetlov et al., 2021a). Additionally, both of the macrolide arrest motifs were also found in cells depleted of eukaryotic initiation factor 5A (eIF5A) (Pelechano and Alepuz, 2017; Schuller et al., 2017), which supports the ribosome in polymerizing problematic sequences, like polyproline stretches in yeast (Gutierrez et al., 2013; Pelechano and Alepuz, 2017; Schuller et al., 2017), suggesting that macrolides like Tel intensify sequences that are more difficult to be polymerized in the first place (Svetlov et al., 2021a). So far only PF846 has been identified as a compound to be highly selective on protein synthesis in eukaryotic ribosomes (Li et al., 2020b; Li et al., 2019; Lintner et al., 2017), and superimposition reveals a partially overlapping binding site with Tel in the NPET (**Fig. 51a-d**).

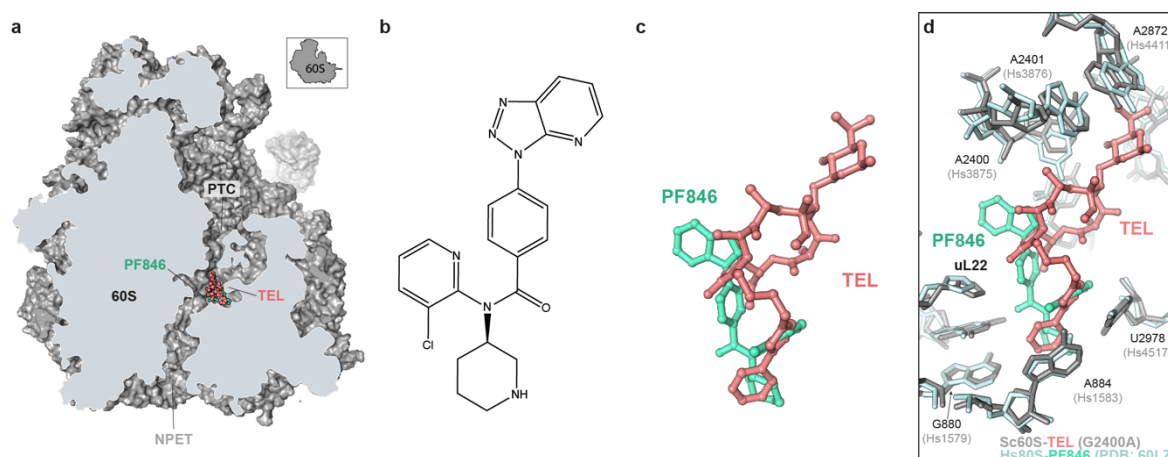


**Figure 51: PF846 binding site compared to Tel in the G2400A mutant Tel-60S-complex.** **a**, Transverse section of the G2400A mutant 60S-Tel-complex with Tel (salmon) bound in the NPET superimposed with Pf846 (turquoise) bound to the human 80S (PDB ID 6OLZ) (Li et al., 2019). **b**, Chemical structure of PF846. **c**, Tel (salmon) and PF846 (turquoise, PDB ID 6OLZ) molecular models superimposed based on 25S and 28S rRNA (Li et al., 2019). **d**, Tel (salmon) with surrounding 25S rRNA nucleotides (grey) in the G2400A mutant Tel-60S-complex superimposed with PF846 (turquoise) with 28S rRNA nucleotides (light blue) of the PF846-80S-complex (Li et al., 2019). Modified from (Svetlov et al., 2021a).

The specificity and mode of action of PF846 is significantly different from Tel, by being less dependent on the PTC substrates by allowing a variety of interactions in the NPET to induce translational slow down on several consecutive mRNA codons inhibiting translation elongation during translocation and termination (Li et al., 2020b; Li et al., 2019; Lintner et al., 2017), while macrolides induce translation inhibition at specific

mRNA motifs (Almutairi et al., 2017; Arenz et al., 2016a; Arenz et al., 2014b; Beckert et al., 2021; Davis et al., 2014; Kannan et al., 2014; Sothiselvam et al., 2016). Despite the differences in mechanism of action the placement in the NPET in overlapping sites and both achieving context-specificity is promising for structure-based drug-design. Together with the findings of drugs like tetracenomycin X that was found to bind both bacterial and eukaryotic ribosomes on the opposite side of the NPET compared to the macrolides (**Fig. 46b,d**) and a sequence-specific inhibition of bacterial translation (Leroy et al., 2022; Osterman et al., 2020), the NPET in close proximity to the PTC emerges as the best suited target for structure-based drug design of compounds with high context-specificity targeting expression of unwanted and highly problematic nascent chains and proteins in human diseases like cancer. Structural alteration and fully synthetic routes for macrolides have been achieved previously (Seiple et al., 2016) and together with our findings a pathway for targeting wildtype eukaryotic ribosomes lies at hand.

## 11.4. Target protection by GTPase HflXr

The direct mechanism of how HflXr utilizes splitting of ribosomes and recycling them for subsequent rounds of translation while conferring resistance to lincomycin and erythromycin has not been conclusively demonstrated (Duval et al., 2018). The structure in this thesis shows that HflXr can stably bind to the 50S ribosomal subunit in presence of GDPNP (**Fig. 19**) and as shown in our publication also with the natural unmodified GTP (Koller et al., 2022b). Similar to the previously reported structure of *E. coli* HflX (Zhang et al., 2015b) the *L. monocytogenes* HflXr binds to the LSU and occupies the A- and P-site overlapping with the binding sites of the tRNAs (**Fig. 41b-c**). Different from HflX, the NTD2-loop of HflXr, which includes an additional two amino acids, penetrates deeper into the PTC and was observed to induce conformational changes to 23S rRNA nucleotides G2538 (EcG2505), U2539 (EcU2506) and A2095 (EcA2062) which are incompatible with antibiotic binding (**Fig. 43a-d**).

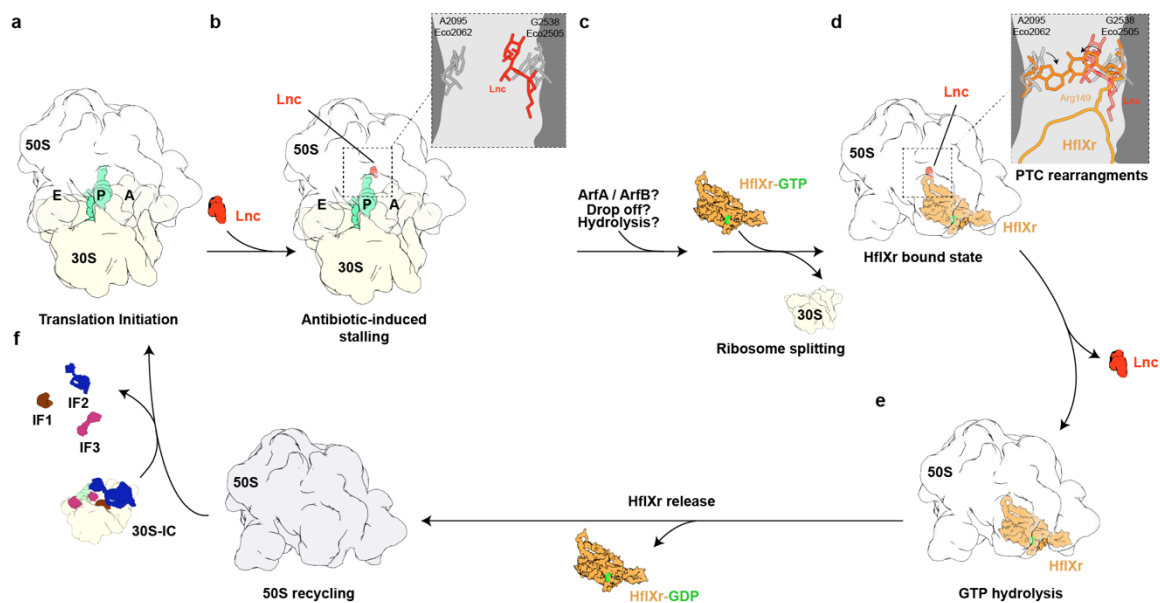


**Figure 52:** Scheme for the proposed mechanism of action of HflXr. **a**, A 70S ribosome during translation initiation (**a**) is stalled by binding of an antibiotic (**b**), like lincomycin (Lnc, red) with the canonical position of 23S rRNA nucleotides G2538 (EcG2505) and A2095 (EcA2062). **c**, For HflXr-GTP to bind the 70S ribosome the peptidyl-tRNA has to leave the ribosome through a currently unknown mechanism (ArfA/ArfB, tRNA drop off or hydrolysis), followed by ribosome splitting induced by HflXr-GTP and subsequent subunit dissociation. **d**, The loop of the HflXr NTD2-loop induces rearrangement of 23S rRNA nucleotides G2538 (EcG2505) and A2095 (EcA2062) in the PTC, leading to antibiotic dissociation. **e**, HflXr-GDP is released after GTP hydrolysis, resulting in a free 50S subunit (**f**) that is available for re-initiation (**a**). Modified from (Koller et al., 2022b).

HflXr is proposed by us to be a type II ribosome protection protein and our model for the mechanism of action (**Fig. 52**) expands the one reported previously (Duval et al., 2018). 70S ribosomes with an antibiotic bound near the PTC are recognized by HflXr and subsequently split into 30S (**Fig. 52a-c**) and 50S with HflXr remaining stably bound (**Fig. 52d**). Conformational changes are induced by the NTD2-loop of HflXr and make drug binding incompatible with the rearranged 23S rRNA nucleotides leading to the dissociation of bound drug (**Fig. 52d-e**). The dissociation of HflXr is triggered by the hydrolysis of GTP to GDP and allows the free 50S subunit to be recycled and reintroduced to a next round of translation (**Fig. 52e-f**). At this point, a general overview of the mechanism of action of HflXr was presented, however, the initial substrate of HflXr remains unclear. The recognition of antibiotic-stalled ribosomes seems impossible in presence of ribosome stalled during elongation with either or both A- and P-site tRNAs. The low splitting activity reported for HflX of polysomes and ribosomes bearing peptidyl-tRNA and an increased efficiency for splitting vacant 70S ribosomes or post-release ribosomes with tRNAs adopting hybrid P/E conformation (Zhang et al., 2015b) support this hypothesis. It was also suggested that other factors could be involved, like ArfA or ArfB, prior to HflX splitting (Zhang et al., 2015b). Interestingly, HflXr confers resistance mainly to antibiotic classes that are able to trigger peptidyl-tRNA 'drop-off' (Menninger and Coleman, 1993; Tenson et al., 2003) which may explain the resulting stalled ribosomes as suitable substrate. As noted in our scheme, the GTP-hydrolysis seems to be unnecessary for HflXr induced splitting but might be essential for dissociation from the 50S subunit after splitting, analogous to *E. coli* and *Mycobacterium* HflX (Rudra et al., 2020; Zhang et al., 2015b). However, HflXr might act directly on antibiotic-stalled complexes, inducing conformational changes at the PTC which makes it incompatible with drug binding, but it remains unclear if HflXr binding and drug release requires GTP hydrolysis. Experiments that would support this hypothesis were performed for other RPPs, such as ARE-ABCs LsaA (Sharkey et al., 2016), MsrE (Su et al., 2018) and TetO/TetM (Burdett, 1996; Connell et al., 2002; Trieber et al., 1998), but require soluble active protein for *in vitro* assays that our collaborators were not able to provide in time. It remains unclear what would keep antibiotics off the ribosome after dissociation and if the conformational changes induced in the PTC are stable after dissociation of the factor as shown for

TetM/TetO (Connell et al., 2003a; Connell et al., 2003b; Connell et al., 2002). This would be rather inefficient as the conformational changes would need to be compatible with multiple rounds of elongation following proper translation initiation. An alternative mechanism would be the rapid efflux of the dissociated antibiotic through an efflux pump out of the living cell. Extended loop HflX and HflXr variants, unlike the short looped exclusive splitting factor HflX, can confer resistance in addition to their splitting factor capabilities that stimulate drug dissociation from the LSU and is supported by rapid drug efflux through an efflux pump. The allosteric mechanism we proposed in this thesis for HflXr is strikingly similar to the proposed mechanism shown for the ARE-ABCF proteins, like *L. monocytogenes* VgaL which confers resistance to the PTC inhibitor antibiotic classes lincosamides, pleuromutilins and streptogramin As (Crowe-McAuliffe et al., 2021; Wilson et al., 2020).

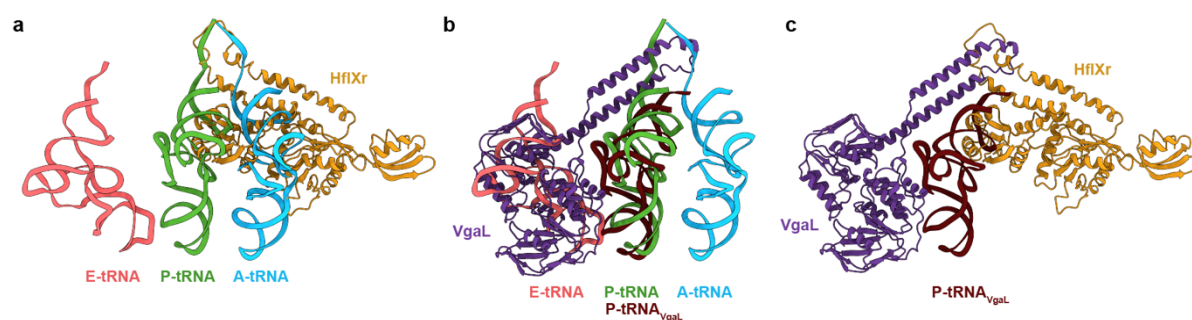


**Figure 53: ARE-ABCF protein VgaL superimposed with HflXr.** a-b, A- (blue), P- (green) and E-site (red) tRNAs (PDB ID 1VY4) superimposed with *L. monocytogenes* HflXr (orange) and *L. monocytogenes* VgaL (purple, PDB ID 7NHN) (Crowe-McAuliffe et al., 2021; Polikanov et al., 2014a). c, *L. monocytogenes* HflXr (orange) superimposed with *L. monocytogenes* VgaL (purple) and P-tRNA<sub>VgaL</sub> (dark red, PDB ID 7HNN) (Crowe-McAuliffe et al., 2021). Modified from (Koller et al., 2022b).

The binding sites of HflXr and VgaL are very distinct, with HflXr entering from the A-site and VgaL entering from the E-site, but both contain a loop region extending from two  $\alpha$ -helices that encroaches into both A- and P-site at the PTC (**Sup.Fig. 16**) (Crowe-McAuliffe et al., 2021). The conformational changes induced by VgaL in the PTC are also proposed to promote drug dissociation but are mechanistically distinct from the conformational changes induced by HflXr, as they do not affect resistance to macrolides or streptogramin Bs in VgaL bound ribosomes as seen for our HflXr structure. For ARE-ABCFs like *Pseudomonas aeruginosa* MsrE, it is known that resistance to the mentioned classes is conferred through longer loop regions that can

penetrate deeper into the NPET and locally interfere with drug binding (Ero et al., 2019; Su et al., 2018). Interestingly, HflXr and VgaL both overlap with the binding sites of oxazolidinones and phenicols of which they are unable to confer resistance to that share binding sites with PTC inhibitory antibiotics that they are able to confer resistance to, such as Lnc and Tia (Crowe-McAuliffe et al., 2021). A possible explanation for HflXr is that while lincosamides and macrolides can stimulate peptidyl-tRNA drop-off (Menninger and Coleman, 1993; Tenson et al., 2003) and become targets of HflXr, both chloramphenicol- and linezolid stalled ribosomes are persistent to peptidyl-tRNA release and do not become a substrate for HflXr-mediated splitting. As shown in a previous publication, the resistance conferred by HflXr is relatively modest and antibiotic sensitivity is not affected by loss of HflXr in strains with VgaL (Duval et al., 2018; Koller et al., 2022b). Increased resistance could only be shown in absence of VgaL and overexpression of the protein was necessary to have observable resistance to some antibiotic classes. This emphasizes that in *L. monocytogenes* the dissociation of antibiotics by ARE-ABCF protein VgaL renders the ribosomes that continue translation elongation phase immune to effects of translation inhibitors, while HflXr induced ribosomal splitting forces 50S subunits to re-enter translation through translation initiation providing a longer time frame for antibiotics to rebind the ribosome (Crowe-McAuliffe et al., 2021). From the evolutionary standpoint it is questionable that the low level of resistance conferred by HflXr, compared to other ARE-ABCFs, as to why bacteria retained homologs of HflX proteins. We propose based on the results in this thesis and our corresponding publication that HflXr may keep its splitting function as a stress factor in an analogous way to HflX with the added benefit of antibiotic resistance and/or on another set of stalled ribosomes as substrates (Koller et al., 2022b).

## 12. References

- Adrian, P.V., Mendrick, C., Loebenberg, D., McNicholas, P., Shaw, K.J., Klugman, K.P., Hare, R.S., and Black, T.A. (2000). Evernimicin (SCH27899) inhibits a novel ribosome target site: analysis of 23S ribosomal DNA mutants. *Antimicrob Agents Chemother* 44, 3101-3106.
- Agrawal, R.K., Spahn, C.M., Penczek, P., Grassucci, R.A., Nierhaus, K.H., and Frank, J. (2000). Visualization of tRNA movements on the Escherichia coli 70S ribosome during the elongation cycle. *J Cell Biol* 150, 447-460.
- Ahn, M., Murugan, R.N., Nan, Y.H., Cheong, C., Sohn, H., Kim, E.H., Hwang, E., Ryu, E.K., Kang, S.W., Shin, S.Y., *et al.* (2011a). Substitution of the GalNAc-alpha-O-Thr(1)(1) residue in drosocin with O-linked glyco-peptoid residue: effect on antibacterial activity and conformational change. *Bioorg Med Chem Lett* 21, 6148-6153.
- Ahn, M., Sohn, H., Nan, Y.H., Murugan, R.N., Cheong, C., Eun Kyoung Ryu, Kim, E.-H., Kang, S.W., Kim, E.J., Shin, S.Y., *et al.* (2011b). Functional and Structural Characterization of Drosocin and its Derivatives Linked O-GalNAc at Thr11 Residue. *Bull. Korean Chem. Soc.* 32, 3327-3332.
- Almutairi, M.M., Svetlov, M.S., Hansen, D.A., Khabibullina, N.F., Klepacki, D., Kang, H.Y., Sherman, D.H., Vazquez-Laslop, N., Polikanov, Y.S., and Mankin, A.S. (2017). Co-produced natural ketolides methymycin and pikromycin inhibit bacterial growth by preventing synthesis of a limited number of proteins. *Nucleic Acids Res* 45, 9573-9582.
- Antimicrobial Resistance, C. (2022). Global burden of bacterial antimicrobial resistance in 2019: a systematic analysis. *Lancet* 399, 629-655.
- Antoun, A., Pavlov, M.Y., Lovmar, M., and Ehrenberg, M. (2006). How initiation factors maximize the accuracy of tRNA selection in initiation of bacterial protein synthesis. *Mol Cell* 23, 183-193.
- Aranda, P.S., LaJoie, D.M., and Jorcyk, C.L. (2012). Bleach gel: a simple agarose gel for analyzing RNA quality. *Electrophoresis* 33, 366-369.
- Archacki, S., and Wang, Q. (2004). Expression profiling of cardiovascular disease. *Hum Genomics* 1, 355-370.

Arenz, S., Bock, L.V., Graf, M., Innis, C.A., Beckmann, R., Grubmuller, H., Vaiana, A.C., and Wilson, D.N. (2016a). A combined cryo-EM and molecular dynamics approach reveals the mechanism of ErmBL-mediated translation arrest. *Nat Commun* 7, 12026.

Arenz, S., Juette, M.F., Graf, M., Nguyen, F., Huter, P., Polikanov, Y.S., Blanchard, S.C., and Wilson, D.N. (2016b). Structures of the orthosomycin antibiotics avilamycin and evernimicin in complex with the bacterial 70S ribosome. *Proc Natl Acad Sci U S A* 113, 7527-7532.

Arenz, S., Meydan, S., Starosta, A.L., Berninghausen, O., Beckmann, R., Vazquez-Laslop, N., and Wilson, D.N. (2014a). Drug sensing by the ribosome induces translational arrest via active site perturbation. *Mol Cell* 56, 446-452.

Arenz, S., Nguyen, F., Beckmann, R., and Wilson, D.N. (2015). Cryo-EM structure of the tetracycline resistance protein TetM in complex with a translating ribosome at 3.9-Å resolution. *Proc Natl Acad Sci U S A* 112, 5401-5406.

Arenz, S., Ramu, H., Gupta, P., Berninghausen, O., Beckmann, R., Vazquez-Laslop, N., Mankin, A.S., and Wilson, D.N. (2014b). Molecular basis for erythromycin-dependent ribosome stalling during translation of the ErmBL leader peptide. *Nat Commun* 5, 3501.

Arenz, S., and Wilson, D.N. (2016a). Bacterial Protein Synthesis as a Target for Antibiotic Inhibition. *Cold Spring Harb Perspect Med* 6.

Arenz, S., and Wilson, D.N. (2016b). Blast from the Past: Reassessing Forgotten Translation Inhibitors, Antibiotic Selectivity, and Resistance Mechanisms to Aid Drug Development. *Mol Cell* 61, 3-14.

Arnez, J.G., and Moras, D. (1997). Structural and functional considerations of the aminoacylation reaction. *Trends Biochem Sci* 22, 211-216.

Ban, N., Nissen, P., Hansen, J., Moore, P.B., and Steitz, T.A. (2000). The complete atomic structure of the large ribosomal subunit at 2.4 Å resolution. *Science* 289, 905-920.

Barlow, J.J., Mathias, A.P., Williamson, R., and Gammack, D.B. (1963). A Simple Method for the Quantitative Isolation of Undegraded High Molecular Weight Ribonucleic Acid. *Biochem Biophys Res Commun* 13, 61-66.



Basu, A., and Yap, M.N. (2017). Disassembly of the *Staphylococcus aureus* hibernating 100S ribosome by an evolutionarily conserved GTPase. *Proc Natl Acad Sci U S A* *114*, E8165-E8173.

Baumann, S., Herrmann, J., Raju, R., Steinmetz, H., Mohr, K.I., Huttel, S., Harmrolfs, K., Stadler, M., and Muller, R. (2014). Cystobactamids: myxobacterial topoisomerase inhibitors exhibiting potent antibacterial activity. *Angew Chem Int Ed Engl* *53*, 14605-14609.

Beckert, B., Leroy, E.C., Sothiselvam, S., Bock, L.V., Svetlov, M.S., Graf, M., Arenz, S., Abdelshahid, M., Seip, B., Grubmuller, H., *et al.* (2021). Structural and mechanistic basis for translation inhibition by macrolide and ketolide antibiotics. *Nat Commun* *12*, 4466.

Belova, L., Tenson, T., Xiong, L., McNicholas, P.M., and Mankin, A.S. (2001). A novel site of antibiotic action in the ribosome: interaction of evernimicin with the large ribosomal subunit. *Proc Natl Acad Sci U S A* *98*, 3726-3731.

Ben-Shem, A., Garreau de Loubresse, N., Melnikov, S., Jenner, L., Yusupova, G., and Yusupov, M. (2011). The structure of the eukaryotic ribosome at 3.0 Å resolution. *Science* *334*, 1524-1529.

Benincasa, M., Scocchi, M., Podda, E., Skerlavaj, B., Dolzani, L., and Gennaro, R. (2004). Antimicrobial activity of Bac7 fragments against drug-resistant clinical isolates. *Peptides* *25*, 2055-2061.

Berisio, R., Harms, J., Schluenzen, F., Zarivach, R., Hansen, H.A., Fucini, P., and Yonath, A. (2003). Structural insight into the antibiotic action of telithromycin against resistant mutants. *J Bacteriol* *185*, 4276-4279.

Berman, H.M., Westbrook, J., Feng, Z., Gilliland, G., Bhat, T.N., Weissig, H., Shindyalov, I.N., and Bourne, P.E. (2000). The Protein Data Bank. *Nucleic Acids Res* *28*, 235-242.

Berthold, N., and Hoffmann, R. (2014). Cellular uptake of apidaecin 1b and related analogs in Gram-negative bacteria reveals novel antibacterial mechanism for proline-rich antimicrobial peptides. *Protein Pept Lett* *21*, 391-398.

Bieling, P., Beringer, M., Adio, S., and Rodnina, M.V. (2006). Peptide bond formation does not involve acid-base catalysis by ribosomal residues. *Nat Struct Mol Biol* *13*, 423-428.

Bikker, F.J., Kaman-van Zanten, W.E., de Vries-van de Ruit, A.M., Voskamp-Visser, I., van Hooft, P.A., Mars-Groenendijk, R.H., de Visser, P.C., and Noort, D. (2006). Evaluation of the antibacterial spectrum of drosocin analogues. *Chem Biol Drug Des* 68, 148-153.

Bishop, J., Leahy, J., and Schweet, R. (1960). Formation of the Peptide Chain of Hemoglobin. *Proc Natl Acad Sci U S A* 46, 1030-1038.

Blaha, G., Stelzl, U., Spahn, C.M., Agrawal, R.K., Frank, J., and Nierhaus, K.H. (2000). Preparation of functional ribosomal complexes and effect of buffer conditions on tRNA positions observed by cryoelectron microscopy. *Methods Enzymol* 317, 292-309.

Blanchard, S.C., Kim, H.D., Gonzalez, R.L., Jr., Puglisi, J.D., and Chu, S. (2004). tRNA dynamics on the ribosome during translation. *Proc Natl Acad Sci U S A* 101, 12893-12898.

Bommakanti, A.S., Lindahl, L., and Zengel, J.M. (2008). Mutation from guanine to adenine in 25S rRNA at the position equivalent to *E. coli* A2058 does not confer erythromycin sensitivity in *Sacchomyces cerevisiae*. *Rna* 14, 460-464.

Borg, A., Pavlov, M., and Ehrenberg, M. (2016). Complete kinetic mechanism for recycling of the bacterial ribosome. *Rna* 22, 10-21.

Borovinskaya, M.A., Shoji, S., Fredrick, K., and Cate, J.H. (2008). Structural basis for hygromycin B inhibition of protein biosynthesis. *Rna* 14, 1590-1599.

Bourgeois, G., Seguin, J., Babin, M., Gondry, M., Mechulam, Y., and Schmitt, E. (2020). Structural basis of the interaction between cyclodipeptide synthases and aminoacylated tRNA substrates. *Rna* 26, 1589-1602.

Bozdogan, B., and Appelbaum, P.C. (2004). Oxazolidinones: activity, mode of action, and mechanism of resistance. *Int J Antimicrob Agents* 23, 113-119.

Brilot, A.F., Korostelev, A.A., Ermolenko, D.N., and Grigorieff, N. (2013). Structure of the ribosome with elongation factor G trapped in the pretranslocation state. *Proc Natl Acad Sci U S A* 110, 20994-20999.

Brodiazhenko, T., Turnbull, K.J., Wu, K.J.Y., Takada, H., Tresco, B.I.C., Tenson, T., Myers, A.G., and Hauryliuk, V. (2022). Synthetic oxepanoprolinamide iboxamycin is highly active against human pathogen *Listeria monocytogenes*. *JAC-Antimicrobial Resistance*.

Bulet, P., Dimarcq, J.L., Hetru, C., Lagueux, M., Charlet, M., Hegy, G., Van Dorsselaer, A., and Hoffmann, J.A. (1993). A novel inducible antibacterial peptide of *Drosophila* carries an O-glycosylated substitution. *J Biol Chem* 268, 14893-14897.

Bulet, P., Hetru, C., Dimarcq, J.L., and Hoffmann, D. (1999). Antimicrobial peptides in insects; structure and function. *Dev Comp Immunol* 23, 329-344.

Bulet, P., Urge, L., Ohresser, S., Hetru, C., and Otvos, L., Jr. (1996). Enlarged scale chemical synthesis and range of activity of drosocin, an O-glycosylated antibacterial peptide of *Drosophila*. *Eur J Biochem* 238, 64-69.

Bulkley, D., Innis, C.A., Blaha, G., and Steitz, T.A. (2010). Revisiting the structures of several antibiotics bound to the bacterial ribosome. *Proc Natl Acad Sci U S A* 107, 17158-17163.

Bulkley, D., Johnson, F., and Steitz, T.A. (2012). The antibiotic thermorubin inhibits protein synthesis by binding to inter-subunit bridge B2a of the ribosome. *J Mol Biol* 416, 571-578.

Burdett, V. (1996). Tet(M)-promoted release of tetracycline from ribosomes is GTP dependent. *J Bacteriol* 178, 3246-3251.

Burley, S.K., Bhikadiya, C., Bi, C., Bittrich, S., Chen, L., Crichlow, G.V., Christie, C.H., Dalenberg, K., Di Costanzo, L., Duarte, J.M., *et al.* (2021). RCSB Protein Data Bank: powerful new tools for exploring 3D structures of biological macromolecules for basic and applied research and education in fundamental biology, biomedicine, biotechnology, bioengineering and energy sciences. *Nucleic Acids Res* 49, D437-D451.

Byrgazov, K., Grishkovskaya, I., Arenz, S., Coudeville, N., Temmel, H., Wilson, D.N., Djinovic-Carugo, K., and Moll, I. (2015). Structural basis for the interaction of protein S1 with the *Escherichia coli* ribosome. *Nucleic Acids Res* 43, 661-673.

Carbone, C.E., Loveland, A.B., Gamper, H.B., Jr., Hou, Y.M., Demo, G., and Korostelev, A.A. (2021). Time-resolved cryo-EM visualizes ribosomal translocation with EF-G and GTP. *Nat Commun* 12, 7236.

Carter, A.P., Clemons, W.M., Brodersen, D.E., Morgan-Warren, R.J., Wimberly, B.T., and Ramakrishnan, V. (2000). Functional insights from the structure of the 30S ribosomal subunit and its interactions with antibiotics. *Nature* 407, 340-348.

Castle, M., Nazarian, A., Yi, S.S., and Tempst, P. (1999). Lethal effects of apidaecin on *Escherichia coli* involve sequential molecular interactions with diverse targets. *J Biol Chem* 274, 32555-32564.

Cathala, G., Savouret, J.F., Mendez, B., West, B.L., Karin, M., Martial, J.A., and Baxter, J.D. (1983). A method for isolation of intact, translationally active ribonucleic acid. *DNA* 2, 329-335.

Cech, T.R. (2000). Structural biology - The ribosome is a ribozyme. *Science* 289, 878-879.

Chan, K.H., Petrychenko, V., Mueller, C., Maracci, C., Holtkamp, W., Wilson, D.N., Fischer, N., and Rodnina, M.V. (2020). Mechanism of ribosome rescue by alternative ribosome-rescue factor B. *Nat Commun* 11, 4106.

Chandrasekaran, V., Juszkievicz, S., Choi, J., Puglisi, J.D., Brown, A., Shao, S., Ramakrishnan, V., and Hegde, R.S. (2019). Mechanism of ribosome stalling during translation of a poly(A) tail. *Nat Struct Mol Biol* 26, 1132-1140.

Chen, V.B., Arendall, W.B., 3rd, Headd, J.J., Keedy, D.A., Immormino, R.M., Kapral, G.J., Murray, L.W., Richardson, J.S., and Richardson, D.C. (2010). MolProbity: all-atom structure validation for macromolecular crystallography. *Acta Crystallogr D Biol Crystallogr* 66, 12-21.

Chen, Y., Kaji, A., Kaji, H., and Cooperman, B.S. (2017). The kinetic mechanism of bacterial ribosome recycling. *Nucleic Acids Res* 45, 10168-10177.

Chesneau, O., Ligeret, H., Hosan-Aghaie, N., Morvan, A., and Dassa, E. (2005). Molecular analysis of resistance to streptogramin A compounds conferred by the Vga proteins of staphylococci. *Antimicrob Agents Chemother* 49, 973-980.

Chinali, G., Moureau, P., and Cocito, C.G. (1984). The action of virginiamycin M on the acceptor, donor, and catalytic sites of peptidyltransferase. *J Biol Chem* 259, 9563-9568.

Choi, J., Marks, J., Zhang, J., Chen, D.H., Wang, J., Vazquez-Laslop, N., Mankin, A.S., and Puglisi, J.D. (2020a). Dynamics of the context-specific translation arrest by chloramphenicol and linezolid. *Nat Chem Biol* 16, 310-317.

Choi, J., O'Loughlin, S., Atkins, J.F., and Puglisi, J.D. (2020b). The energy landscape of -1 ribosomal frameshifting. *Sci Adv* 6, eaax6969.

Clemons, W.M., Jr., May, J.L., Wimberly, B.T., McCutcheon, J.P., Capel, M.S., and Ramakrishnan, V. (1999). Structure of a bacterial 30S ribosomal subunit at 5.5 Å resolution. *Nature* 400, 833-840.

Coatham, M.L., Brandon, H.E., Fischer, J.J., Schummer, T., and Wieden, H.-J. (2016). The conserved GTPase HflX is a ribosome splitting factor that binds to the E-site of the bacterial ribosome. *Nucleic acids research* 44, 1952-1961.

Cociancich, S., Dupont, A., Hegy, G., Lanot, R., Holder, F., Hetru, C., Hoffmann, J.A., and Bulet, P. (1994). Novel inducible antibacterial peptides from a hemipteran insect, the sap-sucking bug *Pyrrhocoris apterus*. *Biochem J* 300 ( Pt 2), 567-575.

Connell, S.R., Tracz, D.M., Nierhaus, K.H., and Taylor, D.E. (2003a). Ribosomal protection proteins and their mechanism of tetracycline resistance. *Antimicrob. Agents Chemother.* 47, 3675-3681.

Connell, S.R., Trieber, C.A., Dinos, G.P., Einfeldt, E., Taylor, D.E., and Nierhaus, K.H. (2003b). Mechanism of Tet(O)-mediated tetracycline resistance. *EMBO J.* 22, 945-953.

Connell, S.R., Trieber, C.A., Stelzl, U., Einfeldt, E., Taylor, D.E., and Nierhaus, K.H. (2002). The tetracycline resistance protein Tet(O) perturbs the conformation of the ribosomal decoding centre. *Mol. Microbiol.* 45, 1463-1472.

Conway, T.W., and Lipmann, F. (1964). Characterization of a Ribosome-Linked Guanosine Triphosphatase in *Escherichia Coli* Extracts. *Proc Natl Acad Sci U S A* 52, 1462-1469.

Cox, G., Thompson, G.S., Jenkins, H.T., Peske, F., Savelsbergh, A., Rodnina, M.V., Wintermeyer, W., Homans, S.W., Edwards, T.A., and O'Neill, A.J. (2012). Ribosome clearance by FusB-type proteins mediates resistance to the antibiotic fusidic acid. *Proc Natl Acad Sci U S A* 109, 2102-2107.

Crick, F. (1970). Central dogma of molecular biology. *Nature* 227, 561-563.

Crick, F.H. (1966a). Codon--anticodon pairing: the wobble hypothesis. *J Mol Biol* 19, 548-555.

Crick, F.H. (1966b). The genetic code--yesterday, today, and tomorrow. *Cold Spring Harb Symp Quant Biol* 31, 1-9.

Crick, F.H., Barnett, L., Brenner, S., and Watts-Tobin, R.J. (1961). General nature of the genetic code for proteins. *Nature* 192, 1227-1232.

Crowe-McAuliffe, C., Graf, M., Huter, P., Takada, H., Abdelshahid, M., Novacek, J., Murina, V., Atkinson, G.C., Hauryliuk, V., and Wilson, D.N. (2018). Structural basis for antibiotic resistance mediated by the *Bacillus subtilis* ABCF ATPase VmlR. *Proc Natl Acad Sci U S A* *115*, 8978-8983.

Crowe-McAuliffe, C., Murina, V., Turnbull, K.J., Huch, S., Kasari, M., Takada, H., Nersisyan, L., Sundsfjord, A., Hegstad, K., Atkinson, G.C., *et al.* (2022). Structural basis for PoxA-mediated resistance to phenicol and oxazolidinone antibiotics. *Nat Commun* *13*, 1860.

Crowe-McAuliffe, C., Murina, V., Turnbull, K.J., Kasari, M., Mohamad, M., Polte, C., Takada, H., Vaitkevicius, K., Johansson, J., Ignatova, Z., *et al.* (2021). Structural basis of ABCF-mediated resistance to pleuromutilin, lincosamide, and streptogramin A antibiotics in Gram-positive pathogens. *Nat Commun* *12*, 3577.

Cui, Z., Li, X., Shin, J., Gamper, H., Hou, Y.M., Sacchettini, J.C., and Zhang, J. (2022). Interplay between an ATP-binding cassette F protein and the ribosome from *Mycobacterium tuberculosis*. *Nat Commun* *13*, 432.

Dao Duc, K., Batra, S.S., Bhattacharya, N., Cate, J.H.D., and Song, Y.S. (2019). Differences in the path to exit the ribosome across the three domains of life. *Nucleic Acids Res* *47*, 4198-4210.

Dar, D., Shamir, M., Mellin, J.R., Koutero, M., Stern-Ginossar, N., Cossart, P., and Sorek, R. (2016). Term-seq reveals abundant ribo-regulation of antibiotics resistance in bacteria. *Science* *352*, aad9822.

Davidovich, C., Bashan, A., Auerbach-Nevo, T., Yaggie, R.D., Gontarek, R.R., and Yonath, A. (2007). Induced-fit tightens pleuromutilins binding to ribosomes and remote interactions enable their selectivity. *Proc Natl Acad Sci USA* *104*, 4291-4296.

Davis, A.R., Gohara, D.W., and Yap, M.N. (2014). Sequence selectivity of macrolide-induced translational attenuation. *Proc Natl Acad Sci U S A* *111*, 15379-15384.

de Visser, P.C., van Hooft, P.A., de Vries, A.M., de Jong, A., van der Marel, G.A., Overkleeft, H.S., and Noort, D. (2005). Biological evaluation of Tyr6 and Ser7 modified drosocin analogues. *Bioorg Med Chem Lett* *15*, 2902-2905.

Dey, S., Biswas, C., and Sengupta, J. (2018). The universally conserved GTPase HflX is an RNA helicase that restores heat-damaged *Escherichia coli* ribosomes. *J Cell Biol* *217*, 2519-2529.

Diaconu, M., Kothe, U., Schlunzen, F., Fischer, N., Harms, J.M., Tonevitsky, A.G., Stark, H., Rodnina, M.V., and Wahl, M.C. (2005). Structural basis for the function of the ribosomal L7/12 stalk in factor binding and GTPase activation. *Cell* 121, 991-1004.

Dincbas-Renqvist, V., Engstrom, A., Mora, L., Heurgue-Hamard, V., Buckingham, R., and Ehrenberg, M. (2000). A post-translational modification in the GGQ motif of RF2 from *Escherichia coli* stimulates termination of translation. *EMBO J* 19, 6900-6907.

Dintzis, H.M. (1961). Assembly of the peptide chains of hemoglobin. *Proc Natl Acad Sci U S A* 47, 247-261.

Dönhöfer, A., Franckenberg, S., Wickles, S., Berninghausen, O., Beckmann, R., and Wilson, D.N. (2012). Structural basis for TetM-mediated tetracycline resistance. *Proc. Natl. Acad. Sci. USA* 109, 16900-16905.

Dunkle, J.A., Wang, L., Feldman, M.B., Pulk, A., Chen, V.B., Kapral, G.J., Noeske, J., Richardson, J.S., Blanchard, S.C., and Cate, J.H. (2011). Structures of the bacterial ribosome in classical and hybrid states of tRNA binding. *Science* 332, 981-984.

Dunkle, J.A., Xiong, L., Mankin, A.S., and Cate, J.H. (2010). Structures of the *Escherichia coli* ribosome with antibiotics bound near the peptidyl transferase center explain spectra of drug action. *Proc Natl Acad Sci U S A* 107, 17152-17157.

Duval, M., Dar, D., Carvalho, F., Rocha, E.P.C., Sorek, R., and Cossart, P. (2018). HflXr, a homolog of a ribosome-splitting factor, mediates antibiotic resistance. *Proc Natl Acad Sci U S A* 115, 13359-13364.

Duval, M., Korepanov, A., Fuchsbaauer, O., Fechter, P., Haller, A., Fabbretti, A., Choulier, L., Micura, R., Klaholz, B.P., Romby, P., *et al.* (2013). *Escherichia coli* ribosomal protein S1 unfolds structured mRNAs onto the ribosome for active translation initiation. *PLoS Biol* 11, e1001731.

Elvekrog, M.M., and Gonzalez, R.L., Jr. (2013). Conformational selection of translation initiation factor 3 signals proper substrate selection. *Nat Struct Mol Biol* 20, 628-633.

Emsley, P., Fotinou, C., Black, I., Fairweather, N.F., Charles, I.G., Watts, C., Hewitt, E., and Isaacs, N.W. (2000). The structures of the H(C) fragment of tetanus toxin with carbohydrate subunit complexes provide insight into ganglioside binding. *J Biol Chem* 275, 8889-8894.

Emsley, P., Lohkamp, B., Scott, W.G., and Cowtan, K. (2010). Features and development of Coot. *Acta Crystallogr D Biol Crystallogr* 66, 486-501.

Erlacher, M.D., Lang, K., Wotzel, B., Rieder, R., Micura, R., and Polacek, N. (2006). Efficient ribosomal peptidyl transfer critically relies on the presence of the ribose 2'-OH at A2451 of 23S rRNA. *J Am Chem Soc* *128*, 4453-4459.

Ero, R., Kumar, V., Su, W., and Gao, Y.G. (2019). Ribosome protection by ABC-F proteins-Molecular mechanism and potential drug design. *Protein Sci* *28*, 684-693.

Eyal, Z., Matzov, D., Krupkin, M., Paukner, S., Riedl, R., Rozenberg, H., Zimmerman, E., Bashan, A., and Yonath, A. (2016). A novel pleuromutilin antibacterial compound, its binding mode and selectivity mechanism. *Sci Rep* *6*, 39004.

Eyal, Z., Matzov, D., Krupkin, M., Wekselman, I., Paukner, S., Zimmerman, E., Rozenberg, H., Bashan, A., and Yonath, A. (2015). Structural insights into species-specific features of the ribosome from the pathogen *Staphylococcus aureus*. *Proc Natl Acad Sci U S A* *112*, E5805-5814.

Fabbretti, A., Schedlbauer, A., Brandi, L., Kaminishi, T., Giuliadori, A.M., Garofalo, R., Ochoa-Lizarralde, B., Takemoto, C., Yokoyama, S., Connell, S.R., *et al.* (2016). Inhibition of translation initiation complex formation by GE81112 unravels a 16S rRNA structural switch involved in P-site decoding. *Proc Natl Acad Sci U S A* *113*, E2286-2295.

Fislage, M., Zhang, J., Brown, Z.P., Mandava, C.S., Sanyal, S., Ehrenberg, M., and Frank, J. (2018). Cryo-EM shows stages of initial codon selection on the ribosome by aa-tRNA in ternary complex with GTP and the GTPase-deficient EF-TuH84A. *Nucleic Acids Res* *46*, 5861-5874.

Florin, T., Maracci, C., Graf, M., Karki, P., Klepacki, D., Berninghausen, O., Beckmann, R., Vazquez-Laslop, N., Wilson, D.N., Rodnina, M.V., *et al.* (2017). An antimicrobial peptide that inhibits translation by trapping release factors on the ribosome. *Nat Struct Mol Biol* *24*, 752-757.

Frank, J., and Agrawal, R.K. (2000). A ratchet-like inter-subunit reorganization of the ribosome during translocation. *Nature* *406*, 318-322.

Fromm, S.A., O'Connor, K.M., Purdy, M., Bhatt, P.R., Loughran, G., Atkins, J.F., Jomaa, A., and Mattei, S. (2022). The translating bacterial ribosome at 1.55 Å resolution by open access cryo-EM. *bioRxiv*.

Fu, Z., Indrisiunaite, G., Kaledhonkar, S., Shah, B., Sun, M., Chen, B., Grassucci, R.A., Ehrenberg, M., and Frank, J. (2019). The structural basis for release-factor activation



during translation termination revealed by time-resolved cryogenic electron microscopy. *Nat Commun* 10, 2579.

Fu, Z., Kaledhonkar, S., Borg, A., Sun, M., Chen, B., Grassucci, R.A., Ehrenberg, M., and Frank, J. (2016). Key Intermediates in Ribosome Recycling Visualized by Time-Resolved Cryoelectron Microscopy. *Structure* 24, 2092-2101.

Gagnon, M.G., Roy, R.N., Lomakin, I.B., Florin, T., Mankin, A.S., and Steitz, T.A. (2016). Structures of proline-rich peptides bound to the ribosome reveal a common mechanism of protein synthesis inhibition. *Nucleic acids research* 44, 2439-2450.

Gamper, H., Li, H., Masuda, I., Miklos Robkis, D., Christian, T., Conn, A.B., Blaha, G., Petersson, E.J., Gonzalez, R.L., Jr., and Hou, Y.M. (2021). Insights into genome recoding from the mechanism of a classic +1-frameshifting tRNA. *Nat Commun* 12, 328.

Gao, N., Zavialov, A.V., Li, W., Sengupta, J., Valle, M., Gursky, R.P., Ehrenberg, M., and Frank, J. (2005). Mechanism for the disassembly of the posttermination complex inferred from cryo-EM studies. *Mol Cell* 18, 663-674.

Gao, Y.G., Selmer, M., Dunham, C.M., Weixlbaumer, A., Kelley, A.C., and Ramakrishnan, V. (2009). The structure of the ribosome with elongation factor G trapped in the posttranslocational state. *Science* 326, 694-699.

Gille, F., and Kirschning, A. (2016). Studies on the synthesis of peptides containing dehydrovaline and dehydroisoleucine based on copper-mediated enamide formation. *Beilstein J Org Chem* 12, 564-570.

Gobbo, M., Biondi, L., Filira, F., Gennaro, R., Benincasa, M., Scolaro, B., and Rocchi, R. (2002). Antimicrobial peptides: synthesis and antibacterial activity of linear and cyclic drosocin and apidaecin 1b analogues. *J Med Chem* 45, 4494-4504.

Goddard, T.D., Huang, C.C., Meng, E.C., Pettersen, E.F., Couch, G.S., Morris, J.H., and Ferrin, T.E. (2018). UCSF ChimeraX: Meeting modern challenges in visualization and analysis. *Protein Sci* 27, 14-25.

Goedert, M. (2015). NEURODEGENERATION. Alzheimer's and Parkinson's diseases: The prion concept in relation to assembled Abeta, tau, and alpha-synuclein. *Science* 349, 1255555.

Goyal, A., Belardinelli, R., Maracci, C., Milon, P., and Rodnina, M.V. (2015). Directional transition from initiation to elongation in bacterial translation. *Nucleic Acids Res* 43, 10700-10712.

Graf, M., Huter, P., Maracci, C., Peterek, M., Rodnina, M.V., and Wilson, D.N. (2018). Visualization of translation termination intermediates trapped by the Apidaecin 137 peptide during RF3-mediated recycling of RF1. *Nat Commun* 9, 3053.

Graf, M., Mardirossian, M., Nguyen, F., Seefeldt, A.C., Guichard, G., Scocchi, M., Innis, C.A., and Wilson, D.N. (2017). Proline-rich antimicrobial peptides targeting protein synthesis. *Natural product reports* 34, 702-711.

Graf, M., and Wilson, D.N. (2019). Intracellular Antimicrobial Peptides Targeting the Protein Synthesis Machinery. *Adv Exp Med Biol* 1117, 73-89.

Grigoriadou, C., Marzi, S., Kirillov, S., Gualerzi, C.O., and Cooperman, B.S. (2007a). A quantitative kinetic scheme for 70 S translation initiation complex formation. *J Mol Biol* 373, 562-572.

Grigoriadou, C., Marzi, S., Pan, D., Gualerzi, C.O., and Cooperman, B.S. (2007b). The translational fidelity function of IF3 during transition from the 30 S initiation complex to the 70 S initiation complex. *J Mol Biol* 373, 551-561.

Grunberg-Manago, M., Dessen, P., Pantaloni, D., Godefroy-Colburn, T., Wolfe, A.D., and Dondon, J. (1975). Light-scattering studies showing the effect of initiation factors on the reversible dissociation of *Escherichia coli* ribosomes. *J Mol Biol* 94, 461-478.

Guenneugues, M., Caserta, E., Brandi, L., Spurio, R., Meunier, S., Pon, C.L., Boelens, R., and Gualerzi, C.O. (2000). Mapping the fMet-tRNA(f)(Met) binding site of initiation factor IF2. *EMBO J* 19, 5233-5240.

Gutierrez, E., Shin, B.S., Woolstenhulme, C.J., Kim, J.R., Saini, P., Buskirk, A.R., and Dever, T.E. (2013). eIF5A promotes translation of polyproline motifs. *Mol Cell* 51, 35-45.

Hansen, J.L., Ippolito, J.A., Ban, N., Nissen, P., Moore, P.B., and Steitz, T.A. (2002). The structures of four macrolide antibiotics bound to the large ribosomal subunit. *Mol Cell* 10, 117-128.

Harms, J., Schluenzen, F., Zarivach, R., Bashan, A., Gat, S., Agmon, I., Bartels, H., Franceschi, F., and Yonath, A. (2001). High resolution structure of the large ribosomal subunit from a mesophilic eubacterium. *Cell* 107, 679-688.

Harms, J.M., Wilson, D.N., Schluenzen, F., Connell, S.R., Stachelhaus, T., Zaborowska, Z., Spahn, C.M., and Fucini, P. (2008). Translational regulation via L11: molecular switches on the ribosome turned on and off by thiostrepton and micrococcin. *Mol Cell* 30, 26-38.

Hartz, D., Binkley, J., Hollingsworth, T., and Gold, L. (1990). Domains of initiator tRNA and initiation codon crucial for initiator tRNA selection by *Escherichia coli* IF3. *Genes Dev* 4, 1790-1800.

Hartz, D., McPheeters, D.S., Traut, R., and Gold, L. (1988). Extension inhibition analysis of translation initiation complexes. *Methods Enzymol.* 164, 419-425.

Herrmann, J., Fayad, A.A., and Muller, R. (2017). Natural products from myxobacteria: novel metabolites and bioactivities. *Natural product reports* 34, 135-160.

Heymann, J.B. (2018). Guidelines for using Bsoft for high resolution reconstruction and validation of biomolecular structures from electron micrographs. *Protein Sci* 27, 159-171.

Hillen, H.S., Lavdovskaia, E., Nadler, F., Hanitsch, E., Linden, A., Bohnsack, K.E., Urlaub, H., and Richter-Dennerlein, R. (2021). Structural basis of GTPase-mediated mitochondrial ribosome biogenesis and recycling. *Nat Commun* 12, 3672.

Hoffmann, R., Bulet, P., Urge, L., and Otvos, L., Jr. (1999). Range of activity and metabolic stability of synthetic antibacterial glycopeptides from insects. *Biochim Biophys Acta* 1426, 459-467.

Hoffmann, T., Krug, D., Bozkurt, N., Duddela, S., Jansen, R., Garcia, R., Gerth, K., Steinmetz, H., and Muller, R. (2018). Correlating chemical diversity with taxonomic distance for discovery of natural products in myxobacteria. *Nat Commun* 9, 803.

Holley, R.W., Apgar, J., Everett, G.A., Madison, J.T., Marquisee, M., Merrill, S.H., Penswick, J.R., and Zamir, A. (1965). Structure of a Ribonucleic Acid. *Science* 147, 1462-1465.

Horinouchi, S., and Weisblum, B. (1980). Posttranscriptional modification of mRNA conformation: mechanism that regulates erythromycin-induced resistance. *Proc Natl Acad Sci U S A* 77, 7079-7083.

Hughes, J., and Mellows, G. (1978). Inhibition of isoleucyl-transfer ribonucleic acid synthetase in *Escherichia coli* by pseudomonic acid. *Biochem J* 176, 305-318.

Hussain, T., Llacer, J.L., Wimberly, B.T., Kieft, J.S., and Ramakrishnan, V. (2016). Large-Scale Movements of IF3 and tRNA during Bacterial Translation Initiation. *Cell* 167, 133-144 e113.

Ingolia, N.T., Ghaemmaghami, S., Newman, J.R., and Weissman, J.S. (2009). Genome-wide analysis in vivo of translation with nucleotide resolution using ribosome profiling. *Science* 324, 218-223.

Irschik, H., Gerth, K., Kemmer, T., Steinmetz, H., and Reichenbach, H. (1983). The myxovalgins, new peptide antibiotics from *Myxococcus fulvus* (Myxobacterales). I. Cultivation, isolation, and some chemical and biological properties. *J Antibiot (Tokyo)* 36, 6-12.

Irschik, H., and Reichenbach, H. (1985). The mechanism of action of myxovalargin A, a peptide antibiotic from *Myxococcus fulvus*. *J Antibiot (Tokyo)* 38, 1237-1245.

Ito, K., and Chiba, S. (2013). Arrest peptides: cis-acting modulators of translation. *Annu Rev Biochem* 82, 171-202.

Jenner, L., Starosta, A.L., Terry, D.S., Mikolajka, A., Filonava, L., Yusupov, M., Blanchard, S.C., Wilson, D.N., and Yusupova, G. (2013). Structural basis for potent inhibitory activity of the antibiotic tigecycline during protein synthesis. *Proc Natl Acad Sci U S A* 110, 3812-3816.

Jin, H., Kelley, A.C., Loakes, D., and Ramakrishnan, V. (2010). Structure of the 70S ribosome bound to release factor 2 and a substrate analog provides insights into catalysis of peptide release. *Proc Natl Acad Sci U S A* 107, 8593-8598.

Jin, H., Kelley, A.C., and Ramakrishnan, V. (2011). Crystal structure of the hybrid state of ribosome in complex with the guanosine triphosphatase release factor 3. *Proc Natl Acad Sci U S A* 108, 15798-15803.

Julian, P., Milon, P., Agirrezabala, X., Lasso, G., Gil, D., Rodnina, M.V., and Valle, M. (2011). The Cryo-EM structure of a complete 30S translation initiation complex from *Escherichia coli*. *PLoS Biol* 9, e1001095.

Jumper, J., Evans, R., Pritzel, A., Green, T., Figurnov, M., Ronneberger, O., Tunyasuvunakool, K., Bates, R., Zidek, A., Potapenko, A., *et al.* (2021). Highly accurate protein structure prediction with AlphaFold. *Nature* 596, 583-589.

Kaledhonkar, S., Fu, Z., Caban, K., Li, W., Chen, B., Sun, M., Gonzalez, R.L., Jr., and Frank, J. (2019). Late steps in bacterial translation initiation visualized using time-resolved cryo-EM. *Nature* 570, 400-404.

Kaminishi, T., Wilson, D.N., Takemoto, C., Harms, J.M., Kawazoe, M., Schluenzen, F., Hanawa-Suetsugu, K., Shirouzu, M., Fucini, P., and Yokoyama, S. (2007). A snapshot of the 30S ribosomal subunit capturing mRNA via the Shine-Dalgarno interaction. *Structure* 15, 289-297.

Kannan, K., Kanabar, P., Schryer, D., Florin, T., Oh, E., Bahroos, N., Tenson, T., Weissman, J.S., and Mankin, A.S. (2014). The general mode of translation inhibition by macrolide antibiotics. *Proc Natl Acad Sci U S A* *111*, 15958-15963.

Kannan, K., Vazquez-Laslop, N., and Mankin, A.S. (2012). Selective protein synthesis by ribosomes with a drug-obstructed exit tunnel. *Cell* *151*, 508-520.

Karray, F., Darbon, E., Oestreicher, N., Dominguez, H., Tuphile, K., Gagnat, J., Blondelet-Rouault, M.H., Gerbaud, C., and Pernodet, J.L. (2007). Organization of the biosynthetic gene cluster for the macrolide antibiotic spiramycin in *Streptomyces ambofaciens*. *Microbiology (Reading)* *153*, 4111-4122.

Kim, S.H., Sussman, J.L., Suddath, F.L., Quigley, G.J., McPherson, A., Wang, A.H., Seeman, N.C., and Rich, A. (1974). The general structure of transfer RNA molecules. *Proc Natl Acad Sci U S A* *71*, 4970-4974.

Kim, T.W., Keum, J.W., Oh, I.S., Choi, C.Y., Park, C.G., and Kim, D.M. (2006). Simple procedures for the construction of a robust and cost-effective cell-free protein synthesis system. *J Biotechnol* *126*, 554-561.

Koller, T.O., Scheid, U., Kösel, T., Herrmann, J., Krug, D., Boshoff, H.I., Beckert, B., Evans, J.C., Schlemmer, J., Sloan, B., *et al.* (2022a). The myxobacterial antibiotic myxovalargin: Biosynthesis, structural revision, total synthesis and molecular characterization of ribosomal inhibition. *ChemRxiv*.

Koller, T.O., Turnbull, K.J., Vaitkevicius, K., Crowe-McAuliffe, C., Roghanian, M., Bulvas, O., Nakamoto, J.A., Kurata, T., Julius, C., Atkinson, G.C., *et al.* (2022b). Structural basis for HflXr-mediated antibiotic resistance in *Listeria monocytogenes*. *Nucleic Acids Res.*

Korostelev, A., Asahara, H., Lancaster, L., Laurberg, M., Hirschi, A., Zhu, J., Trakhanov, S., Scott, W.G., and Noller, H.F. (2008). Crystal structure of a translation termination complex formed with release factor RF2. *Proc Natl Acad Sci U S A* *105*, 19684-19689.

Korostelev, A., Trakhanov, S., Asahara, H., Laurberg, M., Lancaster, L., and Noller, H.F. (2007). Interactions and dynamics of the Shine Dalgarno helix in the 70S ribosome. *Proc Natl Acad Sci U S A* *104*, 16840-16843.

Korostelev, A., Zhu, J., Asahara, H., and Noller, H.F. (2010). Recognition of the amber UAG stop codon by release factor RF1. *EMBO J* *29*, 2577-2585.

Korostelev, A.A. (2022). The Structural Dynamics of Translation. *Annu Rev Biochem* 91, 245-267.

Koutmou, K.S., McDonald, M.E., Brunelle, J.L., and Green, R. (2014). RF3:GTP promotes rapid dissociation of the class 1 termination factor. *Rna* 20, 609-620.

Krieg, P.A., and Melton, D.A. (1984). Functional messenger RNAs are produced by SP6 in vitro transcription of cloned cDNAs. *Nucleic Acids Res* 12, 7057-7070.

Krizsan, A., Prahl, C., Goldbach, T., Knappe, D., and Hoffmann, R. (2015). Short Proline-Rich Antimicrobial Peptides Inhibit Either the Bacterial 70S Ribosome or the Assembly of its Large 50S Subunit. *Chembiochem* 16, 2304-2308.

Krizsan, A., Volke, D., Weinert, S., Strater, N., Knappe, D., and Hoffmann, R. (2014). Insect-derived proline-rich antimicrobial peptides kill bacteria by inhibiting bacterial protein translation at the 70S ribosome. *Angew Chem Int Ed Engl* 53, 12236-12239.

Krupkin, M., Wekselman, I., Matzov, D., Eyal, Z., Diskin Posner, Y., Rozenberg, H., Zimmerman, E., Bashan, A., and Yonath, A. (2016). Avilamycin and evernimicin induce structural changes in rProteins uL16 and CTC that enhance the inhibition of A-site tRNA binding. *Proc Natl Acad Sci U S A* 113, E6796-E6805.

Kucukelbir, A., Sigworth, F.J., and Tagare, H.D. (2014). Quantifying the local resolution of cryo-EM density maps. *Nature methods* 11, 63-65.

Kuhlenkoetter, S., Wintermeyer, W., and Rodnina, M.V. (2011). Different substrate-dependent transition states in the active site of the ribosome. *Nature* 476, 351-354.

Laurberg, M., Asahara, H., Korostelev, A., Zhu, J., Trakhanov, S., and Noller, H.F. (2008). Structural basis for translation termination on the 70S ribosome. *Nature* 454, 852-857.

Leipe, D.D., Wolf, Y.I., Koonin, E.V., and Aravind, L. (2002). Classification and evolution of P-loop GTPases and related ATPases. *J Mol Biol* 317, 41-72.

Lele, D.S., Dwivedi, R., Kumari, S., and Kaur, K.J. (2015a). Effect of distal sugar and interglycosidic linkage of disaccharides on the activity of proline rich antimicrobial glycopeptides. *J Pept Sci* 21, 833-844.

Lele, D.S., Talat, S., and Kaur, K.J. (2013). The Presence of Arginine in the Pro-Arg-Pro Motif Augments the Lethality of Proline Rich Antimicrobial Peptides of Insect Source. *Int. J. Pept. Res. Ther.* 19, 323–330.

Lele, D.S., Talat, S., Kumari, S., Srivastava, N., and Kaur, K.J. (2015b). Understanding the importance of glycosylated threonine and stereospecific action of Drosocin, a Proline rich antimicrobial peptide. *Eur J Med Chem* 92, 637-647.

Leroy, E.C., Perry, T.N., Renault, T.T., and Innis, C.A. (2022). Tetracenomycin X sequesters peptidyl-tRNA during translation of QK motifs. *bioRxiv*, 2022.2008.2009.503329.

Li, Q., Pellegrino, J., Lee, D.J., Tran, A.A., Chaires, H.A., Wang, R., Park, J.E., Ji, K., Chow, D., Zhang, N., *et al.* (2020a). Synthetic group A streptogramin antibiotics that overcome Vat resistance. *Nature* 586, 145-150.

Li, W., Atkinson, G.C., Thakor, N.S., Allas, U., Lu, C.C., Chan, K.Y., Tenson, T., Schulten, K., Wilson, K.S., Hauryliuk, V., *et al.* (2013). Mechanism of tetracycline resistance by ribosomal protection protein Tet(O). *Nat. Commun.* 4, 1477.

Li, W., Chang, S.T., Ward, F.R., and Cate, J.H.D. (2020b). Selective inhibition of human translation termination by a drug-like compound. *Nat Commun* 11, 4941.

Li, W., Ward, F.R., McClure, K.F., Chang, S.T., Montabana, E., Liras, S., Dullea, R.G., and Cate, J.H.D. (2019). Structural basis for selective stalling of human ribosome nascent chain complexes by a drug-like molecule. *Nat Struct Mol Biol* 26, 501-509.

Liang, S.T., Xu, Y.C., Dennis, P., and Bremer, H. (2000). mRNA composition and control of bacterial gene expression. *J Bacteriol* 182, 3037-3044.

Liebschner, D., Afonine, P.V., Baker, M.L., Bunkoczi, G., Chen, V.B., Croll, T.I., Hintze, B., Hung, L.W., Jain, S., McCoy, A.J., *et al.* (2019). Macromolecular structure determination using X-rays, neutrons and electrons: recent developments in Phenix. *Acta Crystallogr D Struct Biol* 75, 861-877.

Limbrick, E., Graf, M., Derewacz, D.K., Nguyen, F., Spraggins, J.M., Wieland, M., Yniguez-Gutierrez, A., Reisman, B.J., Zinshteyn, B., McCulloch, K.M., *et al.* (2020). A bifunctional nitron conjugated secondary metabolite targeting the ribosome. *Journal of the American Chemical Society*.

Lin, J., Zhou, D., Steitz, T.A., Polikanov, Y.S., and Gagnon, M.G. (2018). Ribosome-Targeting Antibiotics: Modes of Action, Mechanisms of Resistance, and Implications for Drug Design. *Annu Rev Biochem* 87, 451-478.

Ling, C., and Ermolenko, D.N. (2015). Initiation factor 2 stabilizes the ribosome in a semirotated conformation. *Proc Natl Acad Sci U S A* 112, 15874-15879.

Lintner, N.G., McClure, K.F., Petersen, D., Londregan, A.T., Piotrowski, D.W., Wei, L., Xiao, J., Bolt, M., Loria, P.M., Maguire, B., *et al.* (2017). Selective stalling of human translation through small-molecule engagement of the ribosome nascent chain. *PLoS Biol* 15, e2001882.

Liu, Q., and Fredrick, K. (2015). Roles of helix H69 of 23S rRNA in translation initiation. *Proc Natl Acad Sci U S A* 112, 11559-11564.

Long, F., Nicholls, R.A., Emsley, P., Graaeulis, S., Merkys, A., Vaitkus, A., and Murshudov, G.N. (2017). AceDRG: a stereochemical description generator for ligands. *Acta Crystallogr D Struct Biol* 73, 112-122.

Lopez-Alonso, J.P., Fabbretti, A., Kaminishi, T., Iturrioz, I., Brandi, L., Gil-Carton, D., Gualerzi, C.O., Fucini, P., and Connell, S.R. (2017). Structure of a 30S pre-initiation complex stalled by GE81112 reveals structural parallels in bacterial and eukaryotic protein synthesis initiation pathways. *Nucleic Acids Res* 45, 2179-2187.

Loveland, A.B., Demo, G., Grigorieff, N., and Korostelev, A.A. (2017). Ensemble cryo-EM elucidates the mechanism of translation fidelity. *Nature* 546, 113-117.

Loveland, A.B., Demo, G., and Korostelev, A.A. (2020). Cryo-EM of elongating ribosome with EF-Tu\*GTP elucidates tRNA proofreading. *Nature* 584, 640-645.

Ludwig, T., Krizsan, A., Mohammed, G.K., and Hoffmann, R. (2022). Antimicrobial Activity and 70S Ribosome Binding of Apidaecin-Derived Api805 with Increased Bacterial Uptake Rate. *Antibiotics (Basel)* 11.

Ma, J., Campbell, A., and Karlin, S. (2002). Correlations between Shine-Dalgarno sequences and gene features such as predicted expression levels and operon structures. *J Bacteriol* 184, 5733-5745.

MacDougall, D.D., and Gonzalez, R.L., Jr. (2015). Translation initiation factor 3 regulates switching between different modes of ribosomal subunit joining. *J Mol Biol* 427, 1801-1818.

Mangano, K., Florin, T., Shao, X., Klepacki, D., Chelysheva, I., Ignatova, Z., Gao, Y., Mankin, A.S., and Vazquez-Laslop, N. (2020). Genome-wide effects of the antimicrobial peptide apidaecin on translation termination in bacteria. *Elife* 9.

Mangano, K., Marks, J., Klepacki, D., Saha, C.K., Atkinson, G.C., Vazquez-Laslop, N., and Mankin, A.S. (2022). Context-based sensing of orthosomycin antibiotics by the translating ribosome. *Nat Chem Biol* 18, 1277-1286.

Mankin, A.S. (2008). Macrolide myths. *Curr Opin Microbiol* 11, 414-421.



Manzella, J.P. (2001). Quinupristin-dalfopristin: a new antibiotic for severe gram-positive infections. *Am Fam Physician* 64, 1863-1866.

Maracci, C., Peske, F., Dannies, E., Pohl, C., and Rodnina, M.V. (2014). Ribosome-induced tuning of GTP hydrolysis by a translational GTPase. *Proc Natl Acad Sci U S A* 111, 14418-14423.

Maracci, C., Wohlgemuth, I., and Rodnina, M.V. (2015). Activities of the peptidyl transferase center of ribosomes lacking protein L27. *Rna* 21, 2047-2052.

Marcaurette, L.A., E.C., R., and Bertozzi, C. (1998). Synthesis of an oxime-linked neoglycopeptide with glycosylation-dependent activity similar to its native counterpart. *Tetrahedron Letters* 39, 8417-8420.

Mardirossian, M., Barriere, Q., Timchenko, T., Muller, C., Pacor, S., Mergaert, P., Scocchi, M., and Wilson, D.N. (2018a). Fragments of the Nonlytic Proline-Rich Antimicrobial Peptide Bac5 Kill *Escherichia coli* Cells by Inhibiting Protein Synthesis. *Antimicrob Agents Chemother* 62.

Mardirossian, M., Grzela, R., Giglione, C., Meinel, T., Gennaro, R., Mergaert, P., and Scocchi, M. (2014). The host antimicrobial peptide Bac71-35 binds to bacterial ribosomal proteins and inhibits protein synthesis. *Chemistry & biology* 21, 1639-1647.

Mardirossian, M., Perebaskine, N., Benincasa, M., Gambato, S., Hofmann, S., Huter, P., Muller, C., Hilpert, K., Innis, C.A., Tossi, A., *et al.* (2018b). The Dolphin Proline-Rich Antimicrobial Peptide Tur1A Inhibits Protein Synthesis by Targeting the Bacterial Ribosome. *Cell Chem Biol* 25, 530-539 e537.

Mardirossian, M., Sola, R., Beckert, B., Collis, D.W.P., Di Stasi, A., Armas, F., Hilpert, K., Wilson, D.N., and Scocchi, M. (2019). Proline-Rich Peptides with Improved Antimicrobial Activity against *E. coli*, *K. pneumoniae*, and *A. baumannii*. *ChemMedChem* 14, 2025-2033.

Mardirossian, M., Sola, R., Beckert, B., Valencic, E., Collis, D.W.P., Borisek, J., Armas, F., Di Stasi, A., Buchmann, J., Syroegin, E.A., *et al.* (2020). Peptide Inhibitors of Bacterial Protein Synthesis with Broad Spectrum and SbmA-Independent Bactericidal Activity against Clinical Pathogens. *J Med Chem* 63, 9590-9602.

Marks, J., Kannan, K., Roncase, E.J., Klepacki, D., Kefi, A., Orelle, C., Vazquez-Laslop, N., and Mankin, A.S. (2016). Context-specific inhibition of translation by ribosomal antibiotics targeting the peptidyl transferase center. *Proc Natl Acad Sci U S A* 113, 12150-12155.

Marshall, R.A., Aitken, C.E., and Puglisi, J.D. (2009). GTP hydrolysis by IF2 guides progression of the ribosome into elongation. *Mol Cell* 35, 37-47.

Matzov, D., Eyal, Z., Benhamou, R.I., Shalev-Benami, M., Halfon, Y., Krupkin, M., Zimmerman, E., Rozenberg, H., Bashan, A., Fridman, M., *et al.* (2017). Structural insights of lincosamides targeting the ribosome of *Staphylococcus aureus*. *Nucleic Acids Res* 45, 10284-10292.

Maxwell, K.N., Fisher, E.A., and Breslow, J.L. (2005). Overexpression of PCSK9 accelerates the degradation of the LDLR in a post-endoplasmic reticulum compartment. *Proc Natl Acad Sci U S A* 102, 2069-2074.

McManus, A.M., Otvos, L., Jr., Hoffmann, R., and Craik, D.J. (1999). Conformational studies by NMR of the antimicrobial peptide, drosocin, and its non-glycosylated derivative: effects of glycosylation on solution conformation. *Biochemistry* 38, 705-714.

McQuillen, K., Roberts, R.B., and Britten, R.J. (1959). Synthesis of Nascent Protein by Ribosomes in *Escherichia Coli*. *Proc Natl Acad Sci U S A* 45, 1437-1447.

Menninger, J.R., and Coleman, R.A. (1993). Lincosamide Antibiotics Stimulate Dissociation of Peptidyl-Transfer RNA from Ribosomes. *Antimicrob Agents Chemother* 37, 2027-2029.

Meteliev, M., Osterman, I.A., Ghilarov, D., Khabibullina, N.F., Yakimov, A., Shabalin, K., Utkina, I., Travin, D.Y., Komarova, E.S., Serebryakova, M., *et al.* (2017). Klebsazolicin inhibits 70S ribosome by obstructing the peptide exit tunnel. *Nat Chem Biol* 13, 1129-1136.

Milon, P., Konevega, A.L., Gualerzi, C.O., and Rodnina, M.V. (2008). Kinetic checkpoint at a late step in translation initiation. *Mol Cell* 30, 712-720.

Milon, P., Maracci, C., Filonava, L., Gualerzi, C.O., and Rodnina, M.V. (2012). Real-time assembly landscape of bacterial 30S translation initiation complex. *Nat Struct Mol Biol* 19, 609-615.

Mitcheltree, M.J., Pisipati, A., Syroegin, E.A., Silvestre, K.J., Klepacki, D., Mason, J.D., Terwilliger, D.W., Testolin, G., Pote, A.R., Wu, K.J.Y., *et al.* (2021). A synthetic antibiotic class overcoming bacterial multidrug resistance. *Nature* 599, 507-512.

Moazed, D., and Noller, H.F. (1989). Intermediate states in the movement of transfer RNA in the ribosome. *Nature* 342, 142-148.

Mohamad, M., Nicholson, D., Saha, C.K., Hauryliuk, V., Edwards, T.A., Atkinson, G.C., Ranson, N.A., and O'Neill, A.J. (2022). Sal-type ABC-F proteins: intrinsic and common mediators of pleuromutilin resistance by target protection in staphylococci. *Nucleic Acids Res* 50, 2128-2142.

Mora, L., Heurgue-Hamard, V., de Zamaroczy, M., Kervestin, S., and Buckingham, R.H. (2007). Methylation of bacterial release factors RF1 and RF2 is required for normal translation termination in vivo. *J Biol Chem* 282, 35638-35645.

Moriarty, N.W., Grosse-Kunstleve, R.W., and Adams, P.D. (2009). electronic Ligand Builder and Optimization Workbench (eLBOW): a tool for ligand coordinate and restraint generation. *Acta Crystallogr D Biol Crystallogr* 65, 1074-1080.

Murina, V., Kasari, M., Hauryliuk, V., and Atkinson, G.C. (2018). Antibiotic resistance ABCF proteins reset the peptidyl transferase centre of the ribosome to counter translational arrest. *Nucleic Acids Res*, doi: 10.1093/nar/gky1050.

Myasnikov, A.G., Marzi, S., Simonetti, A., Giuliadori, A.M., Gualerzi, C.O., Yusupova, G., Yusupov, M., and Klaholz, B.P. (2005). Conformational transition of initiation factor 2 from the GTP- to GDP-bound state visualized on the ribosome. *Nat Struct Mol Biol* 12, 1145-1149.

Nakagawa, S., Niimura, Y., Miura, K., and Gojobori, T. (2010). Dynamic evolution of translation initiation mechanisms in prokaryotes. *Proc Natl Acad Sci U S A* 107, 6382-6387.

Nierhaus, K.H. (1991). The assembly of prokaryotic ribosomes. *Biochimie* 73, 739-755.

Nishima, W., Girodat, D., Holm, M., Rundlet, E.J., Alejo, J.L., Fischer, K., Blanchard, S.C., and Sanbonmatsu, K.Y. (2022). Hyper-swivel head domain motions are required for complete mRNA-tRNA translocation and ribosome resetting. *Nucleic Acids Res* 50, 8302-8320.

Nissen, P., Hansen, J., Ban, N., Moore, P.B., and Steitz, T.A. (2000). The structural basis of ribosome activity in peptide bond synthesis. *Science* 289, 920-930.

Nissen, P., Kjeldgaard, M., Thirup, S., Polekhina, G., Reshetnikova, L., Clark, B.F., and Nyborg, J. (1995). Crystal structure of the ternary complex of Phe-tRNAPhe, EF-Tu, and a GTP analog. *Science* 270, 1464-1472.

Noeske, J., Huang, J., Olivier, N.B., Giacobbe, R.A., Zambrowski, M., and Cate, J.H. (2014). Synergy of streptogramin antibiotics occurs independently of their effects on translation. *Antimicrob Agents Chemother* 58, 5269-5279.

Noller, H.F. (2012). Evolution of protein synthesis from an RNA world. *Cold Spring Harb Perspect Biol* 4, a003681.

O'Connor, M., Gregory, S.T., Rajbhandary, U.L., and Dahlberg, A.E. (2001). Altered discrimination of start codons and initiator tRNAs by mutant initiation factor 3. *Rna* 7, 969-978.

O'Donnell, S.M., and Janssen, G.R. (2002). Leaderless mRNAs bind 70S ribosomes more strongly than 30S ribosomal subunits in *Escherichia coli*. *J Bacteriol* 184, 6730-6733.

Ogle, J.M., Brodersen, D.E., Clemons, W.M., Jr., Tarry, M.J., Carter, A.P., and Ramakrishnan, V. (2001). Recognition of cognate transfer RNA by the 30S ribosomal subunit. *Science* 292, 897-902.

Osterman, I.A., Khabibullina, N.F., Komarova, E.S., Kasatsky, P., Kartsev, V.G., Bogdanov, A.A., Dontsova, O.A., Konevega, A.L., Sergiev, P.V., and Polikanov, Y.S. (2017). Madumycin II inhibits peptide bond formation by forcing the peptidyl transferase center into an inactive state. *Nucleic Acids Res* 45, 7507-7514.

Osterman, I.A., Wieland, M., Maviza, T.P., Lashkevich, K.A., Lukianov, D.A., Komarova, E.S., Zakalyukina, Y.V., Buschauer, R., Shiriaev, D.I., Leyn, S.A., *et al.* (2020). Tetracenomycin X inhibits translation by binding within the ribosomal exit tunnel. *Nat Chem Biol* 16, 1071-1077.

Otvos, L., Jr., O, I., Rogers, M.E., Consolvo, P.J., Condie, B.A., Lovas, S., Bulet, P., and Blaszczyk-Thurin, M. (2000). Interaction between heat shock proteins and antimicrobial peptides. *Biochemistry* 39, 14150-14159.

Palade, G.E. (1955). A small particulate component of the cytoplasm. *J Biophys Biochem Cytol* 1, 59-68.

Pallesen, J., Hashem, Y., Korkmaz, G., Koripella, R.K., Huang, C., Ehrenberg, M., Sanyal, S., and Frank, J. (2013). Cryo-EM visualization of the ribosome in termination complex with apo-RF3 and RF1. *Elife* 2, e00411.

Paranjpe, M.N., Marina, V.I., Grachev, A.A., Maviza, T.P., Tolicheva, O.A., Paleskava, A., Osterman, I.A., Sergiev, P.V., Konevega, A.L., Polikanov, Y.S., *et al.* (2022).

Insights into the molecular mechanism of translation inhibition by the ribosome-targeting antibiotic thermorubin. *bioRxiv*, 2022.2009.2015.508020.

Pelechano, V., and Alepuz, P. (2017). eIF5A facilitates translation termination globally and promotes the elongation of many non polyproline-specific tripeptide sequences. *Nucleic Acids Res* 45, 7326-7338.

Petrelli, D., LaTeana, A., Garofalo, C., Spurio, R., Pon, C.L., and Gualerzi, C.O. (2001). Translation initiation factor IF3: two domains, five functions, one mechanism? *EMBO J* 20, 4560-4569.

Petrychenko, V., Peng, B.Z., de, A.P.S.A.C., Peske, F., Rodnina, M.V., and Fischer, N. (2021). Structural mechanism of GTPase-powered ribosome-tRNA movement. *Nat Commun* 12, 5933.

Pettersen, E.F., Goddard, T.D., Huang, C.C., Meng, E.C., Couch, G.S., Croll, T.I., Morris, J.H., and Ferrin, T.E. (2021). UCSF ChimeraX: Structure visualization for researchers, educators, and developers. *Protein Sci* 30, 70-82.

Pierson, W.E., Hoffer, E.D., Keedy, H.E., Simms, C.L., Dunham, C.M., and Zaher, H.S. (2016). Uniformity of Peptide Release Is Maintained by Methylation of Release Factors. *Cell reports* 17, 11-18.

Pioletti, M., Schlunzen, F., Harms, J., Zarivach, R., Gluhmann, M., Avila, H., Bashan, A., Bartels, H., Auerbach, T., Jacobi, C., *et al.* (2001). Crystal structures of complexes of the small ribosomal subunit with tetracycline, edeine and IF3. *EMBO J* 20, 1829-1839.

Polikanov, Y.S., Aleksashin, N.A., Beckert, B., and Wilson, D.N. (2018). The Mechanisms of Action of Ribosome-Targeting Peptide Antibiotics. *Front Mol Biosci* 5, 48.

Polikanov, Y.S., Steitz, T.A., and Innis, C.A. (2014a). A proton wire to couple aminoacyl-tRNA accommodation and peptide-bond formation on the ribosome. *Nat Struct Mol Biol* 21, 787-793.

Polikanov, Y.S., Szal, T., Jiang, F., Gupta, P., Matsuda, R., Shiozuka, M., Steitz, T.A., Vazquez-Laslop, N., and Mankin, A.S. (2014b). Negamycin interferes with decoding and translocation by simultaneous interaction with rRNA and tRNA. *Mol Cell* 56, 541-550.

Poole, E.S., Brown, C.M., and Tate, W.P. (1995). The identity of the base following the stop codon determines the efficiency of in vivo translational termination in *Escherichia coli*. *EMBO J* 14, 151-158.

Prabhakar, A., Capece, M.C., Petrov, A., Choi, J., and Puglisi, J.D. (2017). Post-termination Ribosome Intermediate Acts as the Gateway to Ribosome Recycling. *Cell Rep* 20, 161-172.

Qin, D., Liu, Q., Devaraj, A., and Fredrick, K. (2012). Role of helix 44 of 16S rRNA in the fidelity of translation initiation. *Rna* 18, 485-495.

Quan, S., Skovgaard, O., McLaughlin, R.E., Buurman, E.T., and Squires, C.L. (2015). Markerless *Escherichia coli* *rrn* Deletion Strains for Genetic Determination of Ribosomal Binding Sites. *G3 (Bethesda)* 5, 2555-2557.

Rabel, D., Charlet, M., Ehret-Sabatier, L., Cavicchioli, L., Cudic, M., Otvos, L., Jr., and Bulet, P. (2004). Primary structure and in vitro antibacterial properties of the *Drosophila melanogaster* attacin C Pro-domain. *J Biol Chem* 279, 14853-14859.

Ramrath, D.J., Lancaster, L., Sprink, T., Mielke, T., Loerke, J., Noller, H.F., and Spahn, C.M. (2013). Visualization of two transfer RNAs trapped in transit during elongation factor G-mediated translocation. *Proc Natl Acad Sci U S A* 110, 20964-20969.

Ramu, H., Vazquez-Laslop, N., Klepacki, D., Dai, Q., Piccirilli, J., Micura, R., and Mankin, A.S. (2011). Nascent peptide in the ribosome exit tunnel affects functional properties of the A-site of the peptidyl transferase center. *Mol Cell* 41, 321-330.

Ratje, A.H., Loerke, J., Mikolajka, A., Brunner, M., Hildebrand, P.W., Starosta, A.L., Donhofer, A., Connell, S.R., Fucini, P., Mielke, T., *et al.* (2010). Head swivel on the ribosome facilitates translocation by means of intra-subunit tRNA hybrid sites. *Nature* 468, 713-716.

Rawat, U., Gao, H., Zavialov, A., Gursky, R., Ehrenberg, M., and Frank, J. (2006). Interactions of the release factor RF1 with the ribosome as revealed by cryo-EM. *J Mol Biol* 357, 1144-1153.

Rawat, U.B., Zavialov, A.V., Sengupta, J., Valle, M., Grassucci, R.A., Linde, J., Vestergaard, B., Ehrenberg, M., and Frank, J. (2003). A cryo-electron microscopic study of ribosome-bound termination factor RF2. *Nature* 421, 87-90.

Rheinberger, H.J., Sternbach, H., and Nierhaus, K.H. (1981). Three tRNA binding sites on *Escherichia coli* ribosomes. *Proc Natl Acad Sci U S A* 78, 5310-5314.

Ringquist, S., Jones, T., Snyder, E.E., Gibson, T., Boni, I., and Gold, L. (1995). High-affinity RNA ligands to *Escherichia coli* ribosomes and ribosomal protein S1: comparison of natural and unnatural binding sites. *Biochemistry* 34, 3640-3648.

Rodnina, M.V. (2018). Translation in Prokaryotes. *Cold Spring Harb Perspect Biol* 10.

Rodnina, M.V., Pape, T., Fricke, R., Kuhn, L., and Wintermeyer, W. (1996). Initial binding of the elongation factor Tu.GTP.aminoacyl-tRNA complex preceding codon recognition on the ribosome. *J Biol Chem* 271, 646-652.

Rodriguez, E.C., Winans, K.A., King, D.S., and Bertozzi, C.R. (1997). A Strategy for the Chemoselective Synthesis of O-Linked Glycopeptides with Native Sugar–Peptide Linkages. *J. Am. Chem. Soc.* 113, 9905–9906.

Rohou, A., and Grigorieff, N. (2015). CTFFIND4: Fast and accurate defocus estimation from electron micrographs. *Journal of structural biology* 192, 216-221.

Roy, B., Liu, Q., Shoji, S., and Fredrick, K. (2018). IF2 and unique features of initiator tRNA(fMet) help establish the translational reading frame. *RNA Biol* 15, 604-613.

Roy, R.N., Lomakin, I.B., Gagnon, M.G., and Steitz, T.A. (2015). The mechanism of inhibition of protein synthesis by the proline-rich peptide oncocin. *Nat Struct Mol Biol* 22, 466-469.

Rudra, P., Hurst-Hess, K.R., Cotten, K.L., Partida-Miranda, A., and Ghosh, P. (2020). Mycobacterial HflX is a ribosome splitting factor that mediates antibiotic resistance. *Proc Natl Acad Sci U S A* 117, 629-634.

Rundlet, E.J., Holm, M., Schacherl, M., Natchiar, S.K., Altman, R.B., Spahn, C.M.T., Myasnikov, A.G., and Blanchard, S.C. (2021). Structural basis of early translocation events on the ribosome. *Nature* 595, 741-745.

Santos, N., Zhu, J., Donohue, J.P., Korostelev, A.A., and Noller, H.F. (2013). Crystal structure of the 70S ribosome bound with the Q253P mutant form of release factor RF2. *Structure* 21, 1258-1263.

Savelsbergh, A., Rodnina, M.V., and Wintermeyer, W. (2009). Distinct functions of elongation factor G in ribosome recycling and translocation. *Rna* 15, 772-780.

Scheidig, A.J., Burmester, C., and Goody, R.S. (1999). The pre-hydrolysis state of p21(ras) in complex with GTP: new insights into the role of water molecules in the GTP hydrolysis reaction of ras-like proteins. *Structure* 7, 1311-1324.

Scheres, S.H. (2012). RELION: implementation of a Bayesian approach to cryo-EM structure determination. *Journal of structural biology* 180, 519-530.

Schlunzen, F., Takemoto, C., Wilson, D.N., Kaminishi, T., Harms, J.M., Hanawa-Suetsugu, K., Szaflarski, W., Kawazoe, M., Shirouzu, M., Nierhaus, K.H., *et al.* (2006). The antibiotic kasugamycin mimics mRNA nucleotides to destabilize tRNA binding and inhibit canonical translation initiation. *Nat Struct Mol Biol* 13, 871-878.

Schlunzen, F., Tocilj, A., Zarivach, R., Harms, J., Gluehmann, M., Janell, D., Bashan, A., Bartels, H., Agmon, I., Franceschi, F., *et al.* (2000). Structure of functionally activated small ribosomal subunit at 3.3 Å Resolution. *Cell* 102, 8.

Schlunzen, F., Harms, J.M., Franceschi, F., Hansen, H.A., Bartels, H., Zarivach, R., and Yonath, A. (2003). Structural basis for the antibiotic activity of ketolides and azalides. *Structure* 11, 329-338.

Schlunzen, F., Pyetan, E., Fucini, P., Yonath, A., and Harms, J. (2004). Inhibition of peptide bond formation by pleuromutilins: the structure of the 50S ribosomal subunit from *Deinococcus radiodurans* in complex with tiamulin. *Mol. Microbiol.* 54, 1287-1294.

Schlunzen, F., Zarivach, R., Harms, J., Bashan, A., Tocilj, A., Albrecht, R., Yonath, A., and Franceschi, F. (2001). Structural basis for the interaction of antibiotics with the peptidyl transferase centre in eubacteria. *Nature* 413, 814-821.

Schmeing, T.M., Huang, K.S., Strobel, S.A., and Steitz, T.A. (2005). An induced-fit mechanism to promote peptide bond formation and exclude hydrolysis of peptidyl-tRNA. *Nature* 438, 520-524.

Schmeing, T.M., and Ramakrishnan, V. (2009). What recent ribosome structures have revealed about the mechanism of translation. *Nature* 461, 1234-1242.

Schmeing, T.M., Voorhees, R.M., Kelley, A.C., Gao, Y.G., Murphy, F.V.t., Weir, J.R., and Ramakrishnan, V. (2009). The crystal structure of the ribosome bound to EF-Tu and aminoacyl-tRNA. *Science* 326, 688-694.

Schmeing, T.M., Voorhees, R.M., Kelley, A.C., and Ramakrishnan, V. (2011). How mutations in tRNA distant from the anticodon affect the fidelity of decoding. *Nat Struct Mol Biol* 18, 432-436.

Schuller, A.P., Wu, C.C., Dever, T.E., Buskirk, A.R., and Green, R. (2017). eIF5A Functions Globally in Translation Elongation and Termination. *Mol Cell* 66, 194-205 e195.



Schuwirth, B.S., Day, J.M., Hau, C.W., Janssen, G.R., Dahlberg, A.E., Cate, J.H., and Vila-Sanjurjo, A. (2006). Structural analysis of kasugamycin inhibition of translation. *Nat Struct Mol Biol* 13, 879-886.

Scocchi, M., Tossi, A., and Gennaro, R. (2011). Proline-rich antimicrobial peptides: converging to a non-lytic mechanism of action. *Cell Mol Life Sci* 68, 2317-2330.

Seefeldt, A.C., Graf, M., Perebaskine, N., Nguyen, F., Arenz, S., Mardirossian, M., Scocchi, M., Wilson, D.N., and Innis, C.A. (2016). Structure of the mammalian antimicrobial peptide Bac7(1-16) bound within the exit tunnel of a bacterial ribosome. *Nucleic acids research* 44, 2429-2438.

Seefeldt, A.C., Nguyen, F., Antunes, S., Perebaskine, N., Graf, M., Arenz, S., Inampudi, K.K., Douat, C., Guichard, G., Wilson, D.N., *et al.* (2015). The proline-rich antimicrobial peptide Onc112 inhibits translation by blocking and destabilizing the initiation complex. *Nat Struct Mol Biol* 22, 470-475.

Seiple, I.B., Zhang, Z., Jakubec, P., Langlois-Mercier, A., Wright, P.M., Hog, D.T., Yabu, K., Allu, S.R., Fukuzaki, T., Carlsen, P.N., *et al.* (2016). A platform for the discovery of new macrolide antibiotics. *Nature* 533, 338-345.

Sharkey, L.K., Edwards, T.A., and O'Neill, A.J. (2016). ABC-F Proteins Mediate Antibiotic Resistance through Ribosomal Protection. *mBio* 7.

Sharkey, L.K.R., and O'Neill, A.J. (2018). Antibiotic Resistance ABC-F Proteins: Bringing Target Protection into the Limelight. *ACS Infect Dis* 4, 239-246.

Shi, X., and Joseph, S. (2016). Mechanism of Translation Termination: RF1 Dissociation Follows Dissociation of RF3 from the Ribosome. *Biochemistry* 55, 6344-6354.

Shine, J., and Dalgarno, L. (1974). The 3'-terminal sequence of *Escherichia coli* 16S ribosomal RNA: complementarity to nonsense triplets and ribosome binding sites. *Proc Natl Acad Sci U S A* 71, 1342-1346.

Shivakumar, A.G., Hahn, J., Grandi, G., Kozlov, Y., and Dubnau, D. (1980). Posttranscriptional regulation of an erythromycin resistance protein specified by plasmic pE194. *Proc Natl Acad Sci U S A* 77, 3903-3907.

Sievers, A., Beringer, M., Rodnina, M.V., and Wolfenden, R. (2004). The ribosome as an entropy trap. *Proc Natl Acad Sci U S A* 101, 7897-7901.

Simonetti, A., Marzi, S., Myasnikov, A.G., Fabbretti, A., Yusupov, M., Gualerzi, C.O., and Klaholz, B.P. (2008). Structure of the 30S translation initiation complex. *Nature* 455, 416-420.

Sohmen, D., Chiba, S., Shimokawa-Chiba, N., Innis, C.A., Berninghausen, O., Beckmann, R., Ito, K., and Wilson, D.N. (2015). Structure of the *Bacillus subtilis* 70S ribosome reveals the basis for species-specific stalling. *Nat Commun* 6, 6941.

Sohmen, D., Harms, J.M., Schlunzen, F., and Wilson, D.N. (2009). Enhanced SnapShot: Antibiotic inhibition of protein synthesis II. *Cell* 139, 212-212 e211.

Sola, R., Mardirossian, M., Beckert, B., Sanghez De Luna, L., Prickett, D., Tossi, A., Wilson, D.N., and Scocchi, M. (2020). Characterization of Cetacean Proline-Rich Antimicrobial Peptides Displaying Activity against ESKAPE Pathogens. *Int J Mol Sci* 21.

Sothiselvam, S., Liu, B., Han, W., Ramu, H., Klepacki, D., Atkinson, G.C., Brauer, A., Remm, M., Tenson, T., Schulten, K., *et al.* (2014). Macrolide antibiotics allosterically predispose the ribosome for translation arrest. *Proc Natl Acad Sci U S A* 111, 9804-9809.

Sothiselvam, S., Neuner, S., Rigger, L., Klepacki, D., Micura, R., Vazquez-Laslop, N., and Mankin, A.S. (2016). Binding of Macrolide Antibiotics Leads to Ribosomal Selection against Specific Substrates Based on Their Charge and Size. *Cell Rep* 16, 1789-1799.

Srinivasan, K., Dey, S., and Sengupta, J. (2019). Structural modules of the stress-induced protein HflX: an outlook on its evolution and biological role. *Curr Genet* 65, 363-370.

Stanley, R.E., Blaha, G., Grodzicki, R.L., Strickler, M.D., and Steitz, T.A. (2010). The structures of the anti-tuberculosis antibiotics viomycin and capreomycin bound to the 70S ribosome. *Nat Struct Mol Biol* 17, 289-293.

Stark, H., Rodnina, M.V., Rinke-Appel, J., Brimacombe, R., Wintermeyer, W., and van Heel, M. (1997). Visualization of elongation factor Tu on the *Escherichia coli* ribosome. *Nature* 389, 403-406.

Steinmetz, H., Irschik, H., Reichenbach, H., H., H., and Höfle, G. (1987). Structure elucidation of the peptide antibiotics myxovalargin A-D. *Chemistry of Peptides and Proteins - Proceedings of the Sixth USSR-FRG Symposium on Chemistry of Peptides and Proteins*, 13-18.

Steitz, J.A., and Jakes, K. (1975). How ribosomes select initiator regions in mRNA: base pair formation between the 3' terminus of 16S rRNA and the mRNA during initiation of protein synthesis in *Escherichia coli*. *Proc Natl Acad Sci U S A* 72, 4734-4738.

Studer, S.M., and Joseph, S. (2006). Unfolding of mRNA secondary structure by the bacterial translation initiation complex. *Mol Cell* 22, 105-115.

Su, W., Kumar, V., Ding, Y., Ero, R., Serra, A., Lee, B.S.T., Wong, A.S.W., Shi, J., Sze, S.K., Yang, L., *et al.* (2018). Ribosome protection by antibiotic resistance ATP-binding cassette protein. *Proc Natl Acad Sci U S A* 115, 5157-5162.

Svetlov, M.S., Cohen, S., Alsuhebany, N., Vazquez-Laslop, N., and Mankin, A.S. (2020). A long-distance rRNA base pair impacts the ability of macrolide antibiotics to kill bacteria. *Proc Natl Acad Sci U S A*.

Svetlov, M.S., Koller, T.O., Meydan, S., Shankar, V., Klepacki, D., Polacek, N., Gydosh, N.R., Vazquez-Laslop, N., Wilson, D.N., and Mankin, A.S. (2021a). Context-specific action of macrolide antibiotics on the eukaryotic ribosome. *Nat Commun* 12, 2803.

Svetlov, M.S., Syroegin, E.A., Aleksandrova, E.V., Atkinson, G.C., Gregory, S.T., Mankin, A.S., and Polikanov, Y.S. (2021b). Structure of Erm-modified 70S ribosome reveals the mechanism of macrolide resistance. *Nat Chem Biol* 17, 412-420.

Syroegin, E.A., Aleksandrova, E.V., and Polikanov, Y.S. (2022a). Structural basis for the inability of chloramphenicol to inhibit peptide bond formation in the presence of A-site glycine. *Nucleic Acids Res* 50, 7669-7679.

Syroegin, E.A., Flemmich, L., Klepacki, D., Vazquez-Laslop, N., Micura, R., and Polikanov, Y.S. (2022b). Structural basis for the context-specific action of the classic peptidyl transferase inhibitor chloramphenicol. *Nat Struct Mol Biol* 29, 152-161.

Talat, S., Thiruvikraman, M., Kumari, S., and Kaur, K.J. (2011). Glycosylated analogs of formaecin I and drosocin exhibit differential pattern of antibacterial activity. *Glycoconj J* 28, 537-555.

Tenson, T., Lovmar, M., and Ehrenberg, M. (2003). The mechanism of action of macrolides, lincosamides and streptogramin B reveals the nascent peptide exit path in the ribosome. *J Mol Biol* 330, 1005-1014.

Tesina, P., Heckel, E., Cheng, J., Fromont-Racine, M., Buschauer, R., Kater, L., Beatrix, B., Berninghausen, O., Jacquier, A., Becker, T., *et al.* (2019). Structure of the 80S ribosome-Xrn1 nuclease complex. *Nat Struct Mol Biol* 26, 275-280.

Tomlinson, J.H., Thompson, G.S., Kalverda, A.P., Zhuravleva, A., and O'Neill, A.J. (2016). A target-protection mechanism of antibiotic resistance at atomic resolution: insights into FusB-type fusidic acid resistance. *Sci Rep* 6, 19524.

Tomsic, J., Vitali, L.A., Daviter, T., Savelsbergh, A., Spurio, R., Striebeck, P., Wintermeyer, W., Rodnina, M.V., and Gualerzi, C.O. (2000). Late events of translation initiation in bacteria: a kinetic analysis. *EMBO J* 19, 2127-2136.

Travin, D.Y., Watson, Z.L., Metelev, M., Ward, F.R., Osterman, I.A., Khven, I.M., Khabibullina, N.F., Serebryakova, M., Mergaert, P., Polikanov, Y.S., *et al.* (2019). Structure of ribosome-bound azole-modified peptide phazolicin rationalizes its species-specific mode of bacterial translation inhibition. *Nat Commun* 10, 4563.

Trieber, C.A., Burkhardt, N., Nierhaus, K.H., and Taylor, D.E. (1998). Ribosomal Protection from Tetracycline Mediated by Tet(O) Interaction with Ribosomes Is GTP-Dependent. *Biol. Chem.* 379, 847-855.

Trobro, S., and Aqvist, J. (2009). Mechanism of the translation termination reaction on the ribosome. *Biochemistry* 48, 11296-11303.

Tsai, K., Stojkovic, V., Lee, D.J., Young, I.D., Szal, T., Klepacki, D., Vazquez-Laslop, N., Mankin, A.S., Fraser, J.S., and Fujimori, D.G. (2022). Structural basis for context-specific inhibition of translation by oxazolidinone antibiotics. *Nat Struct Mol Biol* 29, 162-171.

Tu, D., Blaha, G., Moore, P.B., and Steitz, T.A. (2005). Structures of MLSBK antibiotics bound to mutated large ribosomal subunits provide a structural explanation for resistance. *Cell* 121, 257-270.

Uttenweiler-Joseph, S., Moniatte, M., Lagueux, M., Van Dorsselaer, A., Hoffmann, J.A., and Bulet, P. (1998). Differential display of peptides induced during the immune response of *Drosophila*: a matrix-assisted laser desorption ionization time-of-flight mass spectrometry study. *Proc Natl Acad Sci U S A* 95, 11342-11347.

Vagin, A.A., Steiner, R.A., Lebedev, A.A., Potterton, L., McNicholas, S., Long, F., and Murshudov, G.N. (2004). REFMAC5 dictionary: organization of prior chemical knowledge and guidelines for its use. *Acta Crystallogr D Biol Crystallogr* 60, 2184-2195.

Valle, M., Zaviyalov, A., Li, W., Stagg, S.M., Sengupta, J., Nielsen, R.C., Nissen, P., Harvey, S.C., Ehrenberg, M., and Frank, J. (2003). Incorporation of aminoacyl-tRNA into the ribosome as seen by cryo-electron microscopy. *Nat Struct Biol* 10, 899-906.

van der Stel, A.X., Gordon, E.R., Sengupta, A., Martinez, A.K., Klepacki, D., Perry, T.N., Herrero Del Valle, A., Vazquez-Laslop, N., Sachs, M.S., Cruz-Vera, L.R., *et al.* (2021). Structural basis for the tryptophan sensitivity of TnaC-mediated ribosome stalling. *Nat Commun* 12, 5340.

Vannuffel, P., and Cocito, C. (1996). Mechanism of action of streptogramins and macrolides. *Drugs* 51 Suppl 1, 20-30.

Varadi, M., Anyango, S., Deshpande, M., Nair, S., Natassia, C., Yordanova, G., Yuan, D., Stroe, O., Wood, G., Laydon, A., *et al.* (2022). AlphaFold Protein Structure Database: massively expanding the structural coverage of protein-sequence space with high-accuracy models. *Nucleic Acids Res* 50, D439-D444.

Vazquez-Laslop, N., Klepacki, D., Mulhearn, D.C., Ramu, H., Krasnykh, O., Franzblau, S., and Mankin, A.S. (2011). Role of antibiotic ligand in nascent peptide-dependent ribosome stalling. *Proc Natl Acad Sci U S A* 108, 10496-10501.

Vazquez-Laslop, N., and Mankin, A.S. (2011). Picky nascent peptides do not talk to foreign ribosomes. *Proc Natl Acad Sci U S A* 108, 5931-5932.

Vazquez-Laslop, N., and Mankin, A.S. (2018a). Context-Specific Action of Ribosomal Antibiotics. *Annu Rev Microbiol* 72, 185-207.

Vazquez-Laslop, N., and Mankin, A.S. (2018b). How Macrolide Antibiotics Work. *Trends Biochem Sci* 43, 668-684.

Vazquez-Laslop, N., Ramu, H., Klepacki, D., Kannan, K., and Mankin, A.S. (2010). The key function of a conserved and modified rRNA residue in the ribosomal response to the nascent peptide. *EMBO J* 29, 3108-3117.

Voorhees, R.M., Schmeing, T.M., Kelley, A.C., and Ramakrishnan, V. (2010). The mechanism for activation of GTP hydrolysis on the ribosome. *Science* 330, 835-838.

Wagner, T., Merino, F., Stabrin, M., Moriya, T., Antoni, C., Apelbaum, A., Hagel, P., Sitsel, O., Raisch, T., Prumbaum, D., *et al.* (2019). SPHIRE-crYOLO is a fast and accurate fully automated particle picker for cryo-EM. *Commun Biol* 2, 218.

Wallin, G., and Aqvist, J. (2010). The transition state for peptide bond formation reveals the ribosome as a water trap. *Proc Natl Acad Sci U S A* 107, 1888-1893.

Watson, Z.L., Ward, F.R., Meheust, R., Ad, O., Schepartz, A., Banfield, J.F., and Cate, J.H. (2020). Structure of the bacterial ribosome at 2 Å resolution. *Elife* 9.

Weixlbaumer, A., Jin, H., Neubauer, C., Voorhees, R.M., Petry, S., Kelley, A.C., and Ramakrishnan, V. (2008). Insights into translational termination from the structure of RF2 bound to the ribosome. *Science* 322, 953-956.

Wieland, M., Holm, M., Rundlet, E.J., Morici, M., Koller, T.O., Maviza, T.P., Pogorevc, D., Osterman, I.A., Muller, R., Blanchard, S.C., *et al.* (2022). The cyclic octapeptide antibiotic argyrisin B inhibits translation by trapping EF-G on the ribosome during translocation. *Proc Natl Acad Sci U S A* 119, e2114214119.

Wilson, D.N. (2009). The A-Z of bacterial translation inhibitors. *Crit Rev Biochem Mol Biol* 44, 393-433.

Wilson, D.N. (2014). Ribosome-targeting antibiotics and mechanisms of bacterial resistance. *Nat Rev Microbiol* 12, 35-48.

Wilson, D.N., Hauryliuk, V., Atkinson, G.C., and O'Neill, A.J. (2020). Target protection as a key antibiotic resistance mechanism. *Nat Rev Microbiol*.

Wilson, D.N., Schluenzen, F., Harms, J.M., Starosta, A.L., Connell, S.R., and Fucini, P. (2008). The oxazolidinone antibiotics perturb the ribosomal peptidyl-transferase center and effect tRNA positioning. *Proc Natl Acad Sci U S A* 105, 13339-13344.

Winn, M.D., Ballard, C.C., Cowtan, K.D., Dodson, E.J., Emsley, P., Evans, P.R., Keegan, R.M., Krissinel, E.B., Leslie, A.G., McCoy, A., *et al.* (2011). Overview of the CCP4 suite and current developments. *Acta Crystallogr D Biol Crystallogr* 67, 235-242.

Wintermeyer, W., and Gualerzi, C. (1983). Effect of *Escherichia coli* initiation factors on the kinetics of N-AcPhe-tRNA<sup>Phe</sup> binding to 30S ribosomal subunits. A fluorescence stopped-flow study. *Biochemistry* 22, 690-694.

Wool, I.G., Gluck, A., and Endo, Y. (1992). Ribotoxin recognition of ribosomal RNA and a proposal for the mechanism of translocation. *Trends Biochem Sci* 17, 266-269.

Wu, X.Q., and RajBhandary, U.L. (1997). Effect of the amino acid attached to *Escherichia coli* initiator tRNA on its affinity for the initiation factor IF2 and on the IF2 dependence of its binding to the ribosome. *J Biol Chem* 272, 1891-1895.

Yamashita, K., Palmer, C.M., Burnley, T., and Murshudov, G.N. (2021). Cryo-EM single-particle structure refinement and map calculation using Servalcat. *Acta Crystallogr D Struct Biol* 77, 1282-1291.

Yang, K., Chang, J.Y., Cui, Z., Li, X., Meng, R., Duan, L., Thongchol, J., Jakana, J., Huwe, C.M., Sacchettini, J.C., *et al.* (2017). Structural insights into species-specific features of the ribosome from the human pathogen *Mycobacterium tuberculosis*. *Nucleic Acids Res* 45, 10884-10894.

Zaher, H.S., Shaw, J.J., Strobel, S.A., and Green, R. (2011). The 2'-OH group of the peptidyl-tRNA stabilizes an active conformation of the ribosomal PTC. *EMBO J* 30, 2445-2453.

Zavialov, A.V., Buckingham, R.H., and Ehrenberg, M. (2001). A posttermination ribosomal complex is the guanine nucleotide exchange factor for peptide release factor RF3. *Cell* 107, 115-124.

Zavialov, A.V., Mora, L., Buckingham, R.H., and Ehrenberg, M. (2002). Release of peptide promoted by the GGQ motif of class 1 release factors regulates the GTPase activity of RF3. *Mol Cell* 10, 789-798.

Zhang, J., Pan, X., Yan, K., Sun, S., Gao, N., and Sui, S.F. (2015a). Mechanisms of ribosome stalling by SecM at multiple elongation steps. *Elife* 4.

Zhang, Y., Aleksashin, N.A., Klepacki, D., Anderson, C., Vazquez-Laslop, N., Gross, C.A., and Mankin, A.S. (2022). The context of the ribosome binding site in mRNAs defines specificity of action of kasugamycin, an inhibitor of translation initiation. *Proc Natl Acad Sci U S A* 119.

Zhang, Y., Mandava, C.S., Cao, W., Li, X., Zhang, D., Li, N., Zhang, Y., Zhang, X., Qin, Y., Mi, K., *et al.* (2015b). HflX is a ribosome-splitting factor rescuing stalled ribosomes under stress conditions. *Nat Struct Mol Biol* 22, 906-913.

Zheng, S.Q., Palovcak, E., Armache, J.P., Verba, K.A., Cheng, Y., and Agard, D.A. (2017). MotionCor2: anisotropic correction of beam-induced motion for improved cryo-electron microscopy. *Nature methods* 14, 331-332.

Zhou, J., Korostelev, A., Lancaster, L., and Noller, H.F. (2012). Crystal structures of 70S ribosomes bound to release factors RF1, RF2 and RF3. *Curr Opin Struct Biol* 22, 733-742.

Zhou, J., Lancaster, L., Donohue, J.P., and Noller, H.F. (2013). Crystal structures of EF-G-ribosome complexes trapped in intermediate states of translocation. *Science* 340, 1236086.

Zivanov, J., Nakane, T., Forsberg, B.O., Kimanius, D., Hagen, W.J., Lindahl, E., and Scheres, S.H. (2018). New tools for automated high-resolution cryo-EM structure determination in RELION-3. *Elife* 7.

Zivanov, J., Nakane, T., and Scheres, S.H.W. (2019). A Bayesian approach to beam-induced motion correction in cryo-EM single-particle analysis. *IUCrJ* 6, 5-17.

Zubradt, M., Gupta, P., Persad, S., Lambowitz, A.M., Weissman, J.S., and Rouskin, S. (2017). DMS-MaPseq for genome-wide or targeted RNA structure probing in vivo. *Nature methods* 14, 75-82.

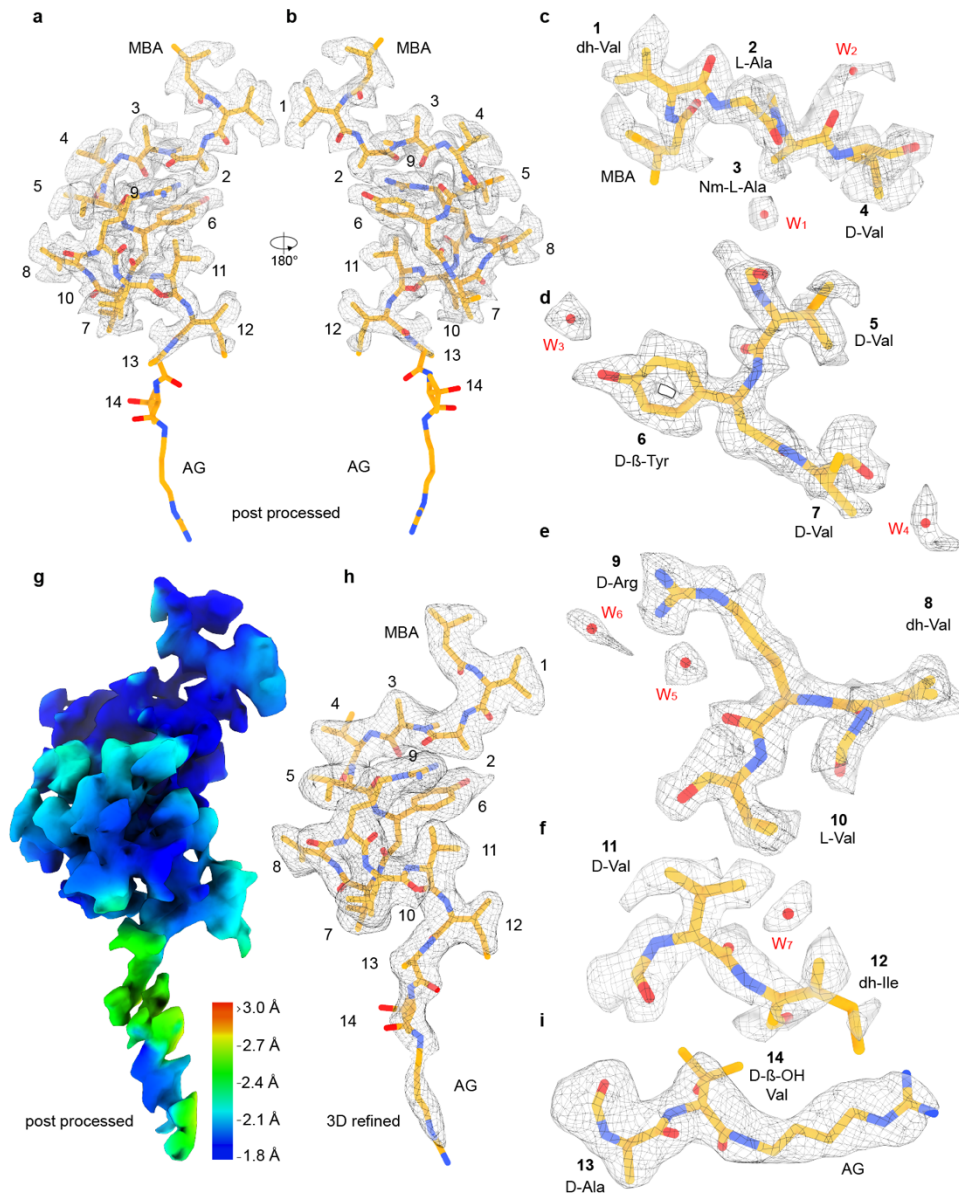


## 13. Supplementary Information

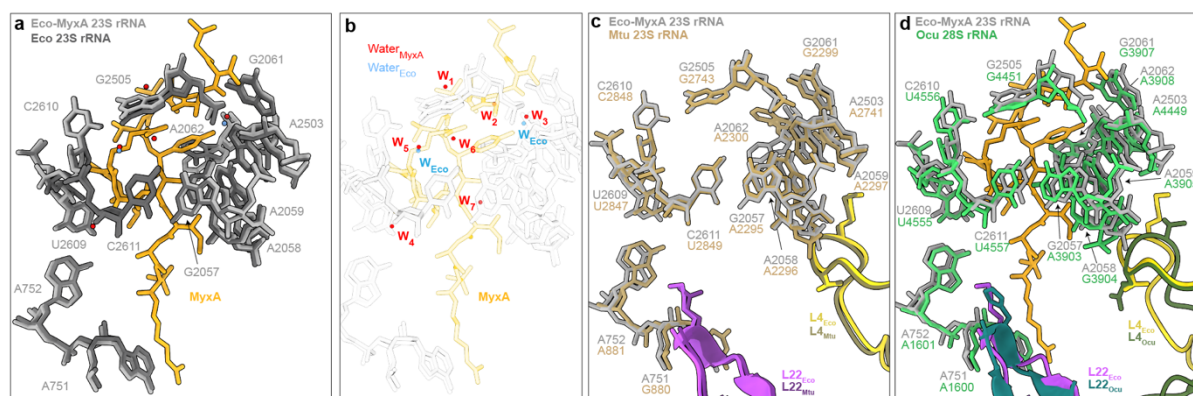
### 13.1. Myxovalargin

**Table 5: Cryo-EM data collection, modelling, and refinement statistics of the myxovalargin-ribosome complexes.**

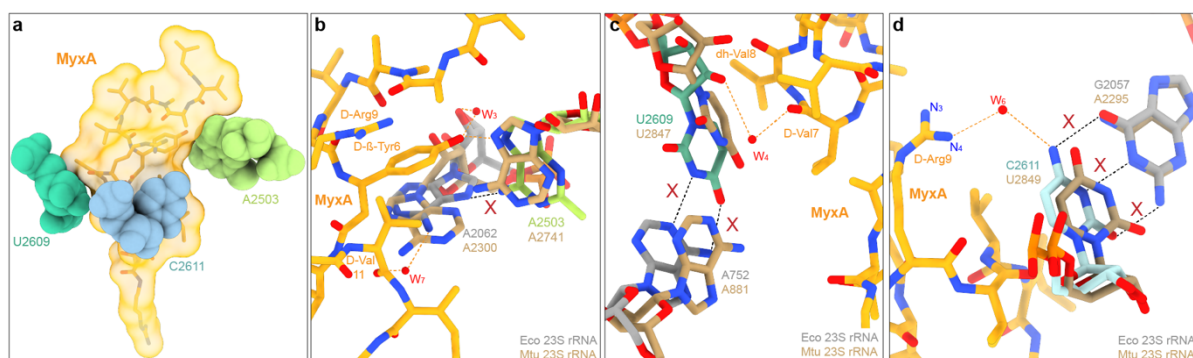
<b>Data collection</b>	<b>MyxA-50S complex PDB ID 7QQ3 EMDB EMD-14121</b>	<b>MyxB-70S complex PDB ID 8B7Y EMDB EMD-15905</b>
Microscope	Titan Krios	Titan Krios
Detector	K2 DDC	Falcon II DDC
Pixel size (Å)	0.828	1.053
Defocus range (µm)	-1.0 to -3.0	-0.7 to -1.2
Voltage (keV)	300	300
Electron dose (e <sup>-</sup> /Å <sup>2</sup> )	1.1	2.5
FSC threshold	0.143	0.143
Initial particle images (no.)	680,054	523,747
Final particle images (no.)	580,425	376,564
<b>Model composition</b>		
Initial model used (PDB code)	7K00	7K00
Protein residues	2896	5307
RNA nucleotides	3016	4614
Magnesium	145	237
Water	28	28
Ligand	1	1
<b>Refinement</b>		
Resolution (Å)	2.1	2.96
Map sharpening B factor(Å <sup>2</sup> )	-10	-40
<b>Validation: proteins</b>		
Poor rotamers (%)	4.22	3.80
Ramachandran outliers (%)	0.42	0.79
Ramachandran allowed (%)	3.55	5.68
Ramachandran favored (%)	96.03	93.54
Bad backbone bonds (%)	0	0.005
Bad backbone angles (%)	0.825	0.737
<b>Validation: RNA</b>		
Correct sugar puckers (%)	99.44	97.69
Good backbone conformations (%)	87.17	80.65
Bad bonds (%)	0.04	0.03
Bad angles (%)	0	0
<b>Scores</b>		
MolProbity	1.81	2.14
Clash score, all atoms	2.7	5.22



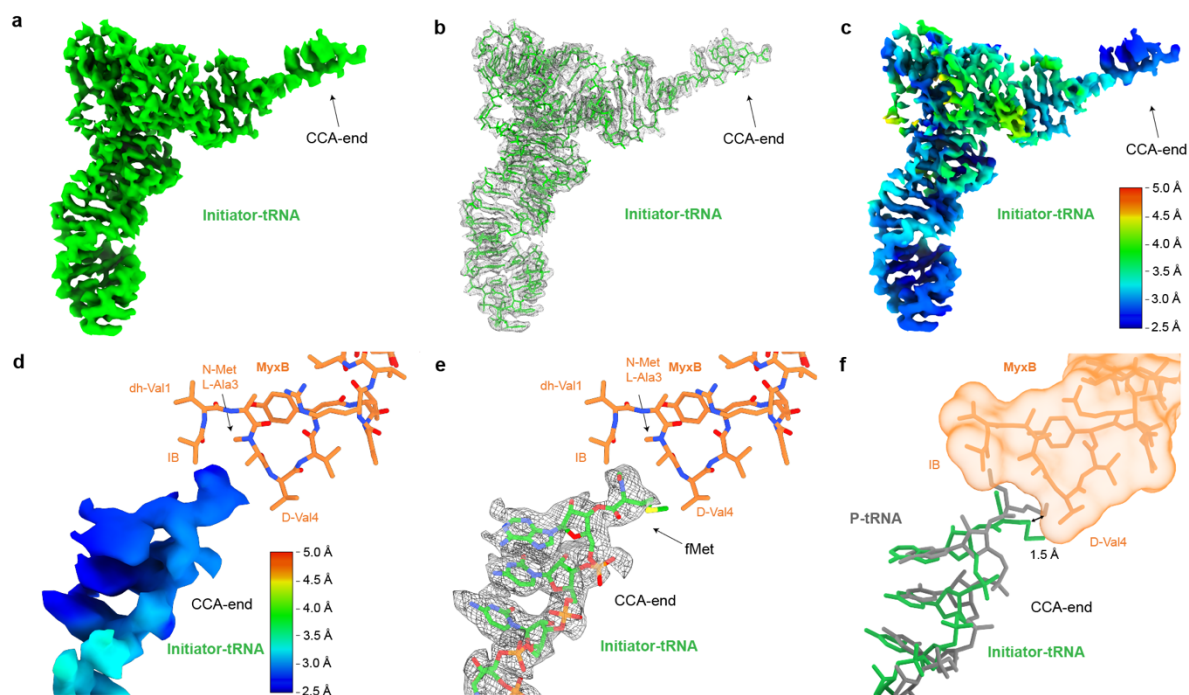
**Supplementary Figure 1: Modelling of MyxA into cryo-EM density of the MyxA-50S-complex.** **a-b**, Molecular model of MyxA (orange) from two perspectives in isolated cryo-EM density (mesh). Residues numbered from 3-methylbutanoic acid (MBA) to agmatine (AG) from 1-14. **c-f**, Zoomed views of molecular modelling of MyxA in isolated density (mesh) with surrounding coordinated water molecules (red). **c**, MBA, dh-Val1, L-Ala2, Nm-L-Ala3 and D-Val4 with waters  $W_1$  and  $W_2$ . **d**, D-Val5, D- $\beta$ -Tyr6, D-Val7 with waters  $W_3$  and  $W_4$ . **e**, dh-Val8, D-Arg9 and L-Val10 with waters  $W_5$  and  $W_6$ . **f**, D-Val11 and dh-Ile12 with water  $W_7$ . **g**, Isolated density of MyxA of the MyxA-50S-complex colored according to local resolution. **h**, Isolated density from the 3D refined map at lower threshold with molecular model of MyxA. **i**, Zoomed view of molecular modelling of D-Ala13, D- $\beta$ -OH-Val14 and AG moiety in isolated density (mesh) at lower threshold.



**Supplementary Figure 2: Superimpositions of the MyxA-50S-complex.** **a**, MyxA-50S-complex 23S rRNA nucleotides (light grey) with MyxA (orange) in the NPET and surrounding water molecules superimposed with the vacant 70S *E. coli* ribosome (dark grey, PDB ID 7K00) (Watson et al., 2020). **b**, Waters  $W_3$  and  $W_5$  (red) observed in MyxA-50S-complex are also present in the vacant 70S *E. coli* ribosome ( $W_{Eco}$ , blue, PDB ID 7K00) (Watson et al., 2020). **c**, MyxA-50S-complex 23S rRNA nucleotides (light grey) with ribosomal proteins  $L4_{Eco}$  (yellow) and  $L22_{Eco}$  (Eco, purple) superimposed with 23S rRNA nucleotides (brown),  $L4_{Mtu}$  (olive) and  $L22_{Mtu}$  (dark purple) from vacant *M. tuberculosis* 70S ribosome (Mtu, PDB ID 7MT7) (Cui et al., 2022). **d**, MyxA-50S-complex 23S rRNA nucleotides (light grey) with MyxA (orange) in the NPET and ribosomal proteins  $L4_{Eco}$  (yellow) and  $L22_{Eco}$  (Eco, purple) superimposed with 28S rRNA nucleotides (green),  $L4_{Ocu}$  (dark turquoise) and  $L22_{Ocu}$  (dark olive) from vacant *O. cuniculus* 70S ribosome (Ocu, PDB ID 6SGC) (Chandrasekaran et al., 2019).



**Supplementary Figure 3: Impact of MyxA<sup>R</sup> resistance mutations on water-mediated interactions.** **a**, Resistance mutations detected in *M. tuberculosis* (PDB ID 5V93) mapped onto *E. coli* 23S rRNA nucleotides A2503 (lime, MtuA2741), U2609 (turquoise, MtuU2847) and C2611 (cyan, MtuU2849) shown as spheres, surrounding MyxA molecular model (orange) represented as surface (Yang et al., 2017). **b**, A2503G (lime, MtuA2741G (brown)) mutation is predicted to break potential hydrogen bond interaction of N6 of  $m^2$ A2503 (grey, A2741(brown)) with N3 of A2062 (grey, MtuA2300 (brown)). This is hypothesized to break hydrogen bonding with  $W_3$  destabilize the stacking of D- $\beta$ -Tyr6 of MyxA with A2062 (MtuA2300). **c**, U2609C (turquoise, MtuU2847C (brown)) mutation is predicted to abolish potential hydrogen bond interactions with  $W_4$  and to break the Watson-Crick-base pair with A752 (grey, MtuA881 (brown)). **d**, C2611G (light blue, MtuU2849G (brown)) mutation is predicted to abolish hydrogen bond interaction with N4 of D-Arg9 with  $W_6$  and break the Watson-Crick-base pair with G2057 (MtuA2295 (brown)). In this position *E. coli* and *M. tuberculosis* have different residues but the predicted impact of the mutation impacts both.

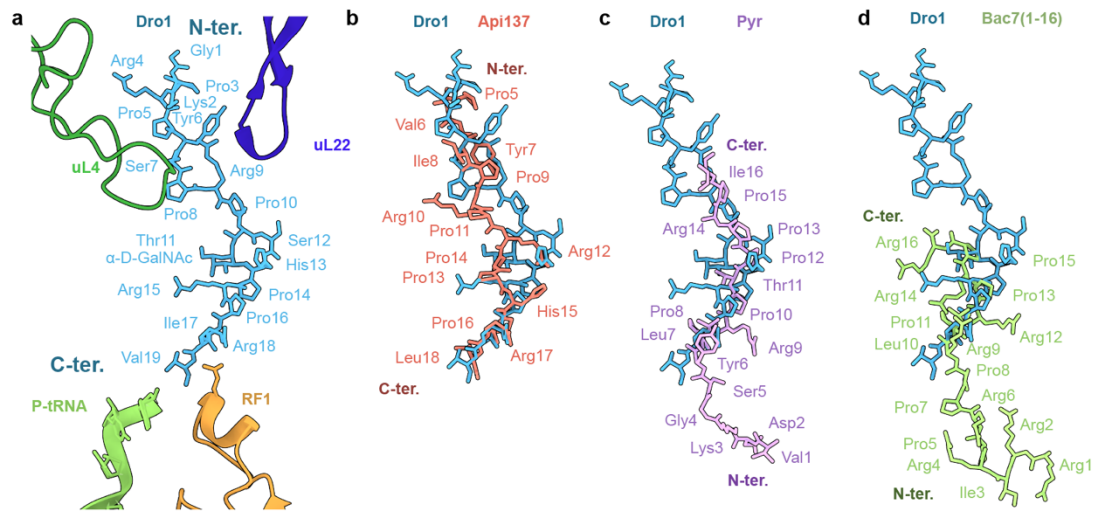


**Supplementary Figure 4: P-tRNA bound to the MyxB-70S-complex.** **a-c**, Isolated density of the initiator fMet-tRNA<sup>fMet</sup> shown as density (**a**, green), mesh with molecular model (**b**, green) and colored according to local resolution (**c**). **d-e**, Molecular model of MyxB (orange) in relative position compared to the isolated density of the CCA-end of the tRNA (**d**) colored according to local resolution (**e**) and with molecular model (mesh). **f**, Initiator fMet-tRNA<sup>fMet</sup> from the MyxB-70S-complex (green) superimposed with the fMet-tRNA<sup>fMet</sup> from the pre-attack state (grey, PDB ID 1VY4) (Polikanov et al., 2014a) with MyxB (orange) shown as surface. The CCA-end of the tRNA in the MyxB-70S-complex is shifted by 1.5 Å to avoid steric clashing with N-terminal residues of MyxB.

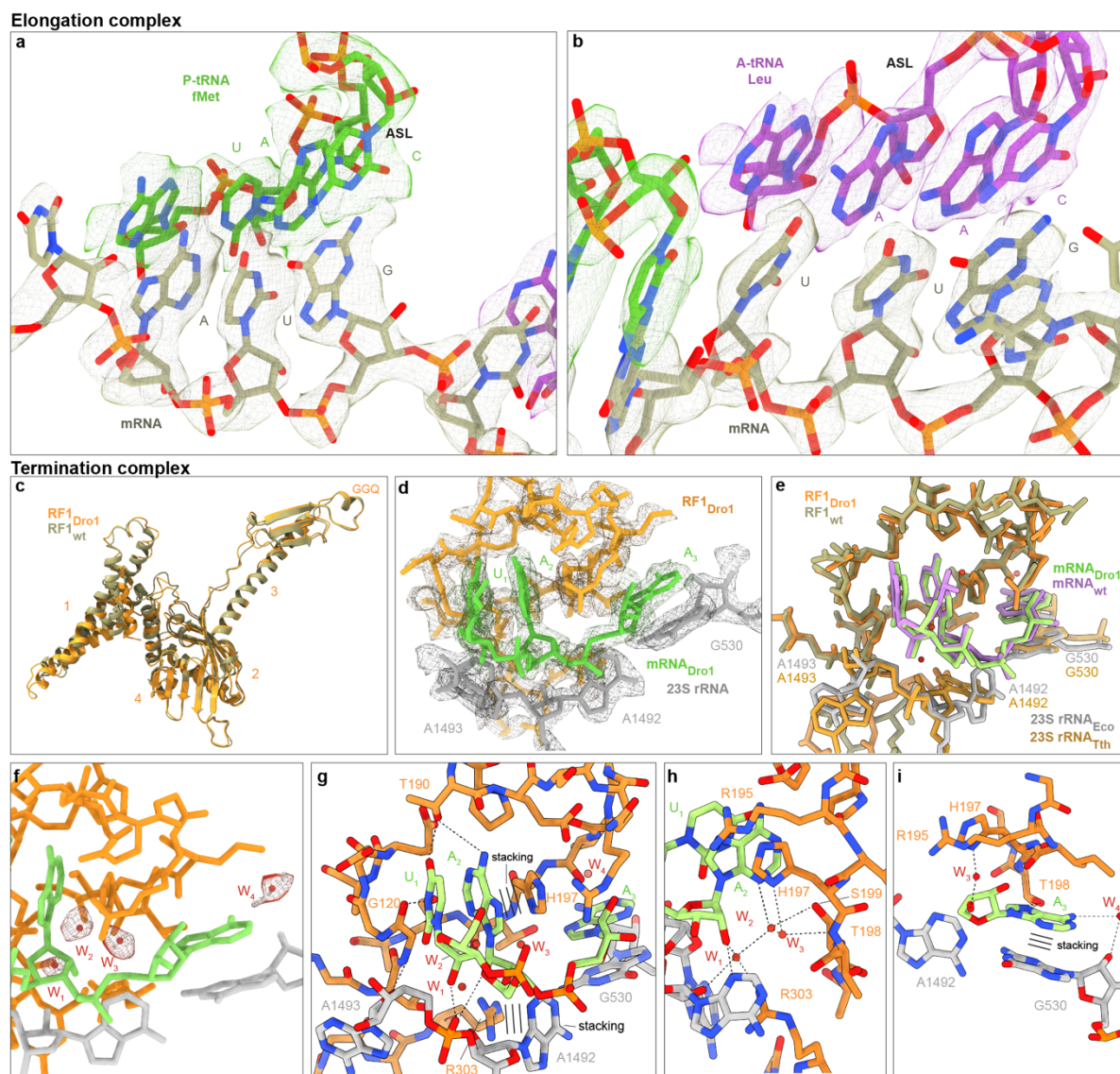
## 13.2. Drosocin

**Table 6: Drosocin data collection, modelling, and refinement statistics.**

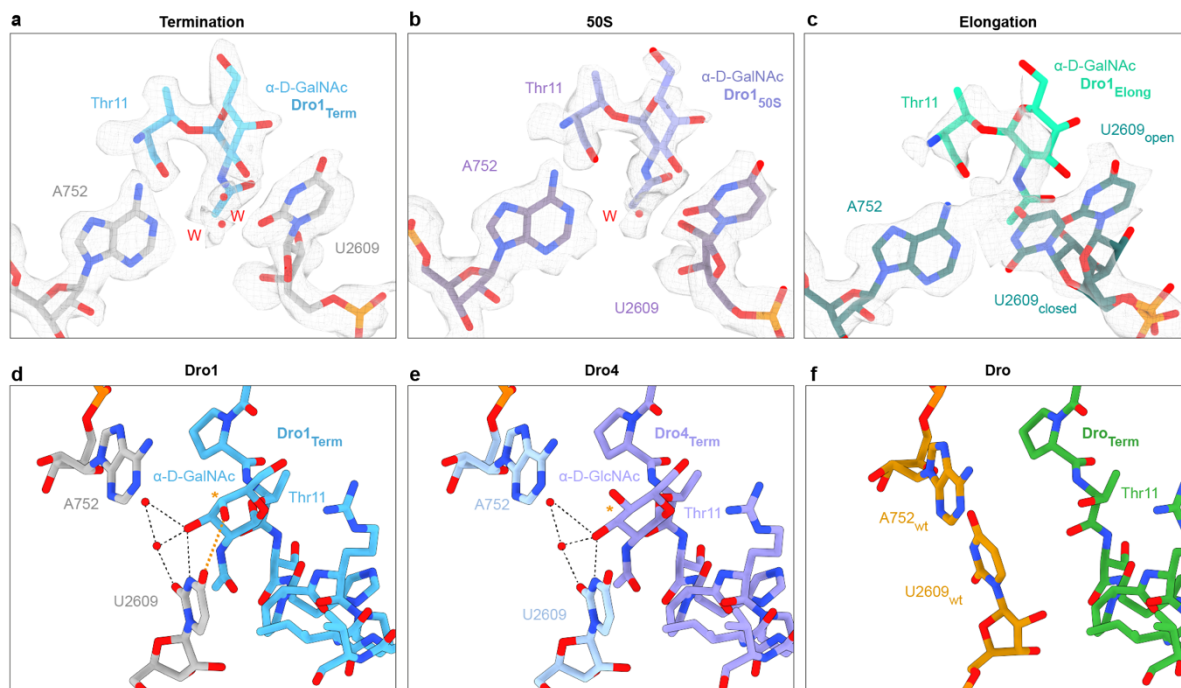
	<b>Termination complex</b>	<b>Elongation complex</b>	<b>50S complex</b>
EMDB ID	<b>EMD-15488</b>	<b>EMD-15523</b>	<b>EMD-15533</b>
PDB ID	<b>8AKN</b>	<b>8AM9</b>	<b>8ANA</b>
Magnification (×)	96,000	96,000	96,000
Electron fluence (e <sup>-</sup> /Å <sup>2</sup> )	40	40	40
Defocus range (μm)	-0.4 to -0.9	-0.4 to -0.9	-0.4 to -0.9
Pixel size (Å)	0.80	0.80	0.80
Initial particles	529,600	529,600	529,600
Final particles	137,449	84,697	159,749
Average resolution (Å) (FSC <sub>0.143</sub> )	2.3	2.8	2.1
<b>Model composition</b>			
Atoms	146,523	142,038	86,889
Protein residues	5,960	5,606	3,196
RNA bases	4,552	4,554	2,872
<b>Refinement</b>			
Map CC around atoms	0.69	0.82	0.84
Map CC whole unit cell	0.65	0.70	0.77
Map sharpening B factor (Å <sup>2</sup> )	-4.7	-26.7	-7.2
Bond lengths (Å)	0.015	0.009	0.011
Bond angles (°)	1.863	1.014	1.659
<b>Validation</b>			
MolProbity score	1.88	2.00	1.40
Clash score	3.77	5.60	2.12
Poor rotamers (%)	2.15	3.55	1.23
<b>Ramachandran statistics</b>			
Favoured (%)	92.76	95.91	94.95
Outlier (%)	1.06	0.27	0.8



**Supplementary Figure 5: Dro1 binding compared to Api137, Pyr and Bac7.** **a**, Position of Dro1 (light blue) in the NPET of the *E. coli* ribosome of the termination complex with P-tRNA (lime), RF1 (orange), uL4 (green) and uL22 (dark blue). **b-d**, Superimposition of Dro1 (light blue) with **(b)** Api137 (salmon) from the Api137-ArfB complex (PDB ID 6YSS) (Chan et al., 2020), and **(c)** Pyrrhocorin (Pyr, purple) from the Pyr-70S complex (PDB ID 5FDV) (Seefeldt et al., 2016) and **(d)** Bac7(1-16) (lime) from the Bac7-70S complex (PDB ID 5F8K) (Seefeldt et al., 2016).



**Supplementary Figure 6: Interactions of the mRNA with 23S rRNA in the elongation and termination complex.** **a**, UAC anticodon stem loop (lime) of the P-site fMet-tRNA interacting with the AUG start codon of the mRNA (light brown) shown in isolated density (mesh). **b**, AAC anticodon stem loop (purple) of the A-site Leu-tRNA interacting with the UUG codon of the mRNA (light brown) shown in isolated density (mesh). **c**, Release factor 1 (RF1<sub>Dro1</sub>) of the termination complex superimposed with a canonical RF1<sub>wt</sub> (olive, PDB ID 4V63) (Laurberg et al., 2008). **d**, Molecular models of RF1<sub>Dro1</sub> (orange), UAA stop codon (lime) of the mRNA and 23S rRNA nucleotides (grey) in isolated density of the termination complex. **e**, RF1<sub>Dro1</sub> (orange), mRNA (lime) and 23S rRNA nucleotides of the termination complex essential for the stop codon recognition superimposed with a canonical termination complex RF1<sub>wt</sub> (olive, PDB ID 4V63), mRNA (purple) and 23S rRNA nucleotides (grey) (Laurberg et al., 2008). **f**, Isolated density of four putative water molecules in close proximity to RF1<sub>Dro1</sub> (orange), mRNA (lime), and 23S rRNA nucleotides (grey) within the termination complex. **g-i**, Potential direct and water-mediated interactions indicated by dotted lines and stacking indicated by three lines. Interactions of the UAA nucleotides of the mRNA stop codon (lime) with side chains G120, T190, H197, T198, S199 and R303 of RF1<sub>Dro1</sub> (orange) as well as A1492, A1493 and G530 nucleotides of the 23S rRNA (grey).



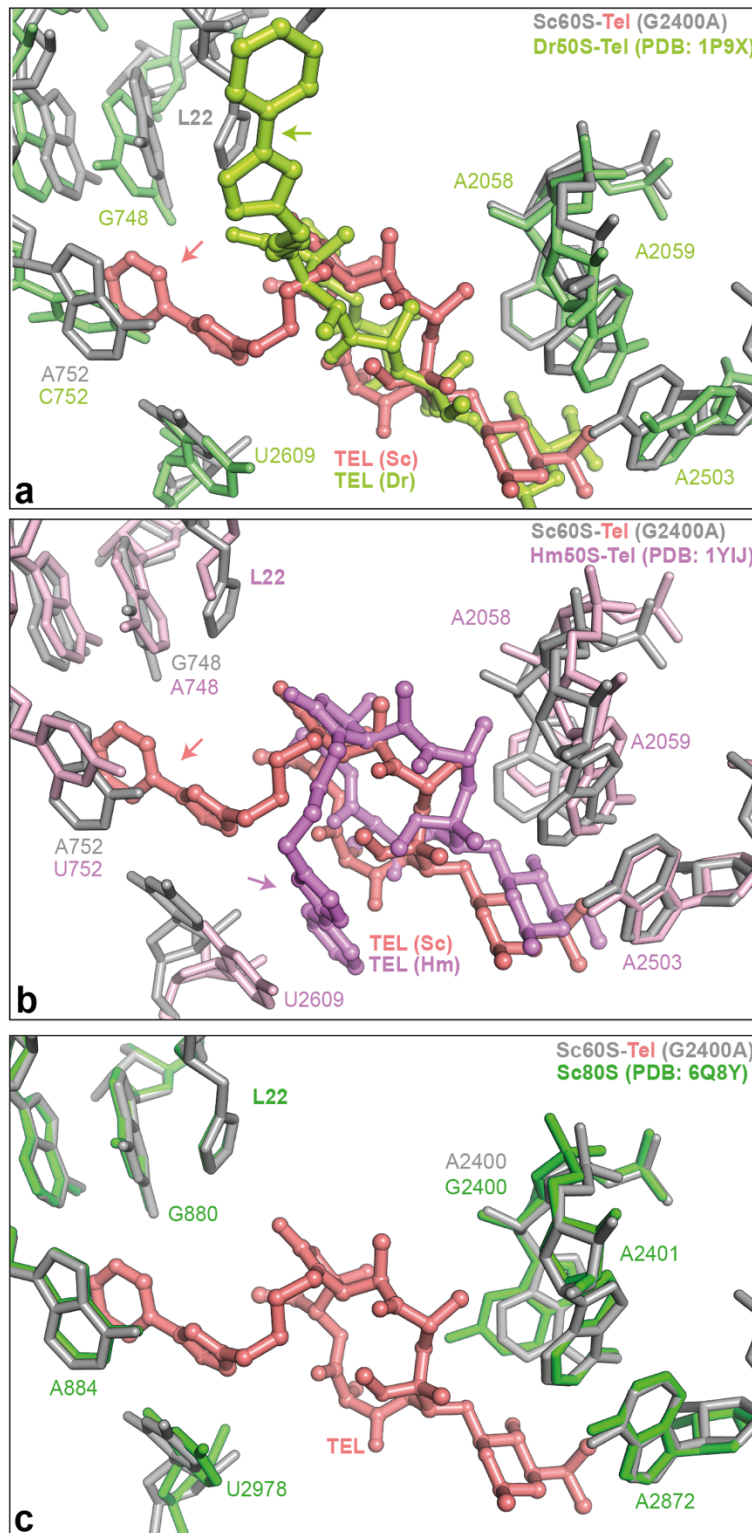
**Supplementary Figure 7: Drosocin sugar modifications.** **a-c**, Molecular model of the O-glycosylation ( $\alpha$ -D-GalNAc) of Thr11 of Dro1 in the termination (**a**), 50S (**b**) and elongation complex (**c**) in isolated density with 23S rRNA nucleotides A752 and U2609 with coordinated waters W (red). **d-f**, Comparison of the open base pair of A752 and U2609 in presence of  $\alpha$ -D-GalNAc in Dro1 (**d**) compared to a *in silico* model of  $\alpha$ -D-GlcNAc in Dro4 (**e**) with an orange asterisks indicating the loss of a potential hydrogen bond in Dro4. In absence of the O-glycosylation in an *in silico* model of Dro (**f**) the base pair is proposed to be closed, indicated by A752 and U2609 from the vacant *E. coli* ribosome (brown, PDB ID 7K00) (Watson et al., 2020).



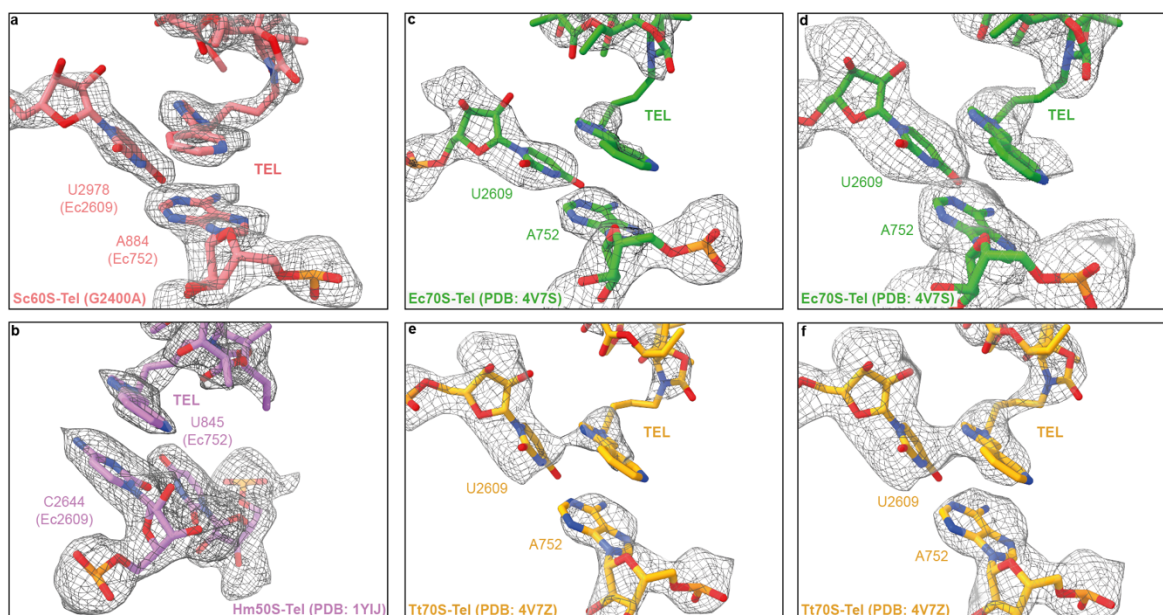
### 13.3. Telithromycin 80S

**Table 7: *S. cerevisiae* 80S-Tel-complex data collection, modelling, and refinement statistics.**

	<b><i>S. cerevisiae</i> Tel-80S-complex</b>
EMDB ID	EMD-11951
PDB ID	7AZY
<b>Data collection</b>	
Electron dose (e <sup>-</sup> /Å <sup>2</sup> )	1.0
Defocus range (µm)	-1.0 to -3.0
Pixel size (Å)	0.822
Initial particles	329,333
Final particles	153,893
Average resolution (Å) (FSC <sub>0.143</sub> )	2.877
<b>Model composition</b>	
Protein residues	6127
RNA bases	3440
<b>Refinement</b>	
Map sharpening B factor (Å <sup>2</sup> )	-10
<b>R.M.S. deviations</b>	
Bond lengths (Å)	0.00
Bond angles (°)	0.02
<b>Validation</b>	
MolProbity score	1.58
Clash score	2-76
Poor rotamers (%)	0.14
<b>Ramachandran statistics</b>	
Favoured (%)	91.17
Outlier (%)	8.40



**Supplementary Figure 8: Alkyl-aryl side chain of Tel is placed differently in different species. a-c,** Tel (salmon) and surrounding 25S rRNA nucleotides (grey) of the G2400A mutant 60S-Tel-complex superimposed with Tel (lime) bound to *D. radiodurans* 50S with 23S rRNA nucleotides (a, light green, PDB ID 1P9X) (Berisio et al., 2003), Tel bound to the *H. marismortui* 50S with 23S rRNA nucleotides (b, pink, PDB ID 1YIJ) (Tu et al., 2005) and the vacant *S. cerevisiae* 60S with 25S rRNA nucleotides (c, green, PDB ID 6Q8Y) (Tesina et al., 2019). Modified from (Svetlov et al., 2021a).



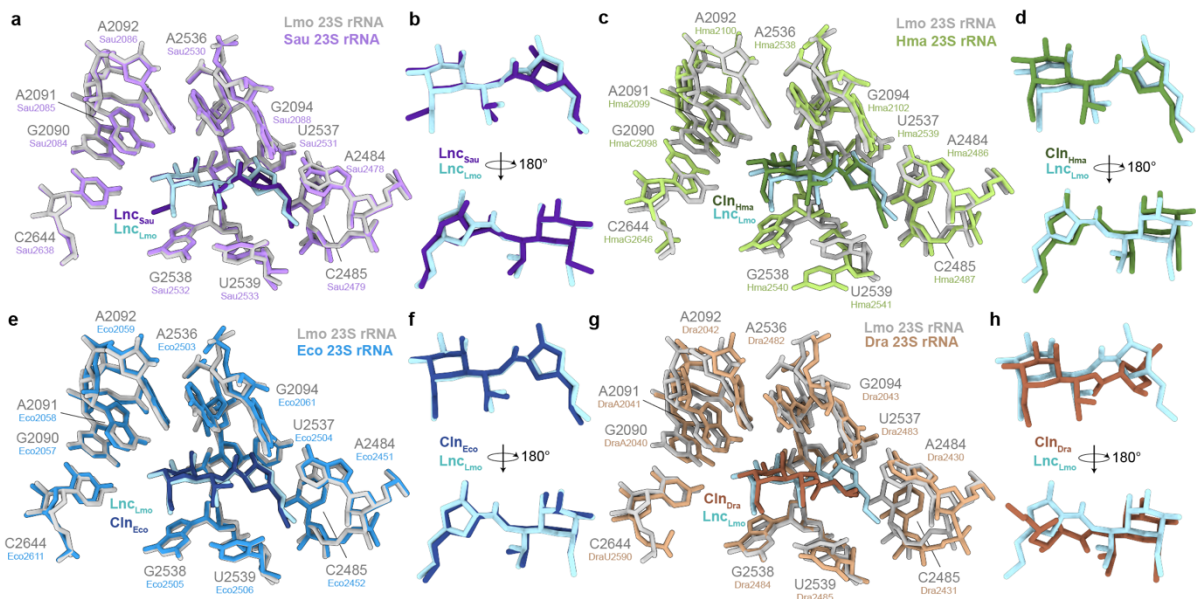
**Supplementary Figure 9: Alkyl-aryl rings of Tel stack onto A752-U2609 base pair.** **a**, Molecular model of Tel (salmon) with 25S rRNA nucleotides (salmo) in isolated density of the G2400A mutant Tel-60S-complex. **b**, Molecular model of Tel (purple) with 23S rRNA nucleotides (purple) of *H. marismortui* (PDB ID 1YIJ) in isolated density (Tu et al., 2005). **c-d**, Molecular model of Tel (green) with 23S rRNA nucleotides (green) of *E. coli* (PDB ID 4V7S) with isolated density at two thresholds (Dunkle et al., 2010). **e-f**, Molecular model of Tel (yellow) with 23S rRNA nucleotides (yellow) of *T. thermophilus* (PDB ID 4V7Z) in isolated density (Bulkley et al., 2010). Modified from (Svetlov et al., 2021a).

### 13.4. *Listeria monocytogenes* complexes

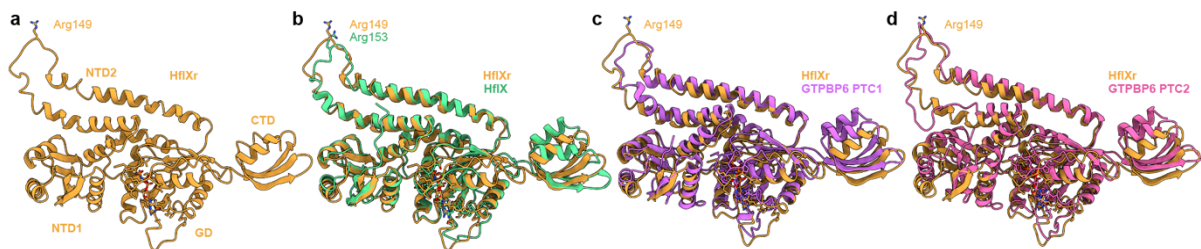
**Table 8: *Listeria monocytogenes* data collections, modelling, and refinement statistics.**

	<b>LmoHflXr-50S</b>	<b>Lmo70S</b>	<b>Lmo70S-Inc</b>	<b>Lmo50S-Inc</b>	<b>LmoHflX-50S</b>
EMDB ID	15161	15204	15175	15864	15670
PDB ID	8A57	8A63	8A5I		
<b>Data collection</b>					
Magnification (×)	165,000	165,000	270,000	270,000	165,000
Electron fluence (e <sup>-</sup> /Å <sup>2</sup> )	35.022	30.255	40.3	40,3	30
Defocus range (µm)	-0.8 to -2.0	-0.5 to -1.5	-0.4 to -1.4	-0.4 to -1.4	-0.6 to -1.6
Pixel size (Å)	0.82	0.82	0.7725	0.7725	0.82
Initial particles	206,159	110,725	506,262	506,262	266,147
Final particles	204,545	14,097	172,106	285,330	76,519
Average resolution (Å) (FSC <sub>0.143</sub> )	2.3	3.1	2.3	2.1	2.76
<b>Model composition</b>					
Atoms	92,760	88,390	89,799		
Protein residues	3,527	2,973	2,973		
RNA bases	3,022	3,022	3,022		
<b>Refinement</b>					
Map CC around atoms	0.75	0.81	0.73		
Map CC whole unit cell	0.61	0.69	0.49		
Map sharpening B factor (Å <sup>2</sup> )	-38.6	-55	-47.2		
<b>R.M.S. deviations</b>					

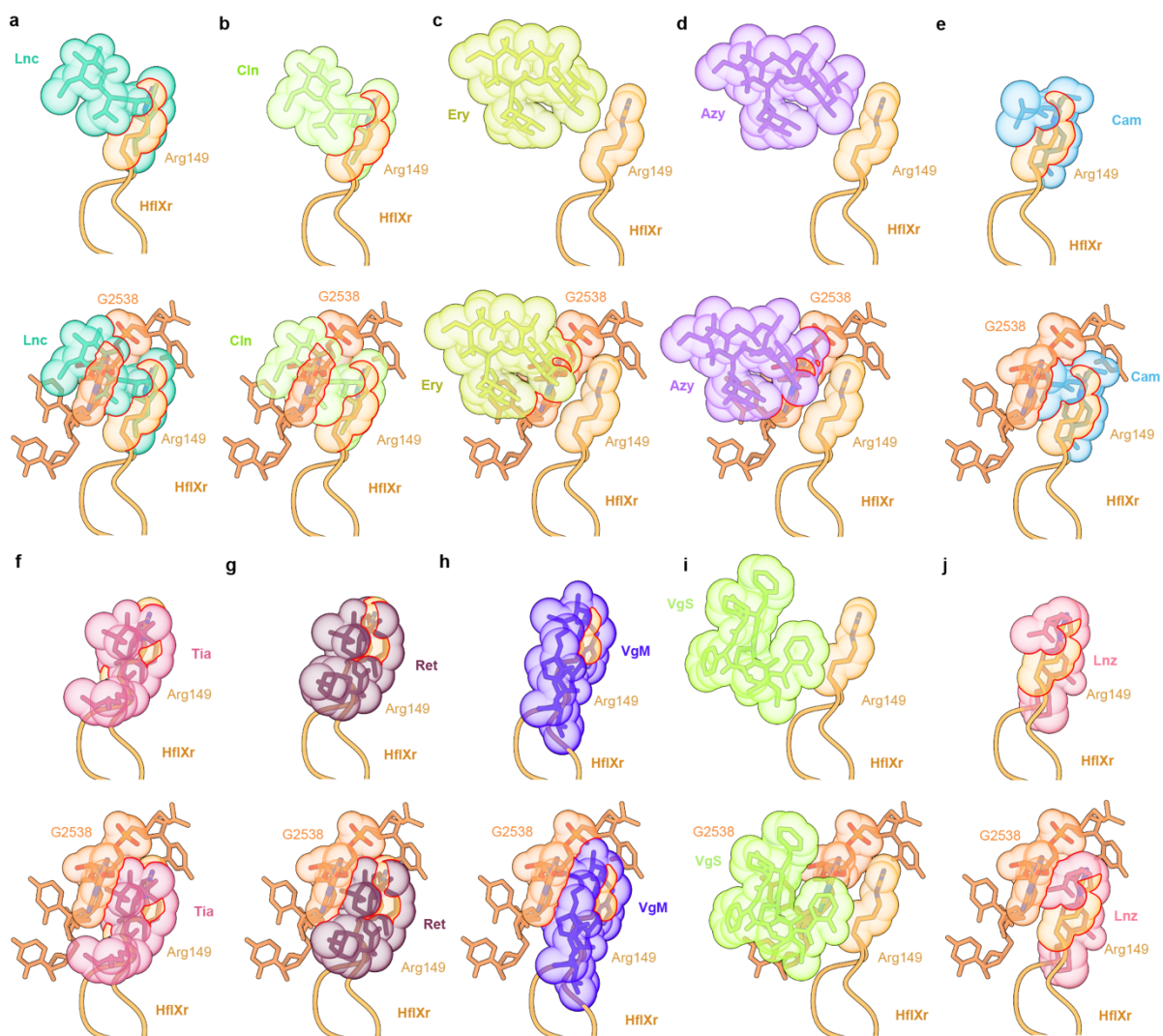
Bond lengths (Å)	0.011	0.011	0.011		
Bond angles (°)	1.727	1.662	1.734		
<b>Validation</b>					
MolProbity score	1.92	1.65	1.86		
Clash score	3.27	2.93	3.32		
Poor rotamers (%)	2.49	1.8	2.48		
<b>Ramachandran statistics</b>					
Favoured (%)	91.72	94.62	93.21		
Outlier (%)	1.21	0.89	1.37		



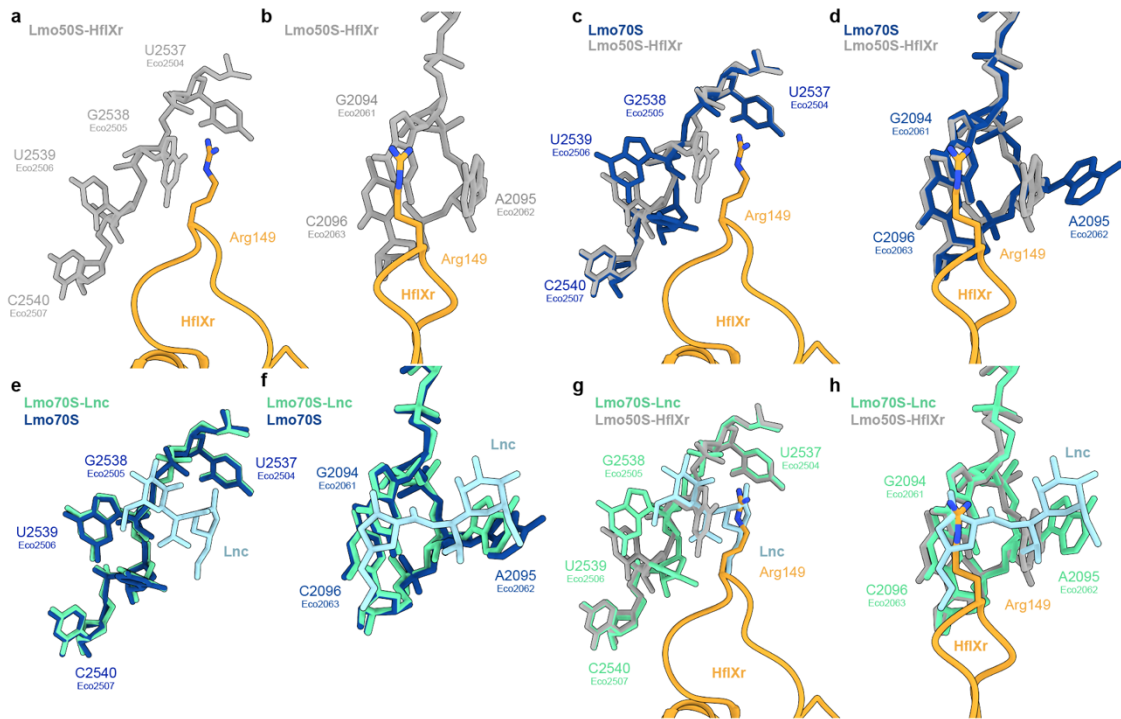
**Supplementary Figure 10: Superimposition of lincomycin and clindamycin bound to ribosomes from different organisms.** a-h, Lincomycin (Lnc<sub>Lmo</sub>, light blue) from the Lnc-70S-complex with surrounding *L. monocytogenes* 23S rRNA nucleotides (grey) superimposed with (a-b) lincomycin (Lnc<sub>Sau</sub>, purple) bound to *S. aureus* with surrounding 23S rRNA nucleotides (light purple) (PDB ID 5HKV) (Matzov et al., 2017), with (c-d) clindamycin (Cln<sub>Hma</sub>, green) bound to *H. marismortui* with surrounding 23S rRNA nucleotides (light green) (PDB ID 1YJN) (Tu et al., 2005), with (e-f) clindamycin (Cln<sub>Eco</sub>, dark blue) bound to *E. coli* with surrounding 23S rRNA nucleotides (blue) (PDB ID 4V7V) (Dunkle et al., 2010) and with (g-h) clindamycin (Cln<sub>Dra</sub>, brown) bound to *D. radiodurans* with surrounding 23S rRNA nucleotides (light brown) (PDB ID 1JZX) (Schlunzen et al., 2001). Additionally, two views of lincomycin (Lnc<sub>Lmo</sub>, light blue) with the antibiotics bound to other structures is shown. Modified from (Koller et al., 2022b).



**Supplementary Figure 11: Superimposition of HflXr with homologs.** a, *L. monocytogenes* HflXr (orange) superimposed with (b) *E. coli* HflX (teal, PDB ID 5ADY) (Zhang et al., 2015b), with (c) human mitochondrial GTPBP6 in PTC1 conformation 1 (purple, PDB ID 7OF4) and with (d) human mitochondrial GTPBP6 in PTC2 conformation 2 (pink, PDB ID 7OF6) (Hillen et al., 2021), aligned based on 23S rRNA. Modified from (Koller et al., 2022b).

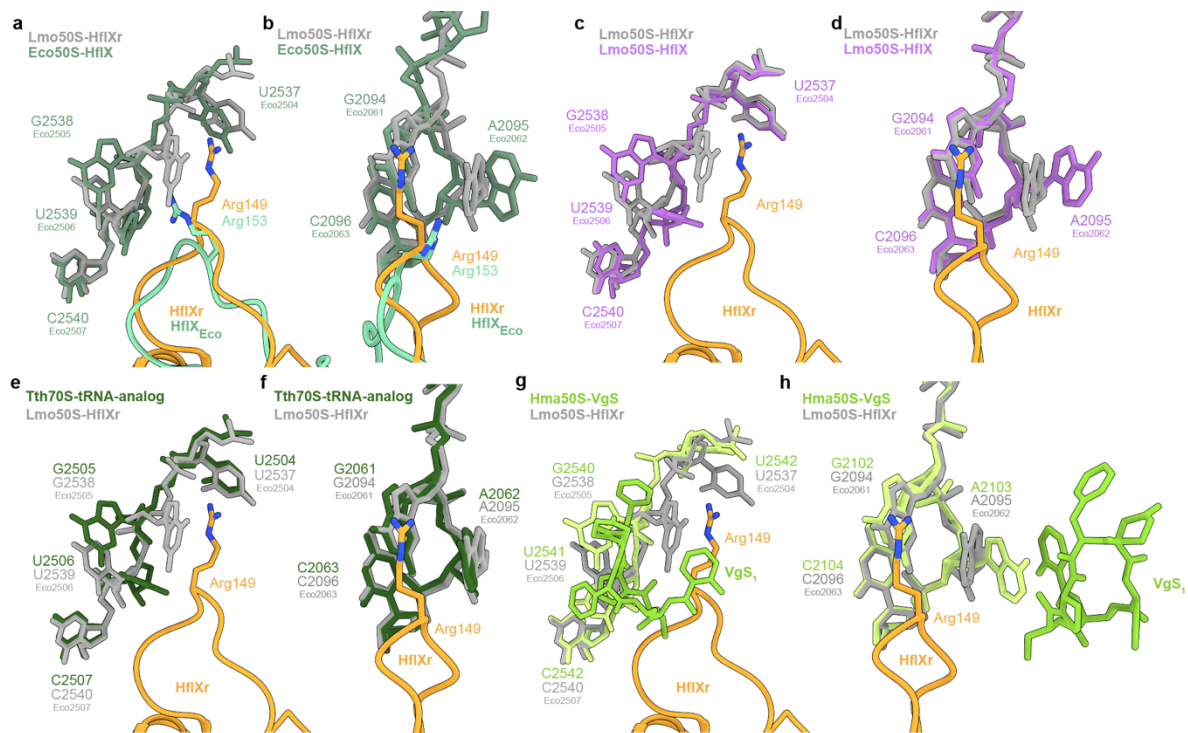


**Supplementary Figure 12: a-j,** Arg149 of the NTD2-loop of *L. monocytogenes* HflXr (orange) shown as sphere with surrounding 23S rRNA nucleotide G2538 shown as sphere (dark orange) superimposed with (a) lincomycin (Lnc, teal), (b) clindamycin (Cln, light green, PDB ID 4V7V) (Dunkle et al., 2010), (c) erythromycin (Ery, yellow, PDB ID 4V7U) (Dunkle et al., 2010), (d) azithromycin (Azi, purple, PDB ID 4V7Y) (Bulkley et al., 2010), (e) tiamulin (Tia, pink, PDB ID 1XBP) (Schlunzen et al., 2004), (f) retapamulin (Ret, dark purple, PDB ID 2OGO) (Davidovich et al., 2007), (g) virginiamycin M (VgM, dark blue, PDB ID 1YIT) (Tu et al., 2005), (h) virginiamycin S1 (VgS1, lime, PDB ID 1YIT) (Tu et al., 2005), (i) chloramphenicol (Cam, blue, PDB ID 4V7W) (Syroegin et al., 2022a) and (j) linezolid (Lnz, light pink, PDB ID 7S1H) (Syroegin et al., 2022b). Modified from (Koller et al., 2022b).

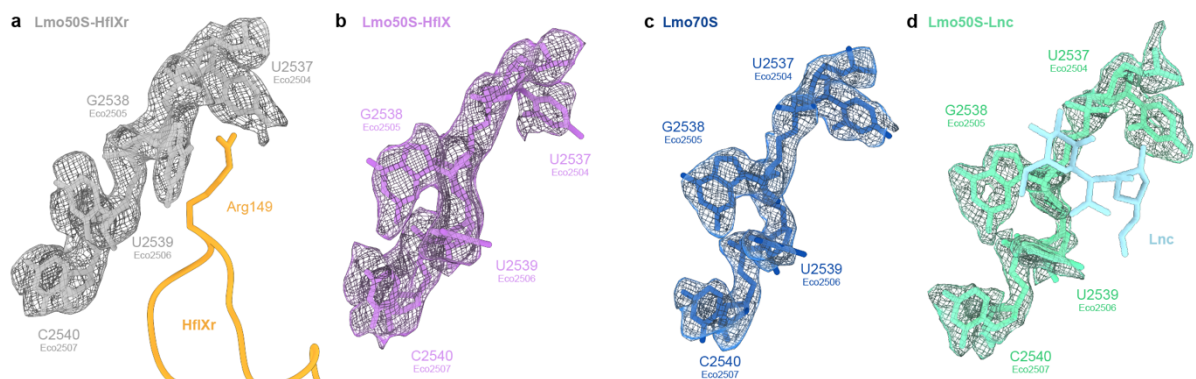


**Supplementary Figure 13: HflXr induces 23S rRNA nucleotide movements at the PTC.** a-b, Arg149 of the NTD2-loop of *L. monocytogenes* HflXr (orange) with surrounding 23S rRNA nucleotides (grey) superimposed with (c-d) vacant *L. monocytogenes* 70S ribosome 23S rRNA nucleotides (dark blue). e-h, Superimposition of lincomycin (Lnc, light blue) bound to *L. monocytogenes* 70S with 23S rRNA nucleotides (teal) with (e-f) vacant *L. monocytogenes* 23S rRNA nucleotides (dark blue) and with (g-h) Arg149 of the NTD2-loop of *L. monocytogenes* HflXr (orange) with surrounding 23S rRNA nucleotides (grey). Modified from (Koller et al., 2022b).





**Supplementary Figure 14: HflXr induces 23S rRNA nucleotide movements at the PTC.** a-h, Arg149 of the NTD2-loop of *L. monocytogenes* HflXr (orange) with surrounding 23S rRNA nucleotides (grey) superimposed with (a-b) Arg153 of the NTD2-loop of *E. coli* HflXr (cyan) with surrounding 23S rRNA nucleotides (dark green, PDB ID 5ADY) (Zhang et al., 2015b), with (c-d) vacant *L. monocytogenes* 70S 23S rRNA nucleotides (purple) refined into the HflXr-50S-GDPNP complex, with (e-f) *T. thermophilus* 23S rRNA (dark green, PDB ID 7RQA) (Syroegin et al., 2022a) in presence of tRNA-analogs and with (g-h) *H. marismortui* 50S 23S rRNA (light green) with Virginiamycin S (VgS<sub>1</sub>, green, PDB ID 1YIT) (Tu et al., 2005). Modified from (Koller et al., 2022b).











**Supplementary Figure 15: Conformational changes of PTC nucleotides are not induced by HflX.** a, Arg149 of NTD2-loop of HflXr (orange) with 23S rRNA nucleotides in cryo-EM density (grey mesh). b, 23S rRNA nucleotides (purple) of the vacant *L. monocytogenes* 70S refined into the cryo-EM density (purple mesh) of the 50S-HflXr-GDPNP-complex. c, 23S rRNA nucleotides (dark blue) of the vacant *L. monocytogenes* 70S in cryo-EM density (blue mesh). d, Lincomycin (Lnc, light blue) with 23S rRNA nucleotides (teal) of the Lmo-70S-Lnc-complex in cryo-EM density (teal mesh). Modified from (Koller et al., 2022b).



## 14. Auflistung der Gefahrstoffe nach GHS


Table 9: Gefahrstoffe nach GHS.

Chemikalie	GHS-Symbol	H-Sätze	P-Sätze
Ammoniumacetat	-	-	-
Ammoniumchlorid		302, 319	305+351+338
Chloramphenicol		318, 351, 361fd	202, 280, 305+351+338, 310, 405, 501
Dinatriumhydrogenphosphat	-	-	-
Dithiothreitol		302, 315, 318	264, 270, 280, 301+312, 302+352, 305+351+338
Dodecyl-beta-D-maltoside		315, 319, 335	261, 264, 303+361+353, 305+351+338+310
EDTA		319, 332, 373	280, 304+340, 312, 305+351+338, 337+313,
Ethan		220, 280	210, 377, 381, 403
Ethanol		225, 319	210, 240, 305+351+338, 403+233
HEPES-Puffer	-	-	-
Kaliumacetat	-	-	-
Kaliumchlorid	-	-	-
Kaliumhydroxid		290, 302, 315	280, 301+330+331, 305+351+338, 308+310

Kanamycin		360	201, 202, 280, 308+313
Lithiumchlorid		302, 315, 319	302+352, 305+351+338
Luciferase-Substrat		373	314, 501
Magnesiumacetat	-	-	-
Magnesiumchlorid	-	-	-
Natriumchlorid	-	-	-
Natriumdihydrogenphosphat	-	-	-
Natriumhypochlorit	 , 9	290, 314, 335, 410	260, 273, 280, 303+361+353, 305+351,338, 310, 390, 403+233
NTP-mix	-	-	-
Putrescine	 6	226, 302, 311, 314, 330	210, 280, 303+361+353, 304+340+310, 305+351+338
Rnase inhibitor	-	-	-
Saccharose	-	-	-
Salzsäure		290, 314, 335	280, 303+361+353, 305+351+338+310
Spermidine		314	260, 280, 303+361+353, 305+351+338, 321, 501
Stickstoff, flüssig		281	282, 336+315, 403
Telithromycin		302, 315, 319, 335	261, 305+351+338
Tris-Puffer	-	-	-

## 15. Eidesstattliche Erklärung

Hiermit erkläre ich an Eides statt, die vorliegende Dissertation selbst verfasst und keine anderen als die angegebenen Hilfsmittel benutzt zu haben.

Timm Oliver Koller  Hamburg, den 13.03.2023